

Investigating the Simple Shear Response of Gravelly Soils Using the Discrete Element Method

by

Nina Zabihi

A dissertation submitted in partial fulfillment
of the requirements for the degree of
Doctor of Philosophy
(Civil Engineering)
in the University of Michigan
2020

Doctoral Committee:

Adjunct Associate Professor Adda Athanasopoulos-Zekkos, Co-Chair
Professor Radoslaw Michalowski, Co-Chair
Professor Yin Lu Young
Adjunct Associate Professor Dimitrios Zekkos

Nina Zabihi

ninazbh@umich.edu

ORCID iD: 0000-0003-2947-1298

© Nina Zabihi 2020

Dedication

To my parents, Fattaneh and Lotfollah, and
my sisters, Roshanak and Maryam,
for their endless love and unwavering support and encouragement

Acknowledgements

First and foremost, I would like to express my deep and sincere gratitude to my doctoral advisor, Dr. Adda Athanasopoulos-Zekkos, for her invaluable guidance and constant support and encouragement throughout my PhD journey. She has been an exceptional teacher, enthusiastic advisor and great mentor. I will forever be grateful for all the things I have learned from her and for the opportunities that she has provided me over the past five years.

I would like to extend my gratitude to my committee members, Professor Radoslaw Michalowski, Dr. Dimitrios Zekkos, and Professor Yin Lu Young for their constructive feedbacks and suggestions at various stages of this research that greatly improved this dissertation. I would also like to thank all the geotechnical faculty members at the University of Michigan, including Professor Richard Woods and Professor Roman Hryciw. They are excellent teachers and I am thankful for everything I have learned from them.

This dissertation would not be possible without the generous support by the National Science Foundation CAREER Grant No. 1351403, the Itasca Educational Partnership research program, the Rackham Graduate Student Research Grant, and the Graduate Student Instructor appointments from the Civil and Environmental Engineering department at the University of Michigan.

I would also like to express my gratitude to the current and former students in the geotechnical engineering group who made our offices a friendly, inclusive and productive research environment. They include Athina Grizi, Jonathan Hubler, Zhijei Wang, Junxing Zheng, William

Greenwood, Sampurna Datta, Dowon Park, Andrea Ventola, Michelle Basham, Goldi Gunawan, and Cassandra Champagne, among others. Thank you all for your friendship and support, and all the pleasant times we have had together.

I would also like to thank my dear friends both inside and outside Ann Arbor for their friendship and companionship during both happy and difficult times. I cannot imagine how my life would have been if I did not share all the good moments and memories with them.

Finally, my deepest and heartfelt appreciation goes to my parents, Fattaneh and Lotfollah, for their unconditional love and endless support during all my life. They have always believed in me and encouraged me to reach for my goals and aim high. I also want to thank my sisters, Roshanak and Maryam, for always being there for me and loving me. I love you all from the bottom of my heart, and I can never thank you enough for all that you have done for me.

Table of Contents

Dedication	ii
Acknowledgements	iii
List of Tables	viii
List of Figures	ix
List of Appendices	xxii
Abstract	xxiii
Chapter 1 Introduction	1
1.1 Motivation	1
1.2 Research Objectives	3
1.3 Organization of Dissertation	5
Chapter 2 Literature Review	7
2.1 Undrained Response of Cohesionless Granular soils	7
2.2 Overview of Laboratory Testing of Gravelly Soils	12
2.3 Simple Shear Test	13
2.4 Continuum Based Numerical Methods in Geotechnical Engineering	17
2.5 Discrete Element Method and PFC3D	19
2.5.1 Law of Motion	24
2.5.2 Force Displacement Law	25
2.5.3 Measurement Quantities	28
2.6 DEM in Modeling Soil Response	30
2.7 Incorporating the Effect of Actual Particle Shape	48
Chapter 3 Monotonic and Cyclic Simple Shear Response of Steel Spheres	57
3.1 Introduction	57

3.2 Large-scale simple shear tests on uniformed-sized chrome steel spheres specimen	58
3.3 3D DEM Modeling of Simple Shear Tests on Uniform Steel Spheres Specimens	64
3.4 Conclusions	88
Chapter 4 DEM Modeling of the Monotonic Simple Shear Response of Pea Gravel	90
4.1 Introduction	90
4.2 Soil Particles Size and Shape Characterization	91
4.3 Development of the DEM Model for Constant Volume Monotonic Simple Shear Test of Pea Gravel	98
4.4 Macroscopic Behavior Measured at Boundaries	104
4.5 Stress measurement at boundaries versus inside specimen core	109
4.6 Non-uniformities inside the specimen	119
4.7 Stress State inside the specimen	137
4.8 Principal stress rotation during shear	143
4.9 Evolution of fabric during shear	145
4.10 Non-coaxiality of principal stress and strain increment	152
4.11 Effect of the non-uniform distribution of rolling resistance	155
4.12 Conclusions	160
Chapter 5 DEM Modeling of the Cyclic Simple Shear Response of Pea Gravel	169
5.1 Introduction	169
5.2 Development of the DEM Model for Constant Volume Cyclic Simple Shear Test of Pea Gravel	170
5.3 Macroscopic Behavior Measured at Boundaries	171
5.4 Stress measurement at boundaries versus inside specimen core	177
5.5 Non-uniformities inside the specimen during cyclic simple shear loading	183
5.6 Principal stress rotation during cyclic simple shear loading	199
5.7 Evolution of fabric during cyclic simple shear loading	201
5.8 Effect of the non-uniform distribution of rolling resistance	210
5.9 Conclusions	212
Chapter 6 Conclusions and Recommendations for Future Research	218
6.1 Development of the DEM Model for Constant Volume Simple Shear Test	218

6.2 Constant Volume Monotonic Simple Shear Response of Pea Gravel at the Micro- and Meso-scale	220
6.3 Constant Volume Cyclic Simple Shear Response of Pea Gravel at the Micro- and Meso-scale	227
6.4 Recommendations for future research	232
Appendices	234
Bibliography	274

List of Tables

Table 3.1 Material and contact properties used in the DEM simulations	69
Table 3.2 List of the simulations considered for the DEM analyses	73
Table 4.1 Mobilized friction angles from simulation and experimental results	109
Table 4.2 degree of fabric anisotropy, in terms of contact normal orientations, at the end of consolidation in DEM simulations of Pea gravel specimen	149

List of Figures

Figure 2.1 Typical monotonic undrained shear behavior of cohesionless soils (Mitchell and Soga, 2005)	9
Figure 2.2 Cyclic undrained shear behavior of contractive cohesionless soils, true liquefaction and limited liquefaction (Chern, 1985).....	10
Figure 2.3 Cyclic undrained shear behavior of dilative cohesionless soils, cyclic mobility (Chern, 1985)	11
Figure 2.4 Monotonic Undrained Response of Fraser River Sand in Simple Shear (Sivathayalan, 1994)	12
Figure 2.5 Cyclic Undrained Response of Fraser River Sand in Simple Shear (Sivathayalan, 1994)	12
Figure 2.6 Ideal direct simple shear condition versus the realistically imposed condition in simple shear device (Degroot et al., 1994)	14
Figure 2.7 Mohr's circle for assumed failure modes in simple shear test (Budhu, 1988).....	16
Figure 2.8 Schematic overview of the sequence of calculations in DEM simulation, a) overall procedure, b) sequence of calculations completed within each time increment (O'Sullivan, 2011)	21
Figure 2.9 Main features in Discrete Element Method (Ng and Dobry, 1994)	22
Figure 2.10 Effect of particle rotation inhibition on results of 2D simulations of drained monotonic triaxial compression test (Ng and Dobry, 1994)	31
Figure 2.11 Effect of particle rotation inhibition on results of 2D simulations of constant volume, strain-controlled cyclic shear tests (Ng and Dobry, 1994).....	32
Figure 2.12 Effect of inter-particle friction coefficient on results of 3D simulations of drained monotonic triaxial compression test (Ng and Dobry, 1994)	32
Figure 2.13 Relationship between microscopic friction angle and macroscopic friction angle from results of 3D simulations of drained monotonic triaxial compression test (Ng and Dobry, 1994).....	32
Figure 2.14 Assembly stress in terms of coefficient of anisotropy (Rothenburg and Bathurst, 1989).....	34
Figure 2.15 Specimen deformation in 2D direct shear test (Thornton and Zhang, 2003)	34
Figure 2.16 Effect of loading condition on the failure surface; Projected on p-q space (left) and e-ln p spaces (right)space (Zhao and Evans, 2011).....	37

Figure 2.17 evolution of average coordination number during undrained (constant volume) triaxial shear test on loose and dense samples at a confining pressure of 50 kPa (Sitharam et al., 2002).....	38
Figure 2.18 Example of undrained stress-controlled cyclic response of loose poly-disperse disks (Sitharam, 2003).....	39
Figure 2.19 Example of undrained stress-controlled cyclic response of dense poly-disperse disks (Sitharam, 2003).....	39
Figure 2.20 Evolution of major principal stress and strain rate orientations in 2D constant load simple shear simulation (Ai et al., 2014)	42
Figure 2.21 Comparison of actual mobilized friction angle with the ones from assumed stress state for simple shear specimen in which horizontal plane coincides with plane of maximum shear or maximum stress obliquity: Drained condition (left), undrained condition(right) (Wijewickreme et al., 2013).....	43
Figure 2.22 Evolution of fabric anisotropy in specimen of glass beads during cyclic loading (Asadzadeh and Soroush, 2017).....	46
Figure 2.23 Rose diagrams of contact normal forces in specimen of glass beads before shearing and during the seventh cycles of shear for $\sigma'_{v0}=100$ kPa and CSR=0.15 – Stronger contacts are denoted as darker bins. (Asadzadeh and Soroush, 2017).....	46
Figure 2.24 Fabric parameters (Ng, 2001).....	49
Figure 2.25 Presenting real shape of particles using clusters; a) outline of real particle, b) superimposing DEM disc element over the real shape; c) representing real shape using cluster of discs; d) various combinations of disks in the form of clusters (Jensen et al., 1999).....	50
Figure 2.26 Modelling the shear surface (bottom boundary) roughness by saw-tooth shapes of different amplitudes and periods; a) saw-tooth period of four times the diameter of the non-clustered particle, $\lambda=4D$; b) saw-tooth period of two times the diameter of the clustered particle, $\lambda=2D$ (The cluster diameter is equal to the diameter of the non-clustered particles) (Jensen et al., 1999)	51
Figure 2.27 Graphs of shear stress at shearing wall (left) and vertical displacement of top wall (right) versus tangential displacement of shearing wall (vertical stress are equal to 50, 100, and 200 MPa for cases L, M, and H, respectively) (Jensen et al., 1999)....	51
Figure 2.28 Graphs of average particles displacement by horizontal layers (left) and average particles rotation (Θ) by horizontal layers (right) versus the tangential displacement of shear wall (g_t) (Jensen et al., 1999).....	52
Figure 2.29 Influence on the number of spheres per clumped element (1, 2, 3, 4) on the geometry of the clumps for angularity = 1 (Salot et al., 2009)	53
Figure 2.30 Influence of angularity on the geometry of elements composed of two spheres (Salot et al., 2009).....	53
Figure 2.31 Particle shapes used in simulations and grain size distribution of a particle assemblage scaled relative to that of Fontainebleau sand (Garcia and Bray, 2018) .	54

Figure 2.32 Particle shapes used in simulations; a) spheres, b) sub-rounded sphere-clusters, c) sub-angular sphere-clusters (Garcia and Bray, 2019)	55
Figure 2.33 Disc and clumps particles used in simulation (Zhou et al., 2013).....	56
Figure 3.1 Schematic of cyclic direct simple shear device used in this study (Zekkos et al., 2018)	59
Figure 3.2 Large scale cyclic direct simple shear device at the University of Michigan (Hubler, 2017)	59
Figure 3.3 Prepared specimen of uniform-sized chrome steel sphere	60
Figure 3.4 Example of vertical strains during monotonic simple shear test ($\sigma'_{v0}=400$ kPa)	61
Figure 3.5 Constant volume monotonic simple shear test results for steel spheres ($D_r=45\%$).....	63
Figure 3.6 Constant volume cyclic simple shear test results for steel spheres ($D_r=45\%$, $CSR=0.07$)	63
Figure 3.7 a) Numerical DEM Model and (b) Experimental specimen of 10,636 chrome steel spheres each.	65
Figure 3.8 DEM simulation results considering different rates of shear for constant volume simple shear test of steel spheres ($\sigma'_{v0}=400$ kPa, $D_r=45\%$)	68
Figure 3.9 Comparison of the results from DEM simulation and the corresponding experimental data for constant volume monotonic simple shear test on steel spheres ($\sigma'_{v0}=400$ kPa, $D_r=45\%$).....	70
Figure 3.10 Horizontal displacement profile of stacked rings during monotonic shear in the DEM simulation of steel spheres for two levels of shear strain: 0.5 and 3.75% ($\sigma'_{v0}=400$ kPa, $D_r=45\%$)	71
Figure 3.11 The DEM simulation results considering actual versus theoretical simple shear strain in specimen of steel spheres ($\sigma'_{v0}=400$ kPa, $D_r=45\%$).....	72
Figure 3.12 Comparison of the DEM simulation results from models A-1 and A-2 for specimen of steel spheres ($\sigma'_{v0}=400$ kPa, $D_r=45\%$)	75
Figure 3.13 Horizontal displacement profile of stacked rings during monotonic shear of steel spheres in models A-1 and A-2 for two levels of shear strain: 0.5 and 3.75% ($\sigma'_{v0}=400$ kPa and $D_r=45\%$)	75
Figure 3.14 Horizontal displacement profile of stacked rings during monotonic shear in models A-1 and B-1 for two levels of shear strain: 0.5 and 3.75% (specimens of steel spheres with $\sigma'_{v0}=400$ kPa and $D_r=45\%$)	76
Figure 3.15 Horizontal displacement profiles of stacked rings during monotonic shear in models A-3 and B-3 compared to those in models A-1 and B-1, respectively, for two levels of shear strain: 0.5 and 3.75% (specimens of steel sphere with $\sigma'_{v0}=400$ kPa and $D_r=45\%$).....	78
Figure 3.16 The DEM simulation results from model A-3 considering actual versus theoretical simple shear strain in specimen of steel spheres ($\sigma'_{v0}=400$ kPa, $D_r=45\%$).....	78

Figure 3.17 Effect of preventing rolling (models A-4, B-4) or sliding (model A-5) at caps on the horizontal displacement profile of stacked rings during monotonic shear for two levels of shear strain: 0.5 and 3.75%	79
Figure 3.18 Horizontal displacement profile of stacked rings during monotonic shear in model A-4 at different theoretical strain levels (specimen of steel spheres with $\sigma'_{v0}=400$ kPa and $D_r=45\%$)	80
Figure 3.19 The DEM simulation results from model A-4 considering theoretical simple shear strain (specimen of steel spheres with $\sigma'_{v0}=400$ kPa and $D_r=45\%$)	81
Figure 3.20 The DEM simulation results from models B-4 and A-5 (specimen of steel spheres with $\sigma'_{v0}=400$ kPa and $D_r=45\%$)	82
Figure 3.21 Horizontal displacement profile of stacked rings during monotonic shear in models C-4 and D-4 for two levels of shear strain: 0.5 and 3.75% ($\sigma'_{v0}=400$ kPa)	84
Figure 3.22 The DEM simulation results from models C-4 and D-4 ($\sigma'_{v0}=400$ kPa).....	85
Figure 3.23 DEM specimen of 47,862 spheres of two different sizes (model A-5-Bidisperse)...	86
Figure 3.24 Simulated monotonic simple shear response of the specimen with two sizes of spherical particles (model A-5-Bidisperse, $\sigma'_{v0}=400$ kPa, $e=0.574$)	87
Figure 3.25 Simulated stress-controlled cyclic simple shear response for specimen of bi-disperse spheres ($\sigma'_{v0}=400$ kPa, $e=0.574$, $CSR=0.09$).....	88
Figure 4.1 Translucent Segregation Table (TST) system (Ohm and Hryciw, 2013).....	93
Figure 4.2 One of ten images taken using the TST of the Pea gravel particles used in the tested specimen (There are 2,550 particles in this image)	93
Figure 4.3 TST data on Distributions (in terms of cumulative number of particles) of size, sphericity, aspect ratio and convexity of tested Pea gravels	94
Figure 4.4 Joint probability of size and rolling resistance coefficient in the assembly of equivalent spheres for the actual Pea gravel particles; (a) 3D view, (b) 2D view	97
Figure 4.5 Spherical particle size distribution curve of simulated specimen	99
Figure 4.6 Rolling resistance coefficient distribution curve of simulated specimen	99
Figure 4.7 (a) Physical and (b) Numerical specimen (21,978 spheres)	100
Figure 4.8 Comparison of the results from DEM simulation of constant volume monotonic simple shear test to the corresponding experimental results for Pea gravel specimen ($\sigma'_{v0}=250$ kPa, $D_r=49\%$): (a) Shear stress vs. shear strain; (b) Stress path; (c) Shear stress normalized by consolidated vertical stress vs. shear strain; (d) Shear stress normalized by vertical stress vs. shear strain; and (e) Pore pressure ratio vs. shear strain.....	103
Figure 4.9 Results from DEM simulation of constant volume monotonic simple shear response of Pea gravel specimen ($D_r=49\%$): (a) Shear stress vs. shear strain; (b) Stress path; (c) Shear stress normalized by consolidated vertical stress vs. shear strain; (d) Shear stress normalized by vertical stress vs. shear strain; and (e) Pore pressure ratio vs. shear strain	105

Figure 4.10	Results from DEM simulation of constant volume monotonic simple shear test of Pea gravel specimen ($D_r=87\%$): (a) Shear stress vs. shear strain; (b) Stress path; (c) Shear stress normalized by consolidated vertical stress vs. shear strain; (d) Shear stress normalized by vertical stress vs. shear strain; and (e) Pore pressure ratio vs. shear strain.....	106
Figure 4.11	Horizontal displacement profile of stacked rings for three levels of boundary shear strain of 0.5, 3.75 and 8% in DEM simulations of constant volume monotonic simple shear response of Pea gravel specimens: $D_r=49\%$ (left) and $D_r=87\%$ (right).....	108
Figure 4.12	The central measurement sphere considered for measurements inside the specimen	111
Figure 4.13	Comparison of the monotonic shear response measured at boundaries and inside the central measurement sphere in DEM simulation of constant volume monotonic simple shear response of Pea gravel specimen ($\sigma'_{v0}=250$ kPa, $D_r=49\%$).....	113
Figure 4.14	Comparison of the monotonic shear response measured at boundaries and inside the central measurement sphere in DEM simulation of constant volume monotonic simple shear response of Pea gravel specimen ($\sigma'_{v0}=250$ kPa, $D_r=87\%$).....	114
Figure 4.15	Comparison of the generated pore pressure ratio based on the measurements at the boundaries and inside the central measurement sphere in DEM simulations of constant volume monotonic simple shear response of Pea gravel specimen: $D_r=49\%$ (left) and $D_r=87\%$ (right)	116
Figure 4.16	Coefficient of lateral pressure during shear in DEM simulations of constant volume monotonic simple shear response of Pea gravel specimen: $D_r=49\%$ (left) and $D_r=87\%$ (right)	118
Figure 4.17	Schematic of the measurement sphere considered for evaluation of non-uniformity inside the specimen (all measurement spheres are at the same elevation as MS1). 120	
Figure 4.18	Void ratio measured inside measurement spheres MS1-MS13 during shear in DEM simulations of constant volume monotonic simple shear response of Pea gravel specimen ($\sigma'_{v0}=250$ kPa and $D_r=49\%$ (left), $D_r=87\%$ (right))	122
Figure 4.19	Distribution of void ratio inside MS1-MS13 in DEM simulations of constant volume monotonic simple shear response of Pea gravel specimen: (a) $\sigma'_{v0}=100$ kPa, (b) $\sigma'_{v0}=250$ kPa, (c) $\sigma'_{v0}=400$ kPa, and (d) evolution of non-uniformity parameter; $D_r=49\%$ (left), $D_r=87\%$ (right).....	123
Figure 4.20	Effective vertical stress (kPa) measured inside measurement spheres MS1-MS13 at the end of consolidation for boundary consolidated vertical stress of 250 kPa in DEM simulation of Pea gravel specimen.....	125
Figure 4.21	Effective vertical stress measured inside measurement spheres MS1-MS13 during shear in DEM simulations of constant volume monotonic simple shear response of Pea gravel specimen ($\sigma'_{v0}=250$ kPa and $D_r=49\%$ (left), $D_r=87\%$ (right)).....	125
Figure 4.22	Distribution of σ'_{zz} inside MS1-MS13 in DEM simulations of constant volume monotonic simple shear response of Pea gravel specimen: (a) $\sigma'_{v0}=100$ kPa, (b) $\sigma'_{v0}=250$ kPa, (c) $\sigma'_{v0}=400$ kPa, and (d) evolution of non-uniformity parameter; $D_r=49\%$ (left), $D_r=87\%$ (right).....	126

Figure 4.23 Shear stress (kPa) measured inside measurement spheres MS1-MS13 at the end of consolidation for boundary consolidated vertical stress of 250 kPa in DEM simulation of Pea gravel specimen.....	128
Figure 4.24 Shear stress measured inside measurement spheres MS1-MS13 during shear in DEM simulations of constant volume monotonic simple shear response of Pea gravel specimen ($\sigma'_{v0}=250$ kPa and $D_r=49\%$ (left), $D_r=87\%$ (right))	128
Figure 4.25 Distribution of τ_{xz} inside MS1-MS13 in DEM simulations of constant volume monotonic simple shear response of Pea gravel specimen: (a) $\sigma'_{v0}=100$ kPa, (b) $\sigma'_{v0}=250$ kPa, (c) $\sigma'_{v0}=400$ kPa, and (d) evolution of non-uniformity parameter; $D_r=49\%$ (left), $D_r=87\%$ (right)	129
Figure 4.26 Stress ratio measured inside measurement spheres MS1-MS13 during shear in DEM simulations of constant volume monotonic simple shear response of Pea gravel specimen ($\sigma'_{v0}=250$ kPa and $D_r=49\%$ (left), $D_r=87\%$ (right))	130
Figure 4.27 Distribution of τ_{xz}/σ'_v inside MS1-MS13 in DEM simulations of constant volume monotonic simple shear response of Pea gravel specimen: (a) $\sigma'_{v0}=100$ kPa, (b) $\sigma'_{v0}=250$ kPa, (c) $\sigma'_{v0}=400$ kPa, and (d) evolution of non-uniformity parameter; $D_r=49\%$ (left), $D_r=87\%$ (right)	131
Figure 4.28 Pore pressure ratio measured inside measurement spheres MS1-MS13 during shear in DEM simulations of constant volume monotonic simple shear response of Pea gravel specimen ($\sigma'_{v0}=250$ kPa and $D_r=49\%$ (left), $D_r=87\%$ (right))	132
Figure 4.29 Distribution of r_u inside MS1-MS13 in DEM simulations of constant volume monotonic simple shear response of Pea gravel specimen: (a) $\sigma'_{v0}=100$ kPa, (b) $\sigma'_{v0}=250$ kPa, (c) $\sigma'_{v0}=400$ kPa, and (d) evolution of non-uniformity parameter; $D_r=49\%$ (left), $D_r=87\%$ (right)	133
Figure 4.30 Shear strain measured inside measurement spheres MS1-MS13 during shear in DEM simulations of constant volume monotonic simple shear response of Pea gravel specimen ($\sigma'_{v0}=250$ kPa and $D_r=49\%$ (left), $D_r=87\%$ (right))	135
Figure 4.31 Distribution of γ_{xz} inside MS1-MS13 in DEM simulations of constant volume monotonic simple shear response of Pea gravel specimen: (a) $\sigma'_{v0}=100$ kPa, (b) $\sigma'_{v0}=250$ kPa, (c) $\sigma'_{v0}=400$ kPa, and (d) evolution of non-uniformity parameter; $D_r=49\%$ (left), $D_r=87\%$ (right)	136
Figure 4.32 Volumetric strain inside the specimen core (MS1) in DEM simulations of constant volume monotonic simple shear response of Pea gravel specimen: $\epsilon_v<0$ and $\epsilon_v>0$ represents contraction and dilation, respectively.	138
Figure 4.33 Stress Mohr circle and calculation of mobilized friction angle.....	138
Figure 4.34 Evolution of ϕ_{mob} , α_{MS1-h} , β_{MS1-h} , α_{MS1-v} and β_{MS1-v} during shear in DEM simulations of constant volume monotonic simple shear response of Pea gravel specimen for specimen of $\sigma'_{v0}=250$ kPa and $D_r=49\%$	141
Figure 4.35 Evolution of ϕ_{mob} , α_{MS1-h} , β_{MS1-h} , α_{MS1-v} and β_{MS1-v} during shear in DEM simulations of constant volume monotonic simple shear response of Pea gravel specimen for specimen of $\sigma'_{v0}=250$ kPa and $D_r=87\%$	141

Figure 4.36 Mohr's circles of stress at the end of consolidation and the stress paths during shear in DEM simulations of constant volume monotonic simple shear response of Pea gravel specimen ($\sigma'_{v0}=250$ kPa, $D_r=49\%$)	142
Figure 4.37 Mohr's circles of stress at the end of consolidation and the stress paths during shear in DEM simulations of constant volume monotonic simple shear response of Pea gravel specimen ($\sigma'_{v0}=250$ kPa, $D_r=87\%$)	142
Figure 4.38 Angle between the direction of major principal stress and XZ, XY and YZ planes during shear in DEM simulations of constant volume monotonic simple shear response of Pea gravel specimen: $D_r=49\%$ (left), $D_r=87\%$ (right).....	144
Figure 4.39 Evolution of angle θ_σ between the major principal stress axis and vertical plane YZ during shear in DEM simulations of constant volume monotonic simple shear response of Pea gravel specimen.....	145
Figure 4.40 Contact force network (force chain) at different boundary shear strains in DEM simulation of constant volume monotonic simple shear response of Pea gravel specimen: $\sigma'_{v0}=250$ kPa and $D_r=49\%$	146
Figure 4.41 Polar histograms of contacts normal at different boundary shear strains in DEM simulation of constant volume monotonic simple shear response of Pea gravel specimen: $\sigma'_{v0}=250$ kPa and $D_r=49\%$	147
Figure 4.42 Orientation of major principal fabric (θ_ϕ) and stress (θ_σ) during shear in DEM simulations of constant volume monotonic simple shear response of Pea gravel specimen: $D_r=49\%$ (left), $D_r=87\%$ (right).....	148
Figure 4.43 Evolution of degree of fabric anisotropy, in terms of contact normal orientations, during shear in DEM simulations of constant volume monotonic simple shear response of Pea gravel specimen:.....	150
Figure 4.44 Evolution of normalized coordination number and normalized void ratio inside the central measurement sphere in DEM simulations of constant volume monotonic simple shear response of Pea gravel specimen: $D_r=49\%$ (Left), $D_r=87\%$ (Right)..	152
Figure 4.45 Evolution of directions of major principal stress and strain rates during shear in DEM simulations of constant volume monotonic simple shear response of Pea gravel specimen: $D_r=49\%$ (left), $D_r=87\%$ (right).....	155
Figure 4.46 Probability distribution of rolling resistance coefficient by: (a) number of particles and (b) volume of particles in DEM simulations of Pea gravel specimen using spherical particles	158
Figure 4.47 Comparison of the results from DEM simulations of constant volume monotonic simple shear response of Pea gravel specimen for the cases of distributed versus uniform rolling resistance coefficient only during shear stage ($\sigma'_{v0}=250$ kPa and $D_r=49\%$)	159
Figure 4.48 Comparison of the results from DEM simulations of constant volume monotonic simple shear response of Pea gravel specimen for the cases of distributed versus uniform rolling resistance coefficient during all simulation stages ($\sigma'_{v0}=250$ kPa and $D_r=49\%$)	160

Figure 5.1 Comparison of the results from DEM simulation of constant volume cyclic simple shear test to the corresponding experimental results for Pea gravel specimen ($\sigma'_{v0}=250$ kPa, $D_r=49\%$, $CSR=0.095$)	171
Figure 5.2 Results from DEM Simulations of constant volume cyclic simple shear response of Pea gravel specimen ($D_r=49\%$ and $CSR=0.095$)	172
Figure 5.3 Coefficient of lateral pressure during shear in DEM simulations of constant volume cyclic simple shear response of Pea gravel specimen ($D_r=49\%$, $CSR=0.095$)	173
Figure 5.4 Results from DEM Simulation of constant volume cyclic simple shear response of Pea gravel specimen ($\sigma'_{v0}=250$ kPa, $D_r=87\%$ and $CSR=0.475$)	174
Figure 5.5 Coefficient of lateral pressure during DEM Simulation of constant volume cyclic simple shear response of Pea gravel specimen ($\sigma'_{v0}=250$ kPa, $D_r=87\%$ and $CSR=0.475$).....	174
Figure 5.6 Comparison of cyclic stress paths with phase transformation (PT) and ultimate state (US) lines from monotonic stress path data from DEM simulations of Pea gravel specimen ($D_r=49\%$).....	175
Figure 5.7 Comparison of cyclic stress paths with phase transformation (PT) and ultimate state (US) lines from monotonic stress path data from DEM simulations of Pea gravel specimen ($\sigma'_{v0}=250$ kPa and $D_r=87\%$).....	176
Figure 5.8 Horizontal displacement profile of stacked rings at boundary shear strain of 3.75% in DEM simulations of constant volume cyclic simple shear response of Pea gravel specimen ($D_r=49\%$).....	177
Figure 5.9 Horizontal displacement profile of stacked rings at boundary shear strain of 3.75% in DEM simulation of constant volume cyclic simple shear response of Pea gravel specimen ($\sigma'_{v0}=250$ kPa, $D_r=87\%$).....	177
Figure 5.10 Comparison of the cyclic shear response measured at boundaries and inside the central measurement sphere in DEM simulations of constant volume cyclic simple shear response of Pea gravel specimen ($\sigma'_{v0}=250$ kPa, $D_r=49\%$, $CSR=0.095$)	179
Figure 5.11 Comparison of the generated pore pressure ratio (right) and coefficient of lateral pressure (left) based on the measurements at the boundaries and inside the central measurement sphere in DEM simulations of constant volume cyclic simple shear response of Pea gravel specimen ($D_r=49\%$, $CSR=0.095$).....	181
Figure 5.12 Comparison of the cyclic shear response measured at boundaries and inside the central measurement sphere in DEM simulations of constant volume cyclic simple shear response of Pea gravel specimen ($\sigma'_{v0}=250$ kPa, $D_r=87\%$, $CSR=0.475$)	182
Figure 5.13 Comparison of the generated pore pressure ratio (right) and coefficient of lateral pressure (left) based on the measurements at the boundaries and inside the central measurement sphere in DEM simulations of constant volume cyclic simple shear response of Pea gravel specimen ($\sigma'_{v0}=250$ kPa, $D_r=87\%$, $CSR=0.475$).....	183
Figure 5.14 Schematic of the measurement sphere considered for evaluation of non-uniformity inside the specimen (all measurement spheres are at the same elevation as MS1).	184

Figure 5.15 Stress ratio (τ_{xz}/σ'_{zz0}) measured inside MS1-MS13 during cyclic shear in DEM simulations of constant volume cyclic simple shear response of Pea gravel specimen: $\sigma'_{v0}=250$ kPa ($D_r=49\%$ and $CSR=0.095$ (left), $D_r=87\%$ and $CSR=0.475$ (right)) ..	185
Figure 5.16 Distribution of Stress ratio (τ_{xz}/σ'_{v0}) inside MS1-MS13 and evolution of non-uniformity parameter in DEM simulations of constant volume cyclic simple shear response of Pea gravel specimen: $\sigma'_{v0}=100, 250, 400$ kPa, $D_r=49\%$ and $CSR=0.095$	186
Figure 5.17 Distribution of Stress ratio (τ_{xz}/σ'_{zz0}) inside MS1-MS13 and evolution of non-uniformity parameter in DEM simulations of constant volume cyclic simple shear response of Pea gravel specimen: $\sigma'_{v0}=250$ kPa, $D_r=87\%$ and $CSR=0.475$	187
Figure 5.18 The applied stress ratio ($(\tau_{xz}-\tau_{xz0})/\sigma'_{zz0}$) measured inside MS1-MS13 in DEM simulations of constant volume cyclic simple shear response of Pea gravel specimen: $\sigma'_{v0}=250$, $D_r=49\%$ and $CSR=0.095$	188
Figure 5.19 Stress ratio (τ_{xz}/σ'_{zz}) measured inside MS1-MS13 during cyclic shear in DEM simulations of constant volume cyclic simple shear response of Pea gravel specimen: $\sigma'_{v0}=250$ kPa ($D_r=49\%$ and $CSR=0.095$ (left), $D_r=87\%$ and $CSR=0.475$ (right)) ..	189
Figure 5.20 Distribution of Stress ratio (τ_{xz}/σ'_{zz}) inside MS1-MS13 and evolution of non-uniformity parameter in DEM simulations of constant volume cyclic simple shear response of Pea gravel specimen: $\sigma'_{v0}=100, 250, 400$ kPa, $D_r=49\%$ and $CSR=0.095$	190
Figure 5.21 Distribution of Stress ratio (τ_{xz}/σ'_{zz}) inside MS1-MS13 and evolution of non-uniformity parameter in DEM simulations of constant volume cyclic simple shear response of Pea gravel specimen: $\sigma'_{v0}=250$ kPa, $D_r=87\%$ and $CSR=0.475$	190
Figure 5.22 Pore pressure ratio measured inside MS1-MS13 during cyclic shear in DEM simulations of constant volume cyclic simple shear response of Pea gravel specimen: $\sigma'_{v0}=250$ kPa ($D_r=49\%$ and $CSR=0.095$ (left), $D_r=87\%$ and $CSR=0.475$ (right)) ..	192
Figure 5.23 Distribution of pore pressure ratio inside MS1-MS13 and evolution of non-uniformity parameter in DEM simulations of constant volume cyclic simple shear response of Pea gravel specimen: $\sigma'_{v0}=100, 250, 400$ kPa, $D_r=49\%$ and $CSR=0.095$	192
Figure 5.24 Distribution of pore pressure ratio inside MS1-MS13 and evolution of non-uniformity parameter in DEM simulations of constant volume cyclic simple shear response of Pea gravel specimen: $\sigma'_{v0}=250$ kPa, $D_r=87\%$ and $CSR=0.475$	193
Figure 5.25 Shear strain measured inside MS1-MS13 during cyclic shear in DEM simulations of constant volume cyclic simple shear response of Pea gravel specimen: $\sigma'_{v0}=250$ kPa ($D_r=49\%$ and $CSR=0.095$ (left), $D_r=87\%$ and $CSR=0.475$ (right))	194
Figure 5.26 Distribution of shear strain inside MS1-MS13 and evolution of non-uniformity parameter in DEM simulations of constant volume cyclic simple shear response of Pea gravel specimen: $\sigma'_{v0}=100, 250, 400$ kPa, $D_r=49\%$ and $CSR=0.095$	195
Figure 5.27 Distribution of shear strain inside MS1-MS13 and evolution of non-uniformity parameter in DEM simulations of constant volume cyclic simple shear response of Pea gravel specimen: $\sigma'_{v0}=250$ kPa, $D_r=87\%$ and $CSR=0.475$	196

Figure 5.28 Volumetric strain measured inside MS1-MS13 during cyclic shear in DEM simulations of constant volume cyclic simple shear response of Pea gravel specimen: $\sigma'_{v0}=250$ kPa ($D_r=49\%$ and $CSR=0.095$ (left), $D_r=87\%$ and $CSR=0.475$ (right)) ..	197
Figure 5.29 Distribution of volumetric strain inside MS1-MS13 and evolution of non-uniformity parameter in DEM simulations of constant volume cyclic simple shear response of Pea gravel specimen: $\sigma'_{v0}=100, 250, 400$ kPa, $D_r=49\%$ and $CSR=0.095$	198
Figure 5.30 Distribution of volumetric strain inside MS1-MS13 and evolution of non-uniformity parameter in DEM simulations of constant volume cyclic simple shear response of Pea gravel specimen: $\sigma'_{v0}=250$ kPa, $D_r=87\%$ and $CSR=0.475$	198
Figure 5.31 Positive direction for angle measurements regarding the XY, XZ and YZ planes .	199
Figure 5.32 Angle between the direction of major principal stress and XZ, XY and YZ planes during cyclic shear in DEM simulations of constant volume cyclic simple shear response of Pea gravel specimen: (a), (b), (c) $\sigma'_{v0}= 100, 250$ and 400 kPa, $D_r=49\%$, $CSR= 0.095$, (d) $\sigma'_{v0}= 250$ kPa, $D_r=87\%$, $CSR= 0.475$	200
Figure 5.33 Evolution of angle θ_σ between the major principal stress axis and vertical plane YZ during cyclic shear in DEM simulations of constant volume cyclic simple shear response of Pea gravel specimen:: (a) $D_r=49\%$, $CSR= 0.095$, (b) $D_r=87\%$, $CSR= 0.475$	201
Figure 5.34 Contact force network (force chain) and corresponding polar histograms of contact normal directions at different instances during cyclic shear in DEM simulations of constant volume cyclic simple shear response of Pea gravel specimen ($\sigma'_{v0}=250$ kPa, $D_r=49\%$, and $CSR=0.095$).....	203
Figure 5.35 Contact force network (force chain) and corresponding polar histograms of contact normal directions at different instances during cyclic shear in DEM simulations of constant volume cyclic simple shear response of Pea gravel specimen ($\sigma'_{v0}=250$ kPa, $D_r=87\%$, and $CSR=0.475$).....	205
Figure 5.36 Evolution of degree of fabric anisotropy, in terms of contact normal orientations, during cyclic shear at instances of $\tau/\sigma'_{v0}= 0$ and $\pm CSR$ in DEM simulations of constant volume cyclic simple shear response of Pea gravel specimen: (a)-(c): $D_r=49\%$, and $CSR=0.095$, (d) $D_r=87\%$, and $CSR=0.475$	209
Figure 5.37 Evolution of normalized coordination number in DEM simulations of constant volume monotonic simple shear response of Pea gravel specimen: $D_r=49\%$, $CSR=0.095$ (Left), $D_r=87\%$, $CSR=0.475$ (Right)	210
Figure 5.38 Comparison of the results from DEM simulations of constant volume cyclic simple shear response of Pea gravel specimen for the cases of distributed versus uniform rolling resistance coefficient ($\sigma'_{v0}=250$ kPa, $D_r=49\%$ and $CSR=0.095$)	212
Figure 6.1 Comparison of the results from DEM simulation of constant volume monotonic simple shear test to the corresponding experimental results for Pea gravel specimen ($\sigma'_{v0}=250$ kPa, $D_r=49\%$).....	221
Figure 6.2 Mohr's circles of stress at the end of consolidation and the stress paths during shear in DEM simulations of constant volume monotonic simple shear response of Pea gravel specimen ($\sigma'_{v0}=250$ kPa, $D_r=49\%$).....	223

Figure 6.3 Evolution of angle θ_σ between the major principal stress axis and vertical direction during shear in DEM simulations of constant volume monotonic simple shear response of Pea gravel specimen	224
Figure 6.4 Comparison of the results from DEM simulation of constant volume cyclic simple shear test to the corresponding experimental results for Pea gravel specimen ($\sigma'_{v0}=250$ kPa, $D_r=49\%$, $CSR=0.095$).....	227
Figure 6.5 Comparison of cyclic stress paths with phase transformation (PT) and ultimate state (US) lines from monotonic stress path data from DEM simulations of Pea gravel specimen: (a) $D_r=49\%$, $CSR=0.095$, (b) $D_r=87\%$, $CSR=0.475$	228
Figure 6.6 Example of complex clumps as numerical representation of soil particles.....	233
Figure A.1 Void ratio measured inside the central measurement sphere with different diameters: $D_r=49\%$ (left) and $D_r=87\%$ (right).....	236
Figure A.2 Shear strain measured inside the central measurement sphere with different diameters: $D_r=49\%$ (left) and $D_r=87\%$ (right)	237
Figure A.3 Vertical stress measured inside the central measurement sphere with different diameters: $D_r=49\%$ (left) and $D_r=87\%$ (right)	238
Figure A.4 Shear stress measured inside the central measurement sphere with different diameters: $D_r=49\%$ (left) and $D_r=87\%$ (right)	239
Figure B.1 Comparison of the monotonic shear response measured at boundaries and inside the central measurement sphere in DEM simulation of constant volume monotonic simple shear response of Pea gravel specimen ($\sigma'_{v0}=100$ kPa, $D_r=49\%$).....	240
Figure B.2 Comparison of the monotonic shear response measured at boundaries and inside the central measurement sphere in DEM simulation of constant volume monotonic simple shear response of Pea gravel specimen ($\sigma'_{v0}=100$ kPa, $D_r=87\%$).....	241
Figure B.3 Comparison of monotonic shear response measured at boundaries and inside the central measurement sphere in DEM simulation of constant volume monotonic simple shear response of Pea gravel specimen ($\sigma'_{v0}=400$ kPa, $D_r=49\%$).....	242
Figure B.4 Comparison of the monotonic shear response measured at boundaries and inside the central measurement sphere in DEM simulation of constant volume monotonic simple shear response of Pea gravel specimen ($\sigma'_{v0}=400$ kPa, $D_r=87\%$).....	243
Figure C.1 Void ratio measured inside measurement spheres MS1-MS13 during shear in DEM simulations of constant volume monotonic simple shear response of Pea gravel specimen for $\sigma'_{v0}=100$ and 400 kPa: $D_r=49\%$ (left), $D_r=87\%$ (right).....	244
Figure C.2 Effective vertical stress measured inside measurement spheres MS1-MS13 during shear in DEM simulations of constant volume monotonic simple shear response of Pea gravel specimen for $\sigma'_{v0}=100$ and 400 kPa: $D_r=49\%$ (left), $D_r=87\%$ (right)	245
Figure C.3 Shear stress measured inside measurement spheres MS1-MS13 during shear in DEM simulations of constant volume monotonic simple shear response of Pea gravel specimen for $\sigma'_{v0}=100$ and 400 kPa: $D_r=49\%$ (left), $D_r=87\%$ (right).....	246

Figure C.4 Stress ratio measured inside measurement spheres MS1-MS13 during shear in DEM simulations of constant volume monotonic simple shear response of Pea gravel specimen for $\sigma'_{v0}=100$ and 400 kPa: $D_r=49\%$ (left), $D_r=87\%$ (right).....	247
Figure C.5 Pore pressure ratio measured inside measurement spheres MS1-MS13 during shear in DEM simulations of constant volume monotonic simple shear response of Pea gravel specimen for $\sigma'_{v0}=100$ and 400 kPa: $D_r=49\%$ (left), $D_r=87\%$ (right).....	248
Figure C.6 Shear strain measured inside measurement spheres MS1-MS13 during shear in DEM simulations of constant volume monotonic simple shear response of Pea gravel specimen for $\sigma'_{v0}=100$ and 400 kPa: $D_r=49\%$ (left), $D_r=87\%$ (right).....	249
Figure D.1 Mohr's circles of stress at boundary shear strain of 0% ($\sigma'_{v0}=250$ kPa and $D_r=49\%$)	250
Figure D.2 Mohr's circles of stress at boundary shear strain of 0.5% ($\sigma'_{v0}=250$ kPa and $D_r=49\%$)	251
Figure D.3 Mohr's circles of stress at boundary shear strain of 1.5% ($\sigma'_{v0}=250$ kPa and $D_r=49\%$)	252
Figure D.4 Mohr's circles of stress at boundary shear strain of 2.5% ($\sigma'_{v0}=250$ kPa and $D_r=49\%$)	253
Figure D.5 Mohr's circles of stress at boundary shear strain of 3.75% ($\sigma'_{v0}=250$ kPa and $D_r=49\%$)	254
Figure D.6 Mohr's circles of stress at boundary shear strain of 5% ($\sigma'_{v0}=250$ kPa and $D_r=49\%$)	255
Figure D.7 Mohr's circles of stress at boundary shear strain of 8% ($\sigma'_{v0}=250$ kPa and $D_r=49\%$)	256
Figure D.8 Mohr's circles of stress at boundary shear strain of 10% ($\sigma'_{v0}=250$ kPa and $D_r=49\%$)	257
Figure D.9 Mohr's circles of stress at boundary shear strain of 12% ($\sigma'_{v0}=250$ kPa and $D_r=49\%$)	258
Figure D.10 Mohr's circles of stress at boundary shear strain of 0% ($\sigma'_{v0}=250$ kPa and $D_r=87\%$)	259
Figure D.11 Mohr's circles of stress at boundary shear strain of 0.2% ($\sigma'_{v0}=250$ kPa and $D_r=87\%$)	260
Figure D.12 Mohr's circles of stress at boundary shear strain of 0.5% ($\sigma'_{v0}=250$ kPa and $D_r=87\%$)	261
Figure D.13 Mohr's circles of stress at boundary shear strain of 1.5% ($\sigma'_{v0}=250$ kPa and $D_r=87\%$)	262
Figure D.14 Mohr's circles of stress at boundary shear strain of 2.5% ($\sigma'_{v0}=250$ kPa and $D_r=87\%$)	263
Figure D.15 Mohr's circles of stress at boundary shear strain of 3.75% ($\sigma'_{v0}=250$ kPa and $D_r=87\%$)	264

Figure D.16 Mohr's circles of stress at boundary shear strain of 5% ($\sigma'_{v0}=250$ kPa and $D_r=87\%$)	265
Figure D.17 Mohr's circles of stress at boundary shear strain of 8% ($\sigma'_{v0}=250$ kPa and $D_r=87\%$)	266
Figure D.18 Mohr's circles of stress at boundary shear strain of 10% ($\sigma'_{v0}=250$ kPa and $D_r=87\%$)	267
Figure D.19 Mohr's circles of stress at boundary shear strain of 11.3% ($\sigma'_{v0}=250$ kPa and $D_r=87\%$)	268
Figure E.1 Comparison of the cyclic shear response measured at boundaries and inside the central measurement sphere in DEM simulations of constant volume cyclic simple shear response of Pea gravel specimen ($\sigma'_{v0}=100$ kPa, $D_r=49\%$, $CSR=0.095$)	269
Figure E.2 Comparison of the cyclic shear response measured at boundaries and inside the central measurement sphere in DEM simulations of constant volume cyclic simple shear response of Pea gravel specimen ($\sigma'_{v0}=400$ kPa, $D_r=49\%$, $CSR=0.095$)	270
Figure F.1 Stress ratio (τ_{xz}/σ'_{zz}) measured inside MS1-MS13 during cyclic shear in DEM simulations of constant volume cyclic simple shear response of Pea gravel specimen for $\sigma'_{v0}=100$ and 400 kPa, $D_r=49\%$ and $CSR=0.095$	271
Figure F.2 Pore pressure ratio measured inside MS1-MS13 during cyclic shear in DEM simulations of constant volume cyclic simple shear response of Pea gravel specimen for $\sigma'_{v0}=100$ and 400 kPa, $D_r=49\%$ and $CSR=0.095$	272
Figure F.3 Shear strain measured inside MS1-MS13 during cyclic shear in DEM simulations of constant volume cyclic simple shear response of Pea gravel specimen for $\sigma'_{v0}=100$ and 400 kPa, $D_r=49\%$ and $CSR=0.095$	272
Figure F.4 Volumetric strain measured inside MS1-MS13 during cyclic shear in DEM simulations of constant volume cyclic simple shear response of Pea gravel specimen for $\sigma'_{v0}=100$ and 400 kPa, $D_r=49\%$ and $CSR=0.095$	273

List of Appendices

Appendix A Selection of the size of Measurement Spheres	235
Appendix B Comparison of the monotonic simple shear response measured at boundaries and inside the central measurement spheres for consolidated vertical stresses of 100 and 400 kPa	240
Appendix C Variation of different measurement quantities inside MS1-MS13 during monotonic shear for consolidated vertical stresses of 100 and 400 kPa	244
Appendix D Evolution of Mohr's circles of stress during constant volume monotonic simple shear for specimens of $\sigma'_{v0}=250$ kPa and $D_r=49\%$ and 87%	250
Appendix E Comparison of the cyclic simple shear response measured at boundaries and inside the central measurement spheres for consolidated vertical stresses of 100 and 400 kPa at relative density of 49%	269
Appendix F Variation of different measurement quantities inside MS1-MS13 during cyclic shear for consolidated vertical stresses of 100 and 400 kPa at relative density of 49%	271

Abstract

Understanding the simple shear behavior of soils is very important in many geotechnical engineering problems such as earthquakes and slope stability. The response of gravelly soils is particularly critical for understanding the performance of earth and rockfill dams, and other gravel embankments and fills. The observed gravelly soil liquefaction during recent earthquakes (2008 Wenchuan, China, 2014 Cephalonia, Greece, and 2016 Kaikoura, New Zealand) have highlighted the need for improved understanding of the seismic response of gravels to improve infrastructure. Given the advances in computational power, particle-based discrete element methods have been progressively used in analyzing soil behavior. However, these models have only been validated by comparing simulation and experimental results using idealized granular materials. When real soil is introduced, existing laboratory tests have used sandy soils that cannot be 1:1 modeled in discrete elements due to the extremely large number of particles that render the needed computational time unrealistic. This dissertation addresses these limitations by validating 3D DEM analyses using results from laboratory tests on real soils, where each particle is accounted for and is characterized by size and shape. Results from 3D Discrete Element Modeling, large scale stacked-ring simple shear laboratory tests and Translucent Segregation Table (TST) tests are integrated to investigate the monotonic and cyclic behavior of Pea gravel specimens.

3D DEM simulations of this study, by considering a realistic algorithm for modeling the movement of stacked rings, indicate that extra caution should be taken and necessary modifications should be applied for testing rounded to sub-rounded granular materials in stacked-ring simple

shear device under constant volume condition to ensure proper imposition of simple shear deformation on the specimen. It is also shown that incorporating both the irregularity and non-uniformity of particles shape by assigning a distribution of rolling resistance to the equivalent spherical particles (used to reduce the computational effort) is crucial for acknowledging the diversity of particle shapes and providing a realistic representation of soil assembly in the numerical simulations. Such simulations are more reliable in predicting the behavior of actual soil and provide valuable information on the complex behavior at the micro- and meso-scale, which can eventually be used in developing more robust constitutive models based on the micromechanical response of granular assemblies.

Results from the DEM simulations in this study allow for a better understanding of soil response during constant volume simple shear testing. For example, evaluating the stress state at the specimen core, it is shown that a single assumption should not be made about the stress state inside the specimen during the whole course of shearing. The DEM simulation results also suggest that the level of density can affect the level of shear strain at which each of the assumptions may be realistic and can be confidently used in interpretation of simple shear test data. The simulation results also provide deeper insight into the existing non-uniformities of stress and strain inside the specimen and into how they compare to the boundary measured ones as done in laboratory. For example, the simulations show that boundary measured shear strain overestimates the average induced shear strain inside the specimen and that the boundary measured pore pressure ratio is more positive in value than the actual one generated inside the specimen. Such information helps in making more accurate interpretation of experimental data for analysis of soil response.

Chapter 1

Introduction

1.1 Motivation

Earthquakes, as one of the most devastating natural hazards, have been one of the major areas of research in various scientific and engineering fields for some decades. Significant damage to infrastructure, crippling of the economy, and loss of life are some of the negative effects of earthquakes that motivate researchers, especially in the field of geotechnical engineering, to look into this phenomenon in more depth. One of the most devastating effects of earthquake are seismically-induced displacements that can occur in the form of either seismic compression in unsaturated soils or soil liquefaction (or ground softening) in saturated loose non-cohesive soils. In soil liquefaction, cyclic loading during earthquake causes the loss of strength in the soil as a result of transferring the effective stress from the soil solid particles to the pore water between soil grains. Until now, most of the research in the field has been focused on the assessment of the probability of triggering of liquefaction; however, to improve the performance-based liquefaction engineering design approach and develop more efficient liquefaction hazard mitigation techniques, it is crucial to assess the liquefaction-induced deformations and get a thorough understanding of the development of liquefaction and its consequences.

Most soil liquefaction research has focused on sands, given the plethora of case studies and that conventional laboratory testing devices are appropriate for the small-size particles of sandy soils. However, the response of gravelly soils during earthquake loading is still not well understood because of fewer well-documented case histories of field liquefaction as well as the lack of large

scale laboratory test devices that can accurately capture material response of large-size particles. The observed gravelly soil liquefactions during recent earthquakes (2008 Wenchuan, China, 2014 Cephalonia, Greece, and 2016 Kaikoura, New Zealand) have highlighted the need for improved understanding and development of more rigorous methods for evaluating the response of gravels during earthquakes to efficiently predict infrastructure behavior.

In addition, most of the models (e.g. using the Finite Element/Difference Methods) describing behavior of the soil during liquefaction consider the soil as a continuum and overlook the particle interactions in the analyses. It is a limitation of these models as the particulate nature of the soil has been recognized to significantly affect the response of the soil under cyclic loading (Ting et al., 1989; Santamarina, 2001; O'Sullivan et al. 2008). The distinct element method (DEM), as proposed originally by Cundall and Strack (1979a) into soil mechanics, is a numerical method for analysis of granular materials (e.g. soil) that is capable of modeling the interactions of individual particles and providing information about the particle displacements, rotations and interactions during simulations. This method is used in this research due to its better capability in modeling the complex response of granular soils compared to traditional ones (e.g. FEM and FDM). Custom-made devices, i.e. the TST (Translucent Segregation Table) and 12"-diameter CSS (Cyclic Simple Shear), are employed to characterize the particle morphology, number of particles and grain size distribution of thousands of particles that will then be monotonically and cyclically sheared. The advantage of the large-scale CSS apparatus is that it can accommodate specimens of gravel-size particles with known total number of particles and particle morphology that will then be modeled 1:1 using the DEM. Such a 1:1 validation of the DEM has never been done before using real soil grains of varying size and shape.

Another motivation for conducting this research is that so far, there has been little documented experimentally validated 3D DEM modelling of simple shear test. Among the existing ones, most of them used either Cambridge-type rectangular specimen with rigid side boundaries or NGI-type cylindrical specimen with wire-reinforced membrane providing lateral confinement (e.g., Wijewickreme et al., 2013; Dabeet, 2014). Moreover, all these studies, even the ones with stacked-rings cylindrical specimen, used small-scale simple shear devices that tested particles in the size range of sands (e.g., Dabeet et al., 2011; Dabeet et al., 2014; Bernhardt et al., 2016; Asadzadeh and Soroush, 2016). Following the necessity of studying the simple shear behavior of gravelly soils, it is important to extent the numerical DEM studies to model larger scale experiments that are compatible with the larger size of gravelly particles.

1.2 Research Objectives

This research aims at understanding the monotonic and cyclic behavior of gravelly soils by integrating 3D Discrete Element Modeling (DEM) analyses, large scale cyclic simple shear (CSS) laboratory test results and Translucent Segregation Table (TST) test data. The overall goal of this research is to gain a deeper understanding of the monotonic and cyclic response of granular soils at the micro- and macro-scale (laboratory test response). The large scale CSS device used in this research allows for testing gravel-size particles knowing their total number, morphology and grain size distribution provided by TST. Knowing this information, it is possible to have a 1:1 representation of the real soil grains to the simulated particles using the discrete element model for a range of geometrical features of the grains. This 1:1 representation and validation improves the confidence in using DEM analyses to model the response of smaller grain size soil materials, such as sands, where the actual number of particles cannot be directly modeled due to computational

capabilities limitations. The fact that DEM models only use a certain number of particles to model sands has led to skepticism on how representative the results are of true field response. A summary of the research tasks and objectives is as follows:

1. Validating the 3D DEM model by comparing results from laboratory testing (both monotonic and cyclic response) of uniform-sized steel spheres to results of virtual specimens comprised of same size and number of spheres:

Before adopting DEM to analyze the response of actual soil, the numerical model is validated by comparing numerical analysis results to results from laboratory testing of steel spheres in stacked-ring simple shear device. Utilizing steel spheres fabricated with tight tolerances in terms of diameter and sphericity and well-known material properties ensures an accurate replication of the specimen in the DEM model.

2. Characterization of gravel specimen using Translucent Segregation Table Test:

The gravel specimen is initially characterized with respect to total number of particles, particle size and morphology using the TST test. This information is used in generating a realistic representation of soil assembly in the DEM model.

3. DEM model calibration and validation using gravel specimens:

3D DEM model for the actual soil assembly is calibrated and validate by comparing the DEM analyses to results from corresponding laboratory tests of gravel specimens fully characterized (every particle accounted for) in terms of number, size and morphology of particles. Once the ability of DEM to capture the response is demonstrated, the model is used with more confidence to investigate the microscopic and macroscopic behaviors that cannot be measured in laboratory tests.

4. Investigating the microscopic and macroscopic characteristics of behavior of the virtual gravel specimen during monotonic and cyclic simple shear loading. The outcomes are valuable for developing more robust constitutive models that incorporates the behavioral characteristics which are rooted in the particulate nature of gravels.

1.3 Organization of Dissertation

This dissertation is organized as follows:

Chapter 2 presents the review of the literature with a main focus on the DEM modeling of granular materials in the field of soil mechanics and geotechnical engineering. The relevant background information on liquefaction of gravelly soils in the field, simple shear testing, and discrete element analysis is also included in this chapter.

Chapter 3 describes the results from the stacked-ring simple shear testing of steel spheres and presents the validation of the DEM model for specimen of uniform-sized steel spheres. Deeper insight into testing of granular material and corresponding DEM modeling of stacked-ring simple shear testing achieved from the outcome of this chapter is used for improving the experiment and simulations of actual soil specimen in the next two chapters.

Chapter 4 presents the characterization of the Pea gravel specimen using TST test and utilization of this information in DEM simulations of monotonic simple shear behavior of actual soil specimen. Different microscopic and macroscopic aspects of the monotonic simple shear behavior of much realistic simulated specimen in constant volume condition are investigated and discussed.

Chapter 5 covers the DEM simulation of cyclic constant volume simple shear response of the Pea gravel in stacked-ring simple shear device, by considering a realistic representation of soil

particles (as in chapter 4). Microscopic and macroscopic aspects of the behavior in constant volume cyclic simple shear loading are evaluated and discussed in this chapter.

Chapter 6 summarizes the main conclusions of this dissertation and offers suggestions for future research.

Chapter 2

Literature Review

Soil liquefaction, defined as the transformation of a soil from the solid state to a liquefied state due to increased pore water pressure and reduced effective stress (Marcuson, 1978), associates with catastrophic loss of strength in soil as cyclic loading (e.g. during earthquake) causes the transfer of stress from the solid particles to the pore water between the soil grains. There are many case histories in the literature that report liquefaction of gravelly soils during historical and recent earthquakes (e.g., Youd et al., 1985; Andrus et al., 1992; Cao et al., 2011; Hamada, 2014; Nikolaou et al., 2014; Cubrinovski et al., 2018). However, the behavior of gravelly soils during earthquake is still not fully understood; and therefore, there is a great need for further investigations into this phenomenon in gravelly soils using both experimental and numerical approaches. There are limited experimental studies available for gravelly soils because of the challenges in conducting large scale experiments. This dissertation aims to improve our understanding of the undrained shear response of gravelly soils through a numerical study using discrete element simulations of constant volume simple shear test. In this regard, this chapter presents the relevant background information on DEM modeling and simple shear testing followed by a review of previously published works on the analysis of soil response using the DEM.

2.1 Undrained Response of Cohesionless Granular soils

The undrained shear behavior of cohesionless soils has been studied by many researchers in the laboratory (e.g., Peacock and Seed, 1968; Boulanger et al., 1993; Vaid and Sivathayalan,

1996; Wijewickreme et al., 2005; Porcino et al., 2008; Hubler et al., 2017). Figure 2.1 shows general behavior of cohesionless soils under undrained monotonic loading conditions at different initial densities. Undrained shearing of loose to medium dense cohesionless soils exhibits peak shear strength at relatively small strains followed by a reduction in strength with further deformation (strain softening). The buildup of excess pore pressure due to the contractive tendency of the soil by shearing is the cause of the strain softening behavior. At the point where there is no further tendency of contraction, the excess pore pressure has reached a maximum value and the strain softening behavior stops. Depending on the initial density state of the specimen, it exhibits one of the two type of behaviors with further shearing: In case of a loose specimen, the stresses and excess pore pressure remains constant and the deformation continues in a steady-state condition (Poulos, 1981). The stress path of the loose specimen also shows reduction of effective stress until reaching the steady state (or ultimate state) line. If the soil is very loose, the generated excess pore pressure can cause reduction of effective stress to zero and induce static liquefaction. For a medium dense specimen, it temporarily remains at this state until the soil shows dilative behavior during which the effective stress and shear strength increase with continuing shear. The phase transformation occurs when the soil switches from contractive (softening) to dilative (hardening) behavior. The dilative behavior continues until the steady state condition is reached. The state of the response during which the shear stress temporarily decreases over a limited range of shear strain is termed as “quasi-steady state” or “flow with limited deformation” (Ishihara, 1993). The stress path for medium dense soil shows recovery of lost stress before reaching the ultimate state. For loose and medium dense soils, the critical stress ratio point is the peak shear strength obtained during the test, and the critical stress ratio line (or collapse surface) is obtained by drawing a line through the critical stress ratio point for each test. For dense specimen, shear

stress continuously increases without displaying any softening behavior. The hardening behavior (due to the dilation tendency of specimen) during shear continues until the steady state (ultimate state) is reached.

It can be observed that regardless of the initial density, the soil finally reaches a unique critical state (steady state) at which the deformation continues without further changes in shear stress and excess pore pressure. It is worth mentioning that the soil behavior is pressure-dependent, which means that at the same initial density, lower/higher effective confining pressure can lead to a more/less dilative response in the soil.

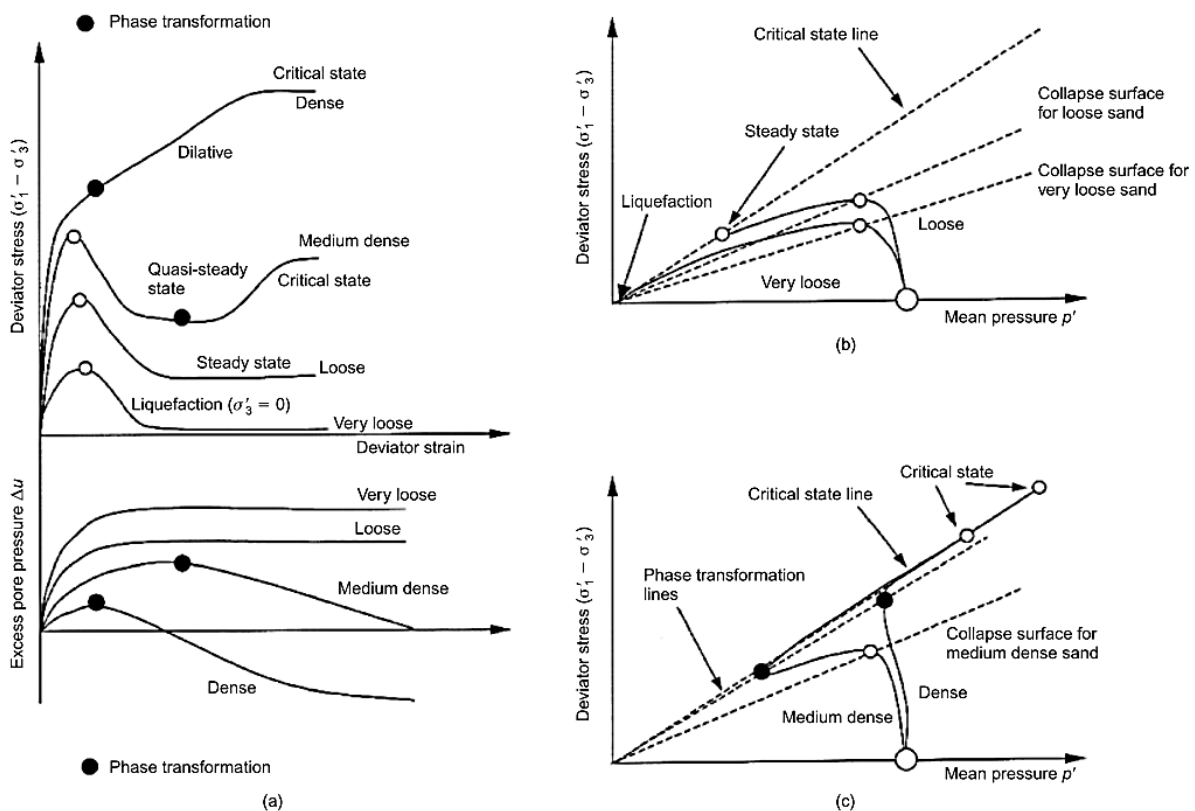


Figure 2.1 Typical monotonic undrained shear behavior of cohesionless soils (Mitchell and Soga, 2005)

Figure 2.2 depicts the cyclic response of contractive saturated cohesionless soils in undrained condition. In Figure 2.2 (a), the shear stress-strain response exhibits strain softening after a number of loading cycles and reaches a steady states with a shear strength referred to as

residual undrained shear strength. Such behavior (defined as true liquefaction) during cyclic loading develops much in the same manner as those observed under monotonic loading of loose soil. In Figure 2.2 (b), the limited liquefaction is observed in the response, during which the steady state is reached briefly over intermediate strains after decrease of shear strength in strain softening and before regaining shear stress in strain hardening. Such behavior is consistent with the monotonic response of medium dense soil. As shown in Figure 2.2 (c), the strain softening associated with limited liquefaction begins at a critical value of effective stress ratio (CSR) and continues until it reaches the phase transformation (PT) state and regains strength until the peak shear strength is reached and the direction of loading reverses. By further cycling along the PT line, the stress path makes the traditionally known butterfly loop. It can be observed in Figure 2.2 (d) that the accumulation of strain during such behavior in cyclic loading is due to both the limited liquefaction and the following cyclic mobility. During cyclic mobility, deformation developed during cyclic loading without any occurrence of strain softening (Castro, 1969; Chern, 1985).

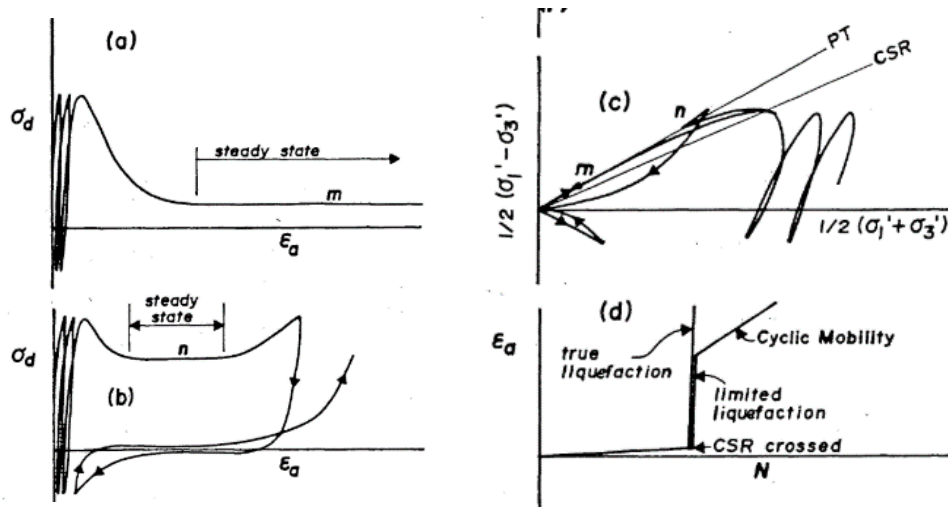


Figure 2.2 Cyclic undrained shear behavior of contractive cohesionless soils, true liquefaction and limited liquefaction (Chern, 1985)

Figure 2.3 depicts the cyclic response of dilative saturated cohesionless soils in undrained condition. Pore pressure and cyclic deformations are progressively developed in the specimen and no deformation is associated with strain softening at any stage during cyclic loading. Such soil specimen experienced small deformation as long as the stress ratio is below the one corresponding to the phase transformation state. When the stress path crosses the PT line during loading phase, significant accumulation of deformation occurs in the specimen. Large increase in pore pressure is experienced during unloading phase which brings the specimen close to the state of zero effective stress while very little change in deformation ensues. Accumulation of deformation with progression of loading cycles in this type of response can be observed in Figure 2.3 (c).

Examples of monotonic and cyclic undrained response of Fraser River Sand tested in a direct simple shear device are shown, respectively, Figure 2.4 and Figure 2.5.

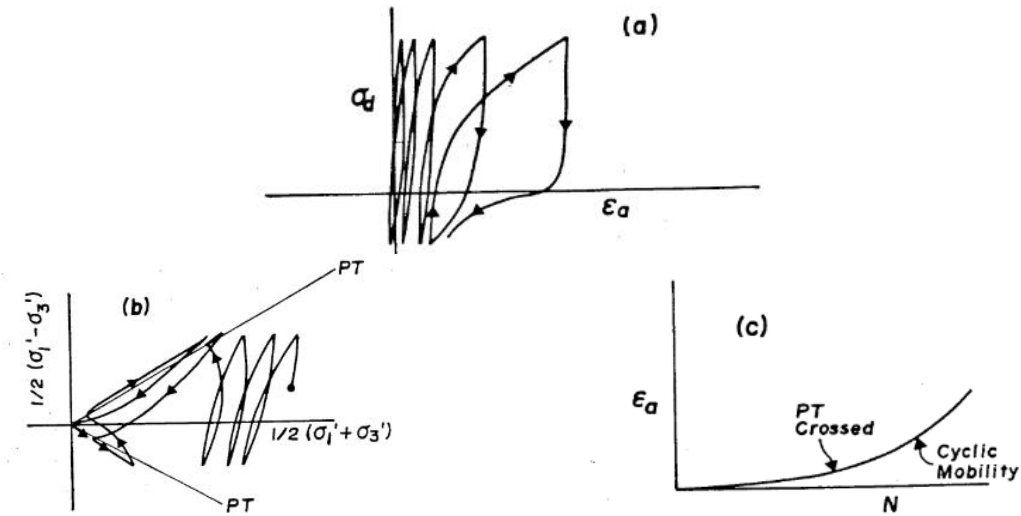


Figure 2.3 Cyclic undrained shear behavior of dilative cohesionless soils, cyclic mobility (Chern, 1985)

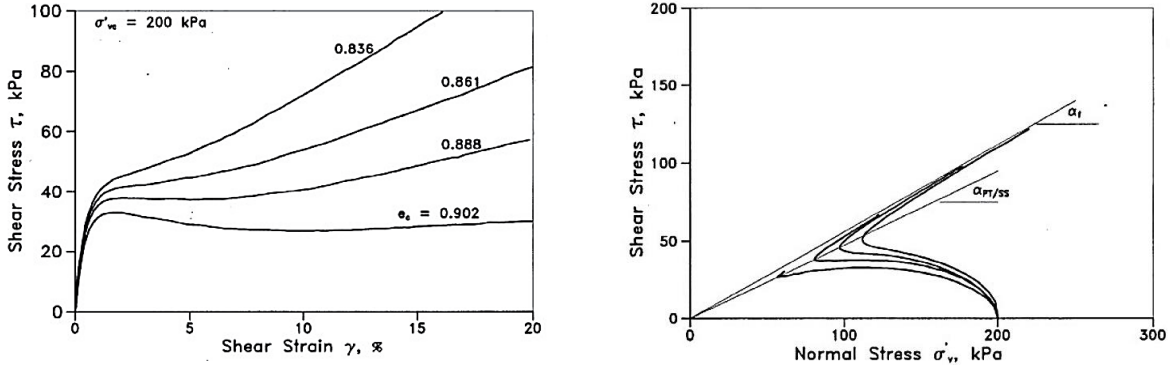


Figure 2.4 Monotonic Undrained Response of Fraser River Sand in Simple Shear (Sivathayalan, 1994)

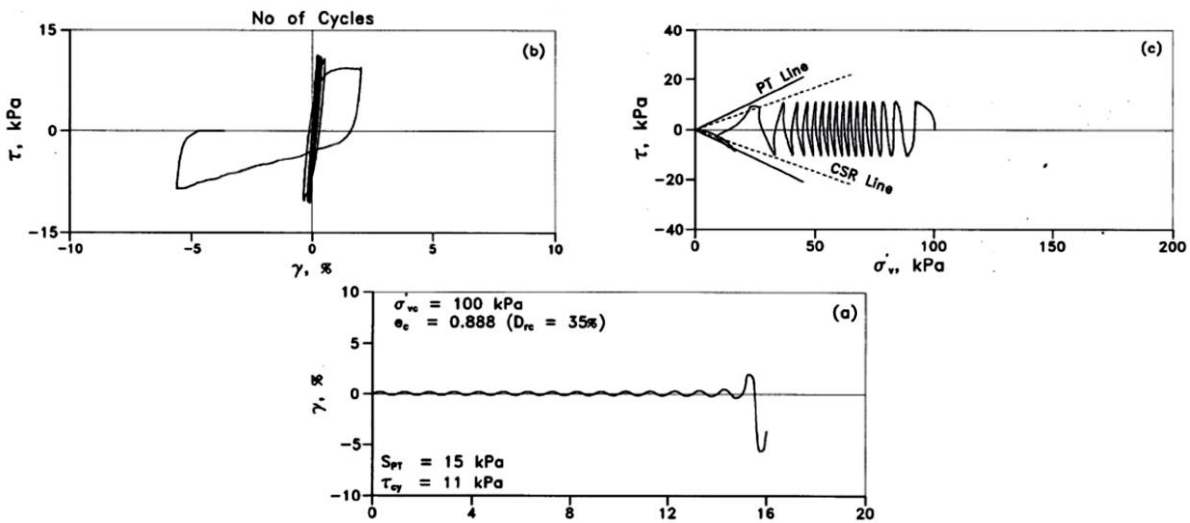


Figure 2.5 Cyclic Undrained Response of Fraser River Sand in Simple Shear (Sivathayalan, 1994)

2.2 Overview of Laboratory Testing of Gravelly Soils

The undrained shear behavior of gravelly soils has not been extensively studied due to the lack of sufficiently large devices that can accommodate adequate number of large gravel particles to accurately capture the material behavior. Moreover, most laboratory testing on gravelly soils and other large size particles (such as rockfills consisting of coarse-grained gravels, cobble and boulder-sized rock fragments) has been conducted on drained condition (e.g., Charles and Watts, 1980; Matsuoka and Liu, 1998; Strahler et al., 2016) as they have been considered to be free-draining.

The observed gravelly soil liquefaction during especially the recent earthquakes (2008 Wenchuan, China, 2014 Cephalonia, Greece, and 2016 Kaikoura, New Zealand) foreground the investigation of undrained shear behavior of gravelly soils. Hubler (2017) used a prototype large scale simple shear device (Zekkos et al., 2018) and investigated the constant volume monotonic, cyclic, and post-cyclic simple shear response of uniform gravels and gravel-sand mixtures.

Although laboratory testing can provide valuable information on the macroscopic behavior of soil specimens by boundary measurements, they are mostly incapable of capturing the local and internal changes that happens within the specimen of such granular materials, and do not provide any results at the micro-scale (particle to particle). Knowledge of the local responses within the specimen along with the response of the soil assembly at the particle-scale helps in explaining the overall behavior of the soil, which can consequently lead to improvement of constitutive models for prediction of soil response. As a result, numerical studies using discrete element method provides invaluable insight into the behavior of the soil and should be used along with the experimental studies to better investigate and understand the soil response.

2.3 Simple Shear Test

Understanding the behavior of soils under simple shear conditions is very important in a large number of geotechnical engineering problems such as earthquakes, slope stability, pile driving, and traffic/pavement loading. There are two commonly used experimental devices to study such behavior of soil: Direct Simple Shear (DSS) device and torsional shear Hollow Cylinder Apparatus (HCA). These devices are believed to be capable of reproducing the field loading conditions which particularly involve the rotation of principal stress axes during plane-strain shearing (Boulanger et al., 1993; Budhu, 1988) and also the vertical propagation of seismic-like

shear wave. Although the HCA has the advantage of allowing the direct measurement and control of all three principal stresses, it is very difficult to prepare the sample for this device. On the other hand, the sample preparation and testing are relatively easy in DSS device. However, it has some limitations that cause difficulty in exact interpretation of DSS test data:

- DSS inability to apply the complementary shear stresses on the vertical faces resulting in non-uniformity of both the shear stress and normal stress distribution across the top and bottom boundaries (Prevost and Høeg, 1976; La Rochelle, 1981; Budhu, 1988; de Josselin de Jong, 1988; Degroot et al., 1994; Dabeet et al., 2015). This limitation of DSS test is a violation of ideal simple shear condition. Figure 2.6 schematically illustrates the difference between the imposed stresses in ideal simple shear condition and in simple shear devices. Numerous studies have investigated this characteristic of DSS device and it has been shown that these non-uniformities can be minimized for large diameter to height ratios (Franke et al., 1979; Vucetic, 1981) and also that the sample core is under ideal simple shear conditions (Budhu and Britto, 1987).

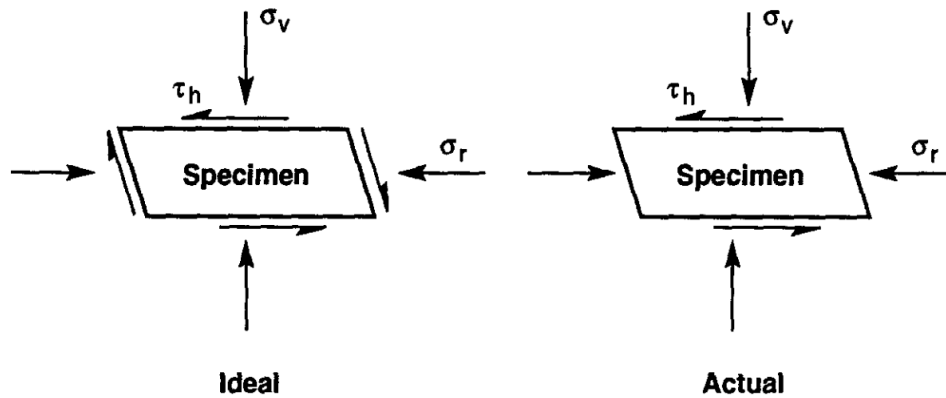


Figure 2.6 Ideal direct simple shear condition versus the realistically imposed condition in simple shear device (Degroot et al., 1994)

- Difficulty of measuring the lateral normal stresses during shearing, which results in an incomplete description of the stress state of the soil. Consequently, the failure mode of the soil needs to be assumed in order to interpret the experimental results and assess the shear strength parameters of the soil. Budhu (1988) showed that even the measured horizontal normal stresses in elaborately instrumented cylindrical devices did not correspond to the intermediate principal stress or the stresses normal to the plane perpendicular to shearing.

Figure 2.7 shows three alternative assumption for stress state at failure in simple shear test.

The most common approach (also known as β -method) assumes that at failure, the horizontal planes are planes of maximum stress obliquity (Figure 2.7 (a)). Based on this assumption, the friction angle of the soil is calculated by the following equation:

$$\Phi = \tan^{-1} \frac{\tau_{yx}}{\sigma'_y} \quad (\text{Eq. 2.1})$$

where τ_{yx} is the measured horizontal stress at failure, and σ'_y is the measured vertical effective stress on horizontal planes at failure. Although many researchers claim that this is an incorrect assumption (Roscoe et al., 1967; DeGroot et al., 1992), it has been widely used in practice as it results in a low and conservative value of friction angle.

In the second approach (also known as α -method), the horizontal planes are assumed to be planes of maximum shear stress (Figure 2.7 (b)). Accordingly, the friction angle of the soil is calculated as:

$$\Phi = \sin^{-1} \frac{\tau_{yx}}{\sigma'_y} \quad (\text{Eq. 2.2})$$

Roscoe et al. (1967) suggested that in drained conditions this assumption is valid only for medium loose sands, and not for dense sands; however, it is a reasonable assumption for undrained test of sands regardless of their density state.

The third approach (not very popular) proposed by de Josselin de Jong (1971) assumes that the failure happens on vertical planes (Figure 2.7 (c)). This approach proposed that the failure in simple shear can either happen on horizontal planes by sliding or on vertical planes by sliding and rotation, and in the case of equal possibility for both of these failure modes as the conditions of the boundaries, the specimen will fail in the mode of least resistance (on vertical plane). In this assumption, vertical planes are considered as the planes of maximum stress obliquity.

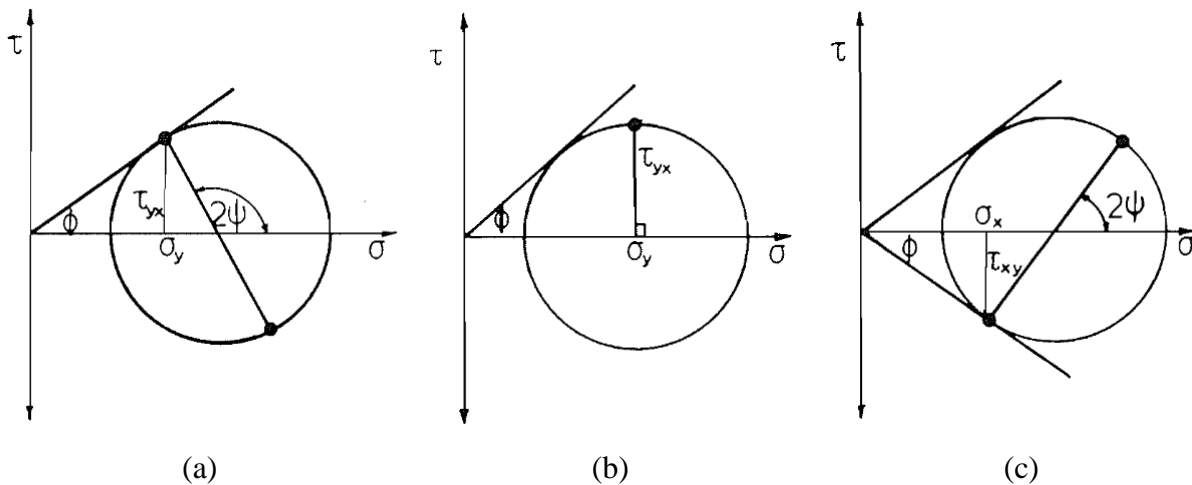


Figure 2.7 Mohr's circle for assumed failure modes in simple shear test (Budhu, 1988)

Despite the above limitations, direct simple shear test has been widely used in the field of geotechnical engineering. It has been used in a significant number of researches for studying the monotonic and cyclic response of sands, silts, and clays (e.g., Peacock and Seed, 1968; Silver and Seed, 1971; Vaid and Chern, 1985; Vucetic and Dobry, 1988; Azzouz et al., 1989; Vaid and Sivathayalan, 1996; Mao and Fahey, 2003; Wijewickreme et al., 2005; Sanin and Wijewickreme, 2006; Porcino et al., 2008; Wijewickreme, 2010). However, there are limited simple shear test data for gravels (e.g., Shaw and Brown, 1986; Chang et al., 2014; Hubler et al., 2017) and municipal solid waste (e.g., Matasovic and Kavazanjian Jr., 1998; Kavazanjian Jr. et al., 1999; Zekkos and Fei, 2017) as they need larger devices for studying their simple shear behavior.

Since the first introduction of direct simple shear test (DSS) by the Swedish Geotechnical Institute (SGI) in 1936 (Kjellman, 1951), different versions of it have been developed. The three commonly used versions are Cambridge type, Norwegian Geotechnical Institute (NGI) type, and stacked-ring type. Cambridge type DSS test developed at the University of Cambridge (Roscoe, 1953) tests a cubic specimen enclosed by rigid side boundaries. In NGI type developed at Norwegian Geotechnical Institute (Bjerrum and Landva, 1966), a cylindrical specimen is enclosed by a wire-reinforced membrane as lateral boundary. The NGI-type was actually a modification of the SGI-type device in which a series of stacked rings were used to prevent lateral expansion. There are also some NGI-type devices that have been further modified and contain pressurized cells (similar to the triaxial test cell) to allow for back pressure saturation, pore pressure measurements and lateral confinement of the specimen (Franke et al., 1979; Boulanger et al., 1993). In this study, the specimens are tested in cylindrical forms that laterally confined by a stack of Teflon-coated aluminum rings.

2.4 Continuum Based Numerical Methods in Geotechnical Engineering

Modeling the behavior of materials, different analytical and numerical methods have been used in both research and practice. Each of them include a set of assumptions and simplifications to achieve the goal. The analytical methods used in geomechanics can provide results and identify the variables affecting the problem solution with less effort; however, they consist of assumptions that are not necessary true in reality, especially in the case of granular materials (e.g., elasticity, isotropy, homogeneity, coaxiality, time independency, etc.). To study the phenomena that are not accessible in experiments and cannot be predicted by analytical method, researchers have been using numerical methods. Using continuum-based numerical methods such as Finite Element

method (FEM) and Finite Difference method (FDM) have been very popular in the field of geotechnical engineering.

Although these continuum-based numerical methods are very powerful tools, they have some limitations especially in modelling the behavior of granular soils. First and foremost, these methods assume the soil as a continuum and use complex constitutive models that do not explicitly consider the particulate nature of soil and the internal interactions at particles scale. In these methods, continuous displacement functions approximating the partial differential equations of continuum mechanics are used to model the element deformation between nodes. Discontinuous media such as soil especially at larger shear strains are excluded from this assumption. One of the other limitations is related to modeling large strains for which frequent remeshing due to excessive mesh distortions is required (Vavourakis et al., 2013).

Continuum-based finite element analysis were used by several researchers to study the direct simple shear element test (e.g., Budhu and Britto, 1987; Dounias and Potts, 1993; Zhuang and Goddard, 1993; Doherty and Fahey, 2011). Although their studies provided insight into the simple shear behavior, the continuum based method cannot fully capture the complex granulate nature of the granular soils. It is while it has been recognized that the most affecting factor in response of the soil, especially during cyclic loading and the associated deformations, is the particulate nature of the soil (e.g., Ting et al., 1989 ; Santamarina, 2001; O’Sullivan et al., 2006) and it has been well documented that particle shape and angularity play significant roles in shear behavior of granular soils (e.g., Sukumaran, 1996; Ashmawy et al., 2003; Cho et al., 2006; Hubler et al., 2014).

2.5 Discrete Element Method and PFC3D

Discrete element method (DEM) is a numerical dis-continuum method that first formulated by Cundall (1971) and Cundall (1974) for application in rock mechanics. This method is then extended to investigate the constitutive laws for soil using two-dimensional disk elements by Cundall and Strack (1979a) and three-dimensional spheres by Cundall and Strack (1979b). It has been shown by Cundall and Hart (1992) that DEM can model discontinuous material better than other numerical methods such as Finite Element Method and Finite Difference Method. Although it may still be difficult to apply such particle method to field-scale problems, with the fast development of computer technology, particle methods such as DEM can replace continuum methods in the future of numerical modelling in soils and rocks (Cundall, 2001).

The DEM algorithm is a dynamic or transient simulation in which the particle interactions are modeled as a dynamic process at discrete time increments while the time evolution of the system is advanced using a simple explicit finite difference technique. Therefore, the timestep should be so small that during each single timestep, the disturbance can only propagate from any particle to its immediate neighbors and not any further. Since a disturbance propagation speed depends on the physical properties of the discrete system, the small timestep satisfying the above constraint can be chosen accordingly. The force acting on any particle at any time instance are calculated exclusively by its interaction with the neighboring elements with which it is in contact. Nonlinear interaction of a large number of particles is possible without excessive memory requirements and the need for an iterative procedure by using such explicit, as opposed to an implicit, numerical scheme

Schematic overview of the sequence of calculations in DEM simulation, assuming the central difference distinct element algorithm proposed by Cundall and Strack (1979a) is depicted

in Figure 2.8(a), and the calculation sequence within each time increment is illustrated in Figure 2.8(b). After complete definition of boundary conditions and the particles, interaction of discrete particles at each time increment are monitored contact by contact and incremental force-displacement rules are used to calculate contact force increments from relative displacement and velocities of the contacting particles. Then, the resultant out-of-balance forces and moments (including body and external ones) are calculated for each particle independently, from which new translational and angular acceleration of each particle are calculated using Newton's second law of motion. These main features of DEM is also graphically shown in Figure 2.9. The particles translational and angular displacement and velocity are then updated by integrating the equation of motion independently for each particle over an explicit and small time step. For new positions and velocities of all particles, the same sequence of calculations repeats.

The above process of DEM calculations allows nondestructive monitoring and tracking of complete information of each particle, contact behavior and internal stresses and strains. Moreover, this method guarantees a sample reproducibility and precise control of external stresses. All of these features make DEM an ideal method for understanding fundamental soil behavior and for developing and validation of constitutive relationships for soils. Because of the capability of this method in modeling dynamic stress propagation through particle contacts, it can also be used to analyze the dynamic behavior of soils in addition to static behavior. Despite of these positive features, high computational expense for DEM modeling is one of its main disadvantages. To guarantee the accuracy and numerical stability of simulations, a very small timestep is required due to the explicit nature of DEM algorithm. Moreover, to properly simulate the soil behavior, it is necessary to consider sufficient number of particles to assure adequate number of contacts along shear surfaces or soil-structure interface. Also, because of treating the particles interaction as a

dynamic process in DEM, it takes a great number of timesteps for dissipation of all dynamic stresses and balancing all internal forces to achieve static equilibrium.

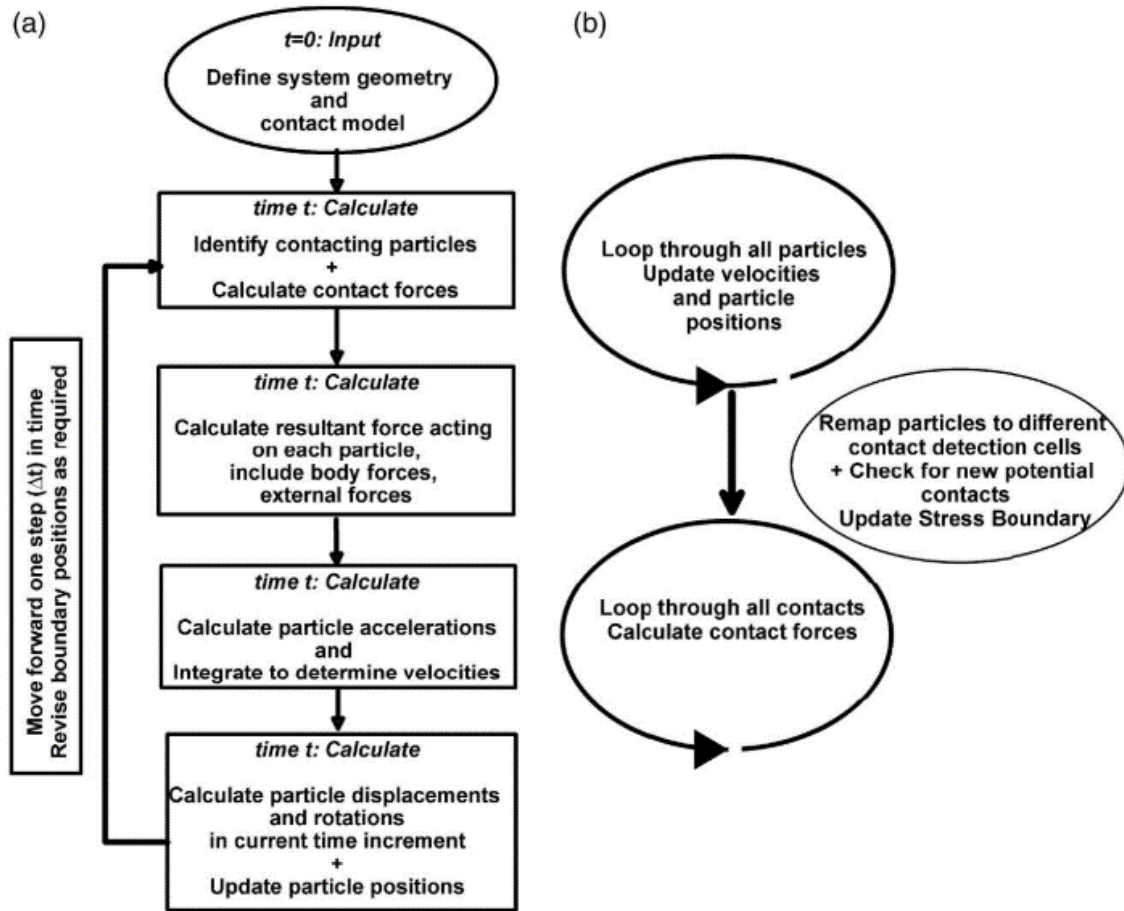


Figure 2.8 Schematic overview of the sequence of calculations in DEM simulation, a) overall procedure, b) sequence of calculations completed within each time increment (O’Sullivan, 2011)

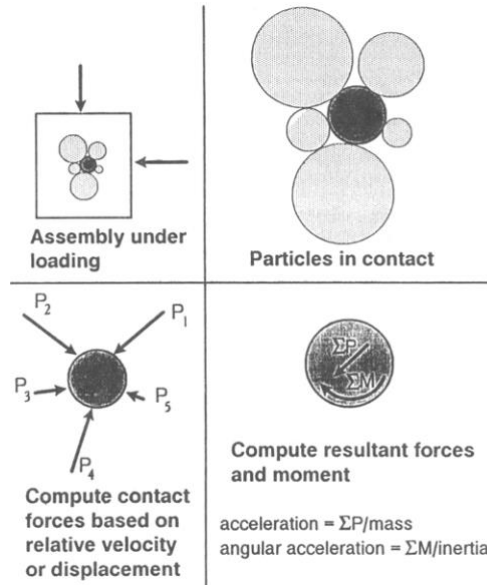


Figure 2.9 Main features in Discrete Element Method (Ng and Dobry, 1994)

A general purpose, distinct element modeling framework is provided by the Particle Flow Code (PFC) program developed by Itasca Consulting Group Inc. (2014). During the DEM simulations using PFC, many rigid bodies with finite size and mass that can move (both translate and rotate) independently of one another interact at pair-wise contacts by means of an internal force and moment. The internal forces and moments are updated based on contact mechanics embodied in particle-interaction laws. The time evolution of this system is computed following an explicit dynamic solution to Newton's laws of motion. The main assumptions underlying the PFC models are summarized as follows:

- The particles are considered as rigid bodies:

As most of the overall deformation of a granular assembly such as sand or gravel are primarily due to the sliding and rotation of the particles as rigid bodies and the opening and interlocking at interfaces and are not because of individual particle deformation, the assumption of particle rigidity is reasonable and there is no need for precise modeling of

particle deformation to obtain a good approximation of the mechanical behavior for such systems.

- Disk with unit thickness and sphere are the fundamental particle shape in 2D and 3D simulations, respectively. They are named balls in PFC.
- Clumps of arbitrary shapes can be created as rigidly attached disks with unit thickness in 2D or spheres in 3D, named pebbles, using the clump logic in PFC.
- Interactions between particles happens at pair-wise contacts by means of internal forces and moments that are updated based on contact mechanics embodied in particle-interaction laws.
- A soft-contact approach in which the rigid particles are allowed to overlap one another at contact points is used for modeling the behavior at physical contacts. In this approach, the contacts occur over an extremely small area (i.e., at a point), and the force-displacement law relates the magnitude of the overlap and/or the relative displacement at the contact point to the contact force.

The PFC particle-flow model also includes walls, which allows applying velocity boundary conditions to assemblies of balls or clumps. Although the equations of motion are satisfied for each ball and clump, they are not satisfied for walls and their motion is specified by user-defined translational or rotational velocities regardless of the contact forces acting on them. Also, walls do not interact with each other as no contacts forms between any two walls. To maintain the numerical stability, the timestep may change during the simulation in accordance to the number of contacts around each particle and the instantaneous stiffness values and masses.

2.5.1 Law of Motion

Translational and rotational motion of a single, rigid particle is determined by the resultant force and moment acting upon it. Position (x), velocity (\dot{x}), and acceleration (\ddot{x}) describe the translational motion of the center of mass, and angular velocity (w) and angular acceleration (\dot{w}) describes the rotational motion of the particle. The equation of motion for translational motion can be written in the vector form:

$$F = m(\ddot{x} - g) \quad (\text{Eq. 2.3})$$

in which F is the resultant force, m is the mass of the particle, and g is the body force acceleration vector (e.g., gravitational loading). The second order Velocity Verlet algorithm (Verlet, 1967) is used to solve this equation. Assuming that Equation 2.3 was solved during the previous cycle at time t and Δt is the timestep for the current cycle, the 1/2 step velocity ($\dot{x}^{(t+\Delta t/2)}$) is calculated as:

$$\dot{x}^{(t+\Delta t/2)} = \dot{x}^{(t)} + \frac{1}{2} \left(\frac{F^{(t)}}{m} + g \right) \Delta t \quad (\text{Eq. 2.4})$$

Accordingly, the position at time $t + \Delta t$ is updated using the 1/2 step velocity as:

$$x^{(t+\Delta t/2)} = x^{(t)} + \dot{x}^{(t+\Delta t/2)} \Delta t \quad (\text{Eq. 2.5})$$

The forces during the current cycle are updated during the force displacement cycle point, leading to the updated acceleration ($\ddot{x}^{(t+\Delta t)}$). The velocity is subsequently updated as:

$$\dot{x}^{(t+\Delta t)} = \dot{x}^{(t+\Delta t/2)} + \frac{1}{2} \left(\frac{F^{(t+\Delta t)}}{m} + g \right) \Delta t \quad (\text{Eq. 2.6})$$

The rotational motion is updated in the same way. The 1/2 step angular velocity is first calculated as:

$$w^{(t+\Delta t/2)} = w^{(t)} + \frac{1}{2} \left(\frac{M^{(t)}}{I} \right) \Delta t \quad (\text{Eq. 2.7})$$

where I is the moment of inertia and M is the resultant moment on the particle. The moments during the current cycle are updated during the force displacement cycle point, leading to the updated angular acceleration ($\dot{w}^{(t+\Delta t)}$). The angular velocity is subsequently updated as:

$$w^{(t+\Delta t)} = w^{(t+\Delta t/2)} + \frac{1}{2} \left(\frac{M^{(t+\Delta t)}}{I} \right) \Delta t \quad (\text{Eq. 2.8})$$

2.5.2 Force Displacement Law

Particles interact with each other and with walls through the forces and moments that develop at contacts. A contact model provides an interaction law to update the internal forces and moments whenever contacting pieces are interacting. Since the hertz and rolling resistance linear contact models are used in this study, their formulations are briefly described in this section.

The Hertz contact model consists of a nonlinear Hertzian component based on an approximation of the theory of Mindlin and Deresiewicz (Mindlin and Deresiewicz, 1953). The continuous nonlinearity in shear is not produced by the current implementation of this contact model in PFC, and the normal force dependent initial shear modulus is used instead (Cundall, 1988). In simulations involving impact, energy can be further dissipated by adding viscous dashpots. No resistance against relative rotation of contacting pieces is considered in this contact model (i.e., the contact moment equals zero ($M_C \equiv 0$)). The contact force is comprised of Hertzian and dashpot components ($F_C = F^h + F^d$).

Considering the non-linear Hertz force (F^h) here, it is resolved into normal and shear components as:

$$F^h = -F_n^h \hat{n}_C + F_s^h \quad (\text{Eq. 2.9})$$

in which normal and shear components are denoted by subscripts n and s, respectively, and \hat{n}_c is the contact unit normal. Shear forces lie on the contact plane and are expressed in the contact plane coordinate system. In 3D:

$$\mathbf{F}_s^h = F_{ss}^h \hat{\mathbf{s}}_c + F_{st}^h \hat{\mathbf{t}}_c \quad (\text{Eq. 2.10})$$

At each time step, the hertz normal force is updated as:

$$F_n^h = \begin{cases} -h_n |g_c|^{\alpha_h} & , \quad g_c < 0 \text{ (Active contact)} \\ 0 & , \quad \text{otherwise} \end{cases} \quad (\text{Eq. 2.11})$$

where g_c indicates the amount of particles overlap, α_h is the power-law exponent with default value of 1.5, and the coefficient h_n depends on the geometrical and mechanical properties of the contacting pieces as:

$$h_n = \frac{3G\sqrt{2\bar{R}}}{3(1-\nu)} \quad (\text{Eq. 2.12})$$

where G , ν , and \bar{R} are the effective shear modulus, Poisson's ratio, and contact radius, respectively. The effective radius of the contact is computed via the radii ($R^{(1)}$ and $R^{(2)}$) of the contacting piece surfaces (the radius of a wall facet is ∞) as:

$$\frac{1}{\bar{R}} = \frac{1}{R^{(1)}} + \frac{1}{R^{(2)}} \quad (\text{Eq. 2.13})$$

For hertz shear force at each time step, it is updated as:

$$\mathbf{F}_s^h = \begin{cases} \mathbf{F}_s^* & , \quad \|\mathbf{F}_s^*\| \leq F_s^\mu \\ F_s^\mu \left(\frac{\mathbf{F}_s^*}{\|\mathbf{F}_s^*\|} \right) & , \quad \text{otherwise} \end{cases} \quad (\text{Eq. 2.14})$$

in which F_s^μ is shear strength and F_s^* is the trial shear force as:

$$F_s^\mu = \mu F_n^h \quad (\text{Eq. 2.15})$$

$$F_s^* = (F_s^h)_0 + k_s \Delta \delta_s \quad (\text{Eq. 2.16})$$

In these equations, μ is contact friction coefficient, $(F_s^h)_0$ is the Hertz shear force at the beginning of the timestep, $\Delta\delta_s$ is the relative shear increment, and k_s is the initial tangent shear stiffness, which depends on the current normal force as:

$$k_s = \frac{2(1-\nu)}{2-\nu} \alpha_h h_n (F_n^h)^{(\alpha_h-1)/\alpha_h} \quad (\text{Eq. 2.17})$$

Rolling resistance linear contact model in PFC is a linear-based model to which a rolling resistance mechanism is added. A torque acting on the contacting pieces is incorporated to counteract rolling motion. This rolling resistance contact model is similar to the one described by Wensrich and Katterfeld (2012) with the exception that it is based on the linear model instead of a Hertz model. The contact force is comprised of linear and dashpot components ($F_C = F^l + F^d$) and the contact moment is non-zero and is equal to the rolling resistance moment ($M_C = M^r$). The linear force is generated by linear springs of constant normal (k_n) and shear (k_s) stiffnesses. Considering the linear force component (F^l) here, it is resolved into normal and shear components as:

$$F^h = -F_n^h \hat{n}_C + F_s^h \quad (\text{Eq. 2.18})$$

Same as in Hertz model, shear forces lie on the contact plane and are expressed in the contact plane coordinate system. In 3D:

$$F_s^l = F_{ss}^l \hat{s}_C + F_{st}^l \hat{t}_C \quad (\text{Eq. 2.19})$$

During each time step, the linear normal force is updated as:

$$F_n^l = \begin{cases} k_n g_s & , g_s < 0 \\ 0 & , \text{otherwise} \end{cases} \quad (\text{Eq. 2.20})$$

where g_s denotes the contacting particles overlap. The linear shear force at each time step is then updated as:

$$F_s^l = \begin{cases} F_s^* & , \|F_s^*\| \leq F_s^\mu \\ F_s^\mu \left(\frac{F_s^*}{\|F_s^*\|} \right) & , \text{otherwise} \end{cases} \quad (\text{Eq. 2.21})$$

in which F_s^μ is shear strength calculated as Equation 2.15 and F_s^* is the trial shear force as:

$$F_s^* = (F_s^1)_0 + k_s \Delta \delta_s \quad (\text{Eq. 2.22})$$

where $(F_s^1)_0$ is the linear shear force at the beginning of the timestep, $\Delta \delta_s$ is the relative shear increment, and k_s is the constant shear stiffness.

The rolling resistance moment at a contact is updated by first incrementing it as:

$$M^r := M^r - k_r \Delta \theta_b \quad (\text{Eq. 2.23})$$

in which $\Delta \theta_b$ is the relative bend-rotation increment (no twisting component is considered for rolling resistance moment) and k_r is rolling stiffness which is related to the shear stiffness (k_s) and effective contact radius \bar{R} (Equation 2.13) as:

$$k_r = k_s \bar{R}^2 \quad (\text{Eq. 2.24})$$

This magnitude of the rolling resistance moment is then checked against the limiting torque (M^*) to be updated as:

$$M^r = \begin{cases} M^r & , \quad \|M_r\| \leq M^* \\ M^* \left(\frac{M^r}{\|M^r\|} \right) & , \quad \text{otherwise} \end{cases} \quad (\text{Eq. 2.25})$$

where the limiting torque (M^*) is defined as:

$$M^* = \mu_r \bar{R} F_n^1 \quad (\text{Eq. 2.26})$$

in which μ_r denotes the rolling resistance coefficient.

2.5.3 Measurement Quantities

In DEM models using PFC, different measurement quantities such as stress, strain rate, and porosity (consequently void ratio) can be measured inside regions called measurement spheres (in 3D) or circles (in 2D). In this section, the assumptions and approximations employed in their computation are briefly described.

The porosity, n , is defined as the ratio of the total volume of the void in the measurement region (V^{void}) to the total volume of this region (V^{reg}):

$$n = \frac{V^{\text{void}}}{V^{\text{reg}}} = 1 - \frac{V^{\text{mat}}}{V^{\text{reg}}} \quad (\text{Eq. 2.27})$$

in which V^{mat} is the total volume of material in the measurement region and is approximated by:

$$V^{\text{mat}} = \sum_{N_b} V^{(b)} + \sum_{\bar{N}_b} \bar{V}^{(b)} - \sum_{N_c} V^{(c)} \quad (\text{Eq. 2.28})$$

where N_b is the number of bodies completely inside the measurement region, $V^{(b)}$ is the volume of such body, \bar{N}_b is the number of bodies intersecting the measurement region, $\bar{V}^{(b)}$ is the volume of those parts of such bodies inside the measurement region, N_c is the number of contacts inside the measurement region and $V^{(c)}$ is the overlap volume of the two bodies at such contacts.

Since stress is a continuum, it is necessary to follow an averaging procedure to transfer the contact forces and particle displacements computed at microscale in a discrete PFC model to a continuum. In this respect, the average stress ($\bar{\sigma}_{ij}$) inside a measurement region is calculated by homogenization over the volume of that region as (Christoffersen et al., 1981):

$$\bar{\sigma}_{ij} = \frac{1}{V^{\text{reg}}} \sum_{N_c} f_i^{(c)} l_j^{(c)} \quad (\text{Eq. 2.29})$$

in which $f_i^{(c)}$ is the i -component of the contact force vector and $l_j^{(c)}$ is the j -component of the branch vector joining the centroids of the two bodies in contact. Due to the fact that the forces in the voids are zero, it is possible to determine local stresses as average values by expressing them directly in terms of discrete contact forces inside a measurement region.

As the velocities in the voids are not zero, a similar approach cannot be followed to determine the local strain rate within a particle assembly. Therefore, the strain rate tensor ($\dot{\alpha}_{ij}$) is determined by minimizing the error between the predicted ($\tilde{v}_i^{(b)}$) and measured ($\tilde{V}_i^{(b)}$) relative

velocities of all bodies with centroids within the measurement region and consequently by solving the following nine equations:

$$\begin{bmatrix} \sum_{N_b} \tilde{x}_1^{(b)} \tilde{x}_1^{(b)} & \sum_{N_b} \tilde{x}_2^{(b)} \tilde{x}_1^{(b)} & \sum_{N_b} \tilde{x}_3^{(b)} \tilde{x}_1^{(b)} \\ \sum_{N_b} \tilde{x}_1^{(b)} \tilde{x}_2^{(b)} & \sum_{N_b} \tilde{x}_2^{(b)} \tilde{x}_2^{(b)} & \sum_{N_b} \tilde{x}_3^{(b)} \tilde{x}_2^{(b)} \\ \sum_{N_b} \tilde{x}_1^{(b)} \tilde{x}_3^{(b)} & \sum_{N_b} \tilde{x}_2^{(b)} \tilde{x}_3^{(b)} & \sum_{N_b} \tilde{x}_3^{(b)} \tilde{x}_3^{(b)} \end{bmatrix} \begin{Bmatrix} \dot{\alpha}_{i1} \\ \dot{\alpha}_{i2} \\ \dot{\alpha}_{i3} \end{Bmatrix} = \begin{Bmatrix} \sum_{N_b} \tilde{V}_i^{(b)} \tilde{x}_1^{(b)} \\ \sum_{N_b} \tilde{V}_i^{(b)} \tilde{x}_2^{(b)} \\ \sum_{N_b} \tilde{V}_i^{(b)} \tilde{x}_3^{(b)} \end{Bmatrix} \quad (\text{Eq. 2.30})$$

where $\tilde{x}_i^{(b)}$ is the predicted relative displacement of each body calculated as:

$$\tilde{x}_i^{(b)} = x_i^{(b)} - \bar{x}_i \quad (\text{Eq. 2.31})$$

in which $x_i^{(b)}$ is the measured centroid location of body (b) and \bar{x}_i is the mean position of the N^b bodies within the measurement region. $\tilde{V}_i^{(b)}$ is the measured relative velocity of body (b) calculated as:

$$\tilde{V}_i^{(b)} = V_i^{(b)} - \bar{V}_i \quad (\text{Eq. 2.32})$$

In this equation, $V_i^{(b)}$ is the measured translational velocity of body (b) and \bar{V}_i is the mean velocity of the N^b bodies within the measurement region.

2.6 DEM in Modeling Soil Response

DEM has been vastly used to model the response of soils in various geotechnical engineering laboratory tests. In this section a review of such studies is presented.

Ting et al. (1989) used a two-dimensional disk-based implementation of the DEM in the program DISC to model one-dimensional compression, direct simple shear and triaxial tests and showed that nonlinear, stress dependent soil behavior can be simulated by 2D DEM models in which the particles rotation are inhibited. The authors also used geotechnical centrifuge scaling relationships to construct reduced-scale model of large scale problems (like bearing capacity and lateral earth pressure tests) with fewer number of simulated particles and showed that DEM is

capable of accurately simulating real geotechnical problems, including those with large local yield zones.

Ng and Dobry (1994) used DEM based computer program CONBAL (Ng and Dobry, 1991) to simulate three type of loading: 1) drained monotonic triaxial compression test in 2D and 3D, 2) drained monotonic shear test in 2D and 3D by increasing shear stress while keeping the normal stresses on the sides of the specimen box constant, and 3) constant volume, strain-controlled cyclic shear test in 2D and 3D. Random arrays of various diameter circles or spheres were used as a crude representative of rounded uniform quartz sand. The authors investigates the effects of inter-granular friction and particle rotations on the numerical results. They found that inhibiting particle rotation results in higher strength and stiffness and larger amount of dilation compared to the simulation with free particle rotation (Figure 2.10 and Figure 2.11). The same effects observed for comparisons between simulations with larger and lower inter-particle friction (Figure 2.12). They also showed that macroscopic friction angle increased linearly with inter-particle (microscopic) friction angle (Figure 2.13).

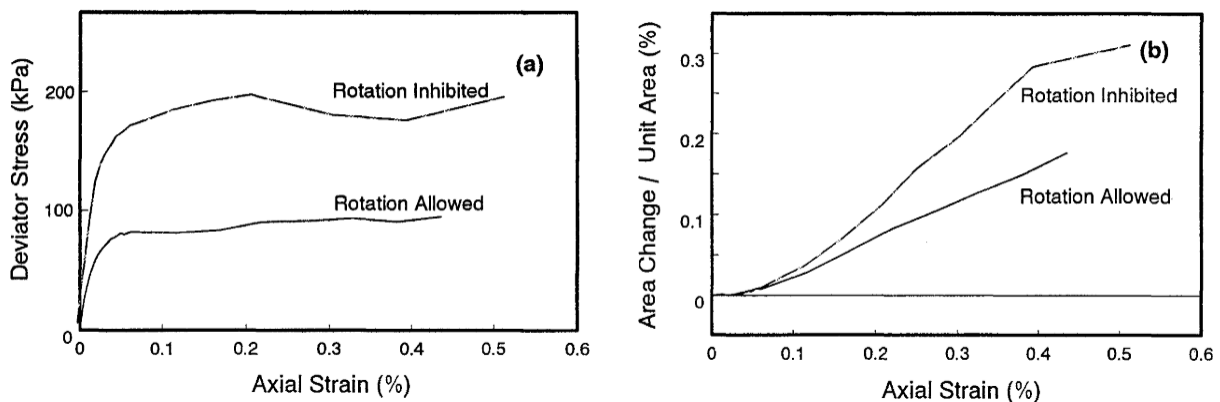


Figure 2.10 Effect of particle rotation inhibition on results of 2D simulations of drained monotonic triaxial compression test (Ng and Dobry, 1994)

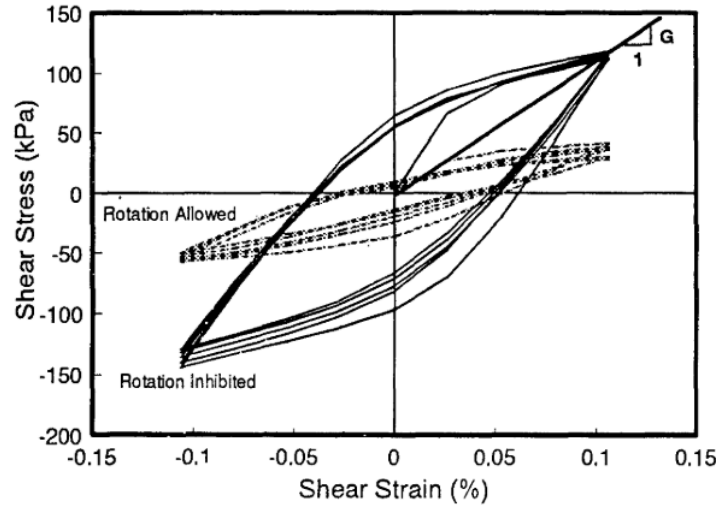


Figure 2.11 Effect of particle rotation inhibition on results of 2D simulations of constant volume, strain-controlled cyclic shear tests (Ng and Dobry, 1994)

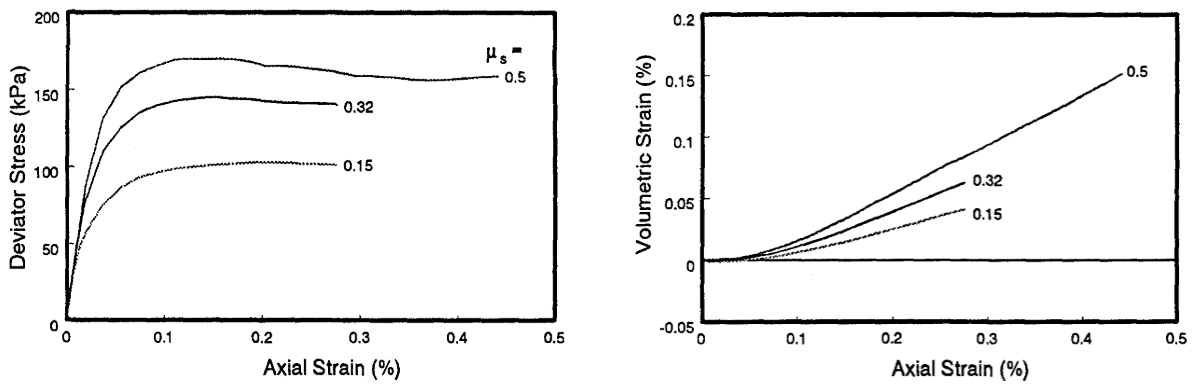


Figure 2.12 Effect of inter-particle friction coefficient on results of 3D simulations of drained monotonic triaxial compression test (Ng and Dobry, 1994)

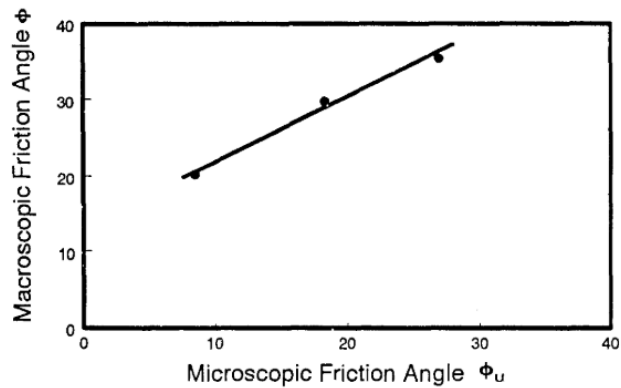


Figure 2.13 Relationship between microscopic friction angle and macroscopic friction angle from results of 3D simulations of drained monotonic triaxial compression test (Ng and Dobry, 1994)

Rothenburg and Bathurst (1989) introduced statistical characteristics of fabric and contact forces to investigate the development of induced anisotropy during shear deformation of plane granular assemblies. They numerically simulated biaxial compression test and used disc-shaped particles. The authors introduced parameters that quantify important features of microstructure such as contact orientation anisotropy and average contact forces, which were explicitly related to the macroscopic parameter of mobilized angle of friction according to the following equation:

$$\sin \Phi = \frac{\sigma_{22} - \sigma_{11}}{\sigma_{22} + \sigma_{11}} = \frac{1}{2} \frac{(a + a_t + a_n)}{1 + \frac{a a_n}{2}} \sim \frac{1}{2} (a + a_t + a_n) \quad (\text{Eq. 2.33})$$

in which, ϕ is the mobilized angle of friction, σ_{11} and σ_{22} are principal stresses in biaxial compression, a is the degree of contact anisotropy, and a_t and a_n are the expressions for the distribution of average tangential components of contact forces and for the distribution of average normal forces, respectively. This equation suggests that the microscopic development in fabric and force anisotropies during shear deformation result in the macroscopic shear stress ratio. It is shown in Figure 2.14 that this equation can accurately relate the macroscopic measure of shear stress to characteristics of microstructure in the condition that the principal direction of stress is coincident with the direction of anisotropy. Bathurst and Rothenburg (1990), Rothenburg and Bathurst (1992), Ouadfel 1998 and Mirghasemi et al. (2002) later verified this relationship for 2D Disc assemblies, 2D ellipse assemblies, 3D ellipsoid assemblies, and 2D polygon-shaped (angular) particle assemblies using DEM, respectively.

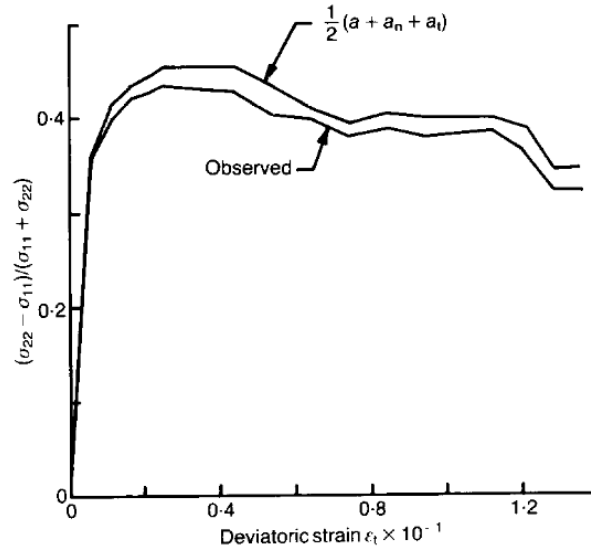


Figure 2.14 Assembly stress in terms of coefficient of anisotropy (Rothenburg and Bathurst, 1989)

Thornton and Zhang (2001) simulated 2D constant volume biaxial compression, simple shear and direct shear tests and suggested that it is not reliable to interpret the material behavior based on wall boundary measurements. Thornton and Zhang (2003) performed 2D DEM simulation of direct shear test under constant volume condition using poly-disperse circles. They *observed* that the deformation was localized in a narrow rectangular shear band of the width of approximately ten particles located at the mid-height of the specimen (Figure 2.15).

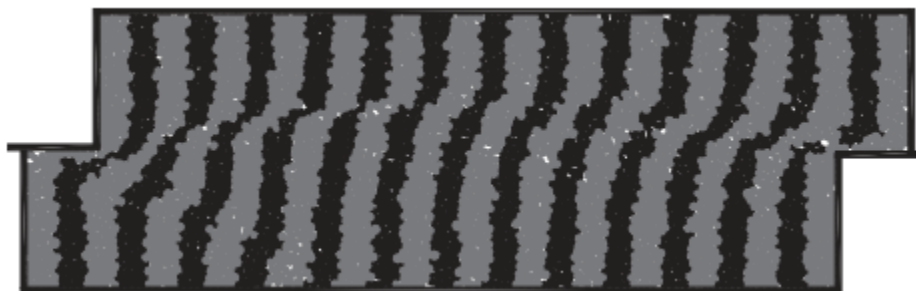


Figure 2.15 Specimen deformation in 2D direct shear test (Thornton and Zhang, 2003)

Cui and O'Sullivan (2006) investigated the microscopic and macroscopic behavior of an idealized granular material (steel spheres) in direct shear test. They performed a 3D DEM analysis with elastic Hertz-Mindlin contact model that uses a no-slip tangential contact model, as proposed

by Mindlin (1949). They validated their DEM model by comparison with a series of physical tests. Although the number of spheres in physical tests were known and replicated in the DEM model, the void ratios could not be exactly match between the numerical and physical specimens (slightly lower void ratio for numerical specimens). However, a relatively good match was obtained for macroscale responses of physical and numerical specimens. The microscale analysis results in this study regarding the stress and strain non-uniformities in direct shear test were found to be in agreement with earlier continuum analysis and 2D DEM analysis. It was also found out that the shear stress calculated inside the specimen decreases as the width of the assumed shearing zone at the mid-height of the specimen increases and therefore shear stresses calculated at the boundary are noticeably lower than the ones calculated near the mid-height of the sample. They observed finite particle displacements and particle rotations perpendicular to the plane of shearing in the shear zone, and also concentrated particle rotations close to the boundaries.

Thornton and Zhang (2006) investigated the shear banding in the 2D DEM simulated samples by pure shear in a biaxial model and studied the non-coaxial flow rule in simple shear deformation as it is generally accepted as the model of displacement in shear band. The simulations were done in both constant volume and constant mean stress conditions. Determining the evolution of principal directions of stress and strain rate, the corresponding non-coaxial flow rule was shown to be equivalent to the one proposed by Tatsuoka et al. (1988) . They also showed that at fully developed flow (when there is no further volume changes), the directions of stress and strain rate are coaxial and the flow rule is equivalent to that proposed by Hill (1950).

Zhao and Evans (2009) assessed the effect of loading (i.e. boundary) condition on the response of granular assemblies by performing 3D DEM simulations of plane strain compression, conventional triaxial compression, and direct shear tests. The simulation results showed generally

good agreement with the experimental results published in literature. Although the model was not calibrated for each of these loading conditions, exactly the same material and model properties were used for the three loading cases and only the problem geometry was changed. They indicated that the DEM can reasonably simulate the differences in the macroscopic behavior (measured at boundaries) between these loading conditions, and the results are in good agreement with the existing empirical relationships.

Zhao and Evans (2011) numerically investigated the behaviors of a granular material at a critical state using 3D DEM simulations of granular assembly behavior under three different loading conditions; plain strain (PS), conventional triaxial compression (CTC), and direct shear (DS). They represented the particles as clumps comprised of two identical overlapping spheres with the aspect ratio (ratio of particle length to the particle width) of 1.5:1 to avoid the significant overestimation of particle rotations of spherical particles during shear. Linear contact model was used and the material properties were selected to be generally consistent with physical counterparts for a uniformly graded clean quartz sand (e.g., Ottawa 20–30 sand). They observed that the deformation of the specimen is predominantly affected by loading condition. They found out that there is no unique critical state line for specimens with different initial void ratios under different loading conditions. They observed that the slope of critical state line in the space of mean effective-deviatoric stress (p - q) is a function of loading condition and the slope of the projection of failure surface on the semi logarithmic space of void ratio-mean effective stress (e , $\ln p$) space, is a function of material property and is independent of the loading condition. Figure 2.16 illustrates the results of their simulations.

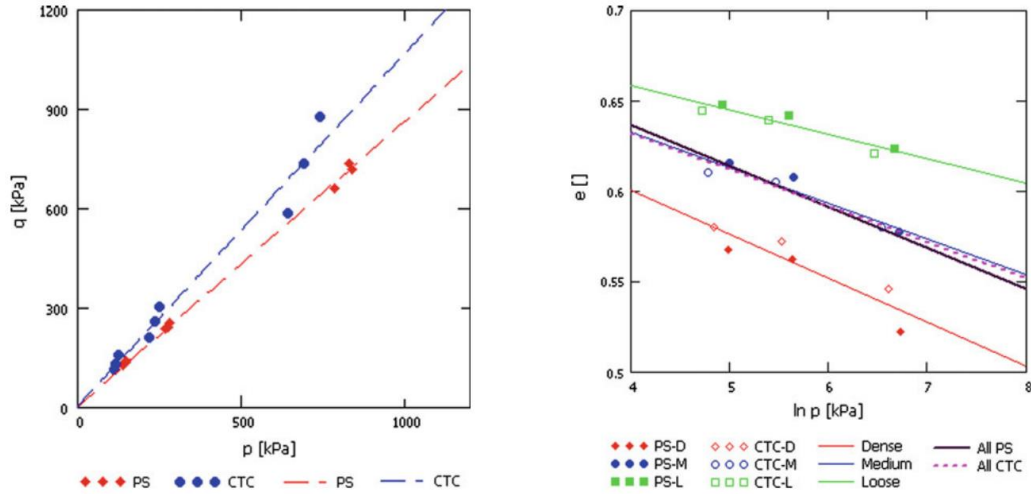


Figure 2.16 Effect of loading condition on the failure surface; Projected on p - q space (left) and e - $\ln p$ spaces (right)space (Zhao and Evans, 2011)

There are also a number of studies that used DEM to simulate the triaxial test. Thornton (2000) simulated a cubical triaxial test using periodic boundaries and poly-disperse spherical particles in order to investigate the quasi-static shear deformation of granular materials. Sitharam et al. (2002) simulated isotropic compression and triaxial static shear tests under drained and undrained (constant volume) conditions. They modelled 3D assemblies of about 1000 poly-dispersed spheres in the size range of 20-100 μm within a periodic space representing an infinite 3D space. They studied the macroscopic behavior of the loose and dense assemblies along with the internal evolution of average coordination number and induced anisotropy during deformation. They showed that particles rearrange during the loading. As can be observed in Figure 2.17, in both dense and loose samples during undrained shear, average coordination number decreases and reaches a constant value at steady state condition. This decrease happens more rapidly in dense specimen.

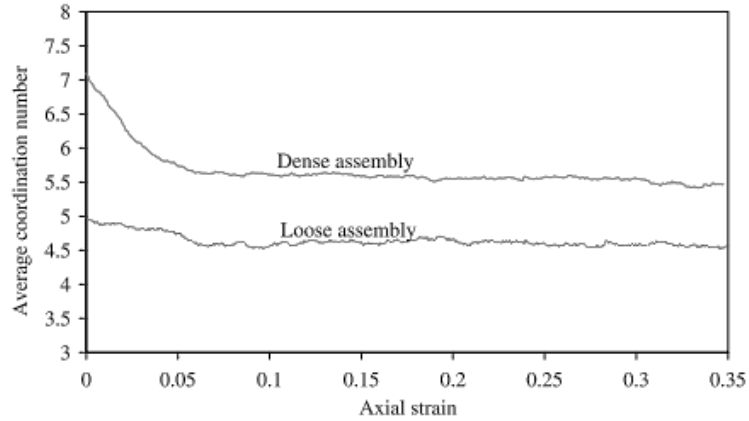


Figure 2.17 evolution of average coordination number during undrained (constant volume) triaxial shear test on loose and dense samples at a confining pressure of 50 kPa (Sitharam et al., 2002)

Sitharam (2003) studied the cyclic behavior of granular material by simulating a series of cyclic biaxial tests in both undrained and drained conditions with constant stress and strain amplitudes. Both loosely and densely packed samples of mono-disperse (uniform) and poly-disperse (well graded) disk particles were considered in the simulations. They showed that cyclic behavior of granular material such as can be satisfactorily simulated by DEM. Examples of their simulation results for undrained (constant volume) stress-controlled cyclic loading are presented in Figure 2.18 and Figure 2.19 for loose and dense poly-disperse disk assemblies, respectively.

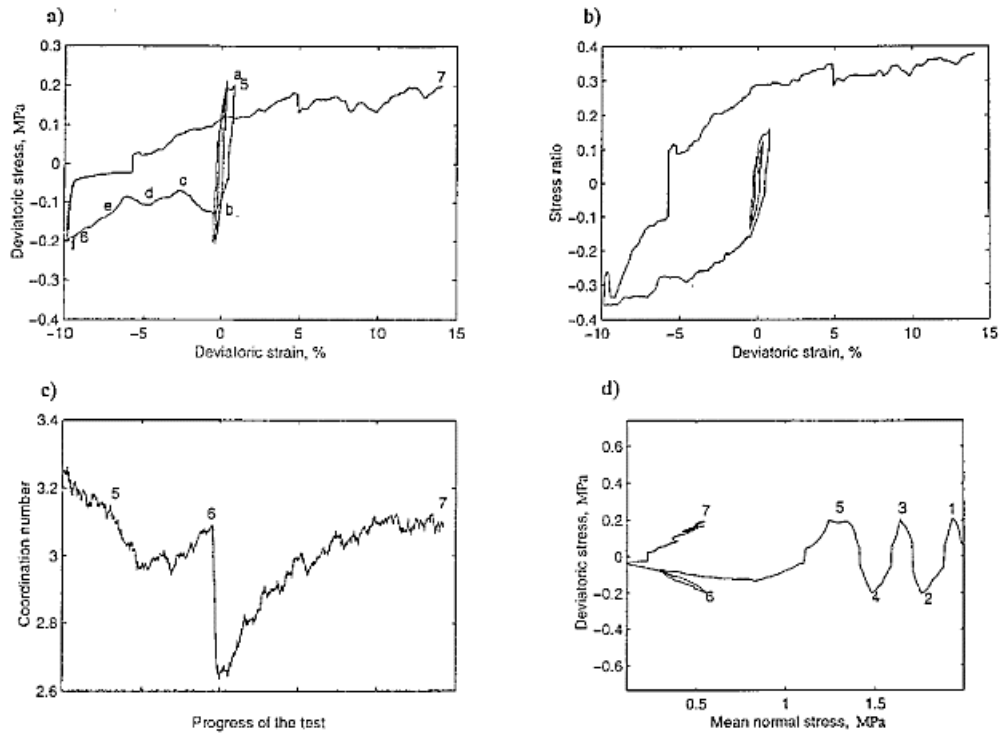


Figure 2.18 Example of undrained stress-controlled cyclic response of loose poly-disperse disks (Sitharam, 2003)

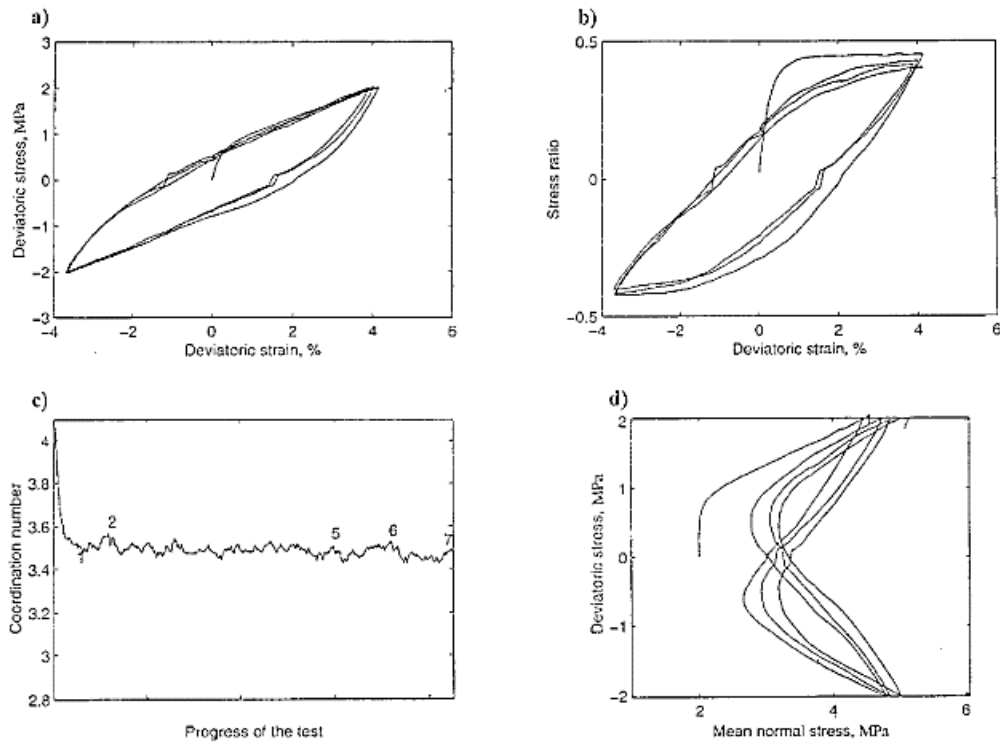


Figure 2.19 Example of undrained stress-controlled cyclic response of dense poly-disperse disks (Sitharam, 2003)

O'Sullivan et al. (2004) examined the response of regularly packed (Faced-centered-cubic (FCC) and hexagonal close (rhombic)) specimens of uniform-sized or poly-disperse steel spheres in triaxial and plane strain compression tests. They considered two different packing configuration to investigate the effect of fabric. Sitharam et al. (2005) used 3D DEM with uniform-sized spherical particles to simulate the triaxial test of a sample of uniform-sized glass beads. Cui et al. (2007) used a mixed boundary approach to improve the computational efficiency in simulating the triaxial test. They suggested that as triaxial apparatus is cylindrical and symmetric around the central axis, only one slice of the specimen is sufficient to be modeled. Therefore, the authors modeled the top and bottom boundaries using planar rigid walls and proposed the usage of circumferential periodic boundaries for the lateral sides of the specimen. They claimed that this type of periodic boundaries are conceptually similar to the widely used rectangular periodic boundaries in DEM. Cheung and O'Sullivan (2008) examined the existing approaches in simulating the latex membrane in triaxial test in both 2D and 3D DEM simulations and developed a more sophisticated and computationally efficient algorithm. O'Sullivan et al. (2008) investigated the response of assemblies of steel spheres in physical and 3D DEM simulated strained-controlled cyclic triaxial tests. After validating the DEM model, they carried out a parametric analysis to study the influence of amplitude of cyclic loading on the macro-scale response and particle-scale interactions. They observed that stress measurements correlates better with the strong fabric tensor and during the cyclic loading, variation of the strong fabric tensor is less than the overall fabric tensor.

Sitharam et al. (2008) used DEM to revisit the methodology proposed by Norris et al. (1997), in which undrained shear response of sands can be predicted from the result of drained triaxial test started from isotropic rebound paths and based on the effective stress concept. One of

the challenges in the laboratory experiments is the difficulty of preparing samples with the exactly same fabric. Sitharam et al. (2008) claimed that this challenge can be overcome by using DEM. They simulated drained and undrained triaxial tests using DEM with poly-disperse spheres and found out excellent correlations between the predicted undrained shear response from drained triaxial simulations and undrained (constant volume) shear simulations. They also conducted laboratory experiments on clean sand to both validate their DEM simulation and revisit the above methodology. They attributed the observed scatters in the predicted and measured undrained shear results from experiments to the difficulty of preparing identical samples with the same initial fabric. They concluded that DEM can satisfactorily simulate the undrained shear response without the explicit incorporation of pore water pressure.

Regarding the DEM simulation of direct simple shear (DSS) test, the documented researches differ mainly in the consideration of boundary conditions. Shen et al. (2010) conducted a 2D DEM study of simple shear test considering both the hinged rigid walls in the parallelepiped sample Cambridge device and the laminar walls which simulate the stack of lateral confining rings often used in the NGI-type device. They suggested that if examining micro-scale behavior is of interest, modeling the correct boundary conditions is very crucial because they observed that even though the macroscopic results may be similar, the microscopic response is affected by the type of boundary walls. In other 2D DEM study, Ai et al. (2014) studied non-coaxial granular behavior in constant load simple shear loading using idealized circular particles. To limit the boundary non-uniformities imposed on the element, they used a discretized wall system as the lateral boundaries. While much of the behavior observed in granular materials in simple shear was captured, the out-of-plane displacements which are present in real granular materials in 3D could not be examined by their 2D model. They observed that in anisotropically consolidated specimens during constant

load simple shear, the direction of principal stress rotates towards that of the principal strain rate. An example of their simulation results is shown in Figure 2.20. A faster approach to coaxiality was also observed for specimen of larger initial void ratio and mean stress. In addition, evaluating the evolution of fabric during shear, they observed that principal fabric direction evolves similarly to the principal stress direction.

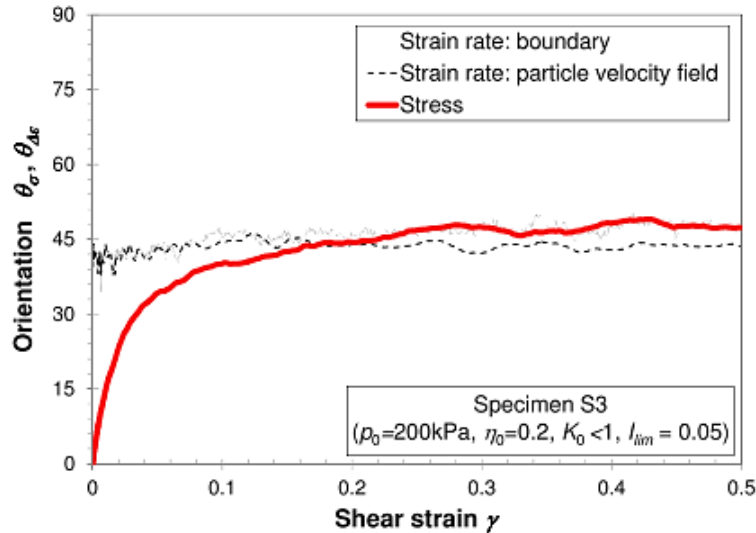


Figure 2.20 Evolution of major principal stress and strain rate orientations in 2D constant load simple shear simulation (Ai et al., 2014)

Dabeet et al. (2011) and Dabeet (2014) modelled monotonic and cyclic small-scale NGI-type simple shear test with a specimen confined by wire-reinforced rubber membrane. They used spherical glass bead as testing materials. They modelled the lateral boundaries of the specimen as a stack of cylindrical walls in DEM. To simulate the shearing phase, they assigned constant pre-defined velocity values to each ring in a way that their movement generates an ideal simple shear deformation along the boundaries. For comparing the macroscopic results of the model with the boundary measurements in experiment, the shear stress at the moving horizontal boundary in the model was calculated by adding the forces (in the direction of shearing) on the horizontal boundary and half of the cylindrical walls adjacent to it, and dividing it by the cross sectional area of the sample

(which is a circle of same diameter as cylindrical walls). Dabeet et al. (2015) investigated stress strain non-uniformity inside DSS specimen under monotonic constant stress loading. To prevent slippage on the horizontal interface, they modeled flat horizontal boundaries with high friction coefficient of 10. They reported non-uniform stress and strain distribution inside the specimen.

Wijewickreme et al. (2013) used DEM to explore the state of stress inside the specimen of glass beads during drained and constant volume simple shear loading. They considered a cylindrical specimen confined with rigid rings for lateral support. During shear, they applied predefined velocities to each of these ring to model a perfect simple shear deformation at the boundaries. They prevent slippage at the interface between specimen and horizontal plates by assigning a very high friction coefficient of 10. They used a linear contact model without ant rolling resistance (glass beads were tested). They observed that by progression of shear, planes of maximum stress obliquity rotate and therefore it is impossible in a typical simple shear laboratory test (without measuring normal stress at vertical boundaries) to calculate the mobilized friction angle accurately. They, however, observed that plane of maximum stress obliquity coincides with the horizontal plane at large shear strains, which makes it reasonable to approximate the mobilized friction angle at such shear strain levels using the stress state on the horizontal plane (Figure 2.21).

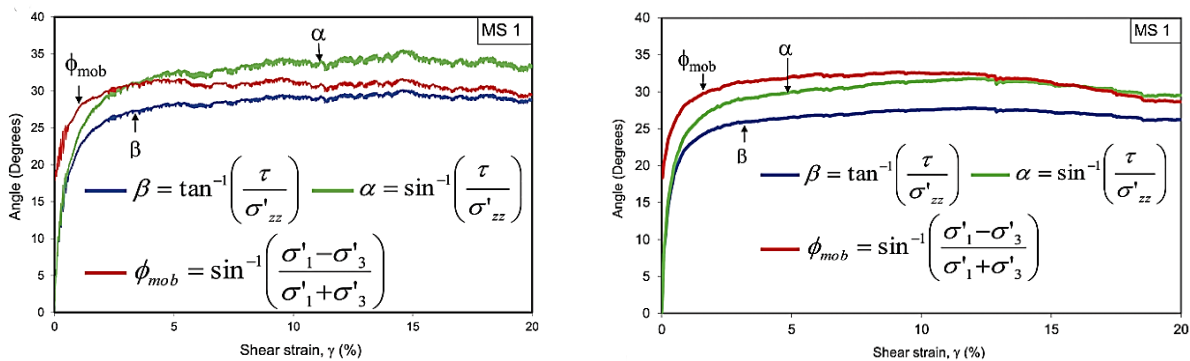


Figure 2.21 Comparison of actual mobilized friction angle with the ones from assumed stress state for simple shear specimen in which horizontal plane coincides with plane of maximum shear or maximum stress obliquity: Drained condition (left), undrained condition(right) (Wijewickreme et al., 2013)

Bernhardt et al. (2014) and Bernhardt et al. (2016) modelled a small-scale stacked ring simple shear test of steel spheres under constant stress condition. The experimental sample was confined by a rubber membrane within a stack of rings. To make rough fixed-particle boundaries and avoid slipping and rolling of spheres along the horizontal boundaries, they used epoxy to attach particles to the top and bottom porous stones. To replicate the experimental glued particles, the particles in contact with horizontal boundaries are assigned to move with the same velocity as their adjacent horizontal boundary and their rotation is also set to zero. During the shear stage, the horizontal boundaries moves as in the experiment, and for the rest of the rings, the position was updated at regular intervals based on a user-defined function. Bernhardt et al. 2014 stated that the velocities of the rings were updated at every 10 cycles with the target of keeping the net force very close to zero. For comparison with experimental results and since the particles are glued, the shear stress at the moving horizontal boundary was calculated by considering the particles out of balance force in addition to the contact forces at the moving horizontal boundary. Bernhardt et al. (2016) found out that specimen inhomogeneity is highly sensitive to the particle size relative to the sample dimensions. They stated that in validation studies, caution should be exercised to ensure large enough ratio of the critical sample dimension to the particle diameter.

Wang and Wei (2016) conducted a 2D DEM study by considering disk-shaped particles to investigate the microstructure behavior of granular materials during cyclic mobility and post liquefaction stage. To eliminate the boundary-induced non-uniformity in the specimen, periodic boundaries were used in their simulations. They defined “centroid distance (D_c)” as the difference between the particle center and the Voronoi cell center in order to represent the particles and voids distribution in the assemblage. In other words, the spatial distribution of voids around the particles was described using D_c . They observed that during undrained cyclic loading, the number of

particles with a large value of D_c decreases, which means that relatively large pores irreversibly redistribute before and after the liquefaction. A strong correlation was also observed between the evolution of D_c and the cyclic mobility and post-liquefaction deformation.

Asadzadeh and Soroush (2016) modelled a small-scale stacked-rings simple shear test under constant stress condition using glass beads as testing materials. In their simulations, “saw-tooth configuration” was modelled for the roughness of the top and bottom boundaries, which is similar to the platens they used in experiment. In both simulation and experiment, the top boundary and its adjacent ring were stationary while the bottom boundary and its adjacent ring moved with a constant velocity. For each of the other rings in the simulation, the velocity was set independently to provide a uniform boundary shear strain (the velocity of the rings varied linearly between zero to the velocity of bottom boundary for, respectively, the ring next to the top boundary and the one next to the bottom boundary). They investigated the stress and strain non-uniformity, the orientation of the failure surface, anisotropy, and non-coaxiality in specimen of glass beads in constant stress simple shear condition.

Asadzadeh and Soroush (2017) modelled the same stacked-ring simple shear test and investigated fabric anisotropy, principal stress rotation, and stress state inside the specimen during constant volume stress-controlled cyclic loading. They observed an almost even distribution of normal and shear stresses inside the specimen except at corners where severe fluctuations occurred. They also observed that non-uniformity of volumetric strain was insignificant at the initial cycles and increased as more loading cycles applied. Their simulations showed the evolution of stress-induced anisotropy inside the specimen (Figure 2.22) and the strong force chains were observed to rotate and get aligned with the major principal direction (Figure 2.23).

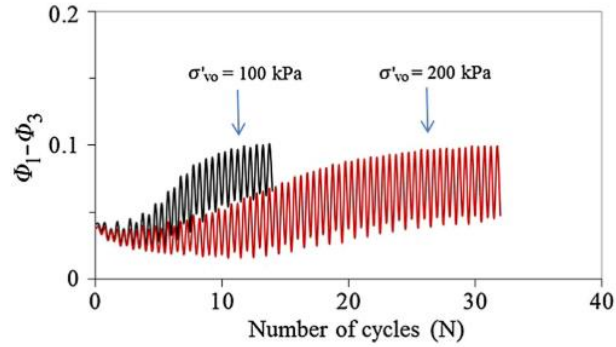


Figure 2.22 Evolution of fabric anisotropy in specimen of glass beads during cyclic loading (Asadzadeh and Soroush, 2017)

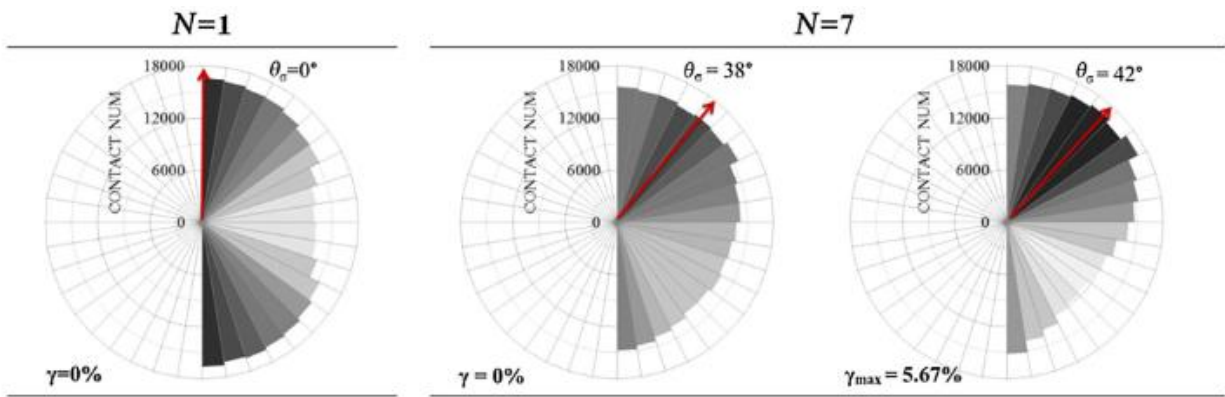


Figure 2.23 Rose diagrams of contact normal forces in specimen of glass beads before shearing and during the seventh cycles of shear for $\sigma'_{v0}=100$ kPa and CSR=0.15 – Stronger contacts are denoted as darker bins. (Asadzadeh and Soroush, 2017)

Zhang and Evans (2018) used both lateral periodic and rigid boundaries to study the strain-controlled cyclic simple shear behavior of cubical specimens of poly-disperse spheres. In case of the specimen with periodic boundaries in lateral sides, the particles adjacent to the rigid horizontal boundaries were laterally translated in conjunction with the platens in order to transfer shear strain to the specimen without any slippage between the particles and platens. They also used linear contact model in their simulations. They observed that stiff boundaries resulted in larger variations in contact anisotropy during cyclic simple shear loading. They associated it to the fact that particle movements near rigid boundaries are significantly restrained. They also observed that due to the boundary restraints in specimen with rigid lateral boundaries, the specimen corners behaved

differently from the specimen center during shear and squeezing-type deformation causing compression occurred near the corners. It is while all parts of the specimen with periodic lateral boundaries experienced pure shear. They suggested that for the simulation of undrained cyclic simple shear tests, it is better to use periodic lateral boundaries.

The effect of boundary asperities on the shear behavior of granular materials has been studied by some researchers. Prevost and Høeg (1976) reported that slippage on the horizontal platen-soil interface in simple shear test can extend non-uniformities toward the central portion of the specimen. Kittu and Bernhardt (2017) reported the influence of different boundary asperities on the peak shear stresses and friction angles in direct shear test. Jing et al. (2017) investigated shearing behavior of a soil-structure interface and observed that the shearing behavior of material and the thickness of shear band are influenced by the properties of both the material and the structure in interface shear devices. Asadzadeh and Soroush (2018) simulated stacked-ring simple shear test under constant volume stress-controlled cyclic loading to study the effect of different common shapes of asperities of horizontal platens surfaces on some macro- and micro-scale response such as liquefaction potential, strong force chain, and stress and strain distribution inside the specimens. They observed that by limiting the slippage, specimen exhibited higher cyclic resistance. They found out that shape of the horizontal platen asperities affects the pattern and degree of the stress and strain non-uniformity. Lower slippage at the particle-platen interfaces decreased the degree of developed non-uniformity. Moreover, higher slippage resulted in concentration of stronger force chains at the corners of the specimen and higher degree of stress non-uniformity.

To reduce the complexity and difficulty of conducting undrained test on saturated samples, many researchers have conducted constant volume test on dry samples. This method which was

first proposed by Taylor (1948) and then applied in simple shear test by Pickering (1973) has been widely used in numerical and experimental studies (e.g., Ng and Dobry, 1994, Wijewickreme et al., 2013, Asadzadeh and Soroush, 2017, Zhang and Evans, 2018). It has been verified that similar results can be obtained in undrained tests of saturated granular materials and constant volume tests of dry ones (Finn et al., 1978, Dyvik et al., 1987, Shafipour and Soroush, 2008) and it has been shown that the changes in measured vertical stress in a constant volume simple shear test is corresponding to the change of pore pressure that would develop in an undrained test.

2.7 Incorporating the Effect of Actual Particle Shape

To simulate the real soil particle shape in DEM simulations while maintaining the required computational time and effort low, different methods has been used in the literature. For example, Dobry and Ng (1992) prohibited spherical particle rotation during shear, Iwashita and Oda (1998) added rolling resistance at contacts, and Ting et al. (1995) used ellipsoidal shapes to simulate the real particles. Clusters or clumps has also been used either as glued together discs/spheres (e.g., Jensen et al., 1999), or as fused overlapping sphere (e.g., Powrie et al., 2005; Zhao and Evans, 2011). Santamarina and Cho (2004) stated that particle size and shape play a significant role in behavior of the soil. They showed that three principal particle shape parameters named sphericity, angularity and roughness are crucial parameters to determine the soil behavior characteristics. Rothenburg and Bathurst (1992) used elliptical particles for representing the soil particles. They showed that particle shape has a significant effect on shear strength, deformation behavior and fabric statistics of particle assemblies. To investigate the effect of particles shapes on strength and deformation behavior, Ting et al. (1995) simulated biaxial compression test of ellipse-shaped particles using 2D DEM. They observed that DEM simulation using 2D ellipse-shaped particles could predict the mechanical behavior of real material much better than using circular-shaped

particles. Regarding the biaxial compression simulations, they concluded that ellipse-shaped particles resulted in higher peak friction angle than circular-shaped particles while the volumetric behavior did not differ as significantly. The authors also assessed the relative importance of particle rotation and translation by decomposing the contact motions during shear and made the conclusion that particle rotation leads to twice as much contact motion for round particles as particle translation. They stated that prevention of particle rolling through particle interlocking is the main source of higher strength in angular particle assemblies.

Ng (2001) investigated the fabric evolution of assemblies of uniform ellipsoids under drained triaxial compression loading at large strains using 3D DEM. They studied the effect of particle shape on fabric evolution by considering four different aspect ratios (varying between 1.2 and 2) for uniform ellipsoidal particles. They considered three fabric parameters to track the evolution: distribution of particle orientations, distribution of branch vectors, and normal vectors (Figure 2.24). The macroscopic results indicated that at large strains, particle shape affects the volume change behavior but not the shear strength. The microscopic results revealed that the difference between branch vector and normal vector increases by the increase in particles aspect ratio.

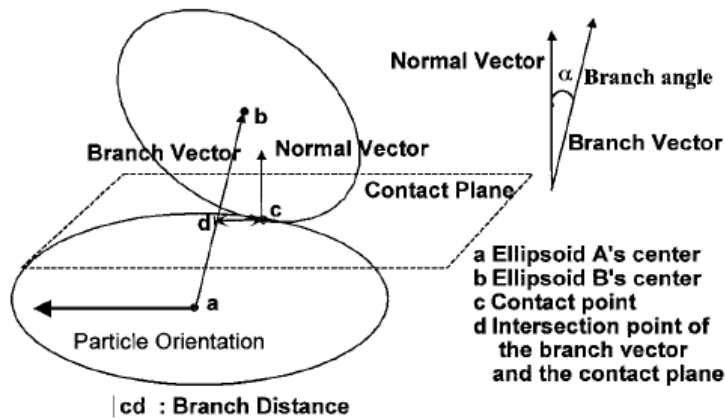


Figure 2.24 Fabric parameters (Ng, 2001)

Jensen et al. (1999) effectively modelled generally-shaped particles by combining smaller circular particles into a rigid configuration called cluster (Figure 2.25). Numerical ring shear experiments were simulated with varying normal loads and particle types (cluster v. non-clusters). The shear surface roughness of the bottom boundary was also modelled as saw-tooth shape with different amplitudes and periods (Figure 2.26). To ensure the formation of possible shear zone within the medium or near the shear surface, the horizontal displacement and rotation of particles in contact with top surface were also prevented. The results of their study is shown in Figure 2.27 and Figure 2.28 . They concluded that geometry dependent behavior of particles (particle interlock and rolling resistance) can be better modelled by clusters.

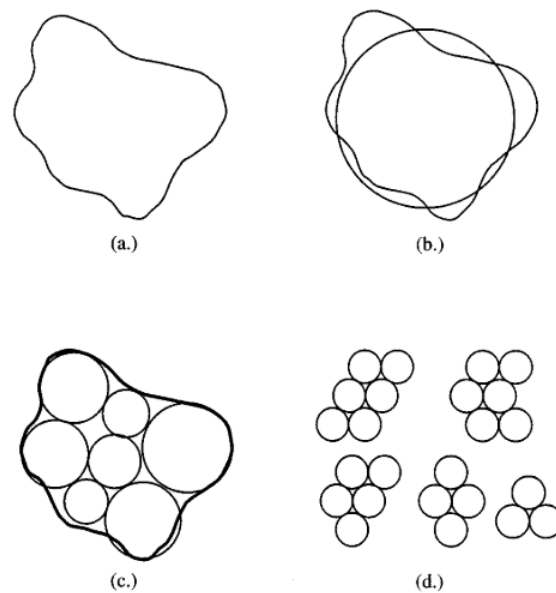


Figure 2.25 Presenting real shape of particles using clusters; a) outline of real particle, b) superimposing DEM disc element over the real shape; c) representing real shape using cluster of discs; d) various combinations of disks in the form of clusters (Jensen et al., 1999)

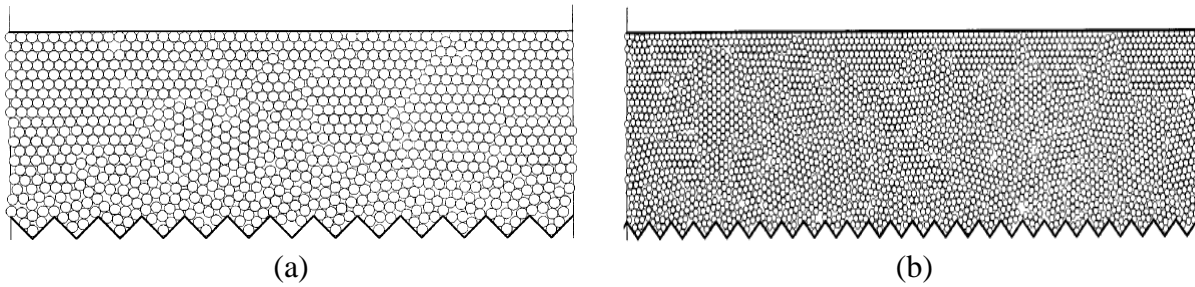


Figure 2.26 Modelling the shear surface (bottom boundary) roughness by saw-tooth shapes of different amplitudes and periods; a) saw-tooth period of four times the diameter of the non-clustered particle, $\lambda=4D$; b) saw-tooth period of two times the diameter of the clustered particle, $\lambda=2D$ (The cluster diameter is equal to the diameter of the non-clustered particles) (Jensen et al., 1999)

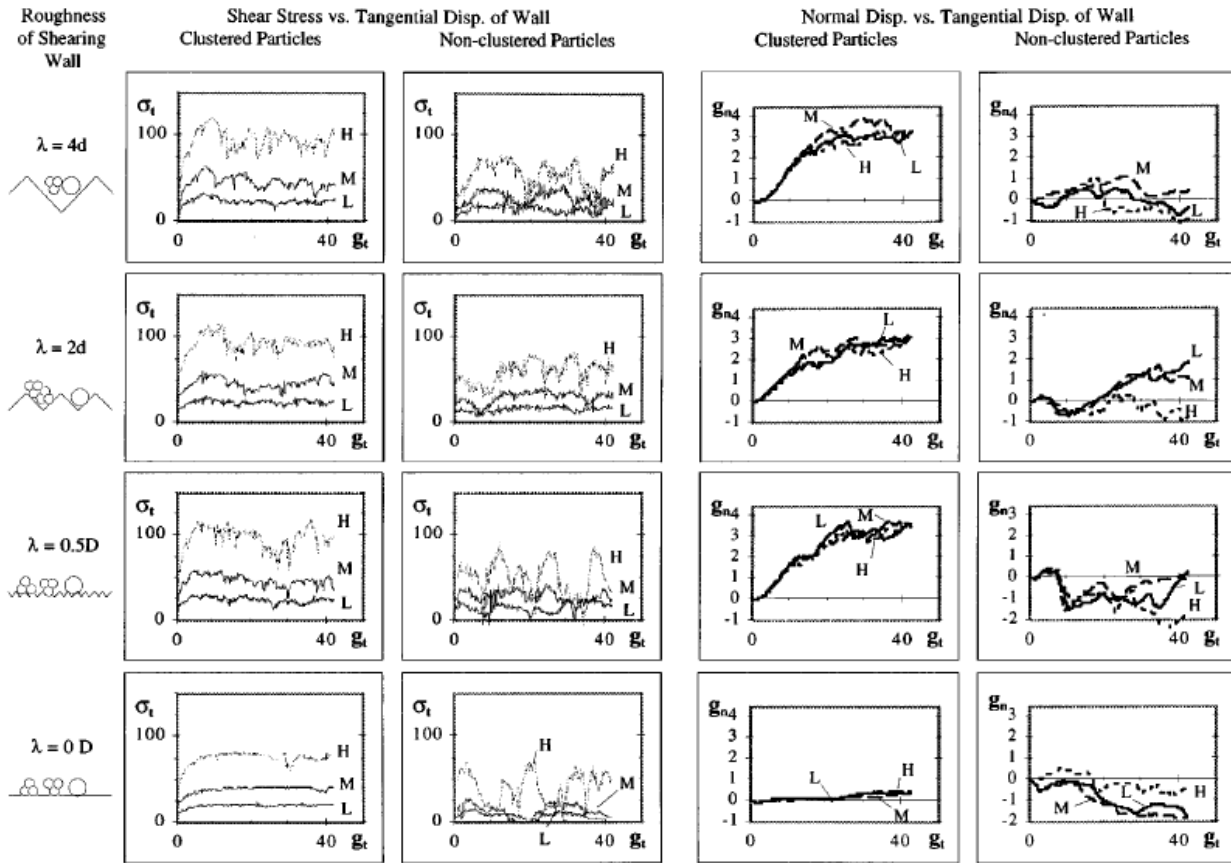


Figure 2.27 Graphs of shear stress at shearing wall (left) and vertical displacement of top wall (right) versus tangential displacement of shearing wall (vertical stress are equal to 50, 100, and 200 MPa for cases L, M, and H, respectively) (Jensen et al., 1999)

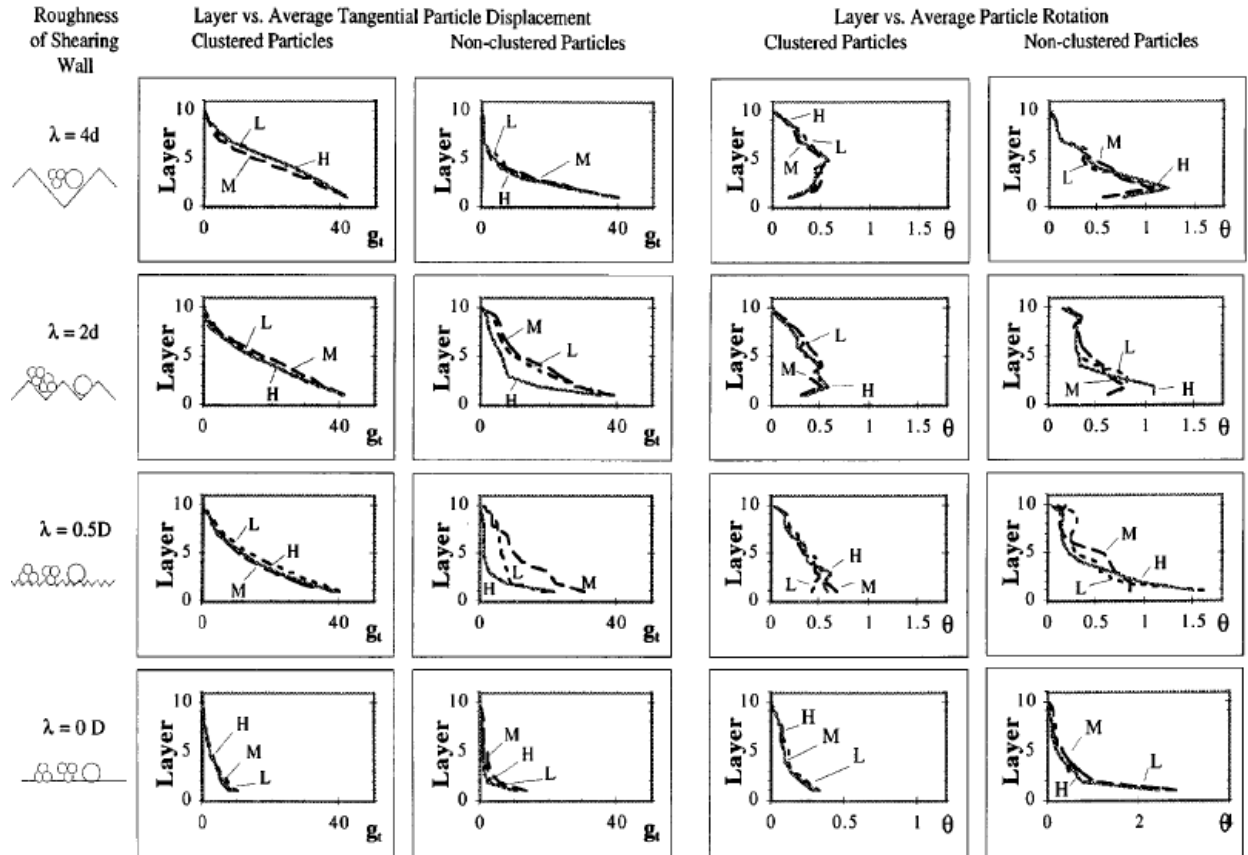


Figure 2.28 Graphs of average particles displacement by horizontal layers (left) and average particles rotation (Θ) by horizontal layers (right) versus the tangential displacement of shear wall (g_t) (Jensen et al., 1999)

Geng (2010) used two-sphere clumps as particles for investigating the influence of particle shape in simulation of the biaxial test and cavity expansion. The simulation results showed that the sample of clumps gives a larger peak stress and higher ultimate stress in the biaxial test and a higher cavity pressure in cavity expansion test than the sample of spheres and compared qualitatively well with experimental results.

Lim and McDowell (2005) simulated the shape of railway ballasts using clumps with simple cubes of 8 spheres. They observed that due to better particle interlocking, the simulated specimen with the eight-ball clumps exhibited much more realistic response during box tests compared with specimens of spheres.

Salot et al. (2009) used combination of spheres to generate non-convex particles and the consisting spheres were either interlocking or not. To simplify their geometry, the radii of the spheres making up an element were considered identical. They defined the morphology of particles using two parameters of number of composing spheres and angularity. They used angularity as quantification of the concave aspect of particles and calculated it as the ratio of the distance between the centers of two spheres (d) to their diameter ($2R$). This parameter was also used as a characterization of element slenderness. Figure 2.29 and Figure 2.30 show some of the different clumps they used. Figure 2.29 also shows the influence of the number of composing spheres on the shape of the generated clumps with angularity of 1 and Figure 2.30 illustrates the effect of angularity on the geometry of clumps of two spheres. It can be observed that for angularity value greater than 1, the composing spheres are not in contact but can still be considered as a rigid body. A maximum limit for the angularity value depending on the sample's granulometry was considered so that particles can never cross each other.

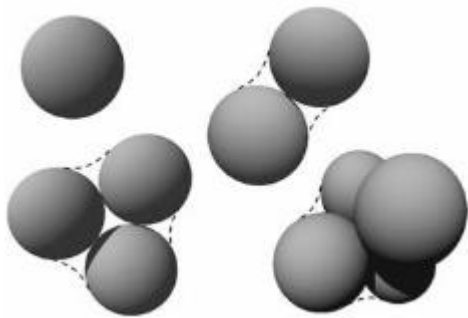


Figure 2.29 Influence on the number of spheres per clumped element (1, 2, 3, 4) on the geometry of the clumps for angularity = 1 (Salot et al., 2009)




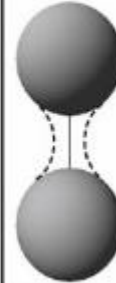
Ang (-)			
0.0	0.5	1.0	1.5
			

Figure 2.30 Influence of angularity on the geometry of elements composed of two spheres (Salot et al., 2009)

Garcia and Bray 2018 studied development of shear rupture in granular media due to boundary deformation using 3D DEM simulation of direct shear test. The particle shapes and size distribution used in the simulation is shown in Figure 2.31. Using such particles incorporated the inherent resistance to rolling of irregularly shaped particles and resulted in realistic response of the particle assembly.

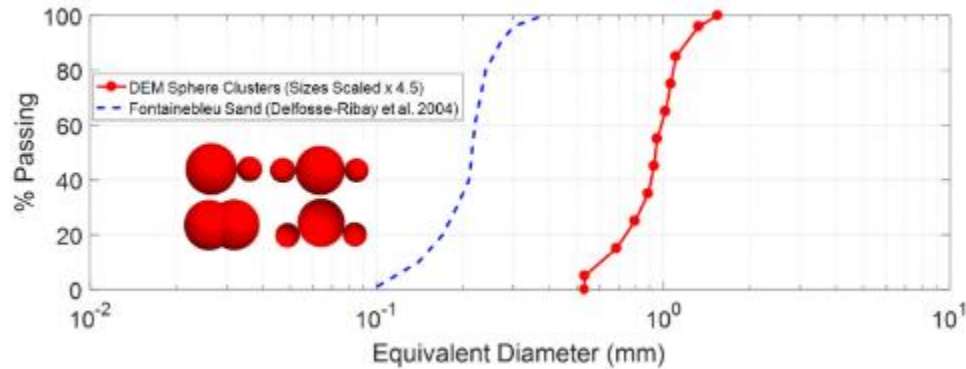


Figure 2.31 Particle shapes used in simulations and grain size distribution of a particle assemblage scaled relative to that of Fontainebleau sand (Garcia and Bray, 2018)

Garcia and Bray (2019) investigated the macroscopic and microscopic responses of granular materials in constant stress direct shear test. To investigate the effect of irregularly shaped particles on volumetric dilation and mobilized friction angles, they compare the responses for specimen of spheres and sphere-clusters. They used the three sets of particle shapes shown in Figure 2.32. They observed that peak strengths and dilations were significantly higher for sphere-cluster assemblies than sphere assemblages at similar relative densities. They attributed it to the inherent rotation resistance of sphere clusters.

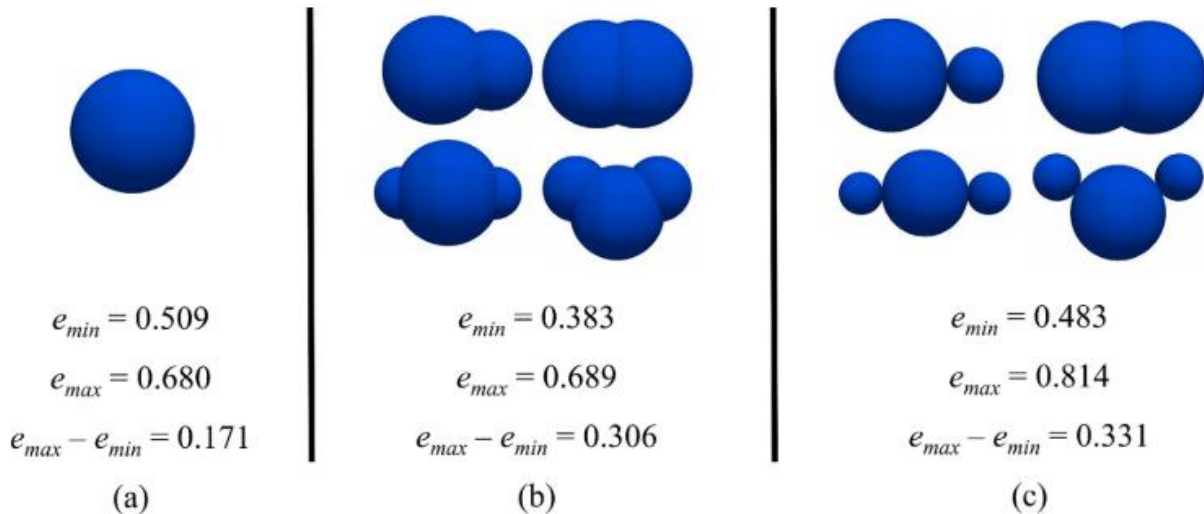


Figure 2.32 Particle shapes used in simulations; a) spheres, b) sub-rounded sphere-clusters, c) sub-angular sphere-clusters (Garcia and Bray, 2019)

Belheine et al. (2009) conducted a 3D spherical discrete model with rolling resistance in order to incorporate the roughness of grains. They observed that the larger the value of the rolling resistance, the higher the resulting peak stress. The similar approach of considering rolling resistance at contacts to incorporate the particle shape into DEM simulation with circular or spherical particles has also been used by other researchers such as Iwashita and Oda (1998), Plassiard et al. (2009) and Wang and Li (2014).

Zhou et al. (2013) compared the rolling resistance effects provided by contact models and those by particle non-circular shapes. Figure 2.33 shows different particles shapes used in their study. The rolling resistance contact model was only used in simulations with disc particles. They observed that both mechanisms of particle anti-rotation resulted in enhanced shear strength and dilatancy behavior of granular assemblies. However, they observed at the microscopic scale that these enhancement achieved by a higher amount of particle rotation in a disc assembly while by a higher particle interlocking effect in an irregular-shaped clump assembly. They also observed that the localization modes of particle rotation and shear strain at the peak state is different between

the two mechanisms. For the disc assemblies with rolling resistant contact model, a clear localization band was observed while localization pattern was more uniform in clump assemblies.

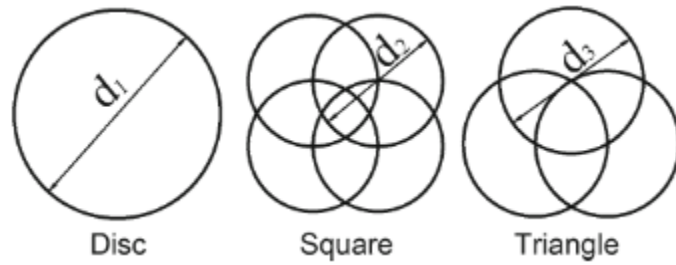


Figure 2.33 Disc and clumps particles used in simulation (Zhou et al., 2013)

Chapter 3

Monotonic and Cyclic Simple Shear Response of Steel Spheres

3.1 Introduction

Simple shear behavior of granular materials tested in the 12" stacked-ring simple shear device under constant volume conditions is studied for uniform-sized steel spheres for the purpose of model validation and gaining better insight into the DEM modeling of such experiment. The grade 25 chrome steel spheres of 3/8 in. diameter supplied by Thompson Precision Ball are used in this study. This material and size are selected for the following reasons:

- The uniform shape of this material can be precisely modelled using DEM.
- The tolerance on diameter and sphericity of these spheres are precisely controlled during fabrication (tolerance of 0.000025 inch (0.0006 mm), for both diameter and sphericity).
- The physical properties of this material are well known, resulting in less required calibration effort and higher confidence in their numerical simulation. Moreover, the exact number of particles being tested in the laboratory is known and can therefore be exactly replicated in the DEM simulation.
- The specific size of spheres (3/8 in., 9.5 mm) used in this study is selected to be close to the D_{50} of the Pea Gravel that is used later in this research.

Overall, using such idealized materials allows for a direct comparison of simulations using DEM with physical test data for validation purposes. After demonstrating the ability of DEM

model to capture the response of this idealized material, the model will be extended to consider more realistic soil particles.

3.2 Large-scale simple shear tests on uniformed-sized chrome steel spheres specimen

A prototype large scale cyclic direct simple shear device of the Norwegian Geotechnical Institute (NGI) type which was developed as part of a cooperation between the University of Michigan and GeoComp Corporation (Zekkos et al., 2018) is used to conduct the monotonic and cyclic simple shear experiments. This large scale device makes it possible to test larger sized particles (e.g. gravels) in the laboratory. The schematic and a photograph of the device is shown in Figure 3.1 and Figure 3.2, respectively. This device allows for testing cylindrical specimens with nominal diameter of 307.5 mm and maximum height of 137 mm and therefore D/H ratio of at least 2.2. ASTM D6528-07 (2007) recommends the maximum particle tested to be not larger than 1/10 of the specimen height. In the experiments of this study, specimen height ranged from about 108 to 110 mm; therefore, the 3/8 in. spheres satisfy the standard requirements.

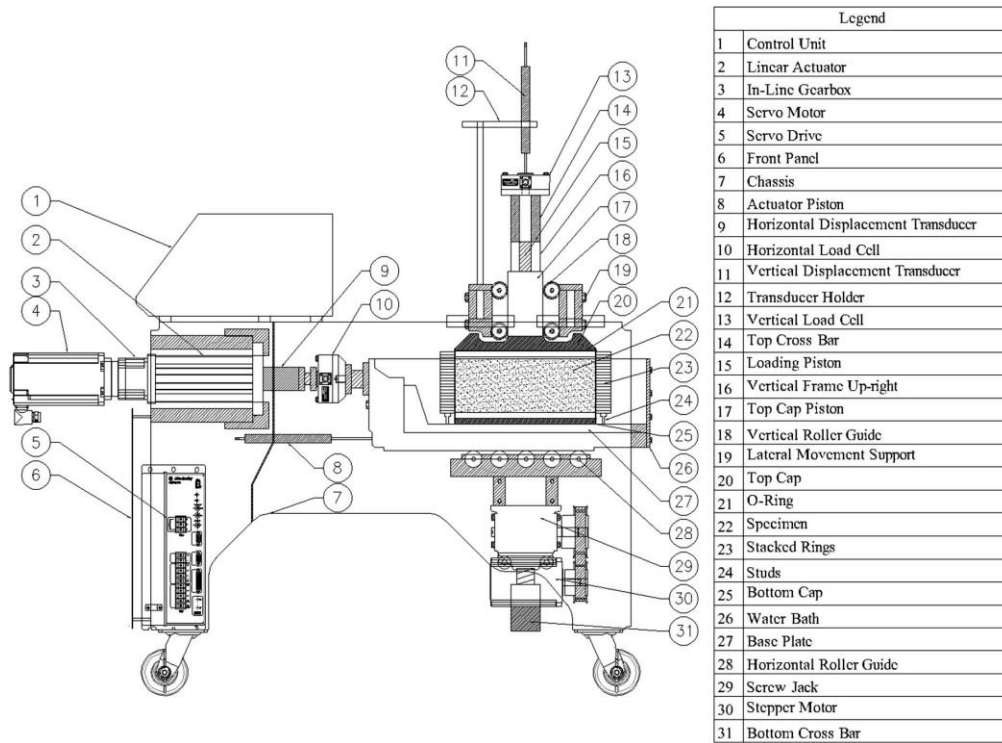


Figure 3.1 Schematic of cyclic direct simple shear device used in this study (Zekkos et al., 2018)

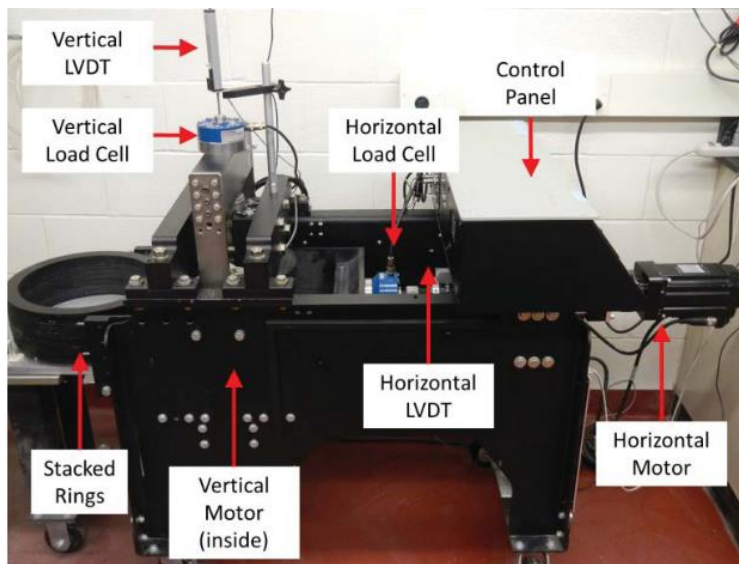


Figure 3.2 Large scale cyclic direct simple shear device at the University of Michigan (Hubler, 2017)

The specimens are prepared within a stack of 17 Teflon-coated circular aluminum rings of 6.65 mm in thickness that have minimal friction against each other. The specimens are prepared by placing the chrome steel spheres loosely in layers using a small shovel until filling the

cylindrical space confined by stacked rings. Photographs of a prepared sample inside the stacked rings is shown in Figure 3.3.



Figure 3.3 Prepared specimen of uniform-sized chrome steel sphere

The specimen is then consolidated under the specific vertical stresses of either 250 or 400 kPa prior to shearing to achieve target void ratio of between 0.652 and 0.675 ($D_r=45\pm 2\%$, considering the minimum and maximum index void ratio of spheres packing be 0.35 and 0.92, respectively (Smith et al., 1929)). This consolidated specimen is then sheared either monotonically or cyclically. Monotonic tests are strain-controlled and the shearing is applied by moving the bottom cap with the constant velocity of about $5.4e-6$ m/s. The cyclic tests are stress-controlled with the CSR of 0.07 and a loading frequency of 0.33 Hz. Monotonic and cyclic simple shear tests are all performed at a constant volume, where changes in measured vertical stress correspond to the change of pore pressure that would develop in an undrained test (e.g., Finn et al., 1978, Dyvik et al., 1987, Shafipour and Soroush, 2008). The vertical movement of the top cap in the device is controlled by a closed loop Proportional-Integral-Derivative (PID) controller with feedback either provided by the load-cell or the displacement transducer to provide load or displacement control. During the monotonic tests, the vertical PID controller values are set to $P=2$, $I=3$, and $D=0$ for both consolidation and monotonic shear stages. During cyclic tests, these values are set as $P=1$, $I=1.5$,

and $D=0$ during consolidation and $P=10$, $I=15$, and $D=0$ during cyclic shearing. To ensure the constant volume condition during these experiments, the vertical strain of the specimen during shear is monitored. In all of the experiments the vertical strain is kept below 0.025% according to the constant volume threshold for axial strain recommended by Hubler (2017) and Basham et al. (2019). As an example, the vertical strains during the monotonic shear test with consolidated vertical stress of 400 kPa is shown in Figure 3.4.

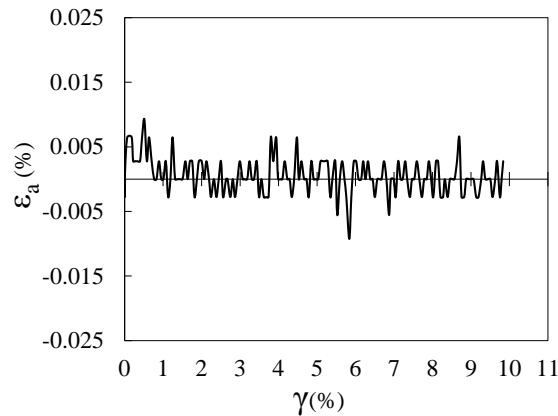


Figure 3.4 Example of vertical strains during monotonic simple shear test ($\sigma'_{v0}=400$ kPa)

The monotonic and cyclic responses observed in the laboratory are shown in Figure 3.5 and Figure 3.6, respectively. Assuming that the shear deformation is completely transferred into the specimen and simple shear deformation is perfectly imposed on the lateral boundaries, the shear strain (γ) is calculated by dividing the horizontal displacement of the bottom cap by the height of the specimen at the end of consolidation. The shear stress (τ) is equal to the load needed to move the bottom cap divided by the area of the bottom cap, and effective vertical stress (σ'_v) is calculated by dividing the force exerted on the top cap divide by the area of the top cap. The area of the top and bottom caps is equal to the cross sectional area of the specimen. For the cyclic test, liquefaction is defined as 3.75% single amplitude shear strain, which is a common strain criteria value that has been used in cyclic simple shear testing to define liquefaction (e.g., Vaid and

Sivathayalan, 1996; Porcino et al., 2008). Pore pressure ratio (r_u) is defined as the ratio of the changes in measured vertical stress to the initial value. It can be observed that, as expected, by increasing the consolidated vertical stress, peak shear stress increases in monotonic loading. More cycles of loading is also needed for the specimen of higher consolidated vertical stress to reach single amplitude shear strain of 3.75% (liquefaction initiation). During monotonic loading and for both consolidated vertical stresses, the specimens experience a significant drop in shear strength through strain softening and then reaches the steady state with a very low residual shear strength. The stress path also shows continuous reduction of effective stress until it reaches close to zero. During cyclic loading, the shear stress-strain response exhibits strain softening after a number of loading cycles and reaches a steady states with a very low residual undrained shear strength and undergoes a large deformation. Such behaviors during monotonic and cyclic loading are similar to the undrained response of loose granular materials. However, with relative density of about 45%, it was expected that the specimen shows a behavior that is more similar to the undrained response of medium dense granular materials, in which the specimen goes through phase transformation at some point during loading and exhibits strain hardening at larger shear strain levels.

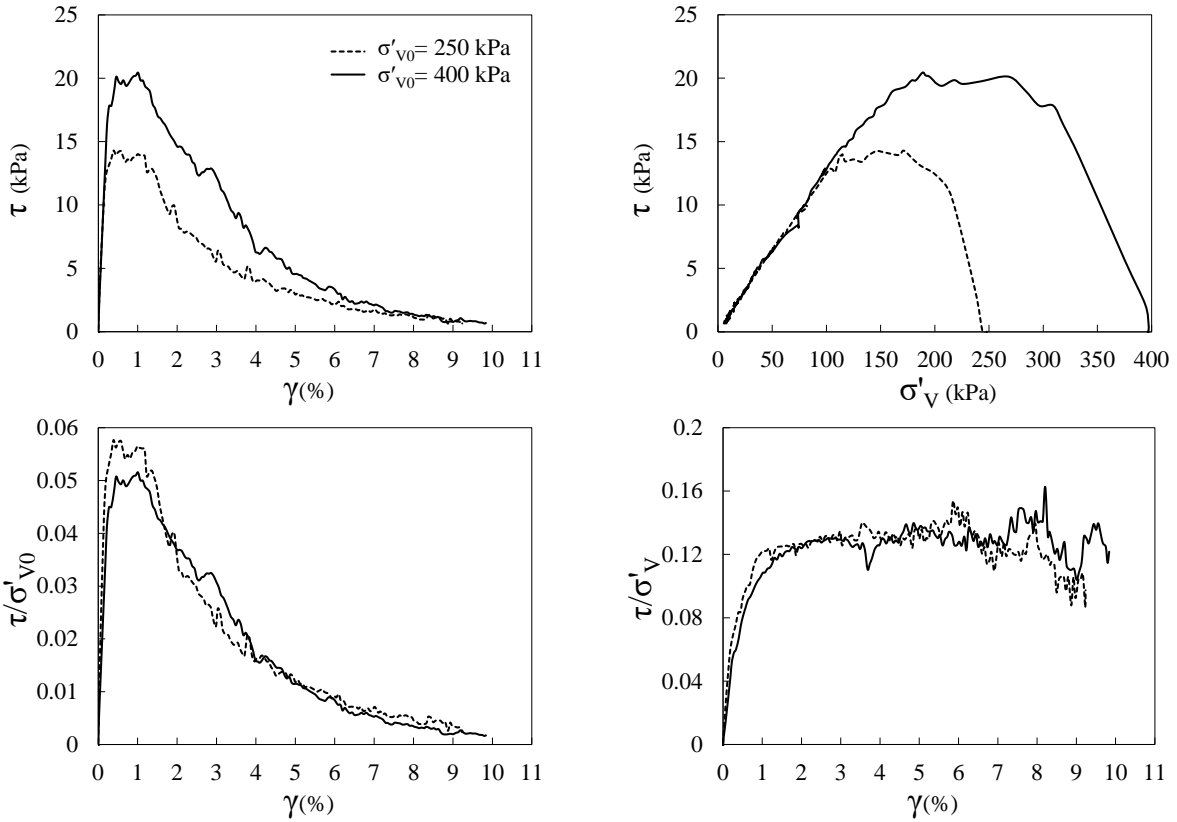


Figure 3.5 Constant volume monotonic simple shear test results for steel spheres ($D_r=45\%$)

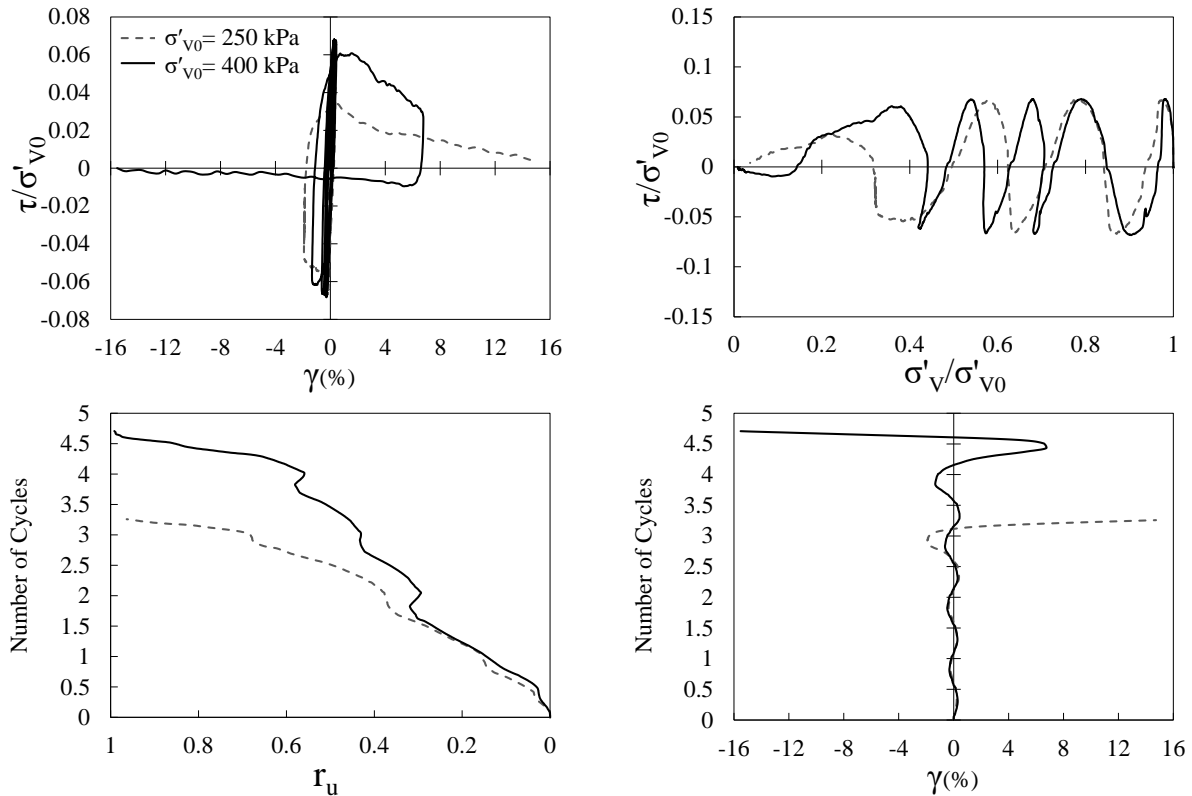


Figure 3.6 Constant volume cyclic simple shear test results for steel spheres ($D_r=45\%$, $CSR=0.07$)

3.3 3D DEM Modeling of Simple Shear Tests on Uniform Steel Spheres Specimens

The commercially available discrete element code software PFC^{3D} 5.00 developed by Itasca Consulting Group Inc. (2014) is used to numerically model the monotonic and cyclic simple shear response of the uniform-sized chrome steel spheres tested in the laboratory. In this regard, the experimental specimen is numerically replicated with the same overall size and the same number and size of particles. The bottom and top caps are modeled as planar wall elements, and the confining rings are modelled as stacked cylindrical wall elements of the same number, diameter and thickness as in the lab. This cylindrical space is then filled with the same number of spheres as in the experiment. Radius expansion is used for initial preparation of the sample. This method has been used by many researchers (e.g., Jiang et al., 2003, Belheine et al., 2009, Dabeet et al., 2011, Gu et al., 2014, Wang and Li, 2014, Asadzadeh and Soroush, 2018, Garcia and Bray, 2018). In this dynamic sample preparation method, particles are initially randomly placed at a fraction of their actual size as a non-contacting cloud within the specified boundaries. Their sizes are then expanded to their actual ones using a series of multipliers. The particle size increase results in particles contacting each other and boundaries, causing a significant energy in the system. Therefore, the model needs to cycle after each stage of radius expansion to reduce the buildup energy. In this study the friction value between all the elements are set as zero during the radius expansion. After this step, the friction values that are to be used in the simulation are assigned to the spheres and boundaries. Then, gravity is activated inside the model and it cycles again to equilibrate. Figure 3.7 shows an actual specimen in the lab and the corresponding numerical one at the end of preparation stage.

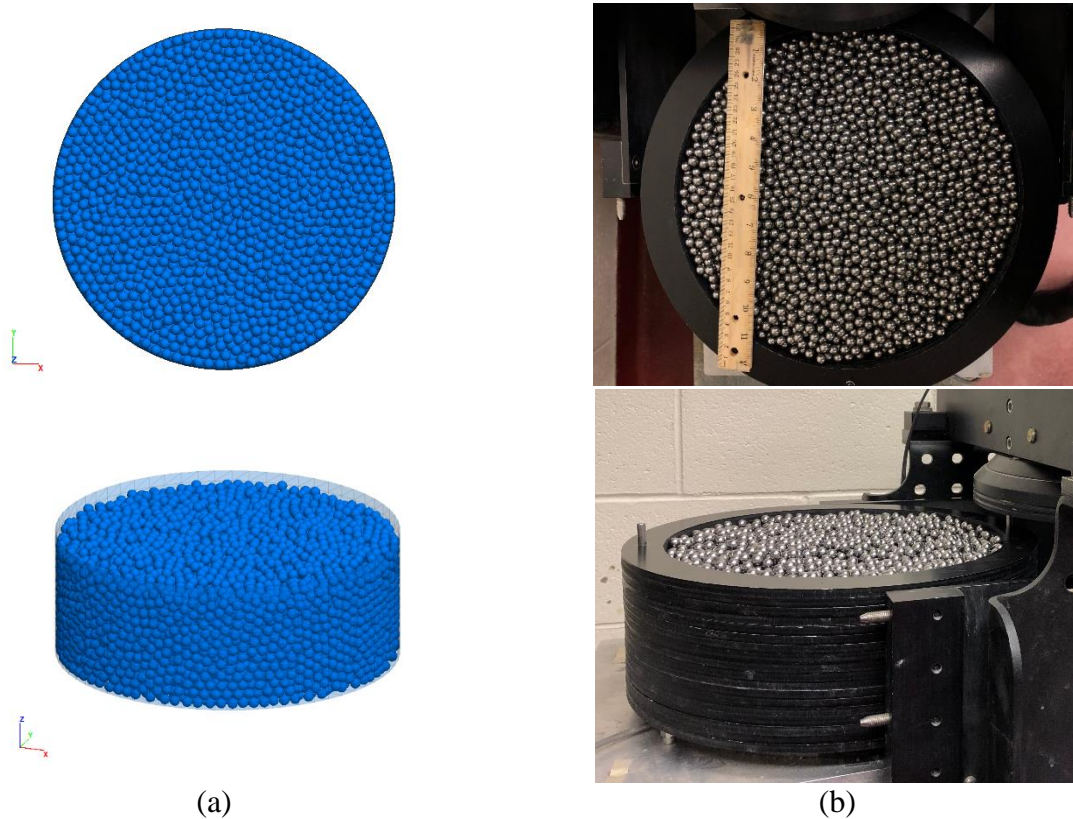


Figure 3.7 a) Numerical DEM Model and (b) Experimental specimen of 10,636 chrome steel spheres each.

After the initial assembly, the sample is consolidated to a target vertical stress in steps by moving the top cap horizontally utilizing the servo control algorithm in PFC. Servo-controlled walls moves with a varying velocities proportional to the difference between the current applied force on them and the target one until the target force is reached. To achieve a numerical sample with the same void ratio as the experimental one, the inter-particle friction values may need to be adjusted during the preparation and/or consolidation stages and may be different from the actual value. However, it is set back to actual value during the shearing stage. Controlling the inter-particle frictions to achieve a target void ratio has been used by a number of researchers (e.g., Thornton, 2000; Huang et al., 2014; Salazar et al., 2015; Bernhardt et al., 2016; Wang and Wei, 2016; Zhang and Evans, 2018). In overall, higher (lower) the inter-particle friction is, the looser

(denser) the simulated sample would be. In this study, the numerical specimens with void ratio between 0.652 and 0.675 (like the experimental one) at the end of consolidation are considered. This range of void ratios are corresponding to range of relative density of $45\pm 2\%$, considering the minimum and maximum index void ratio of spheres packing be 0.35 and 0.92, respectively. These values are equivalents of the minimum porosity of 0.26 for close hexagonal array packing of homogenous spheres and maximum porosity of 0.48 for simple cubical array packing (Smith et al., 1929). To remove additional kinetic energy during the initial assembly and consolidation stages, local damping coefficient of maximum 0.1 is assigned to spheres at different points during simulation. Local damping which is a body-based damping can be used in PFC models to establish equilibrium and conducting quasi-static deformation simulations.

For modelling the shearing stage, the actual laboratory experiment conditions during the test should be considered. In the lab, the top cap is kept stationary and the force applied on it is measured during the test to calculate the effective vertical stress changes while the bottom cap is moved at a specific low velocity that satisfies the quasi-static condition. The force needed to make this movement is measured to calculate the shear stress. Ideally, it is expected that the horizontal displacement of the bottom cap moves the adjacent particles and consequently gets transfer into the whole specimen through the particle-boundaries and inter-particles contacting points. As the rings are frictionless, the movement of the rings is only because of the movement of the contained particles, and there is no externally displacement imposed to them by the device. In other words, the disturbance occurred by the movement of bottom cap is transferred to the rings through the particles.

In this study, the lab testing conditions during the shear phase are simulated numerically. In other words, the movement of the rings in the simulation are set to follow the equations of

motion, same as in the lab. In PFC, wall motion does not obey the equations of motion and they only can translate or rotate with user-defined translational velocity and angular velocity (or spin). As a result, user-defined functions are added to the sequence of operations executed during each calculation cycle. These user-defined functions for rings translational movement in direction of shear follow the same algorithm that PFC utilizes for updating the particles movement. In this user-defined functions, the following equation of translational motion in direction of shear for rings are solved during each calculation cycle using the second order Velocity Verlet algorithm (Verlet, 1967):

$$F_{RS} = m_R \ddot{x}_{RS} \quad (\text{Eq. 3.1})$$

where F_{RS} is the resultant force in the direction of shear acting on the ring, m_R is the mass of the ring, and \ddot{x}_{RS} is the translational acceleration of the ring in direction of the shear. Since in the simulations of this study, the gravitational acceleration vector is perpendicular to the direction of shear, this parameter is not included in the equation. Supposing that the previous cycle solved Equation 3.1 at time t and that the timestep resolved for the current cycle is Δt , the 1/2 step velocity of the ring in direction of shear ($\dot{x}_{RS}^{(t+\Delta t/2)}$) is calculated as:

$$\dot{x}_{RS}^{(t+\Delta t/2)} = \dot{x}_{RS}^{(t)} + \frac{1}{2} \left(\frac{F_{RS}^{(t)}}{m_R} \right) \Delta t \quad (\text{Eq. 3.2})$$

and the position at time $t+\Delta t$ is updated using the 1/2 step velocity as:

$$x_{RS}^{(t+\Delta t/2)} = x_{RS}^{(t)} + \dot{x}_{RS}^{(t+\Delta t/2)} \Delta t \quad (\text{Eq. 3.3})$$

During the force displacement cycle point, the forces are updated for the current cycle, leading to the updated acceleration ($\ddot{x}_{RS}^{(t+\Delta t)}$). The velocity of the ring is subsequently updated as:

$$\dot{x}_{RS}^{(t+\Delta t)} = \dot{x}_{RS}^{(t+\Delta t/2)} + \frac{1}{2} \left(\frac{F_{RS}^{(t+\Delta t)}}{m_R} \right) \Delta t \quad (\text{Eq. 3.4})$$

To speed-up the simulation during shear stage, higher rate of the shear can be used in the model until the quasi-static conditions satisfies and the response remains unchanged for smaller shear rates. This technique has been used by different researchers to accelerate the simulation (e.g., Dabeet et al., 2015; Asadzadeh and Soroush, 2016). In the simulations of this study, the bottom cap is displacing horizontally with a constant velocity of 4.8×10^{-3} m/s. With time step of average value of about 1×10^{-6} second/computational cycle, the bottom cap is displaced about 4.8×10^{-9} meters during each computational cycle. As shown in Figure 3.8, the simulation result is not affected by considering smaller shear rates. Moreover, the average unbalanced force ratio during the shearing stage for the higher rate remains mostly smaller than 1×10^{-3} . Therefore, the applied shear rate assures the quasi-static condition during shearing of the simulated specimen.

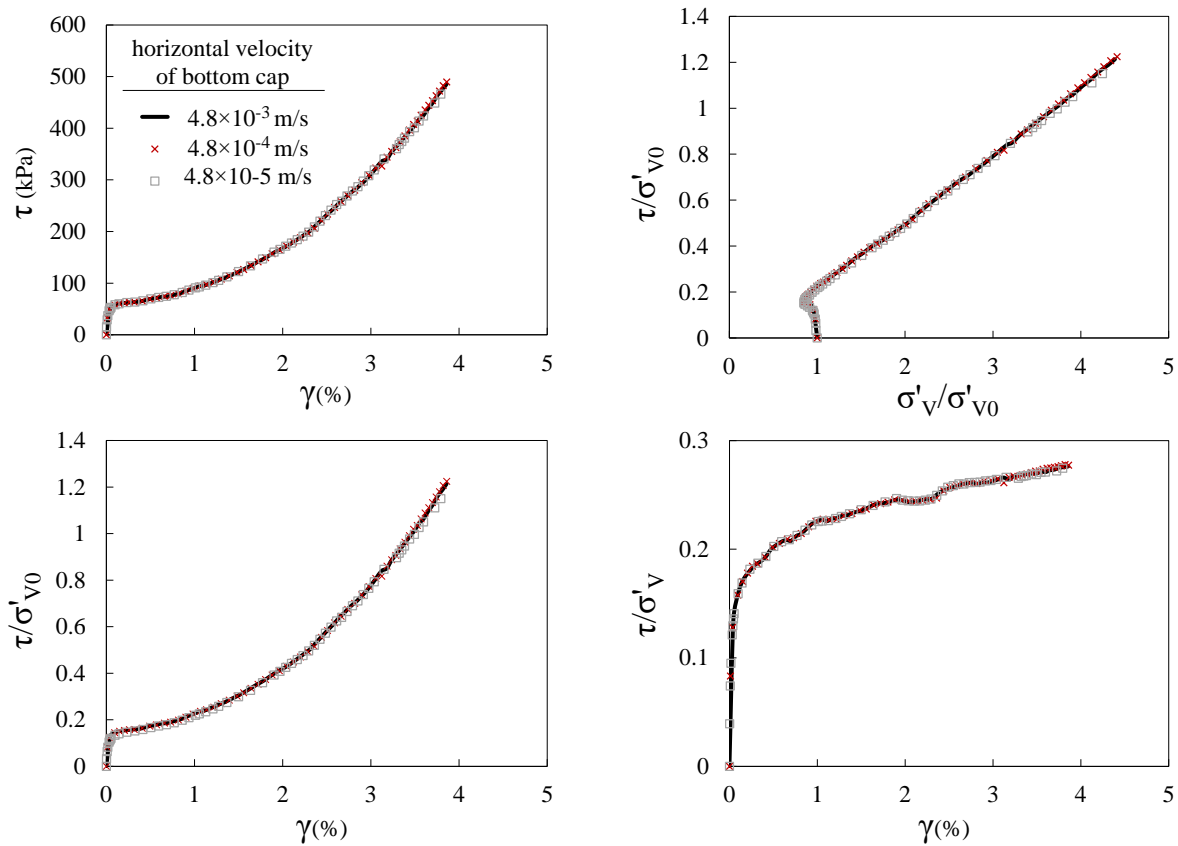


Figure 3.8 DEM simulation results considering different rates of shear for constant volume simple shear test of steel spheres ($\sigma'_{v0}=400$ kPa, $D_t=45\%$)

In the simulations described below, the response of the material under the consolidated vertical stress of 400 kPa is modelled. The specimen consists of 10636 uniform-sized spheres of 3/8 in. diameter. The Hertz contact model is used here. This contact model consists of a nonlinear formulation based on an approximation of the theory of Mindlin and Deresiewicz (Mindlin and Deresiewicz, 1953). The material and contact properties are listed in Table 3.1. **Error! Reference source not found.** These values are either provided by the manufacturer or used by other researchers for the same material or are in the range of values for a property of a specific material. The friction coefficient at cap boundaries are considered as 0.125.

Table 3.1 Material and contact properties used in the DEM simulations

Parameter	Value	Reference
Shear Modulus (GPa)		
spheres	78.1	manufacturer
walls	25.9	in range for Aluminum
Poisson's Ratio		
sphere	0.28	from Cui and O'Sullivan (2006)
walls	0.33	in range for Aluminum
Friction Coefficient		
Inter-sphere	0.096	from Cui and O'Sullivan (2006)
At ring boundaries	0	frictionless rings
Density of spheres (kg/m ³)	7.83×10 ³	manufacturer
Mass of rings (gr)	584	measured

The macro-scale result of this model is compared with the corresponding experimental one in Figure 3.9. Same as in experiment, the vertical effective stress is calculated on the stationary top cap as the total normal forces on it divided by specimen cross-sectional area, and shear stress is calculated on the bottom cap as the total horizontal shear forces in direction of shearing (x-direction) on it divided by the specimen cross-sectional area. Assuming that simple shear deformation perfectly occurs in specimen for both simulation and experiment, the shear strain is calculated by dividing the displacement of bottom cap by the height of the consolidated specimen.

It can be observed that although the overall response is the same in both simulation and experiment, their results are somewhat different. The simulation shows a stiffer and stronger response than the experiment and it has a larger amount of strain softening. As the material of the spheres and boundaries are known in this test, the material properties cannot be varied significantly and the possible level of parameter values variation did not resolve this difference between the simulation and experimental results. Looking into what is happening at the boundaries of the specimen in the simulation sheds light on the causes of such discrepancy between the experimental and simulation results.

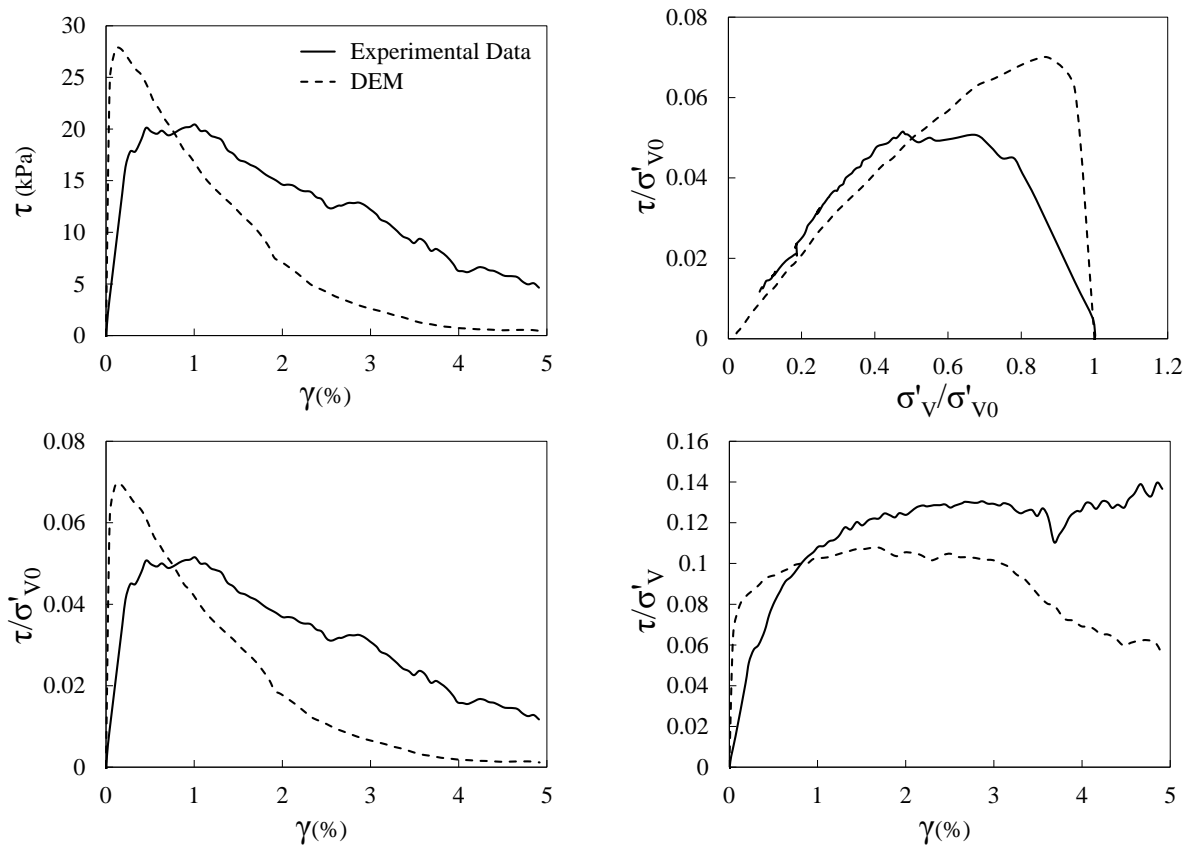


Figure 3.9 Comparison of the results from DEM simulation and the corresponding experimental data for constant volume monotonic simple shear test on steel spheres ($\sigma'_{v0}=400$ kPa, $D_r=45\%$)

The horizontal displacement profile of the stacked rings during shearing stage of the simulation is shown in Figure 3.10 at two shear strain levels of 0.5% (small strain at the beginning

of the shear) and 3.75% (larger strain as shearing continues). These values of the shear strain are calculated based on the bottom cap displacement. These profiles are compared to the theoretical continuous simple shear deformation at the lateral boundaries (solid line) in which the caps and rings displacement varies linearly from the corresponding displacement at the bottom cap to zero at the top cap (as shown in a small sketch in Figure 3.10). It should be mentioned that since at the end of consolidation (in both experimental and simulated specimen), the top cap is placed inside the most top ring, this ring remains stationary with the top cap during shear.

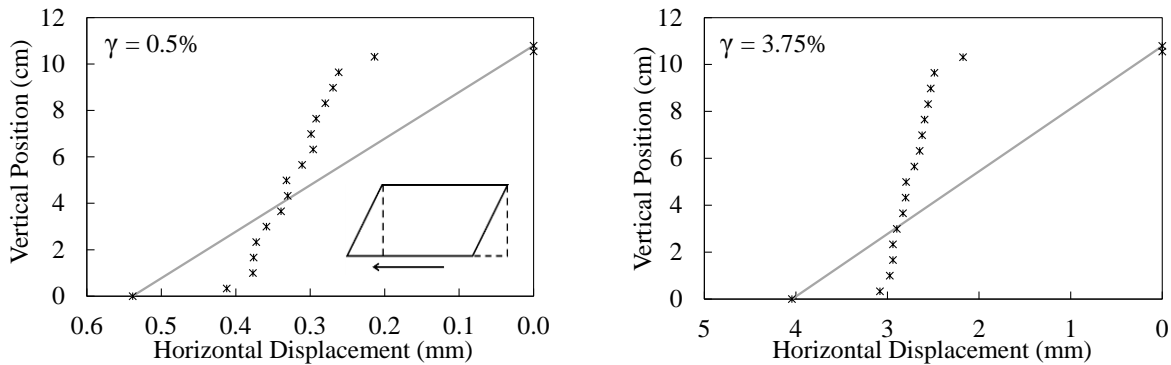


Figure 3.10 Horizontal displacement profile of stacked rings during monotonic shear in the DEM simulation of steel spheres for two levels of shear strain: 0.5 and 3.75% ($\sigma'_{v0}=400$ kPa, $D_r=45\%$)

Significant displacement gaps can be observed at the bottom and top caps in the simulation which can be as a result of sliding and/or rolling of particles at the boundaries. Although there is not any way to accurately measure the displacement of the rings individually for the device in the lab, some sliding could also be observed just visually at the caps, which at these deformation levels could not be visually noticed easily. Using the ring displacement profile shown in Figure 3.10, the actual simple shear strain of the specimen can be achieved by linear regression through the only ring displacement profiles (not including the caps and the most top ring stuck with the top cap). Figure 3.11 shows the comparison of shear stress-strain graphs by considering theoretical and actual shear strains.

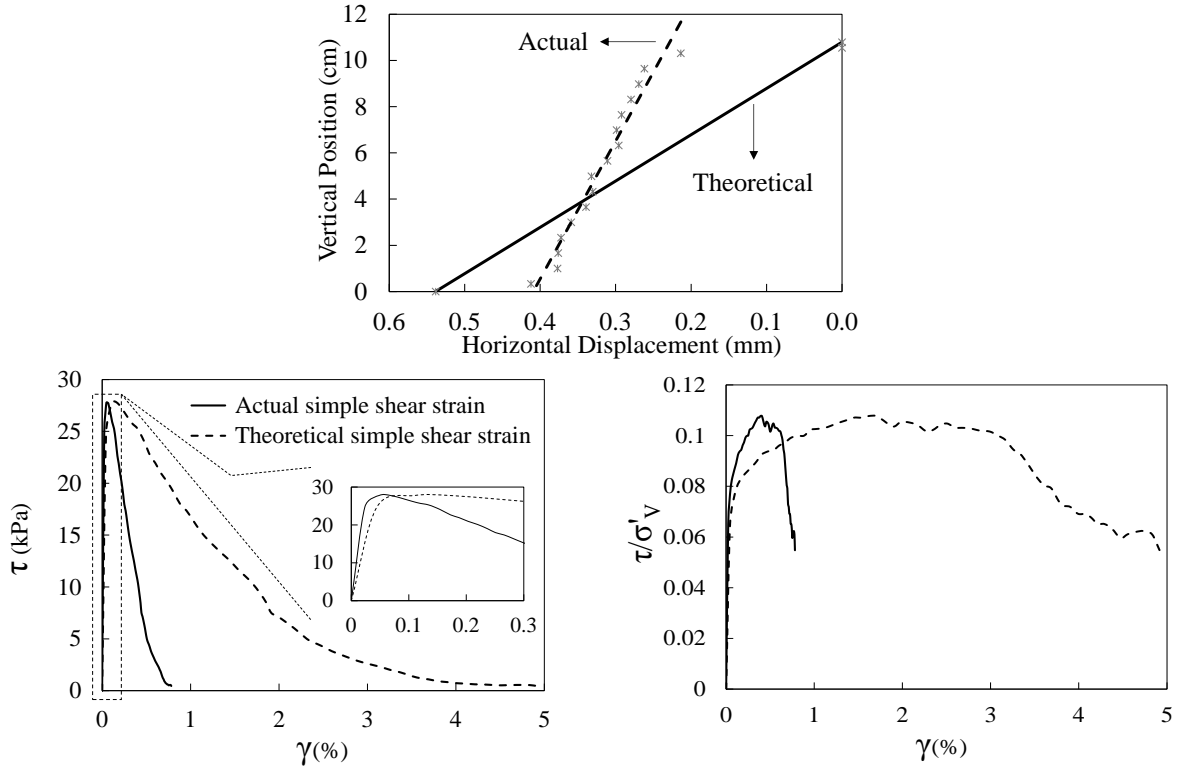


Figure 3.11 The DEM simulation results considering actual versus theoretical simple shear strain in specimen of steel spheres ($\sigma'_{v0}=400$ kPa, $D_r=45\%$)

The numerical observations claim that for the tested steel spheres, the simple shear deformation was not imposed at the boundaries, and most of the shearing happened at the interface of the steel spheres and caps and mostly the interface shear stresses were captured. To study this in more depth, two groups of numerical simulations are considered to help in gaining more insight of what is exactly happening at the boundaries during the test and in finding if the experiment can be improved to impose the theoretical simple shear deformation on the boundaries for tested steel spheres. These two groups are named A and B. All the parameters are the same in these two groups except the friction coefficient at contacts between steel spheres and caps. In group A (including the model already discussed), the friction coefficient between steel spheres and caps are 0.125 (corresponding to low friction angle of about 7°) while in group B, it is a high value of 1.0 (corresponding to high friction angle of 45°). It should be mentioned that the consolidated void

ratio of simulated specimens of both groups are very close despite the difference in the friction coefficient values at the contacts between caps and steel spheres. Further differences among the simulations in each group relate to how the shear stage is modelled. Table 3.2 summarizes these simulations with a brief description. More details will be provided in the following sections. It should be mentioned that only for presentation purposes, in all models regardless of whether the theoretical shear deformation exists or not, shear strain is calculated and shown on plots as the ratio of bottom cap displacement to the consolidated height. This does not cause any problem in comparisons between models since all the numerical specimens are generated at similar void ratios and consequently similar consolidated height.

Table 3.2 List of the simulations considered for the DEM analyses

Simulation Group	Name	Description
A (friction coefficient at cap boundaries = 0.125)	A-1	Bottom cap moves with a predefined velocity, and the movements of the ring follow the equation of motion in the direction of shear.
	A-2	Rings are all moving together like a rigid wall following equation of motion while bottom cap moves with a predefined velocity
	A-3	Adjacent rings to both caps are fixed to the caps, and the other rings movements follow the equation of motion in the direction of shear.
	A-4	The rotation of spheres in contact with top and bottom caps just before shearing is fixed so no rolling happens at caps during shear (sliding is allowed). The movements of all rings follow the equation of motion in the direction of shear.
	A-5	The movement (in the direction of shear) of spheres in contact with top and bottom caps just before shearing are fixed so no sliding happens at caps during shear (rolling is allowed). The movements of all rings follow the equation of motion in the direction of shear.
B (friction coefficient at cap boundaries = 1.0)	B-1	Same as in A-1.
	B-3	Same as in A-3.
	B-4	Same as in A-4.

Model A-1 is the simulation of what happens during the experiment in the lab. The bottom cap is moved with the predefined velocity while the top cap is fixed, and the rings move following equations of motions as a result of the deformation being transferred from the bottom cap through the sphere assembly. Shear stress is calculated as the total horizontal force in the direction of shear (x-direction) induced on bottom cap divided by the cross-sectional area of specimen. The result of this simulation has been shown in Figure 3.9 and Figure 3.10. To reexamine the claim that in the lab the shear deformation is not completely transfer into the specimen and the measured shear stress is mostly from the shearing at the interface of the spheres assembly and bottom cap, the results of model A-1 are compared with those of model A-2. In model A-2, all the rings (except the most top ring which is stuck to top cap as described) are fixed to move together as one single rigid cylindrical wall following the equations of motion while the bottom cap is moving. Like in model A-1, the shear stress is calculated based on the shear forces acting on bottom cap. The results of these two models in term of macro-scale shear response and ring displacement profile is shown in Figure 3.12 and Figure 3.13, respectively. As it can be observed, shear responses of both models are very close to each other which supports the claim that most of the shear in the lab happens at the interface with the bottom cap rather than inside the specimen. The existing minor discrepancies between the responses can be attributed to a difference in the level of lateral restraints in these models. Because of the discrete nature of the sphere assembly, the movement of the bottom cap can cause local displacements on the adjacent spheres in contact with that. The propagation of these displacements in model A-1 can cause global shear deformation in the specimen as can be seen in its rings' displacement while the global shear deformation is prevented in model A-2 because of constraints on the individually lateral displacement of the rings.

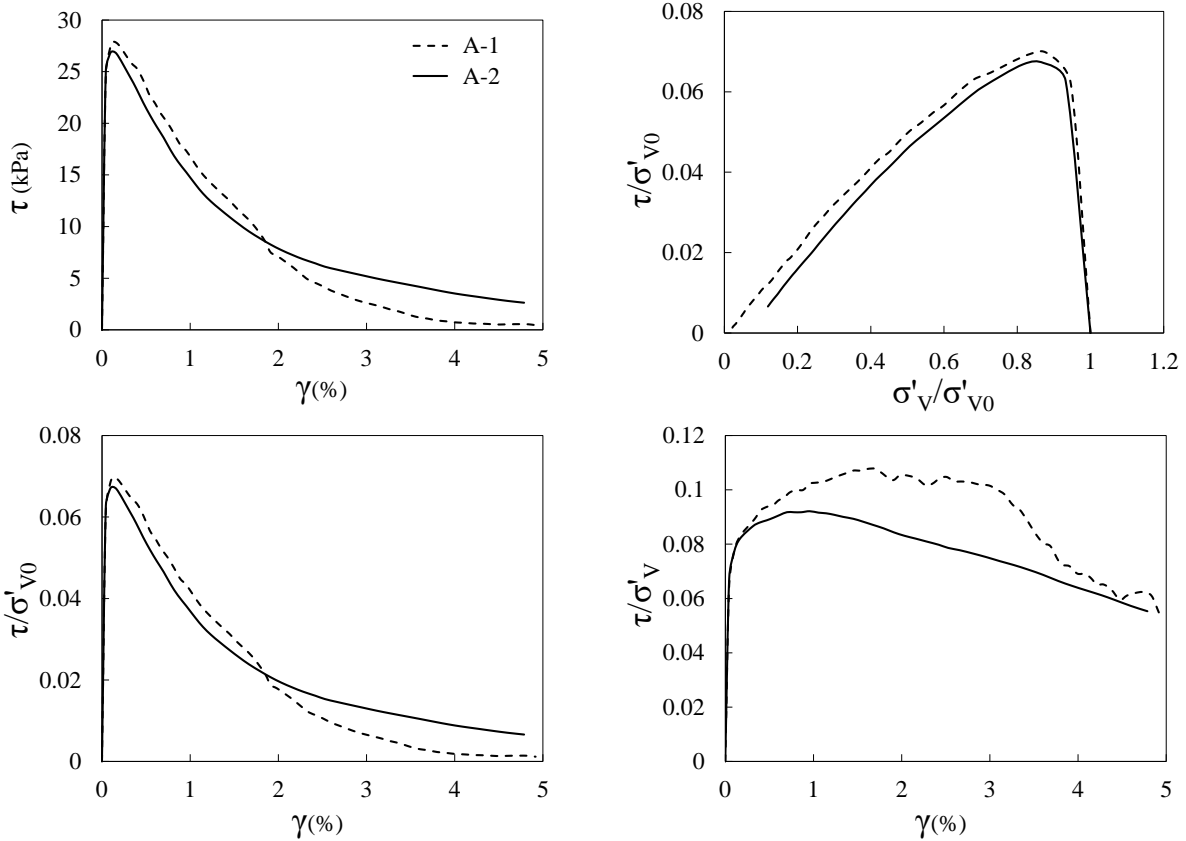


Figure 3.12 Comparison of the DEM simulation results from models A-1 and A-2 for specimen of steel spheres ($\sigma'_{v0}=400$ kPa, $D_r=45\%$)

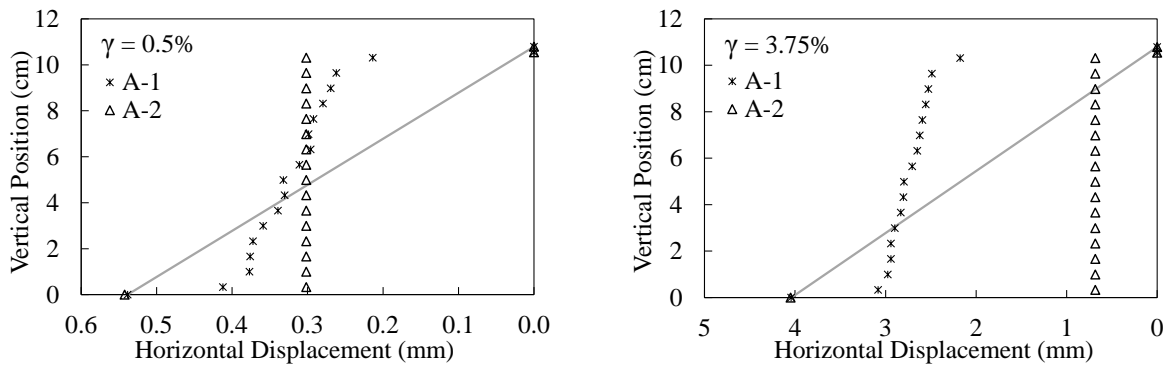


Figure 3.13 Horizontal displacement profile of stacked rings during monotonic shear of steel spheres in models A-1 and A-2 for two levels of shear strain: 0.5 and 3.75% ($\sigma'_{v0}=400$ kPa and $D_r=45\%$)

To check if the transfer of shear deformation into the sample can be improved by increasing the friction at the caps, the results of model A-1 and B-1 are compared. These two models are the same in all aspects other than the friction coefficient at contacts between spheres and the horizontal

caps. In all models of group B, this value is 1.0 which is corresponding to a high friction angle of 45° . Comparison of the rings displacement profiles shown in Figure 3.14, it can be observed that even a high friction coefficient of 1.0 at the caps is not sufficient to guarantee the complete transfer of deformation into the specimen. Increasing the bottom cap friction lowers the amount of displacement gap at the bottom cap but simultaneously increases the displacement gap at the top cap. The relative amount of changes in displacement gap at two caps are in a way that the ring profiles of model B-1 are more inclined than the ones in model A-1 for smaller level of shear strain; which implies that the shear deformation transferred into the specimen in model B-1 is more than model A-1. However, at higher shear strains in model B-1, the gap at the top cap increases with higher rate than that on bottom cap. This is reasonable because the contacts at the top cap decreases as the loose specimen contracts in shear, and although the friction coefficient is high, the normal stresses at these contacts are not high enough anymore to cause a high level of friction resistance. On the other hand, the high friction at the bottom cap causes higher grip at the interface which in combination with lower friction resistance at the top results in the specimen displaces further relative to the top cap.

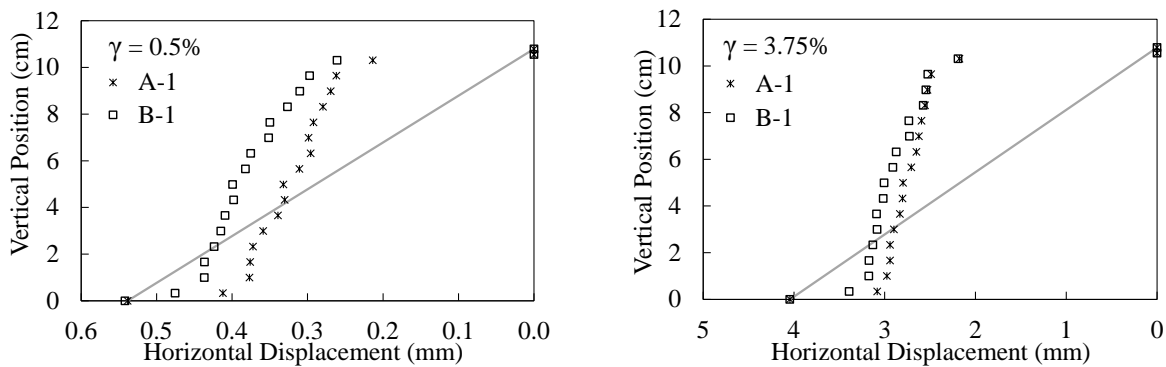


Figure 3.14 Horizontal displacement profile of stacked rings during monotonic shear in models A-1 and B-1 for two levels of shear strain: 0.5 and 3.75% (specimens of steel spheres with $\sigma'_{v0}=400$ kPa and $D_r=45\%$)

Observing the results of models A-1 and B-1 in which there are noticeable displacement gaps at top and bottom boundaries, in models A-3 and B-3, the adjacent ring to each cap is fixed to them during simulation. In other words, the bottom cap and the next bottom rings moved together with the same velocity while the top cap (and the very top ring stuck to it in experiment) and the top ring next to it are stationary. The rest of the rings move following the equation of motion. It can be observed in Figure 3.15 *Figure 3.15* that fixing the movement of the end rings to their adjacent caps results in improvement of shear deformation transfer into the specimen. However, in both cases, this transfer is still partial, and the desired simple shear deformation is not imposed on the specimen. Figure 3.16 illustrates the comparison of shear stress-strain graphs in model A-3 by considering theoretical and actual shear strain values. Again, the actual shear strain values for the specimen is achieved by linear regression of the ring profile considering only free moving rings. The theoretical shear strain is calculated based on the displacement of bottom cap assuming that the shear deformation is completely transferred into the specimen and a continuous simple shear deformation is imposed on the boundaries. It confirms the previous observation that by fixing the caps to their adjacent rings the transfer of shear deformation into the specimen is improved. Since the bottom ring is externally moving with the bottom cap, the shear stress in this model is calculated by adding the total horizontal forces (in the direction of shearing) exerted on the bottom cap and the adjacent ring divided by the specimen cross-sectional area. As more shear deformation is transferred into the specimen, the simulation of shear responses better resembles the typical undrained shear behavior of loose to medium dense cohesionless granular materials (e.g., Vaid and Chern, 1985; Yamsiri and Soga, 2010); the shear stress increases up to a peak value followed by a strain-softening until it reaches phase transformation and after that strain hardening occurs in the specimen response.

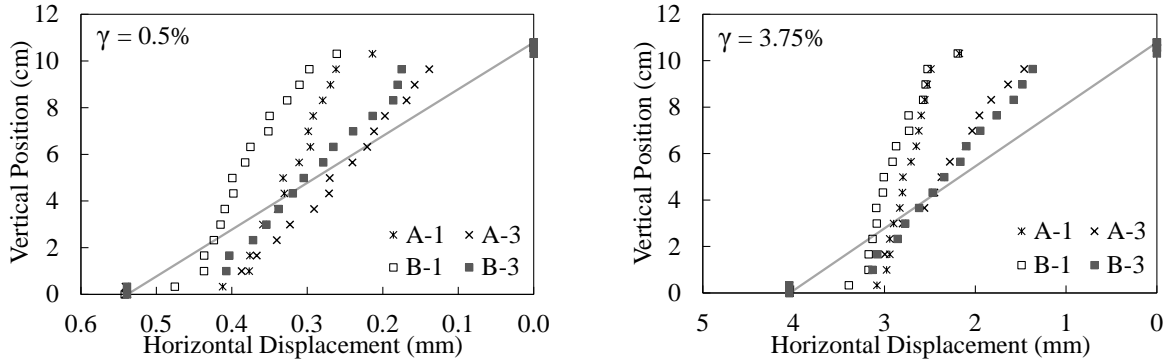


Figure 3.15 Horizontal displacement profiles of stacked rings during monotonic shear in models A-3 and B-3 compared to those in models A-1 and B-1, respectively, for two levels of shear strain: 0.5 and 3.75% (specimens of steel sphere with $\sigma'_{v0}=400$ kPa and $D_r=45\%$)

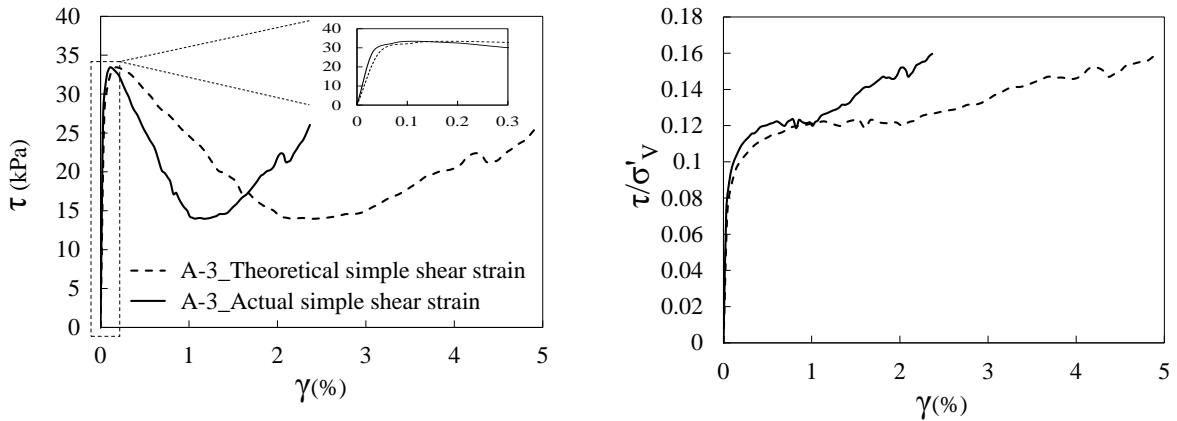


Figure 3.16 The DEM simulation results from model A-3 considering actual versus theoretical simple shear strain in specimen of steel spheres ($\sigma'_{v0}=400$ kPa, $D_r=45\%$)

Due to the fact that the steel spheres can freely rotate and they do not have any resistance against rolling, further simulations are run with the aim of finding a way to improve the complete transfer of shear deformation from the bottom cap into the specimen. In models A-4, B-4, and A-5, all the rings move following the law of motion while some constraints are applied on the spheres in contact with the caps. In models A-4 and B-4, the spheres that are in contact with the caps at the end of the consolidation stage are identified and their rotation and spin (angular velocity) are set to zero and therefore the rolling of spheres is prevented at the caps during shear. In model A-5, sliding of spheres at the caps is prevented (instead of rolling in model A-4) by fixing the displacement of the spheres in contact with the caps at the end of the consolidation to their

contacting caps. It should be mentioned that only the component of displacement in direction of shear is set to follow this constraint. In this model, the shear stress is calculated as the total horizontal force in direction of shear on the bottom cap and the constrained spheres divided by the cross sectional area of the specimen. Figure 3.17 illustrates the rings displacement profile for models A-4, B-4, and A-5 and their comparison with models A-1 and B-1 in which there are no constraints applied on the spheres in contact with the caps. Preventing the boundary spheres at caps in model A-4 from rotating reduces the shear deformation transfer into the specimen. It reveals that fixing the rolling of the boundary spheres cannot guarantee the transfer of shear deformation into the specimen when there is not enough large friction available at caps. In model B-4, with a high friction coefficient of 1.0 (corresponding to friction angle of 45°) at caps, the resultant ring profile resembles a continuous simple shear deformation. It can also be observed that preventing sliding at the caps by constraining the displacement of spheres to their contacting caps (model A-5) can guarantee the complete transfer of shear deformation into the specimen, even if no constraints applied to their free rotation.

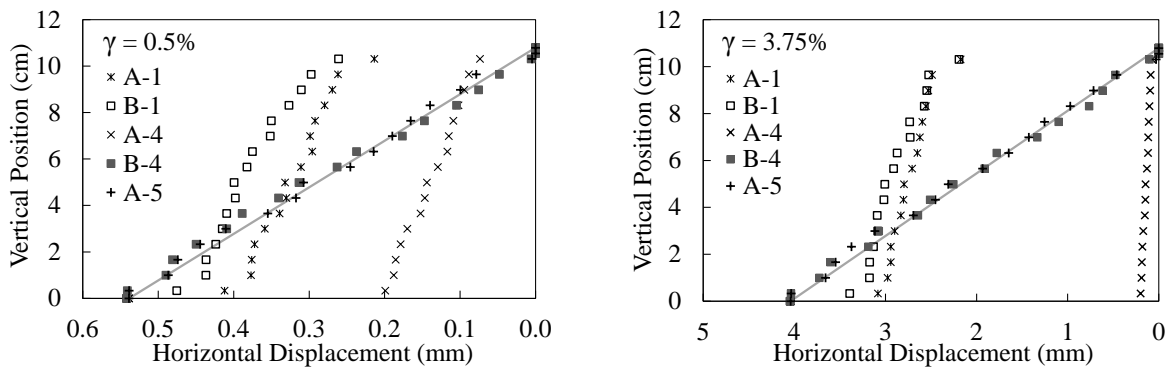


Figure 3.17 Effect of preventing rolling (models A-4, B-4) or sliding (model A-5) at caps on the horizontal displacement profile of stacked rings during monotonic shear for two levels of shear strain: 0.5 and 3.75%

As can be seen in Figure 3.17, preventing the boundary spheres at caps in model A-4 from rotating and rolling reduces the shear deformation transfer into the specimen, and especially

increase the amount of displacement gap at the bottom cap. Looking into the ring profile for model A-4 as the displacement of bottom cap increases (Figure 3.18) implies that the shearing at the interface of bottom cap and the sphere assembly reaches a steady state condition at very early stages of shear. It can be observed in Figure 3.18 that while the bottom cap continues displacing, the rings profile and position stays unchanged after the equivalent simple shear strain of 0.5%. The macroscale shear response of the specimen measured at top and bottom caps shown in Figure 3.19 agrees with observations of rings profiles.

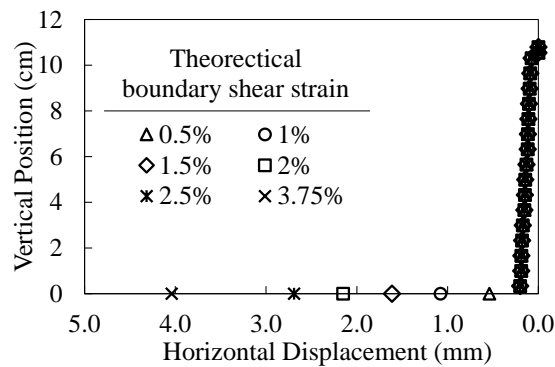


Figure 3.18 Horizontal displacement profile of stacked rings during monotonic shear in model A-4 at different theoretical strain levels (specimen of steel spheres with $\sigma'_{v0}=400$ kPa and $D_r=45\%$)

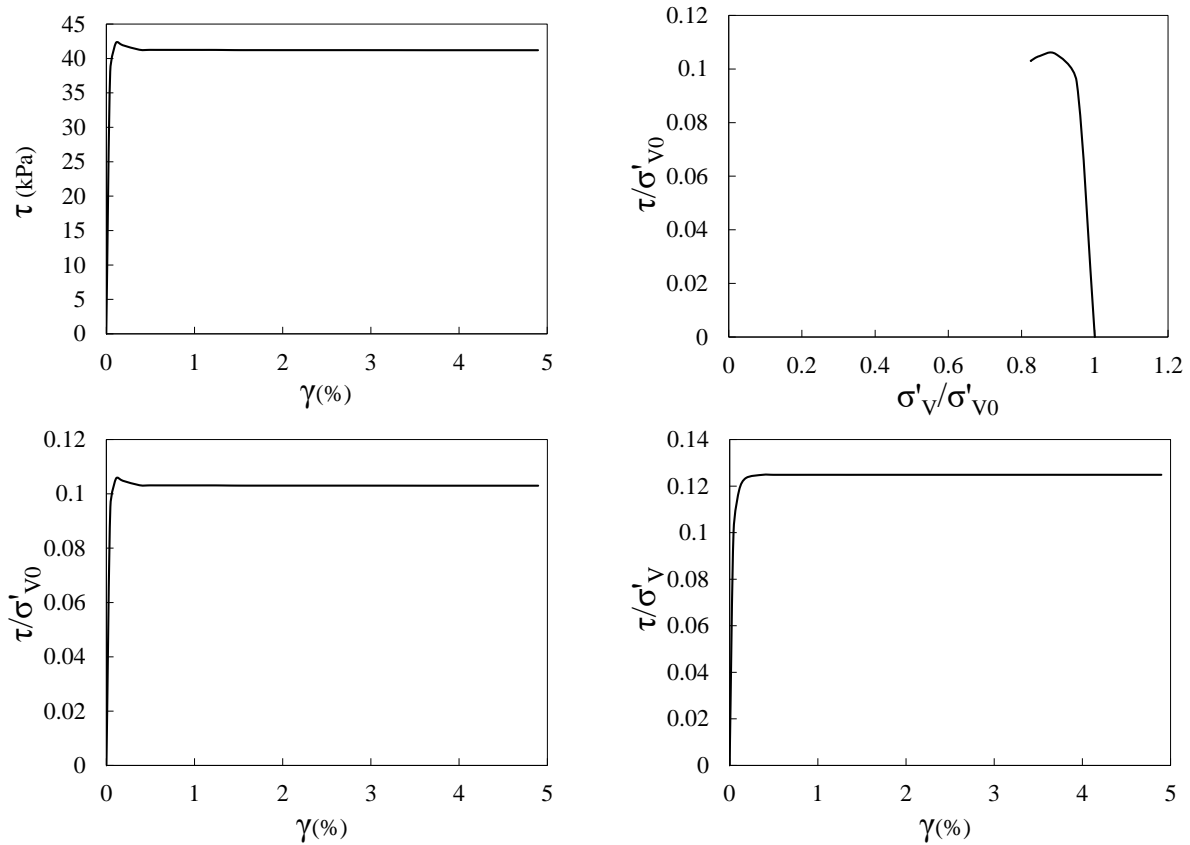


Figure 3.19 The DEM simulation results from model A-4 considering theoretical simple shear strain (specimen of steel spheres with $\sigma'_{v0}=400$ kPa and $D_r=45\%$)

In models B-4 and A-5, the ring displacement profiles are similar to the theoretical simple shear deformation, which implies the complete transfer of deformation from the bottom cap into the specimen. Consequently, it can be observed in Figure 3.20 that the macroscopic shear response of these specimen follow the pattern of the undrained shear response of cohesionless granular materials.

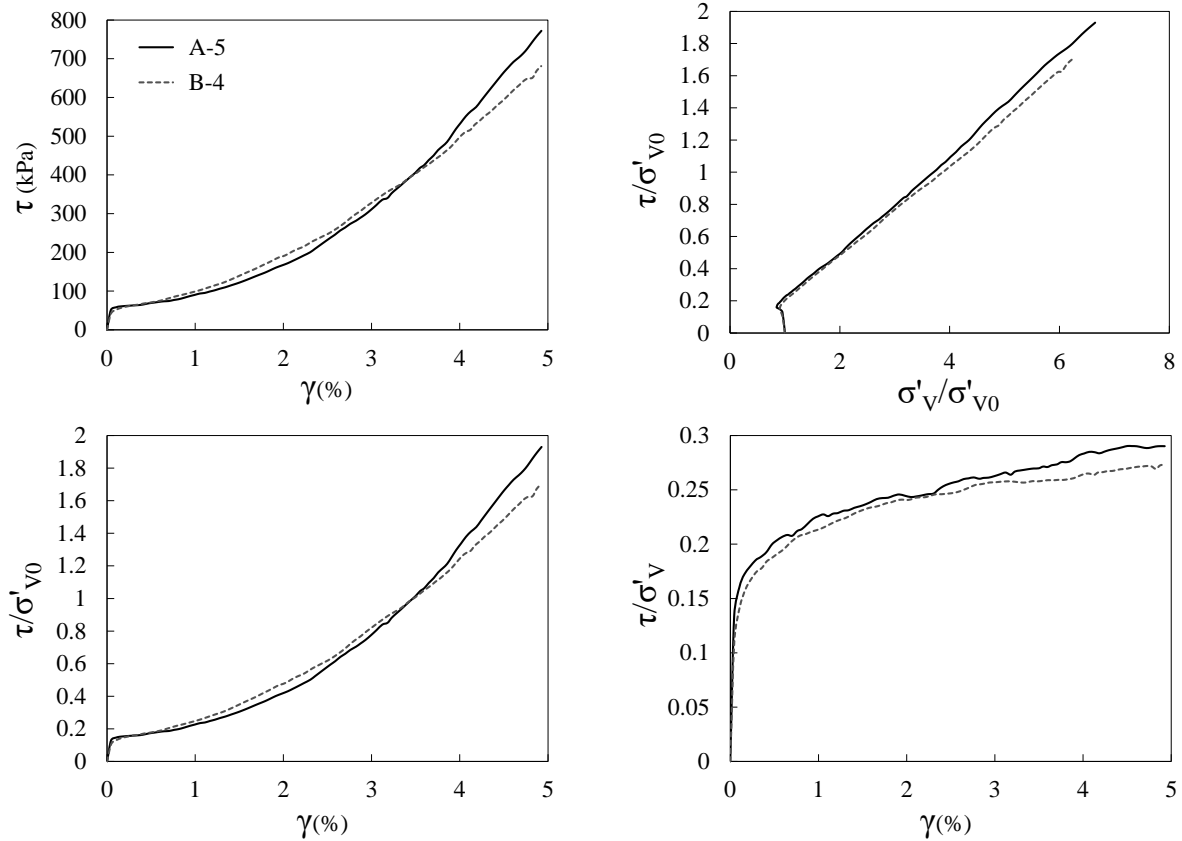


Figure 3.20 The DEM simulation results from models B-4 and A-5 (specimen of steel spheres with $\sigma'_{v0}=400$ kPa and $D_r=45\%$)

Comparing the results of models A-1, A-4, and A-5 with the ones from B-1 and B-4, it can be concluded that in case of testing spherical-shaped granular materials with low particle frictions such as chrome steel spheres, rolling and sliding at the horizontal boundaries in stacked ring simple shear device can prevent adequate transfer of shear deformation to induce true simple shear deformation in the specimen. Depending on the level of local sliding potential (at each particle-cap contact), constraining the free rotation of the boundary spheres may worsen or improve this transfer. In other words, preventing the rolling alone at horizontal boundaries is not necessarily sufficient for complete transfer of shear deformation. In case of low friction coefficient at the contacts between spheres and horizontal boundaries, preventing the boundary spheres from rotation intensifies the deviation of specimen deformation from true simple shear. On the other

hand, preventing the rotation and rolling of boundary spheres in combination with high friction coefficient at sphere-caps contacts, which results in lower local sliding potential, assures the simple shear deformation in the specimen.

Overall, to ensure that the simple shear deformation is sufficiently imposed on the specimen of steel spheres and the shear and vertical stresses measured at the horizontal boundaries in the experiment are indicators of simple shear response of the specimen, the boundary particles should be attached (glued) to the caps. However, because of the large size of simple shear device at the University of Michigan and especially the top cap being a built-in part of it, it is not viable to glue the spherical particles to the caps without causing permanent changes to parts of the device. As a result, there are limitations in testing such low friction and freely rotating particulate materials.

From a geotechnical engineering point of view, the main interest is using this device for capturing the simple shear behavior of granular soils which are much more frictional and consist of particles with irregular shapes that cause some resistance against rotation and rolling. In this regard, some simulations are done to preliminarily examine the testing of gravels in simple shear device. Two simulations named C-4 and D-4 are done (the naming is based on the similarity to models A-4 and B-4 in terms of applied constraints on the spheres in contact with horizontal boundaries). These preliminary models are the same as models group A and B in terms of specimen and particle shape, size, number, and material properties except the inter-particle and particle-caps friction coefficient values. In these two models, the inter-particle friction coefficient is equal to 0.5 which is a value used as friction coefficient for sand particles in literature (e.g., Wang and Mok, 2008, Garcia and Bray, 2019). It should be mentioned that the specimens in these models have the same void ratio at the end of consolidation as the ones in group A and B. To achieve that, the inter-

particle friction coefficient is set to smaller value of 0.096 until the end of consolidation and then set to 0.5 during shear stage. The value of friction coefficient at contacts between particles and caps are 0.25 and 0.5 in models C-4 and D-4, respectively. The rotation of the boundary spheres at caps are also prevented during shear in these models to simulate the non-sphericity of the particles only at the cap boundaries. The rings profiles in these models are illustrated in Figure 3.21. It can be observed that for assembly of higher friction granular materials with non-spherical particles like gravels, the sufficient friction at the boundaries assures the complete transfer of shear to impose simple shear deformation in the specimen. In case of relatively low cap friction coefficient (compare to inter-particle one), it can be seen in results of model C-4 in Figure 3.21 and Figure 3.22 that the shear is mainly occurs at the interface of the particles and the caps and the response reaches steady state condition very quickly and the behavior does not show any strain hardening. For higher cap frictions, the simple shear deformation is satisfactorily imposed on the specimen, and the behavior is similar to the undrained shear response of cohesionless granular materials.

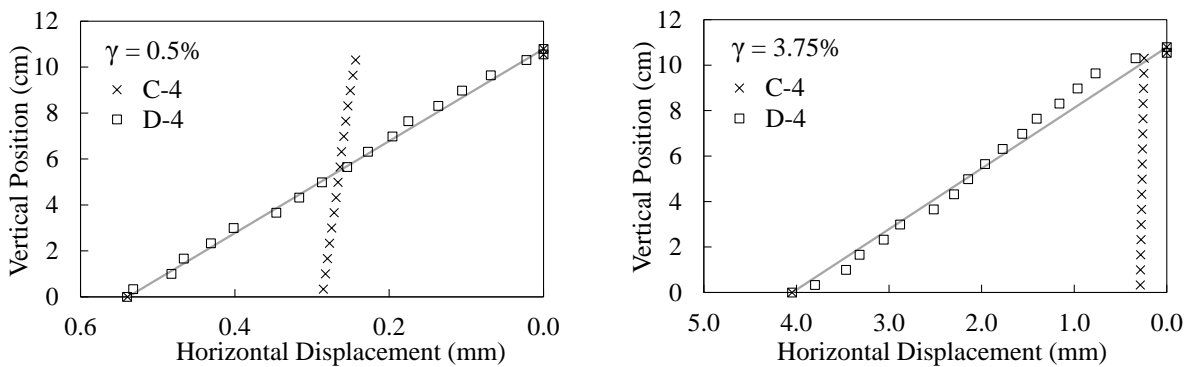


Figure 3.21 Horizontal displacement profile of stacked rings during monotonic shear in models C-4 and D-4 for two levels of shear strain: 0.5 and 3.75% ($\sigma'_{v0}=400$ kPa)

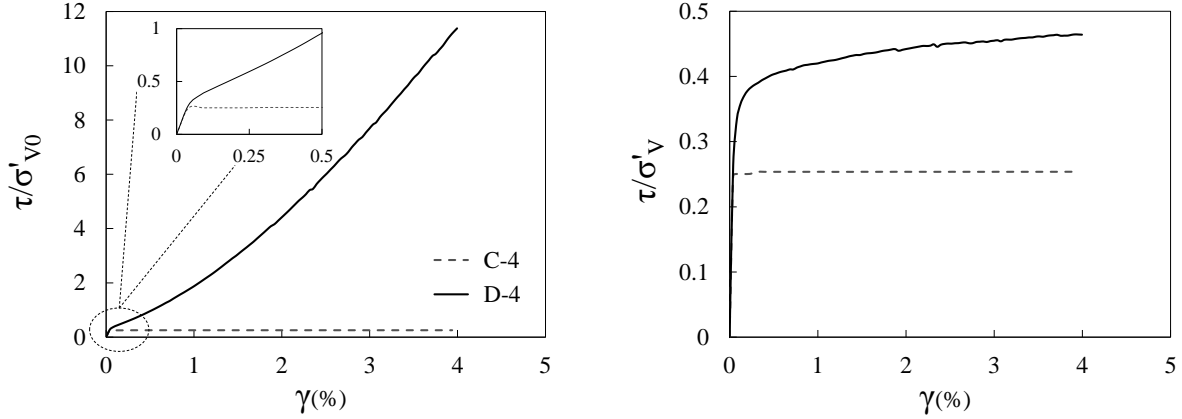


Figure 3.22 The DEM simulation results from models C-4 and D-4 ($\sigma'_{v0}=400$ kPa)

Incorporating different particle sizes are also considered in DEM simulations. Model A-5-Bidisperse simulates the monotonic simple shear test on a steel sphere assembly with two different particle sizes. One size is equal to the sphere sizes in model A-5, and the other size is half of it. To make the two models comparable, the value of D_{50} and total volume of the spherical particles are considered the same in these two models. Accordingly, the number of spherical particles of each size can be calculated. Assuming D as the diameter of spheres in model A-5 ($D=3/8$ in.), to have $D_{50}=D$ in model A-5-Bidisperse, the total volume of the spheres with the size of $D/2$ should be equal to the half of the total volume of all particles:

$$n_{D/2} \times \frac{4}{3} \pi \left(\frac{D}{4}\right)^3 = \frac{1}{2} \left(n_{D/2} \times \frac{4}{3} \pi \left(\frac{D}{4}\right)^3 + n_D \times \frac{4}{3} \pi \left(\frac{D}{2}\right)^3 \right) \quad (\text{Eq. 3.5})$$

In this equation, n_D and $n_{D/2}$ are the number of particles with the sizes of D and $D/2$, respectively. For the same total particle volumes in models A-5 and A-5-Bidisperse:

$$\frac{n_D}{2} \times \frac{4}{3} \pi \left(\frac{D}{4}\right)^3 + n_D \times \frac{4}{3} \pi \left(\frac{D}{2}\right)^3 = 10636 \times \frac{4}{3} \pi \left(\frac{D}{2}\right)^3 \quad (\text{Eq. 3.6})$$

Solving equations 3.5 and 3.6 simultaneously, the numbers of spheres with sizes D and $D/2$ in model A-5-Bidisperse are 5318 and 42544, respectively, and the total number of spheres are 47862. Figure 3.23 shows the generated numerical specimen of spheres of two sizes.

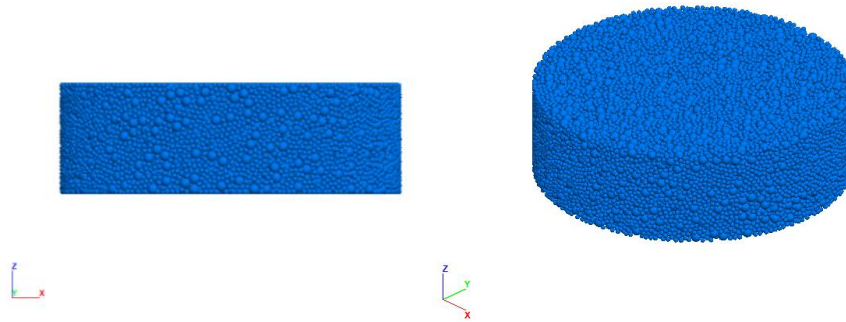


Figure 3.23 DEM specimen of 47,862 spheres of two different sizes (model A-5-Bidisperse)

Although everything except the size and number of particles are the same in models A-5 and A-5-Bidisperse, the model with larger numbers of smaller particles are more compressible and model A-5-Bidisperse has the void ratio of 0.574 at the end of consolidation comparing to the void ratio of 0.665 in model A-5. It should be noted that the density state of these two models cannot be directly compared as the mono-disperse and bi-disperse spheres packing do not have the same index void ratios. Figure 3.24 illustrates the response of the simulated specimen during shear. The typical constant volume simple shear response of granular materials can be observed which shows that the DEM model can qualitatively capture the behavior of the assemblies with more than one particle size.

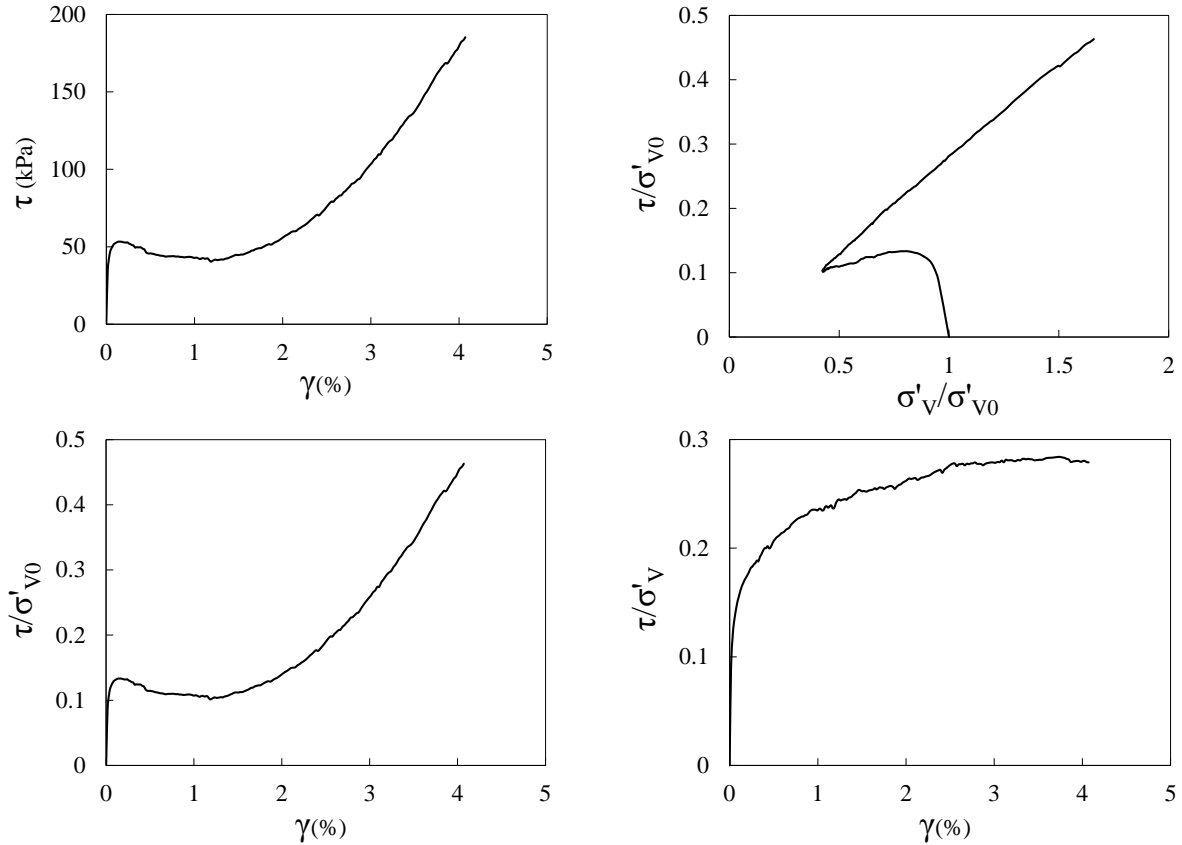


Figure 3.24 Simulated monotonic simple shear response of the specimen with two sizes of spherical particles (model A-5-Bidisperse, $\sigma'_{v0}=400$ kPa, $e=0.574$)

The capability of the DEM model to capture the cyclic simple shear response is also qualitatively investigated by running simulations of cyclic simple shear of bi-disperse steel spheres. The specimen prepared with the same features as the one for monotonic simulation (model A-5-Bidisperse) in terms of number and size of spheres, and material properties. The specimen is consolidated under the vertical stress of 400 kPa to achieve a specimen with void ratio of 0.665. Then it undergoes a stress-controlled cyclic shear of $CSR=0.09$ by displacing the bottom cap horizontally following the servo control algorithm in PFC and reversing the direction of movement whenever the shear stress ratio reaches the specified CSR value. Figure 3.25 shows the simulated cyclic shear response. It can be seen that the DEM model is capable of capturing the important characteristic of cyclic simple shear behavior of granular material, such as hysteretic shear stress-

strain behavior, degradation of shear modulus and accumulation of excess pore pressure and shear strain.

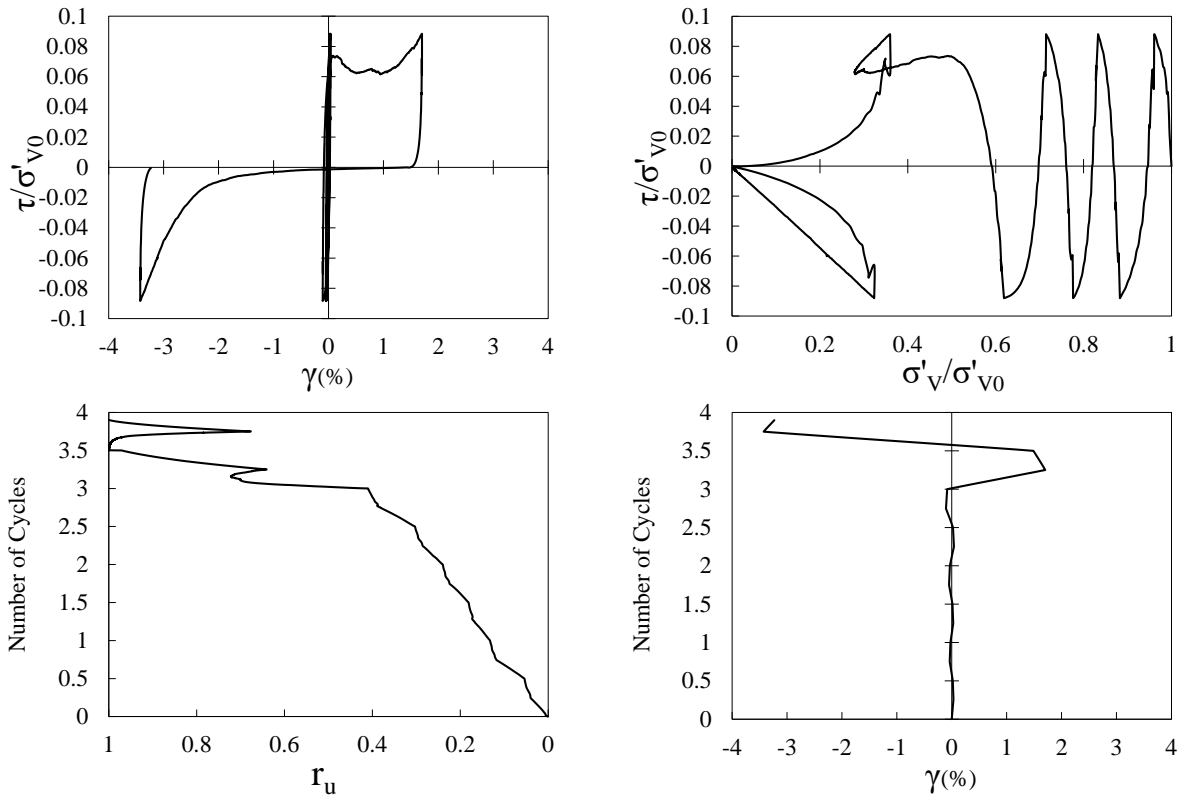


Figure 3.25 Simulated stress-controlled cyclic simple shear response for specimen of bi-disperse spheres ($\sigma'_{v0}=400$ kPa, $e=0.574$, $CSR=0.09$)

3.4 Conclusions

This chapter presented results from DEM simulations that considered a realistic algorithm for modeling the movement of stacked rings. It was shown that free rotation and low friction of steel spheres can prevent the complete transfer of shear deformation from the externally moving boundary into the specimen. Therefore, the simple shear deformation may not be imposed on the specimen as desired, and the experimental data of shear displacements and forces cannot be confidently used to reliably evaluate the simple shear behavior of the steel sphere assembly. Numerically examining a number of modifications for testing steel spheres in stacked-ring simple shear device, it is concluded that the steel spheres in contact with planar boundaries should be

attached to them (e.g. by using glue) in order to avoid any slippage and rolling at these boundaries and obtaining reliable data from the experiments. Overall, in case of granular material with particles of low rolling resistance (e.g. rounded particles) and/or low friction, caution should be taken for stacked-ring simple shear testing under constant volume to ensure the proper transfer of shear deformation from the moving boundary and the decent imposition of simple shear deformation on the specimen.

Finally, it was shown that the developed DEM model is capable of qualitatively capturing the monotonic and cyclic simple shear response under constant volume condition.

Chapter 4

DEM Modeling of the Monotonic Simple Shear Response of Pea Gravel

4.1 Introduction

In this chapter, the monotonic constant volume simple shear response of Pea gravel in stacked ring simple shear test is simulated using the discrete element method and different aspects of behavior at the micro- and macro-scale are studied. To improve the computational efficiency of the simulations, the soil particles are simulated as spherical bodies in the model. However, to incorporate the irregularity and non-sphericity of the real particle shapes, rolling resistance is artificially added at the contacts to prevent the free rotation of spherical particles in the simulation and to mimic the resistance against rolling and rotation in actual soil particles. In previous studies in which spherical particles (or disks in 2D) represented the real soil particles, researchers either completely prohibited the particles rotations during shear stage (e.g. Dobry and Ng, 1992) or added similar rolling resistance parameter at all contacts (Iwashita and Oda, 1998; Wang and Li, 2014; Gutierrez and Muftah, 2015; Roessler et al., 2019). Such approaches disregard the variety of particle shapes in a soil assembly and by assuming a similar rolling resistance parameter through all the specimen imply similar shape of the same level of rolling resistance for all the particles in an actual specimen. However, the non-uniformity of particle shape (and consequently, level of resistance against rotation) is acknowledged in this study and is accounted for by considering a non-uniform distribution of rolling resistance in the simulations. This information, in addition to the number and size of the particles, is obtained directly from the shape characteristics of the Pea gravel particles in the actual soil specimen using a robust image-based method.

Overall, a more realistic and representative model of a Pea gravel specimen in terms of number, size, and rolling resistance of particles is developed and used to better understand the behavior of this material at micro- and macro-scale in monotonic constant volume simple shear condition.

4.2 Soil Particles Size and Shape Characterization

An image-based system developed by Ohm and Hryciw (2013) is used in this research to rapidly determine the number of particles, particle size distribution and particle shape and morphology of the Pea gravel specimens that were already tested by Basham (2019, personal communication) using the large scale simple shear device and are modelled using DEM in this research. This method is appropriate to use for coarse sands and gravels. This system utilizes a back-lit tilting translucent segregation table (TST) (Ohm and Hryciw, 2013) that allows the segregation of particles with wide range of sizes prior to photographing the specimen from above. This is possible by using the segregation bridges with different underpass clearances. For samples with wide range of particle sizes, this is a very crucial testing feature as without segregation by size, the smaller particles may get hidden behind larger particles in the image; however, it is not very necessary for uniformed-size particles. This feature can also provide an approximation of the thickness of particles. Figure 4.1 shows the translucent segregation table system. Another positive feature of this method is that there is no need to detach the particles from each other, and the experiment can proceed successfully only if the particles rest on the translucent plate in a single layer. After the photo is taken by the camera, the soil particles in the image are digitally separated using an image-processing method called watershed (Beucher and Lantuejoul, 1979; Vincent and Soille, 1991) segmentation and each particle is individually accounted for in the analysis. After

digital segmentation of particles, each particle is fitted to an equivalent ellipse of the same area and then the largest dimension (d_1), intermediate dimension (d_2), aspect ratio (elongation), sphericity and convexity of every particles can be found. For achieving these information for every particles in this study, parts of the image-processing Matlab code developed and described by Zheng and Hryciw (2015) is used.

Since the Pea gravel specimen used in this research weighs approximately 14 kg, the entire sample cannot be placed on the device and be photographed at once. Therefore, it is divided in 10 parts of 1-2 kg each, to be photographed in 10 separate TST tests. As the tested soil sample consists of relatively uniform size particles, segregation bridges are not used in this study. Figure 4.2 shows an example of one of the captured images. Having the shape and morphology of each particle determined using TST, the distribution of them can be known. The grain size, sphericity, aspect ratio and convexity distribution curves for the tested Pea gravel sample is represented in Figure 4.3. These distributions are shown in terms of cumulative number of particles, which is different from the classical representation of particle size distribution in terms of cumulative mass of the particles. However, by assuming the smallest dimension of particle (d_3) to be a fraction (≤ 1) of the intermediate size, these distribution curves can also be drawn in terms of cumulative volume of particles. Grain size is defined as the particle intermediate dimension (d_2), aspect ratio is the ratio of largest dimension (d_1) to intermediate dimension (d_2). Sphericity is defined as area sphericity which was first proposed by Tickell (1931) as ratio of the projected area of the particle to the area of the minimum circumscribing circle. At the two extremes, $S_A=1$ for a circular projected area of a particle and $S_A=0$ in case that projection of a particle is a line. Finally, convexity is computed as defined by Altuhafi et al. (2012) as ratio of the projected area of the particle to the area of the smallest circumscribing convex polygon.

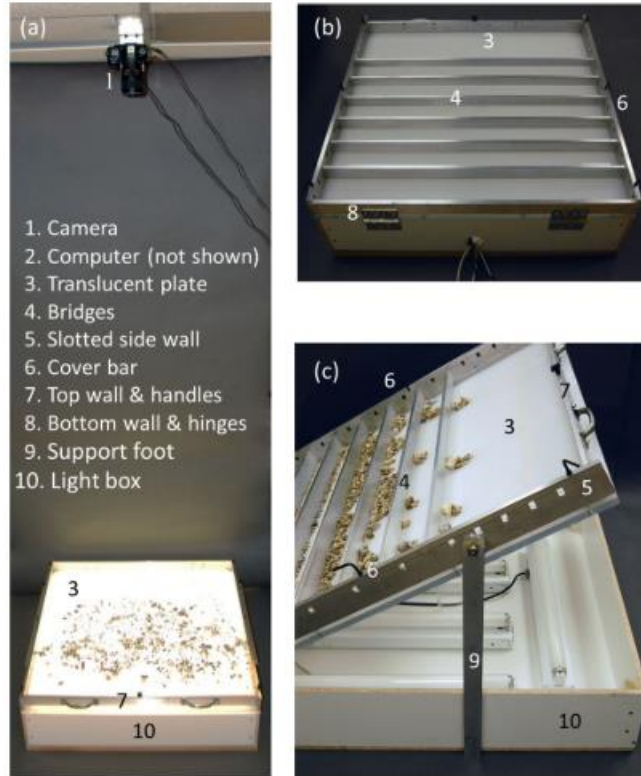


Figure 4.1 Translucent Segregation Table (TST) system (Ohm and Hryciw, 2013)

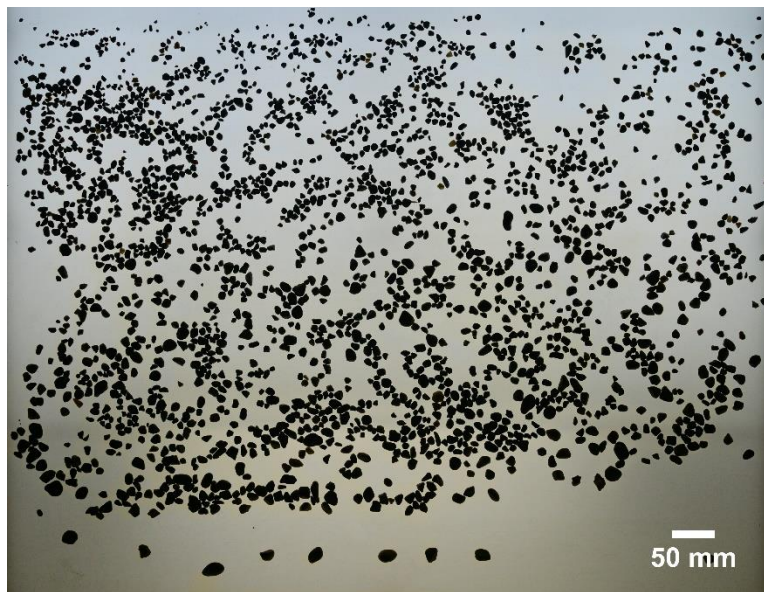


Figure 4.2 One of ten images taken using the TST of the Pea gravel particles used in the tested specimen
 (There are 2,550 particles in this image)

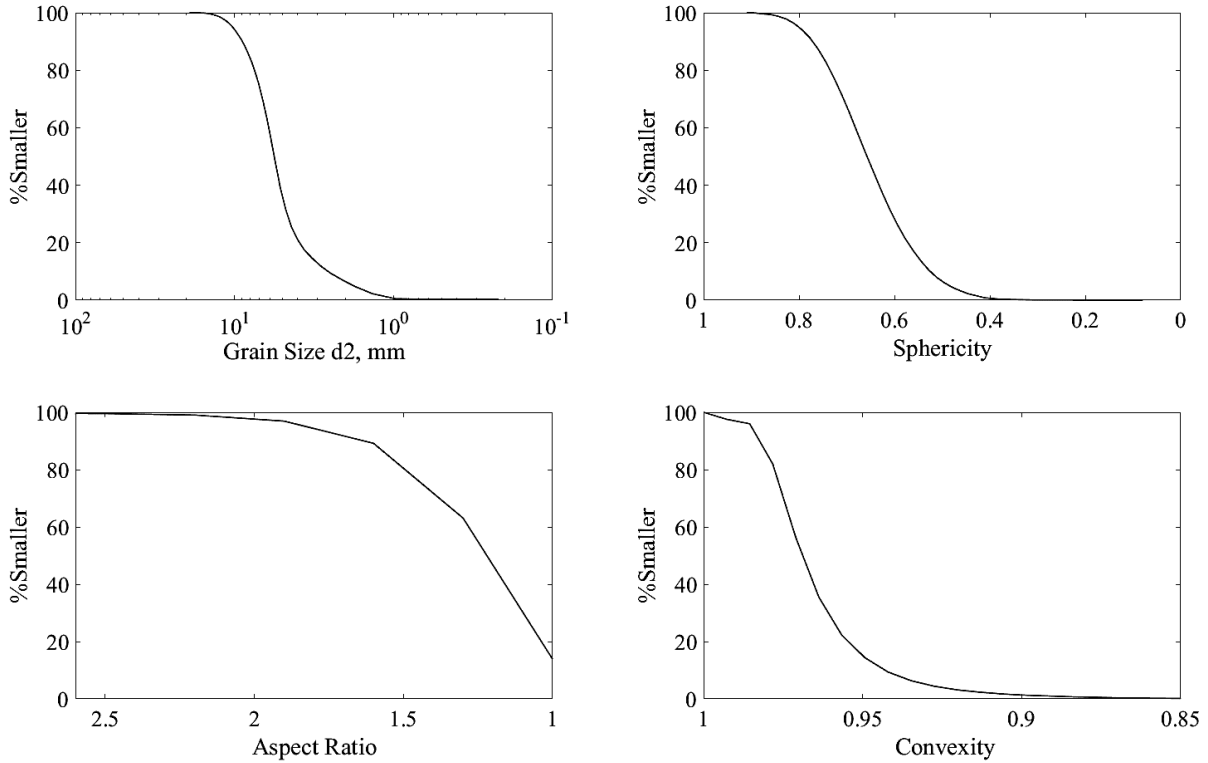


Figure 4.3 TST data on Distributions (in terms of cumulative number of particles) of size, sphericity, aspect ratio and convexity of tested Pea gravels

It should be noted that size in the TST results is defined as the intermediate dimension (d_2) of the fitted ellipse to the image of the particle with the same area; while, for the spheres in DEM, the size is defined as the diameter. Therefore, it is crucial to find the equivalent size distribution for spheres based on the TST results. The following procedure was followed to find the equivalent size distribution curve for the poly-disperse spherical particles to be generated in DEM simulations:

To obtain the same total volume for the same number of particles in both the simulations and the real soil specimen, the size of spheres is calculated by equating the sphere volume and the real particle volume. To find the volume of particles from the TST images, the smallest dimension of the particles is assumed to be a fraction of the intermediate ones. Since the tested soil was of relatively uniform size particles, it is reasonable to assume the same ratio of smallest dimension to

intermediate dimension for all the particles. Therefore, the total volume of the soil particles based on TST results can be approximated as:

$$V_{s,TST} = \sum_{i=1}^n V_{p,TST} = \sum_{i=1}^n \frac{4}{3} \pi d_{1i} d_{2i} d_{3i} = \frac{4}{3} \pi \beta \sum_{i=1}^n AR_i d_{2i}^3 \quad (\text{Eq. 4.1})$$

in which, $V_{s,TST}$ is the total volume of the soil particles from TST images, $V_{p,TST}$ is the volume of each particle from TST images (by assuming particles as ellipsoids), n is the total number of particles, d_{1i} , d_{2i} , d_{3i} and AR_i are the largest, intermediate, smallest dimensions and aspect ratio of each particle (d_{1i}/d_{2i}), respectively, and β is the ratio of smallest to intermediate dimension of particle (d_{3i}/d_{2i}).

On the other hand, the actual total volume of soil particles can be calculated by the total dry weight and the specific gravity of the sample as:

$$V_{s,actual} = \frac{W_s}{G_s \gamma_w} \quad (\text{Eq. 4.2})$$

where, $V_{s,actual}$, W_s and G_s are the actual total volume, total weight and specific gravity of soil particles and γ_w is unit weight of water. By equating $V_{s,TST}$ (Eq. 4.1) and $V_{s,actual}$ (Eq. 4.2), the value of β is found. Then, the diameter of each equivalent spheres (D_{si}) is calculated as:

$$D_{si} = 2d_{2i} \sqrt[3]{\beta AR_i} \quad (\text{Eq. 4.3})$$

Eventually, the equivalent size distribution of specimen of spheres can be obtained and be used in simulation.

To incorporate the irregular shape of the particles and to account for particles non-sphericity that causes resistance against free rotation, rolling resistance is considered for equivalent spheres in the DEM simulations. The rolling resistance coefficient (μ_r) associated to each sphere is assumed to be a function of the corresponding particle sphericity as:

$$\mu_{ri} = 0.3 \times (1 - S_{Ai}) \quad (\text{Eq. 4.4})$$

in which S_{Ai} is the sphericity of each particle. The multiplier of 0.3 (<1) is assumed in this equation to prevent overestimating the rotation resistance of particles because: (1) in DEM simulations, the value of rolling resistance coefficient considered separately at each contact to obtain the total resisting moment on the sphere. Therefore, in the case of the rounded to sub-rounded particles such as the tested Pea gravel (Hubler et al., 2017), it would be reasonable to use such smaller multiplier when estimating the rolling resistance coefficient based only on the overall sphericity of the particles. (2) In reality, the real shape of the particles can cause rotation as well as resisting it (Wensrich and Katterfeld, 2012). However, the rolling resistance considered for spheres in DEM simulations always opposes the rolling motion.

Finally, knowing the total number, size (diameter) and rolling resistance coefficient for each equivalent sphere, the joint probability of size and rolling resistance coefficient for the equivalent spherical particles assembly is achieved and is shown as two-dimensional histograms of Figure 4.4. These distributions are shown in terms of number of particles. This statistical information is used in numerically generating an assembly of particles relatively similar to the actual physical one.

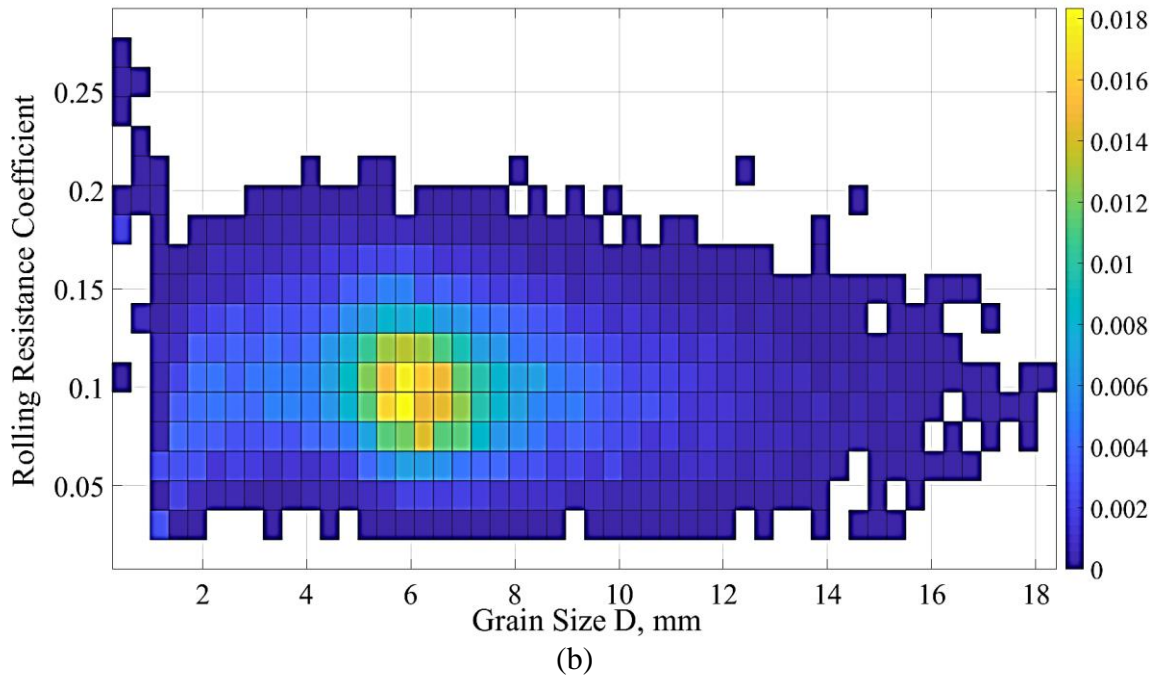
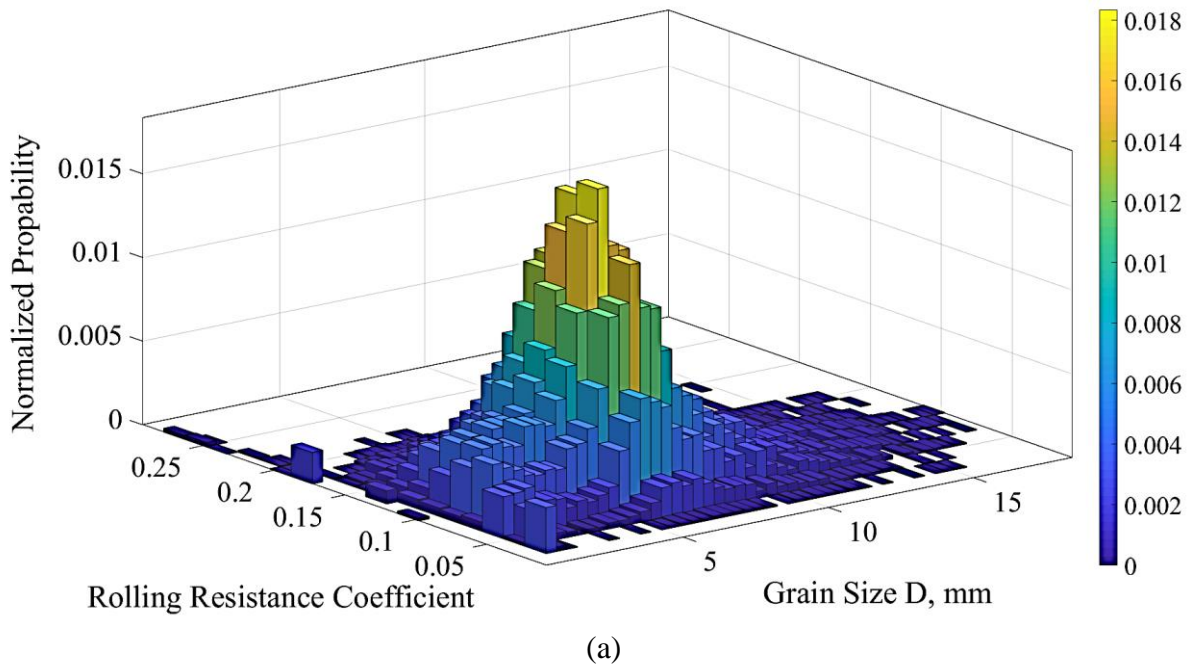


Figure 4.4 Joint probability of size and rolling resistance coefficient in the assembly of equivalent spheres for the actual Pea gravel particles; (a) 3D view, (b) 2D view

4.3 Development of the DEM Model for Constant Volume Monotonic Simple Shear Test of Pea Gravel

The monotonic constant volume simple shear response of pea gravel in stacked ring simple shear device is modelled using DEM by simulating the soil particles as equivalent spheres with added rolling resistance to account for the non-sphericity of actual soil particles. The soil specimen tested in the laboratory for the calibration of the DEM model is numerically replicated with the same overall size. Following the observations made in Chapter 3, to ensure adequate shear transfer from the moving horizontal plate into the specimen and to minimize overall slippage at the interface between the specimen and the horizontal plates during shear, thicker rings are used at the most top and bottom (which were fixed to the adjacent horizontal plates). Therefore, the specimen is laterally confined within a stack of 15 rings (13 thin rings with thickness of 6.65 mm and 2 thick rings at the most ends). The end rings are three times thicker than the thin ones; however, only about 5/6 of their thickness are in contact with the soil during shear and the rest is out of the specimen and helps in fixing them to the adjacent horizontal plates.

To numerically replicate the experimental specimen, the bottom and top caps are modeled as planar wall elements, and the confining rings are modelled as stacked cylindrical wall elements of the same number, diameter and thickness as those in the laboratory. This cylindrical space is then filled with the spherical particles, the size and number of which were obtained from TST (Figure 4.4). It should be mentioned that spheres smaller than 3.7 mm in diameter are not considered in the modelling. Such small spheres constitute less than 1% of the total solid volume of the assembly; therefore, they can be not considered in generating the specimen without affecting the overall behavior. This also helps in decreasing the simulation time as presence of smaller

particles results in smaller timestep. The resultant size distribution curve of the spheres in the simulated specimen is shown in Figure 4.5 based on both the volume and number of particles.

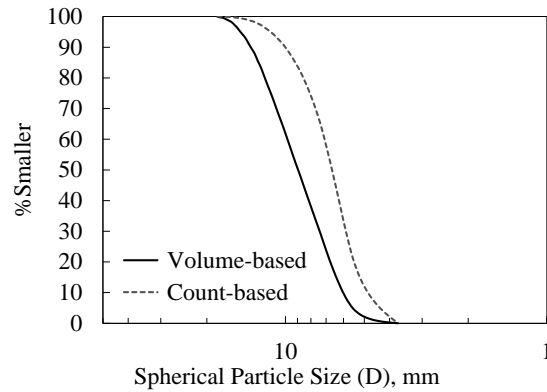


Figure 4.5 Spherical particle size distribution curve of simulated specimen

Radius expansion is used for initial preparation of the specimen. In this study, the friction value between all the elements and the rolling resistance coefficient for spheres are set as zero during the radius expansion. After this step, the distribution of rolling resistance coefficient is assigned to spheres based on the statistical results from TST (Figure 4.4) and the friction coefficient is set to the desired value. Figure 4.6 shows the resultant rolling resistance distribution of the spheres in the specimen. Gravity is activated inside the model at this point and it cycles to equilibrate. Figure 4.7 shows an actual specimen in the lab and the corresponding numerical one at the end of preparation stage.

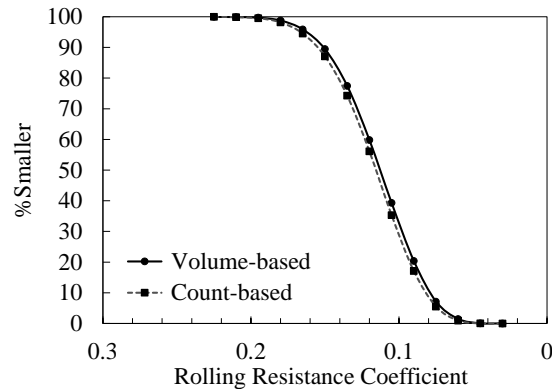


Figure 4.6 Rolling resistance coefficient distribution curve of simulated specimen

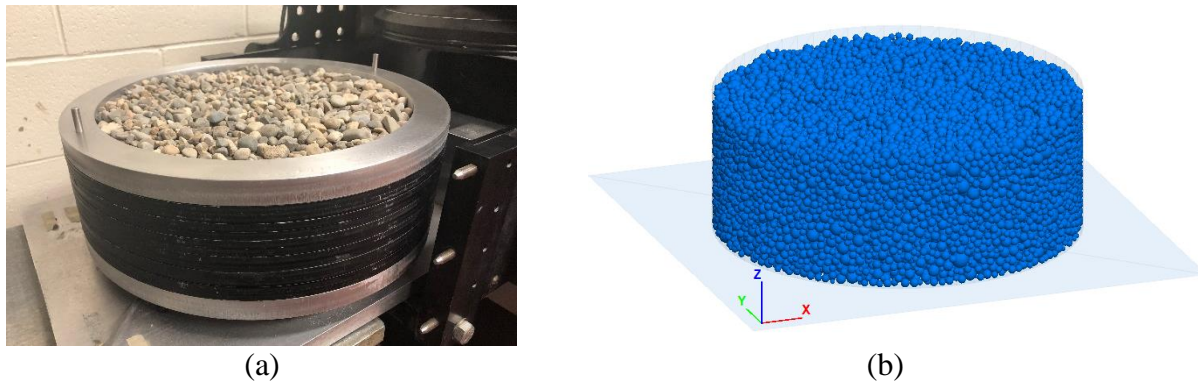


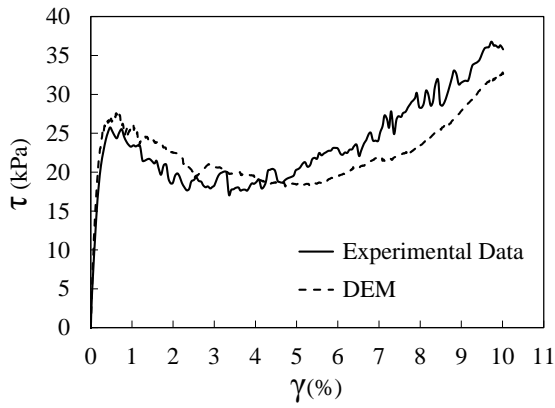
Figure 4.7 (a) Physical and (b) Numerical specimen (21,978 spheres)

After the initial assembly, the specimen is consolidated to a target vertical stress in steps by moving the top cap horizontally utilizing the servo control algorithm in PFC. In this study, the simulated specimens are consolidated under vertical stresses of 100, 250, and 400 kPa at two level of void ratio of 0.675 ± 0.002 and 0.6 ± 0.002 . These values are the same as the void ratio of the real Pea gravel specimens at the relative densities of $49 \pm 1\%$ and $87 \pm 1\%$, respectively, having the index void ratios of $e_{\min} = 0.574$ and $e_{\max} = 0.772$ (Hubler et al., 2017). In this dissertation, the relative density and vertical stress mentioned for the numerical specimens are the values for the corresponding physical laboratory Pea gravel specimen. To achieve the numerical specimen with the desired void ratio, we need to adjust the rolling resistance coefficient and/or friction values during the preparation and/or consolidation stages, which may be different from the values used during shear (e.g, Thornton, 2000; Gong, 2008; Huang et al., 2014; Salazar et al., 2015; Bernhardt et al., 2016; Wang and Wei, 2016; Zhang and Evans, 2018). At different point during the simulation of the initial assembly and consolidation stages, local damping coefficient of maximum 0.1 was assigned to spheres to remove additional kinetic energy and to expedite reaching to equilibrium.

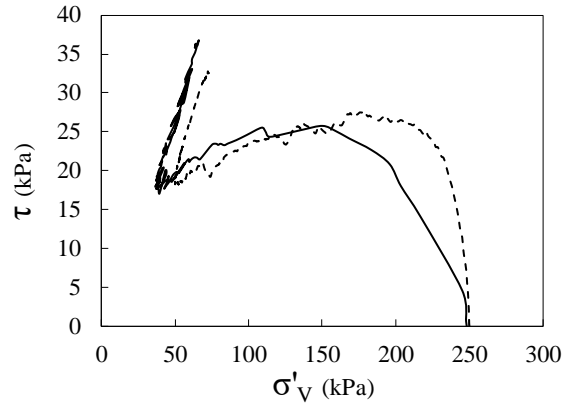
To simulate the constant volume condition during shear, movement of the top and bottom plates is prevented in the vertical direction. For modelling the strain-controlled shearing, the bottom cap and the adjacent ring are displaced horizontally with a low constant velocity of 4.8×10^{-3} m/s while the top cap and the adjacent rings are kept stationary. The movements of the rest of stacked rings in the simulation are set to follow the equation of motion in the direction of shearing. The horizontal displacement of the bottom cap and the adjacent ring is about 4.3×10^{-6} mm during each computational cycle with an average time step value of about 9×10^{-7} second/computational cycle. The average unbalanced force ratio during the shearing stage for this shear rate remains mostly smaller than 1×10^{-3} . Moreover, the value of the shear stress at the top and bottom of the specimen are within 2.5% of each other during most of the shear stage (Garcia and Bray, 2018). Therefore, the applied shear rate assures the quasi-static condition during shearing of the simulated specimen.

The rolling resistance linear contact model provided in PFC is used in the simulations. The contact model parameters are selected based on the calibration of the DEM model to capture the experimental monotonic constant volume simple shear response of pea gravel specimen consolidated under vertical stress of 250 kPa at relative density of 49%. The normal spring stiffness is 7.5×10^6 for spheres and 1.0×10^5 N/m for the boundary walls. The ratio of normal to shear spring stiffness (k_n/k_s) is considered as 1. The coefficient of friction (μ) at the ring boundaries is set to zero analogous to low friction lateral boundaries in the laboratory. The coefficient of friction for the horizontal walls is considered the same as that for the spheres. It is 0.365 (equivalent to friction angle of 20°) during most of the shear. However, some variations are applied to this value during shear to account for physical factors such as the non-uniformity of surface roughness of real particles, and the initial transition from at rest consolidated condition into sheared phase.

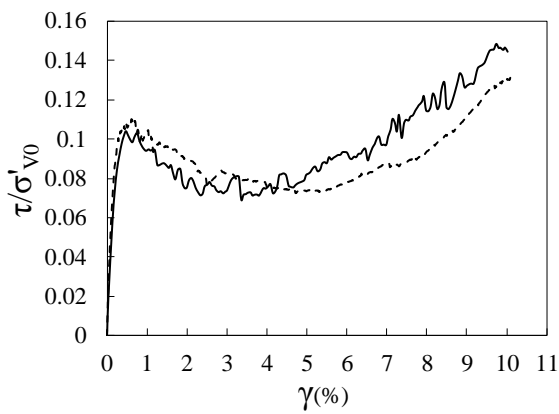
The coefficient of friction starts from higher value of 0.5 at the initiation of shear. This value gradually decreases to 0.365 in about 0.5% of shear strain. After that for the medium level of shear strain (up to about shear strain of 2.5%) this value is set to 0.325 (equivalent to friction angle of 18°), and then it is set back to 0.365 for higher shear strains. It should be mentioned that all these changes were applied gradually enough to not perturb the stability of the specimen. Considering this set of parameters, the simulation provided good agreement with experimentally observed constant volume simple shear response of Pea gravel as shown in Figure 4.8. The stresses and strains are defined the same as for experimental results interpretation. The shear stress (τ) was defined as the horizontal force in direction of shear applied on the bottom cap and the adjacent ring divided by the area of the bottom cap which is equal to the cross-sectional area of the specimen. The vertical stress (σ'_v) was calculated as the normal stress applied on the top cap divided by the cross-sectional area of the specimen. Generated pore pressure is defined as the difference between the vertical stress applied on the top cap at each time instance and the initial consolidated vertical stress. The pore pressure ratio (r_u) was defined as the ratio of the generated pore pressure to the consolidated vertical stress. Shear strain (γ) is defined as the ratio of the displacement of bottom cap to the height of the specimen. The close comparison between the experimental and simulation results in Figure 4.8 indicates the capability of the model with the considered set of contact parameters to predict the behavior of the real specimen.



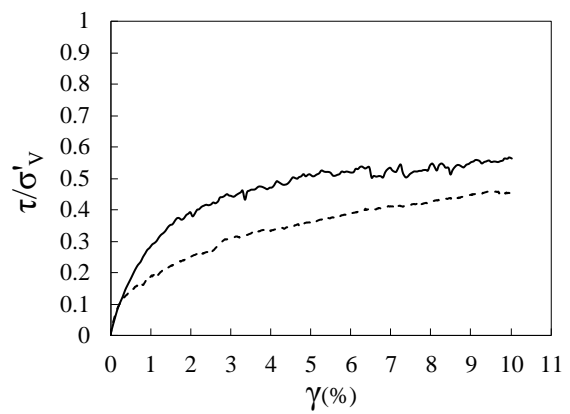
(a)



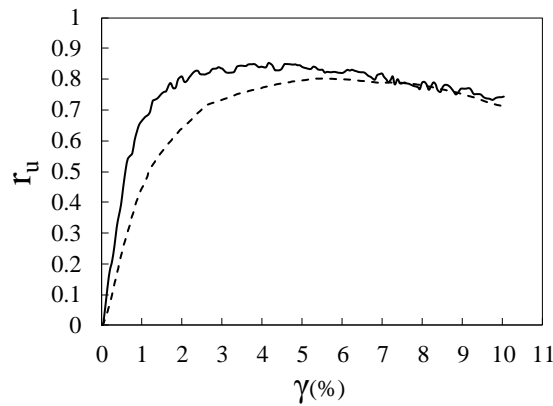
(b)



(c)



(d)



(e)

Figure 4.8 Comparison of the results from DEM simulation of constant volume monotonic simple shear test to the corresponding experimental results for Pea gravel specimen ($\sigma'_{v0}=250$ kPa, $D_r=49\%$): (a) Shear stress vs. shear strain; (b) Stress path; (c) Shear stress normalized by consolidated vertical stress vs. shear strain; (d) Shear stress normalized by vertical stress vs. shear strain; and (e) Pore pressure ratio vs. shear strain

4.4 Macroscopic Behavior Measured at Boundaries

Results from DEM simulations of constant volume monotonic simple shear test measured at boundaries are presented in Figure 4.9 and Figure 4.10 for specimens of relative densities of 49% and 87%, respectively. Figure 4.9(a) and Figure 4.10(a) illustrate the shear stress-shear strain relationship for $\sigma'_{v0}=100, 250, \text{ and } 400$ kPa. As expected, the peak shear strength (τ_p) increases by increasing the vertical stress. For the looser specimen ($D_r=49\%$), noticeable post-peak strain softening is observed for $\sigma'_{v0}=100$ and 250 kPa which is larger for the smaller vertical stress. Strain hardening happened in all cases of vertical stress and relative density. Figure 4.9(b) and Figure 4.10(b) show the stress path for each consolidated vertical stress. The peak shear stress, phase transformation (PT), and ultimate state (US) lines are shown on these figures. Figure 4.9(c) and Figure 4.10(c) show the evolution of shear stress normalized by consolidated vertical stress during shear. For both relative densities, the increase rate of τ/σ'_{v0} during strain hardening decreased as consolidated vertical stress increased. Figure 4.9(d) and Figure 4.10(d) show changes of shear stress normalized by vertical stress during shear. As shear strain increased, this ratio reached a constant value for all the consolidated vertical stresses. Figure 4.9(e) and Figure 4.10(e) show pore pressure ratio generated during shear. Generation of positive and negative pore pressure was observed in specimen of $D_r=49\%$ and $D_r=87\%$, respectively. Overall, more densely packed specimens showed stronger response and have a higher tendency for dilative behavior. The observed behaviors are in agreement with the typical undrained response of cohesionless granular soils at different levels of relative density. The effect of consolidated vertical stress on the response is also consistent with that observed by Hubler (2017) in constant volume monotonic simple shear testing of Pea gravel specimens in laboratory.

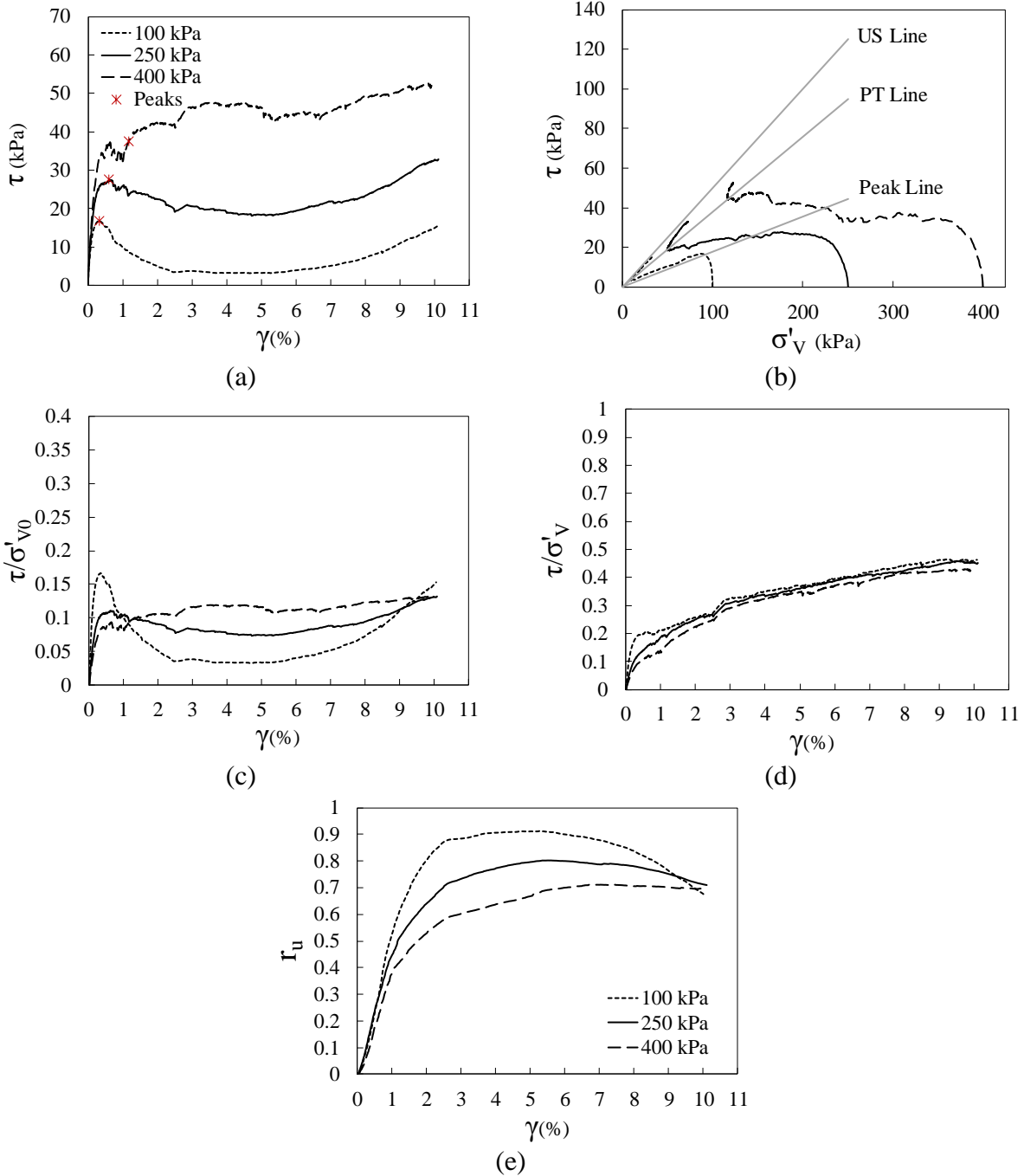


Figure 4.9 Results from DEM simulation of constant volume monotonic simple shear response of Pea gravel specimen ($D_r=49\%$): (a) Shear stress vs. shear strain; (b) Stress path; (c) Shear stress normalized by consolidated vertical stress vs. shear strain; (d) Shear stress normalized by vertical stress vs. shear strain; and (e) Pore pressure ratio vs. shear strain

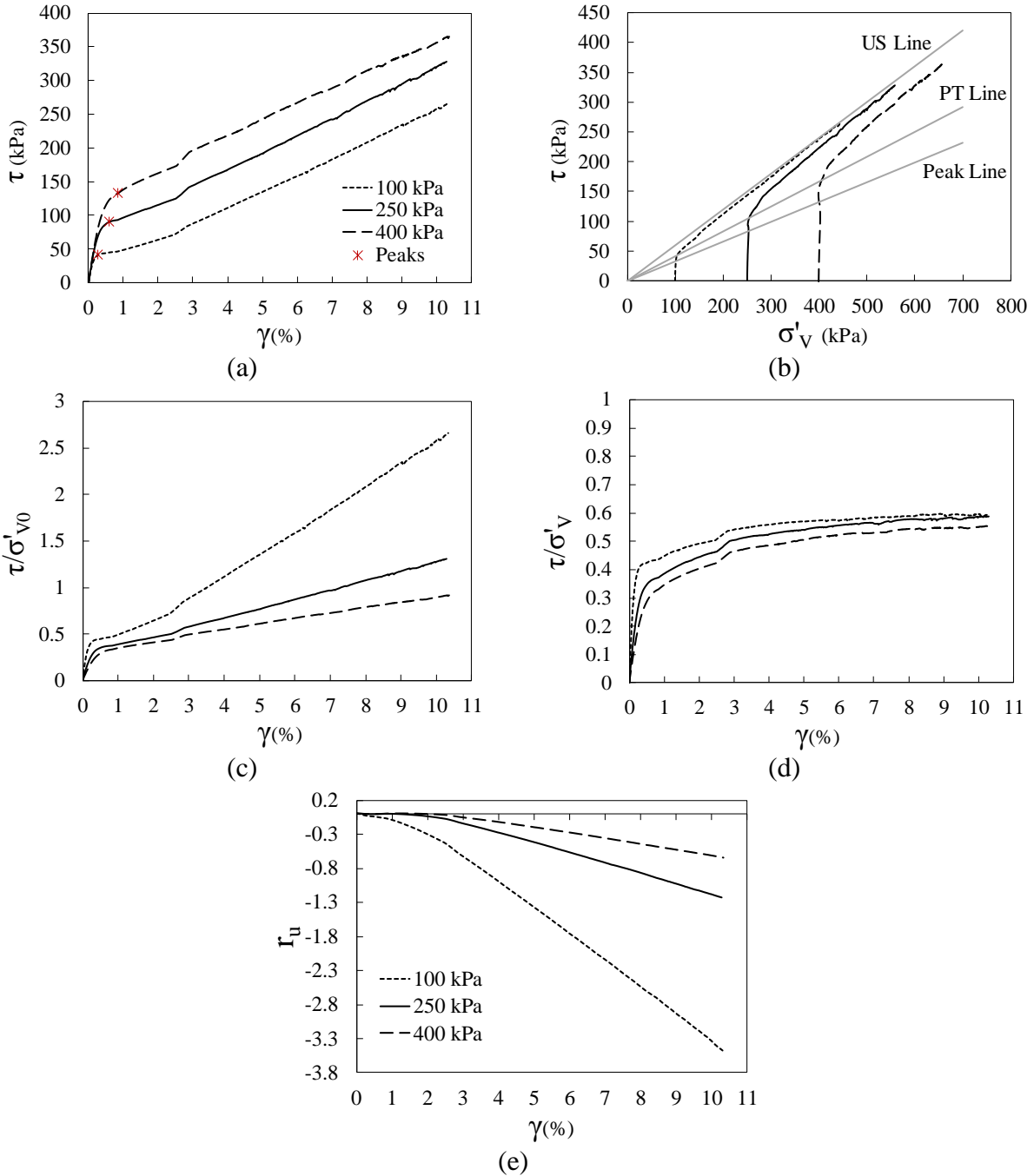


Figure 4.10 Results from DEM simulation of constant volume monotonic simple shear test of Pea gravel specimen ($D_r=87\%$): (a) Shear stress vs. shear strain; (b) Stress path; (c) Shear stress normalized by consolidated vertical stress vs. shear strain; (d) Shear stress normalized by vertical stress vs. shear strain; and (e) Pore pressure ratio vs. shear strain

To ensure that shear deformation is adequately transferred from the moving bottom cap into the specimen, the profiles of ring displacement is monitored during shearing for all the simulations. Figure 4.11 shows the horizontal displacement profile of the stacked rings at three shear strain level of 0.5% (small strain at beginning of the shear), 3.75% (medium strain during shear) and 8% (larger strain as shearing continued). Theoretical continuous simple shear deformation at the lateral boundaries is also shown as solid line on these figures. In such theoretical condition that no slippage and/or rolling happens at the horizontal boundaries, rings displacement varies linearly from the corresponding displacement at the bottom cap and the adjacent ring to zero at the top cap and the adjacent ring. Comparing the ring displacement profiles with the theoretical continuous simple shear deformation at lateral boundaries in Figure 4.11, it is justified that the simple shear condition is adequately imposed on the specimens.

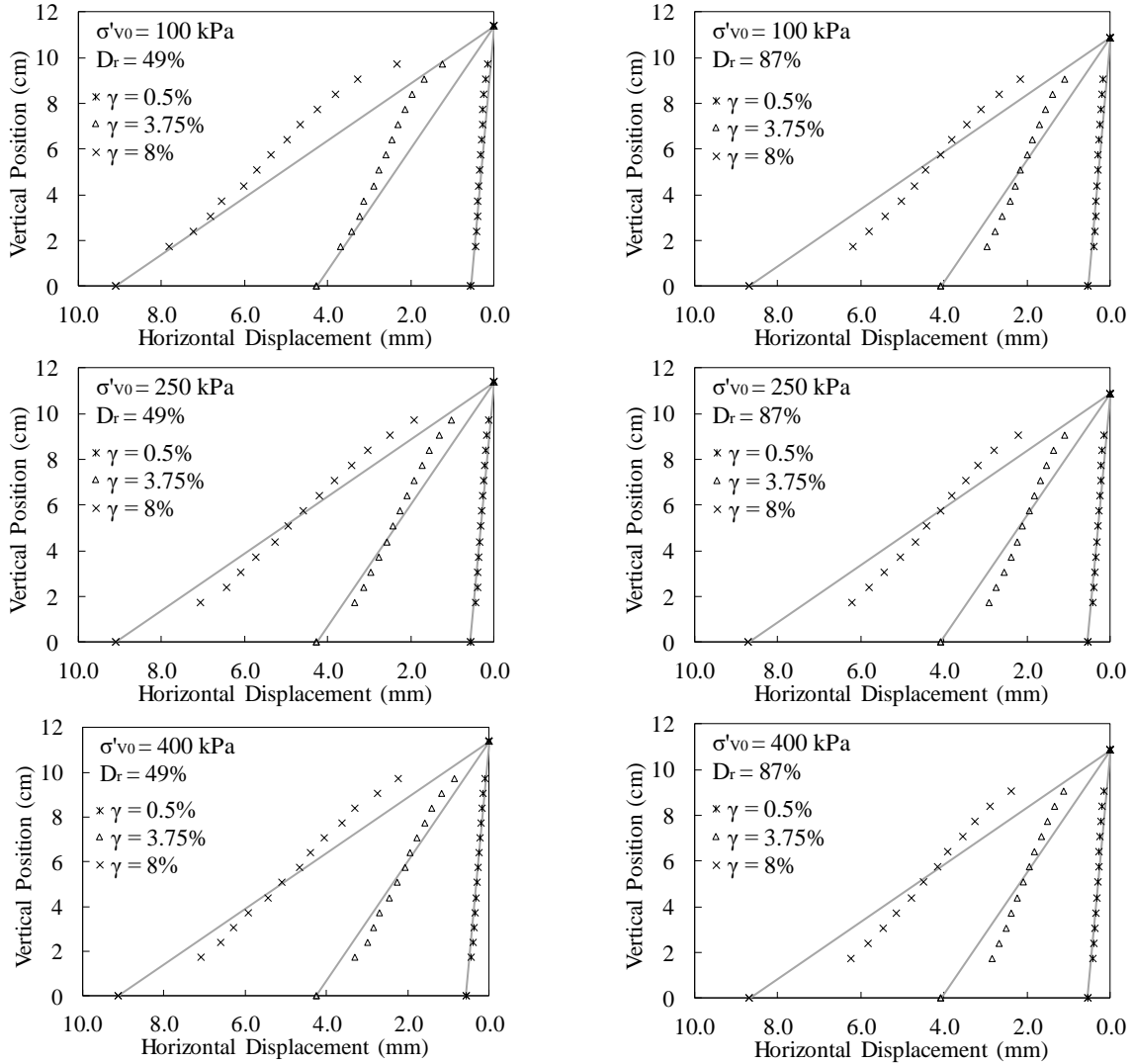


Figure 4.11 Horizontal displacement profile of stacked rings for three levels of boundary shear strain of 0.5, 3.75 and 8% in DEM simulations of constant volume monotonic simple shear response of Pea gravel specimens: $D_r=49\%$ (left) and $D_r=87\%$ (right)

Hubler et al. (2017) conducted series of monotonic constant volume simple shear test on uniform pea gravel at relative densities of 47% and 87%. To calculate the mobilized friction angle for the simple shear tests, they assumed that the horizontal plane is the plane of the maximum shear stress and therefore calculated the friction angle as $\phi = \sin^{-1}(\tau/\sigma'_{v0})$. For comparison purposes, the same assumption is made here to calculate the friction angle for the simulated specimen. Table 4.1 presents the comparison of calculated friction angles in their experiments and this study at

peak, phase transformation and ultimate state. It should be mentioned that as their experimental specimen were prepared at $\pm 3\%$ of the reported relative density values, relative densities of 49% and 87% same as that of simulated specimen in this study are indicated in Table 4.1. In overall, the friction angles are close in simulation of this study and their experiments. However, the differences between the friction angles for two level of relative densities are larger in simulations. For $D_r=49\%$, simulated results underestimate the experimental ones for the friction angles at peak and phase transformation states while makes a good estimation of that at ultimate state. In case of $D_r=87\%$, higher friction angles are calculated for peak and ultimate states in the simulations.

Table 4.1 Mobilized friction angles from simulation and experimental results

	Friction angle (φ°)					
	Peak		Phase transformation		Ultimate state	
	$D_r=49\%$	$D_r=87\%$	$D_r=49\%$	$D_r=87\%$	$D_r=49\%$	$D_r=87\%$
DEM Simulations (This study)	10	19	23	25	30	37
Experiments (Hubler et al. 2017)	14	16	27	27	30	31

4.5 Stress measurement at boundaries versus inside specimen core

In simple shear experiment, the forces measured during shear are commonly the vertical and horizontal forces on the horizontal boundaries and this information at the vertical boundaries or inside the specimen is usually unavailable. Assuming a uniform distribution of stress on the horizontal boundaries, the shear and vertical stresses are calculated by averaging the horizontal and vertical forces, respectively, over the whole area of the horizontal boundaries. Although it is a common assumption made by researchers and practitioners in the field, the non-uniformity of stresses has been shown to exist over the horizontal boundaries (e.g. Prevost and Høeg, 1976; Budhu, 1984). Discrete element method, utilizing a particulate approach, overcomes the

experimental challenge of measuring different quantities such as stress inside the specimen. It is used here to check the reliability of the boundary measurement in representing the response of the specimen in simple shear condition. The stresses inside the specimen are calculated by homogenization over the volume of the measurement spherical region (V_{MS}) as (Christoffersen et al., 1981):

$$\bar{\sigma}_{ij} = \frac{1}{V_{MS}} \sum_{k=1}^{N_C} f_i^k l_j^k \quad (\text{Eq. 4.5})$$

where $\bar{\sigma}_{ij}$ is stress tensor, N_C is the number of inter-particle contacts inside the measurement sphere, f_i^k is the i-component of contact force and l_j^k is the j-component of branch vector connecting the centers of the contacting spheres of the k^{th} contact force.

Since the stresses at the center of the specimen is more uniform and less influenced by boundary effect (e.g. Budhu and Britto, 1987; Prevost and Høeg, 1976), the measurement sphere is considered at the center of the specimen. The diameter of this measurement sphere (D_{MS}) is selected as $D_{MS}/D_{50}=8$ after a sensitivity analysis of different measured quantities (stress, strain, and void ratio) to the size of the central measurement sphere at different vertical stresses and relative densities. D_{50} is the diameter of the sphere than which 50% by volume of the spheres in the specimen have smaller diameters. The relevant figures are presented in 0. The value of 8 for D_{MS}/D_{50} is selected based on the overall results of sensitivity analysis and also the fact that the edge of the measurement sphere has adequate distance from the boundaries so that the boundary effects are minimized, and the uniformity condition is satisfied inside it. The central measurement sphere with the selected diameter covered about the middle two third of the specimen height and was inside the one third of the specimen diameter (Figure 4.12).

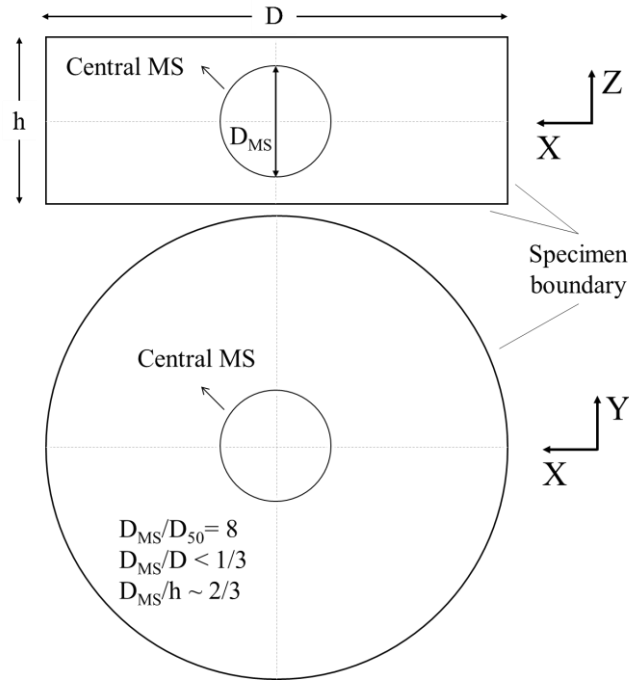


Figure 4.12 The central measurement sphere considered for measurements inside the specimen

The comparison of the constant volume simple shear response measured at boundaries and inside the central measurement sphere (named MS1) are presented in Figure 4.13 and Figure 4.14 for consolidated vertical stress of 250 kPa and relative densities of 49% and 87%, respectively. The corresponding figures for consolidated vertical stresses of 100 and 400 kPa are presented in Appendix B. The shear strain in these figures are considered as the boundary shear strain of the specimen calculated as ratio of displacement of bottom cap to the consolidated height of the specimen. Although the overall trend of the responses are similar, there are quantitative differences between them. For both levels of relative density, boundary measurements underestimate the peak shear stress (τ_p) at the specimen center. The peak shear stress measured on the boundary, as done in laboratory, underestimates the peak shear stress at the specimen center by an average of 33%. Shear response measured at the boundaries of the looser specimen shows lower rate of strain softening than that measured at center of the specimen. Similar rate of the strain hardening are

observed for measurements at boundaries and specimen center. Normalizing the shear stress by consolidated vertical stress, same observations are made for τ/σ'_{v0} versus shear strain graphs; however, the differences between the two measurements are smaller for the normalized shear stress responses. The stress ratio τ/σ'_v measured at both boundaries and specimen center increased as shearing goes on and approaches a constant value at higher shear strains; nevertheless, boundary measurements results in smaller values for both relative densities and underestimate the stress ratio inside the specimen core by an average of 13%. The same observations of comparison between the measured stress ratio at horizontal boundaries and core of the specimen are made by Budhu (1979) in constant load simple shear test on Leighton Buzzard Sand.

The corresponding figures for consolidated vertical stresses of 100 and 400 kPa are also presented in Appendix B. Level of consolidated vertical stress is not observed to have any noticeable effect on the comparison between the shear stress-strain response measured at horizontal boundaries and the specimen core. It should be mentioned that a non-zero shear stress at the beginning of the shearing exists in the measurement sphere region which is a result of the relative movement and rearrangement of particles occurring during vertically consolidation of sample to target vertical stress. This initial values are 1.7, 7.3 and 9.8 kPa for specimens of $D_r=49\%$ and consolidated vertical stress of 100, 250, and 400 kPa, respectively, and 3.9, 10.6, and 12.7 kPa for specimens of $D_r=87\%$ and consolidated vertical stress of 100, 250, and 400 kPa, respectively.

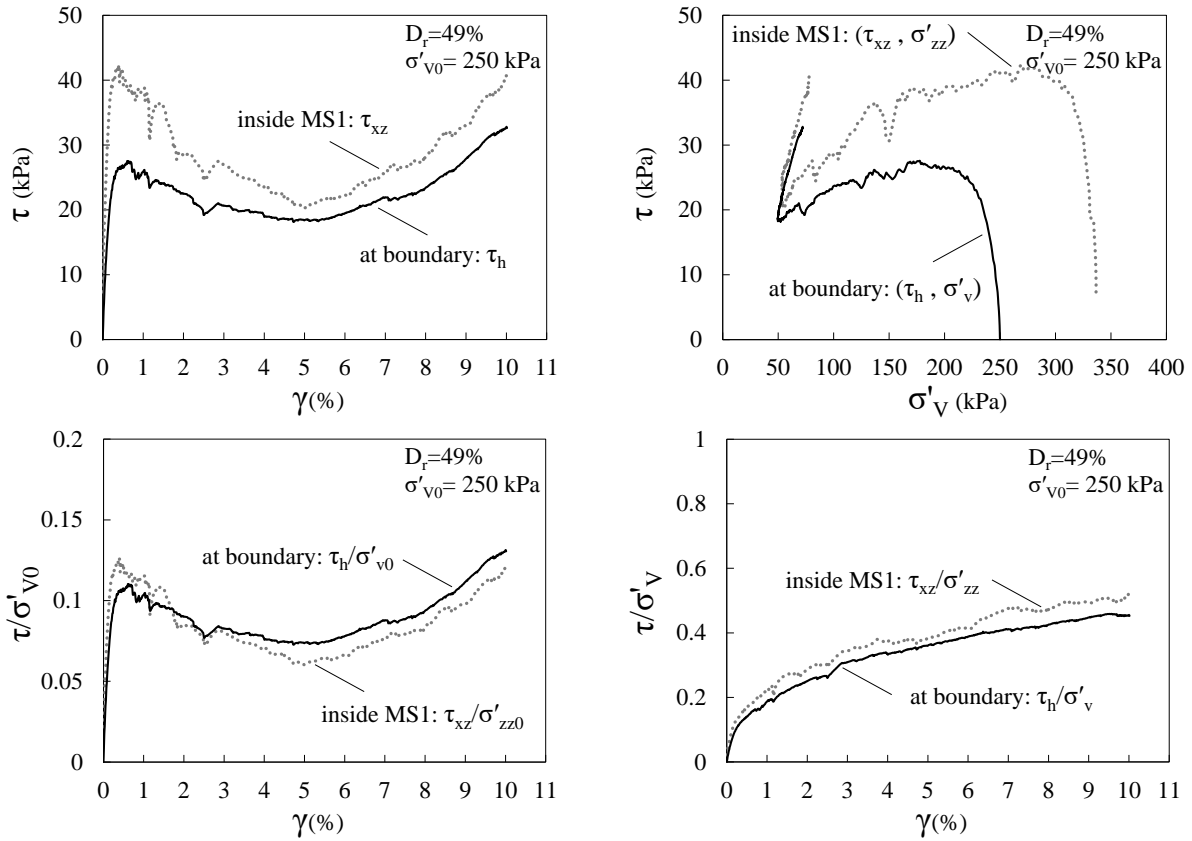


Figure 4.13 Comparison of the monotonic shear response measured at boundaries and inside the central measurement sphere in DEM simulation of constant volume monotonic simple shear response of Pea gravel specimen ($\sigma'_{v0} = 250$ kPa, $D_r = 49\%$)

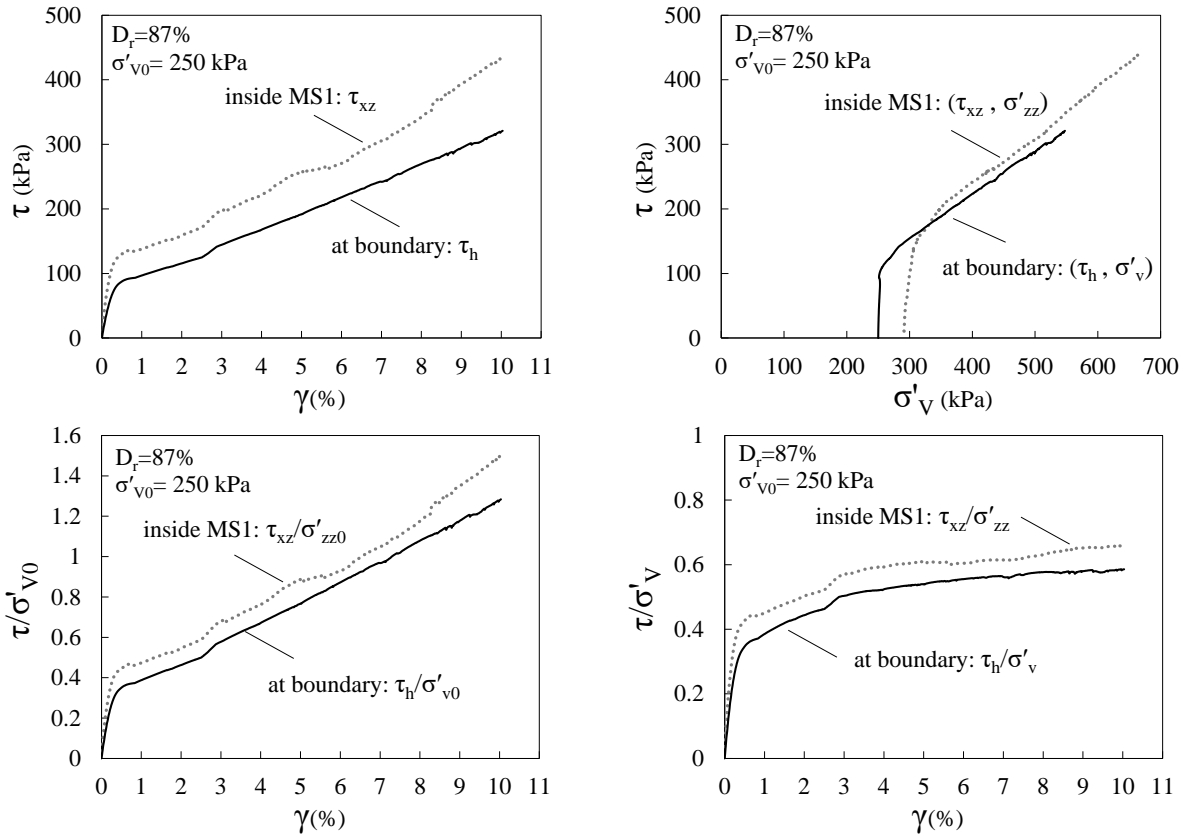


Figure 4.14 Comparison of the monotonic shear response measured at boundaries and inside the central measurement sphere in DEM simulation of constant volume monotonic simple shear response of Pea gravel specimen ($\sigma'_{v0}=250$ kPa, $D_r=87\%$)

In simulating a constant volume simple shear test of dry specimen as an equivalent of undrained shear test of fully saturated specimen, the pore pressure ratio is calculated based on the changes of measured vertical stress at the top horizontal boundary, similar to the experimental calculation of this parameter. This boundary measured value is compared to those calculated based on the measurement inside the central measurement sphere. Figure 4.15 shows this comparison for all cases of consolidated vertical stress and relative density. For comparison purposes, the pore pressure ratio inside the central measurement sphere is calculated in two ways. In the first case, change of normal component of stress tensor in the vertical direction (σ'_{zz}) is considered, in similarity to boundary based measurement. In the second case, the true definition of pore pressure

as the change in mean effective stress (p') is considered and pore pressure ratio is calculated as $(p' - p'_0)/p'_0$, in which:

$$p' = \frac{\sigma'_{xx} + \sigma'_{yy} + \sigma'_{zz}}{3} \quad (\text{Eq. 4.6})$$

where σ'_{xx} and σ'_{yy} are normal stresses in x and y direction and p'_0 is initial mean effective stress at the beginning of the shear. It can be observed that calculating the pore pressure ratio based on the vertical stresses measured either at boundaries or inside the measurement spheres leads to more positive value than the true pore pressure ratio that generated inside the central part of the specimen. For specimens of $D_r=49\%$, the calculated pore pressure ratio based on the boundary measured vertical stresses overestimates the true pore pressure ratio at the specimen core by an average of about 20%. However, it should be mentioned that during the first 0.3% shear strain, the amount of overestimation is higher and reaches to as high as 100%. In case of $D_r=87\%$, the overestimation is about 80-100% at the smaller shear strains and gradually decreases to 25-50% at shear strains higher than 5%. It can be concluded that it is conservative to determine the pore pressure ratio in the laboratory based on the measurement of vertical stress on the stationary horizontal boundary.

Overall, these results show that the boundary measurements in constant volume simple shear test in the lab provide a conservative estimate of the soil strength and generated pore pressure at the specimen core.

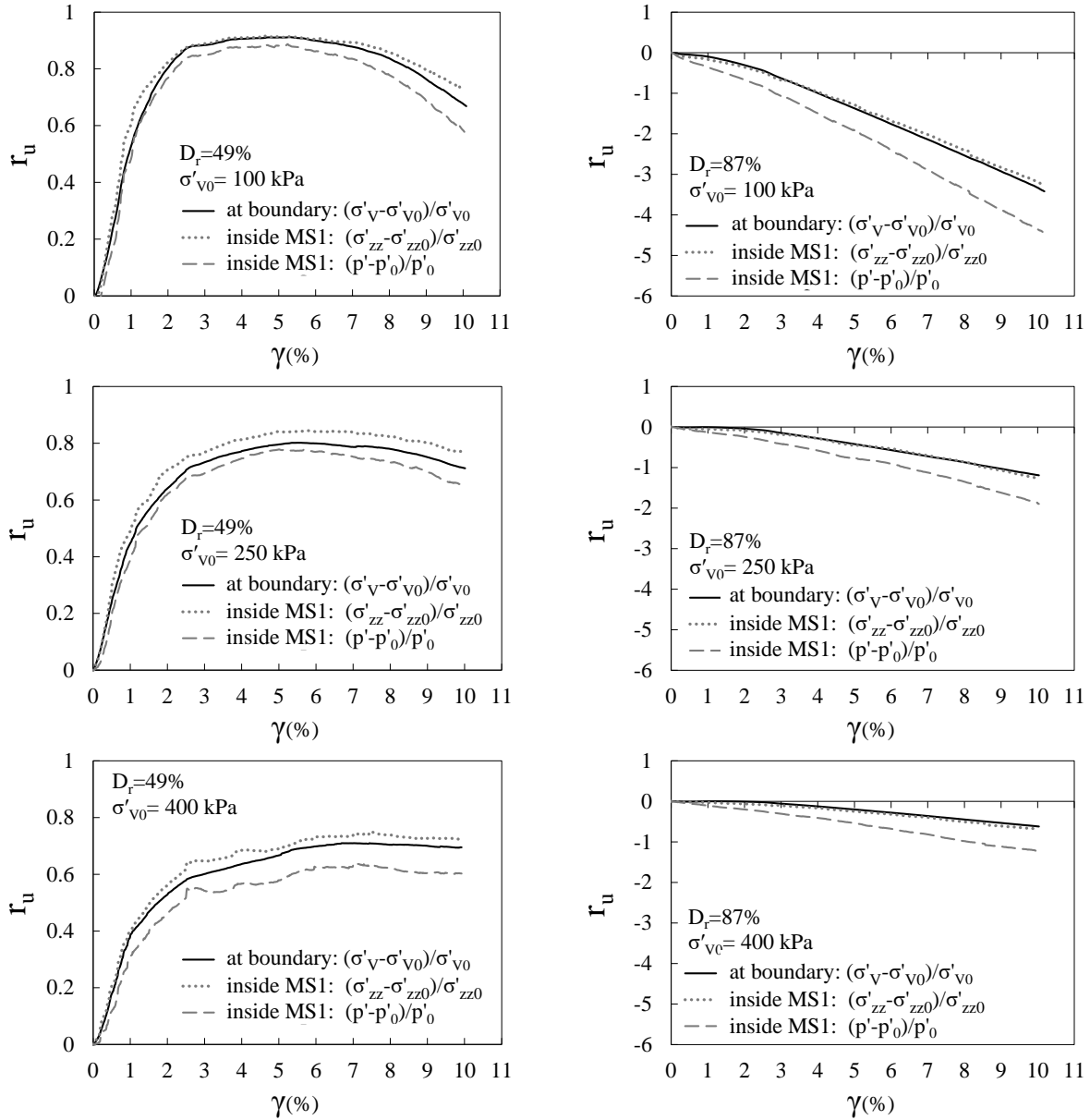


Figure 4.15 Comparison of the generated pore pressure ratio based on the measurements at the boundaries and inside the central measurement sphere in DEM simulations of constant volume monotonic simple shear response of Pea gravel specimen: $D_r=49\%$ (left) and $D_r=87\%$ (right)

Previous researchers have typically used the term coefficient of lateral pressure and the symbol K to describe the ratio of horizontal stress to vertical stress at the boundaries of and inside the specimen in simple shear devices (e.g., Airey and Wood, 1987; Dabeet, 2014; Asadzadeh and Soroush, 2017). The same term and symbol are used in this study. The coefficient of lateral pressure is calculated based on the stress measurements at boundaries and central measurement sphere, and the comparison is shown for all cases of consolidated vertical stress and relative density in Figure 4.16. Coefficients of lateral pressure parallel and perpendicular to the direction of the shear (K_x and K_y , respectively) measured at the specimen core (inside MS1) are calculated as:

$$K_x = \frac{\sigma'_{xx}}{\sigma'_{zz}} \quad (\text{Eq. 4.7})$$

$$K_y = \frac{\sigma'_{yy}}{\sigma'_{zz}} \quad (\text{Eq. 4.8})$$

Assuming the same value of coefficient of lateral pressure in all horizontal directions, the average coefficient of lateral boundary inside the measurement sphere is quantified following equations 4.6, 4.7, and 4.8 as:

$$K_{\text{avg,MS1}} = 0.5 \times \left(\frac{3p'}{\sigma'_{zz}} - 1 \right) \quad (\text{Eq. 4.9})$$

The coefficient of lateral pressure is also determined at boundary as the ratio of radial stress (σ'_r) on the vertical boundaries (rings) to the vertical stress (σ'_v) on the top horizontal boundary. The radial stress is calculated as the sum of the normal forces acting on the rings divided by the lateral surface area of the specimen.

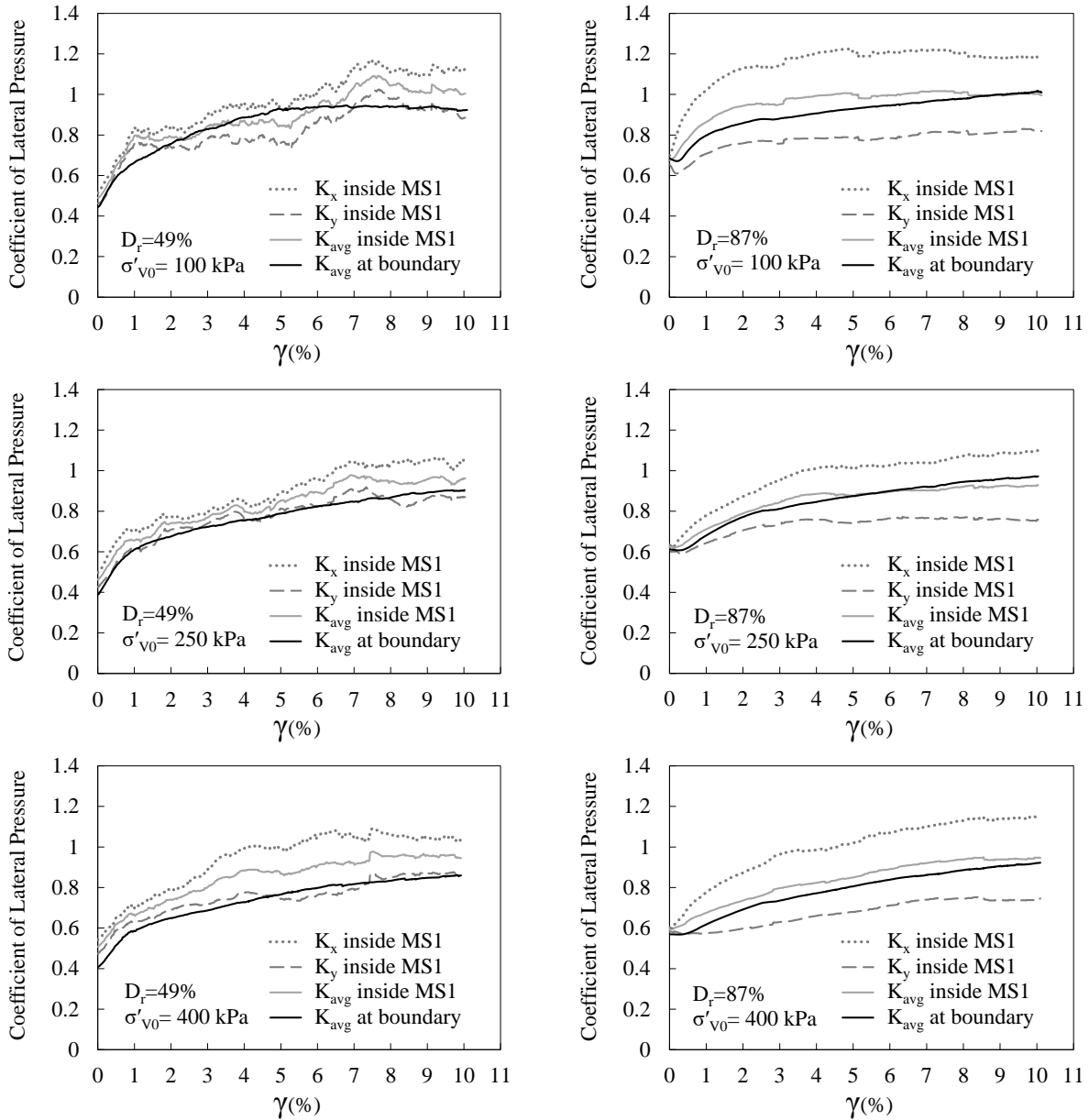


Figure 4.16 Coefficient of lateral pressure during shear in DEM simulations of constant volume monotonic simple shear response of Pea gravel specimen: $D_r=49\%$ (left) and $D_r=87\%$ (right)

For all the consolidated vertical stresses and relative densities, the coefficient of lateral pressure parallel to the direction of shearing is larger than the one in the perpendicular direction ($K_x > K_y$). The rate of increase of coefficient of lateral pressure is also larger in the parallel direction and the difference between the increase rate in parallel and perpendicular directions is higher for denser specimen. Quantitatively, the average value of K_x/K_y at the end of consolidation is 1.14 and

1.02 for specimens of $D_r=49\%$ and 87% , respectively. This implies the existence of initial anisotropy in the specimen that can be attributed to the anisotropic distribution of inter-particle contacts developed during the preparation and consolidation stages. It should be mentioned that initial anisotropy has even been reported in an assembly of glass balls fallen freely under gravity (Kallstenius and Bergau, 1961). As shearing proceeds, the difference between K_x and K_y increases and at the shear strain of about 10%, the average value for K_x/K_y reaches to 1.23 and 1.48 for specimens of $D_r=49\%$ and 87% , respectively.

Coefficient of lateral pressure determined as average value at the boundaries is mostly close to the K_y (perpendicular to direction of shear) measured at the center of the looser specimen. However, for denser specimen, this value is closer to the K_{avg} measured inside the specimen center. For none of the cases, the average value calculated at boundaries estimates coefficient of lateral pressure parallel to the direction of shear (K_x), which is consistent with the observations made by Budhu (1985) in simple shear tests on dense and loose Leighton Buzzard sand at constant vertical load using NGI-type wire-reinforced circular simple shear device.

4.6 Non-uniformities inside the specimen

Absence of complementary shear developed on the lateral boundaries in direct simple shear test and also local slippages at the interface between soil and the horizontal boundaries have been known to cause non-uniformities of stress and strain distribution inside the specimen (e.g., Budhu, 1984; Airey and Wood, 1987; Prevost and Høeg, 1976). DEM has been used before to investigate the non-uniformity of stress and strain during simple shear test for specimen of freely rotating spherical particles (Dabeet et al., 2015; Asadzadeh and Soroush, 2018). In this part, the distributions of the different measured quantities are evaluated in the simulated specimen which is

more realistically represent the real soil in terms of number, size and rolling resistance distribution of particles.

For this purpose, 13 spherical measurement regions are considered over the cross sectional area and at the mid-height of the specimen (Figure 4.17).

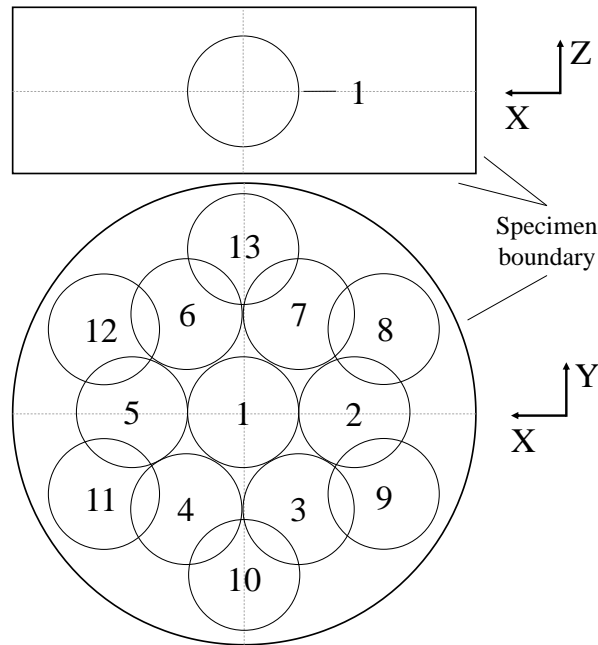


Figure 4.17 Schematic of the measurement sphere considered for evaluation of non-uniformity inside the specimen (all measurement spheres are at the same elevation as MS1)

The following definition is used to quantify the non-uniformity of different measurement quantities:

$$\text{Non-uniformity parameter (\%)} \text{ of quantity } X = \frac{X_{max} - X_{min}}{X_{avg}} \times 100 \quad (\text{Eq. 4.10})$$

in which, X_{max} , X_{min} , and X_{avg} are the maximum, minimum, and average measured value of the quantity X measured inside the measurement spheres at each instance. Similar definition has been used by other researchers. For example, Wijewickreme and Vaid (1991) used a similar definition to assess the variation of stress ratio across the wall of hollow cylindrical torsional shear specimen in laboratory. A similar definition was also used by Dabeet (2014) to evaluate stress non-

uniformity in discrete element simulated specimen of glass beads in NGI-type simple shear test. In the current study, the value of the non-uniformity parameter is reported in percent and if at any instance, the average value for any parameter is negative, the absolute value is considered in calculation of non-uniformity parameter.

In the following analyses, the non-uniformity of void ratio, vertical and shear stresses, stress ratio shear, pore pressure ratio and shear and volumetric strains are assessed in the specimen over the considered measurement spheres. For each quantity, variation of it inside all the measurement spheres is first presented for specimens of $D_r=49\%$ and 87% at consolidated vertical stress of 250 kPa as examples. The corresponding figures for specimens at consolidated vertical stresses of 100 and 400 kPa are presented in Appendix C. Then, the variation of the maximum, minimum and average value of the quantity measured inside the measurement spheres is shown for all specimens, and finally the evolution of non-uniformity quantified using equation 4.9 is presented and discussed.

The void ratio measured inside the measurement spheres during shear is shown in Figure 4.18 for specimens at consolidated vertical stress of 250 kPa. As shown the measured value of void ratio inside measurement spheres are smaller than the overall void ratio of the specimen. This difference is rooted in the fact that the total void ratio of the specimen is affected by the boundary geometry. However, calculating the void ratio inside measurement spheres, as explained in chapter 2, for particles intersecting with the edges of the measurement spheres, the portions inside the measurement sphere are still accounted for. Another observation is that the evolution of void ratio is not the same in all the measurement spheres and redistribution of void ratio can be seen in the specimen during shear. Pore spaces change as void ratio is redistributed during shear. Such non-uniform change in pore spaces causes the redistribution of pore pressure and migration of pore

water through pore spaces in saturated specimens. It has also been shown in DEM simulation of undrained monotonic triaxial test (Guo and Yu, 2015) that by redistribution of porosity under external loading, the pore water flows in directions consistent with the variation of porosity.

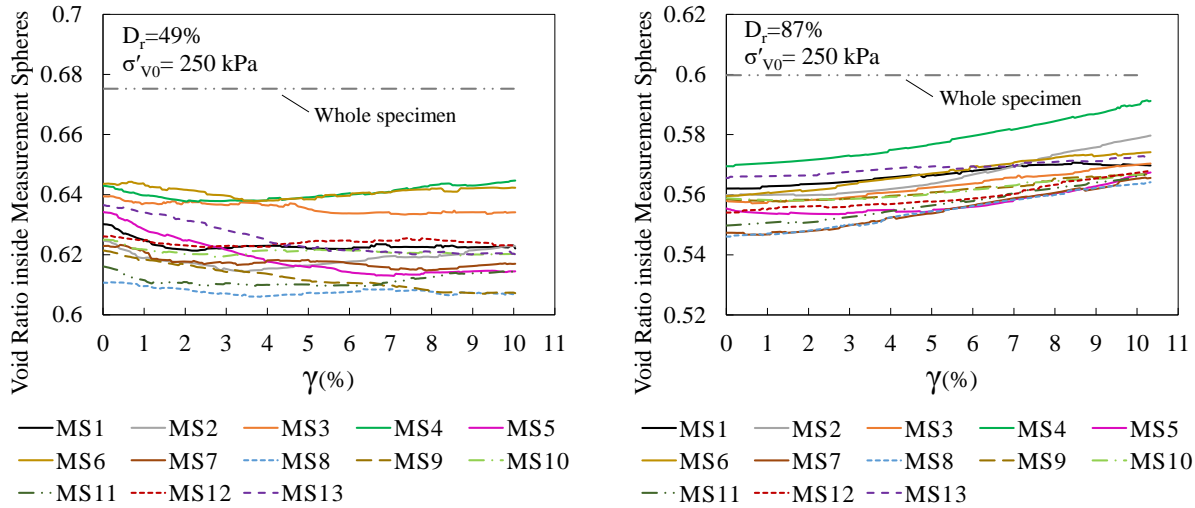


Figure 4.18 Void ratio measured inside measurement spheres MS1-MS13 during shear in DEM simulations of constant volume monotonic simple shear response of Pea gravel specimen ($\sigma'_{v0}=250$ kPa and $D_r=49\%$ (left), $D_r=87\%$ (right))

In Figure 4.19, the range and average of the void ratio values measured inside the measurement regions are shown for all the cases of the consolidated vertical stress and relative density. The evolution of non-uniformity parameter during shear is also shown in this figure. It can be observed that the non-uniformity of distribution of void ratio starts from 4-6% at the end of consolidation and does not experience significant changes up to boundary shear strain of 10%.

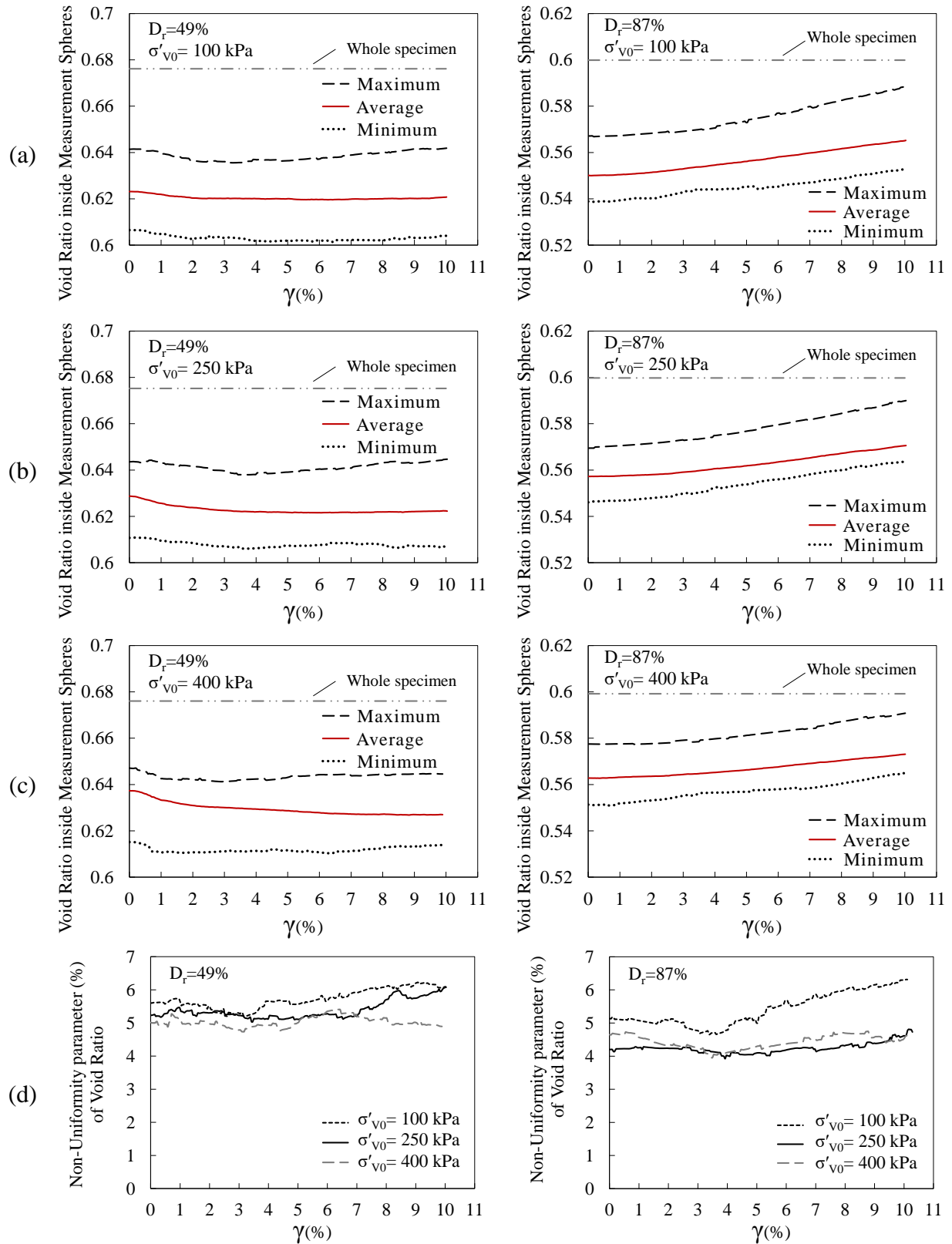


Figure 4.19 Distribution of void ratio inside MS1-MS13 in DEM simulations of constant volume monotonic simple shear response of Pea gravel specimen: (a) $\sigma'_{v0}=100$ kPa, (b) $\sigma'_{v0}=250$ kPa, (c) $\sigma'_{v0}=400$ kPa, and (d) evolution of non-uniformity parameter; $D_r=49\%$ (left), $D_r=87\%$ (right)

The distribution of vertical effective stress (σ'_{zz0}) at the end of consolidation measured inside MS1-MS13 across the mid-height of the specimen is shown in Figure 4.20 for boundary consolidated vertical stress of 250 kPa. The effective vertical stress is non-uniformly distributed across the specimen and the non-uniformity parameter at the end of consolidation is about 43% and 20% for specimen with relative density of 49% and 87%, respectively. Figure 4.21 shows the variation of the vertical effective stress inside measurement spheres MS1 to MS13 for those specimen. The variation of the range of measured effective vertical stress, the average value and the non-uniformity parameter is presented for all cases of vertical stress and relative density in Figure 4.22. For the case of $D_r=49\%$, the non-uniformity parameter starts with a value between 20% to 50% and reaches to about 30% at boundary shear strain of 10%. For specimens of $D_r=87\%$, this value starts from about 20-25% and reaches to about 30% at boundary shear strain of 10%. In Figure 4.22 (a)-(c), the corresponding value measured at the top boundary (σ'_v) is also shown for comparison. It can be observed that for all cases, the boundary measured effective vertical stress is between the minimum and average measured values inside the specimen at the end of consolidation. As shear proceeds, this value becomes closer to the bottom range of the effective vertical stresses measured inside the specimen.

Comparing the values of the vertical stress measured inside the specimen and at the horizontal boundary at the end of the 1D consolidation of the specimen, it can be concluded that measurement of the vertical effective stress on the top cap, as is done in laboratory, underestimates the actual consolidated vertical effective stress at locations inside the specimen by maximum of 18-26% for looser specimen and by maximum of 14-19% for denser specimen. No specific effect is observed of the level of applied vertical stress. As shear proceeds, the boundary measured value of the vertical effective stress gets closer to the minimum local value measured inside the

specimen. The change in vertical effective stress at different locations inside the specimen happens in way that at the shear strain of about 10%, the boundary measured value underestimates the actual vertical effective stress inside the specimen by the maximum of 23-26% in denser specimen (which is higher than that at the beginning of shear). However, the level of underestimation in looser specimen remains about the same.

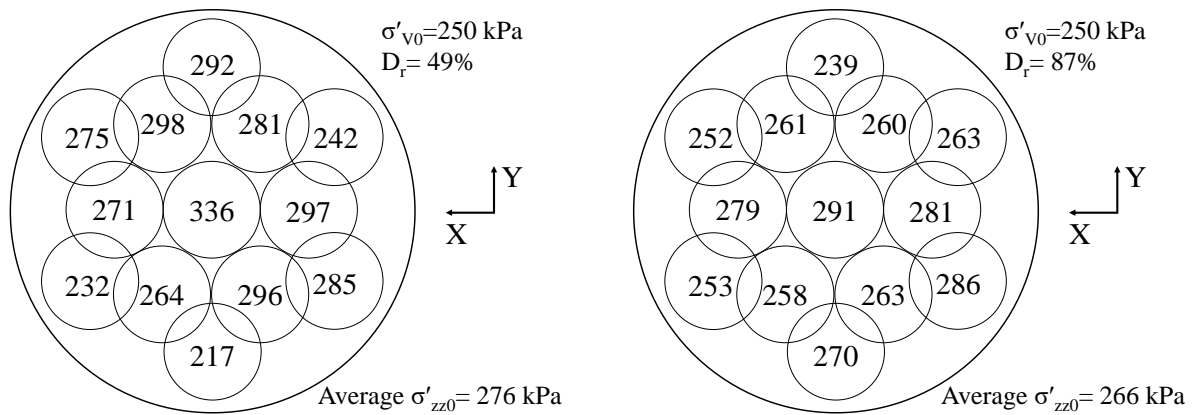


Figure 4.20 Effective vertical stress (kPa) measured inside measurement spheres MS1-MS13 at the end of consolidation for boundary consolidated vertical stress of 250 kPa in DEM simulation of Pea gravel specimen

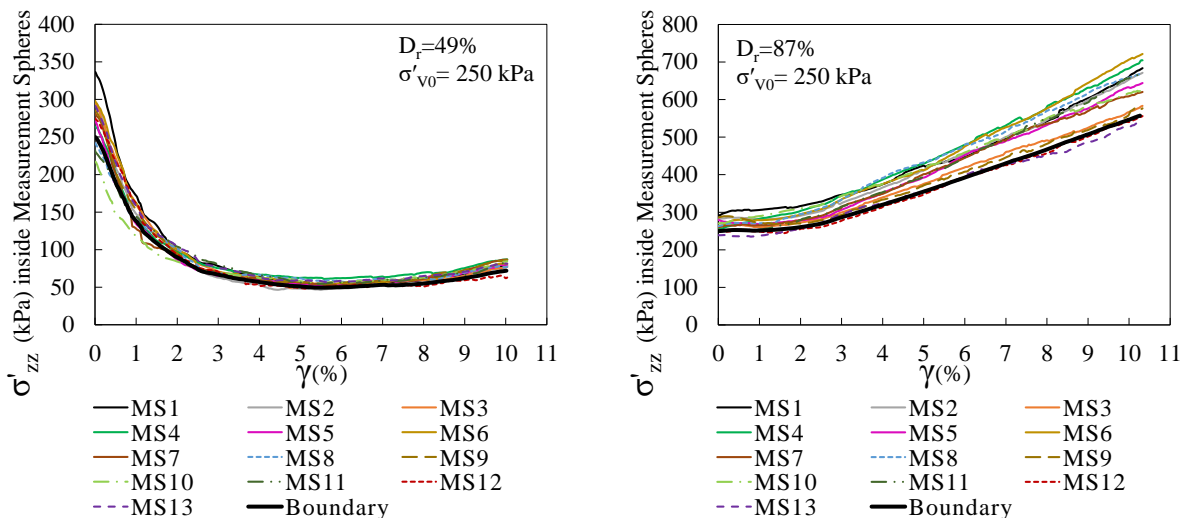


Figure 4.21 Effective vertical stress measured inside measurement spheres MS1-MS13 during shear in DEM simulations of constant volume monotonic simple shear response of Pea gravel specimen ($\sigma'_{v0}=250$ kPa and $D_r=49\%$ (left), $D_r=87\%$ (right))

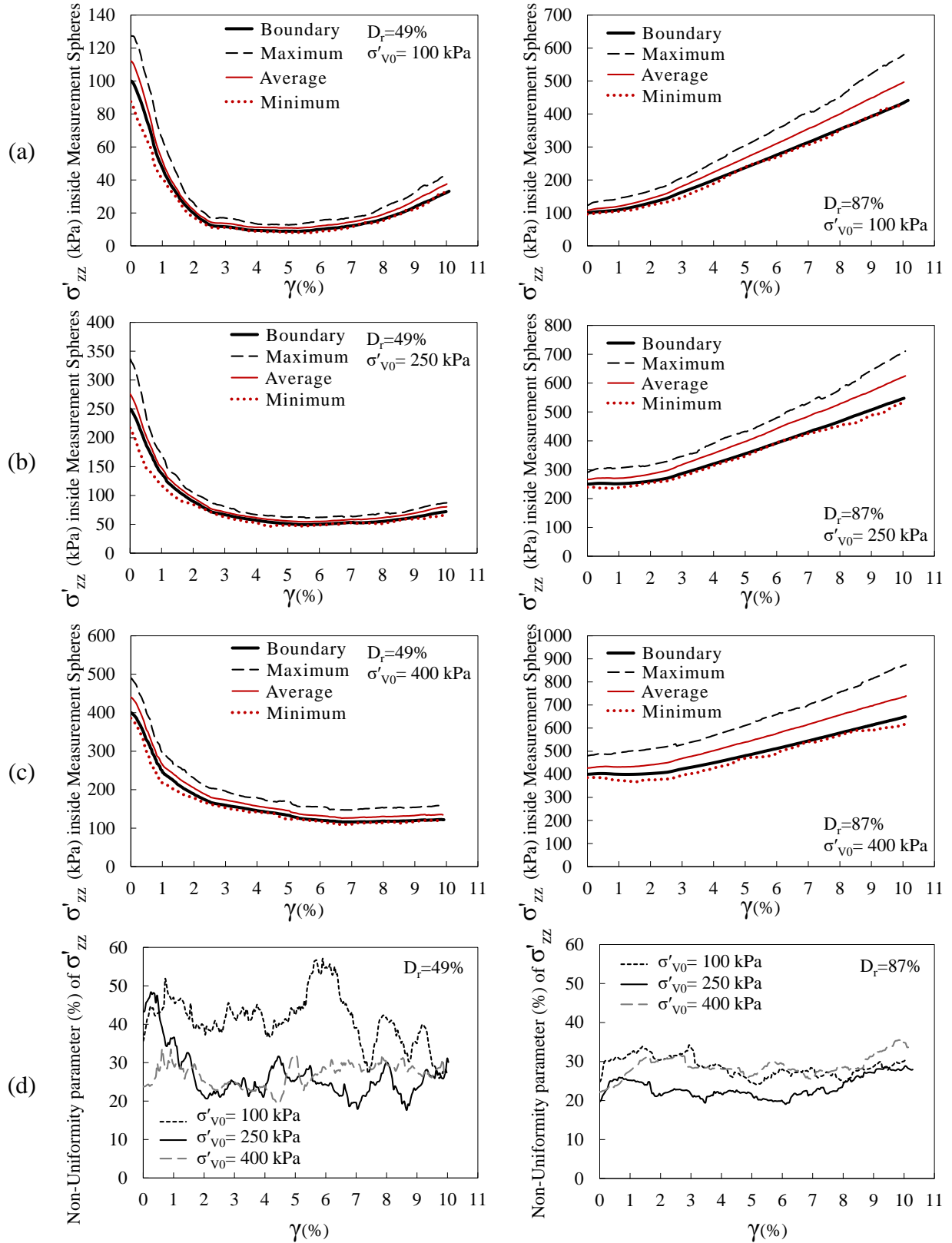


Figure 4.22 Distribution of σ'_{zz} inside MS1-MS13 in DEM simulations of constant volume monotonic simple shear response of Pea gravel specimen: (a) $\sigma'_{v0}=100$ kPa, (b) $\sigma'_{v0}=250$ kPa, (c) $\sigma'_{v0}=400$ kPa, and (d) evolution of non-uniformity parameter; $D_r=49\%$ (left), $D_r=87\%$ (right)

The distribution of shear stress (τ_{xz0}) measured inside MS1-MS13 at the end of the consolidation is shown in Figure 4.23 for specimen of consolidated vertical stress of 250 kPa. These initial shear stresses are generated in the specimen as a result of relative movement and rearrangement of particles during the one dimensional consolidation before the shear stage. At this point, there is a high non-uniformity in distribution of the shear stress inside the specimen. Also, the small average value and relatively large range of shear stresses inside the measurement spheres result in very high value of non-uniformity parameter as can later be seen in small graphs in Figure 4.25 (d).

Figure 4.24 shows the shear stress (τ_{xz}) measured inside MS1-MS13 versus the boundary shear strain for specimens of consolidated vertical stress of 250 kPa. The range, average and non-uniformity parameter of the shear stress distribution inside the specimen for all cases of consolidated vertical stress and relative density is presented in Figure 4.25. In all cases, the non-uniformity parameter experiences a very sharp drop over less than 0.1% of shear strain at the beginning of shearing. For the specimens of $D_r=49\%$, the non-uniformity parameter decreases to about 25% at shear strain level of 1-3% and reaches to about 40-50% at shear strain of 10%. For the case of $D_r=87\%$, the non-uniformity parameter decreases to 35-45% at shear strain level of 4-5% and reaches to 50-60% at shear strain of 10%.

Comparing the boundary measured shear stress (τ_h) to the range of the shear stresses inside the specimen in Figure 4.25, it can be observed that the boundary measured shear stress is between the minimum and average values of shear stress measured inside the specimen. In case of $D_r=87\%$ and for most of the shearing stage, this value is closer to the minimum value measured inside the specimen.

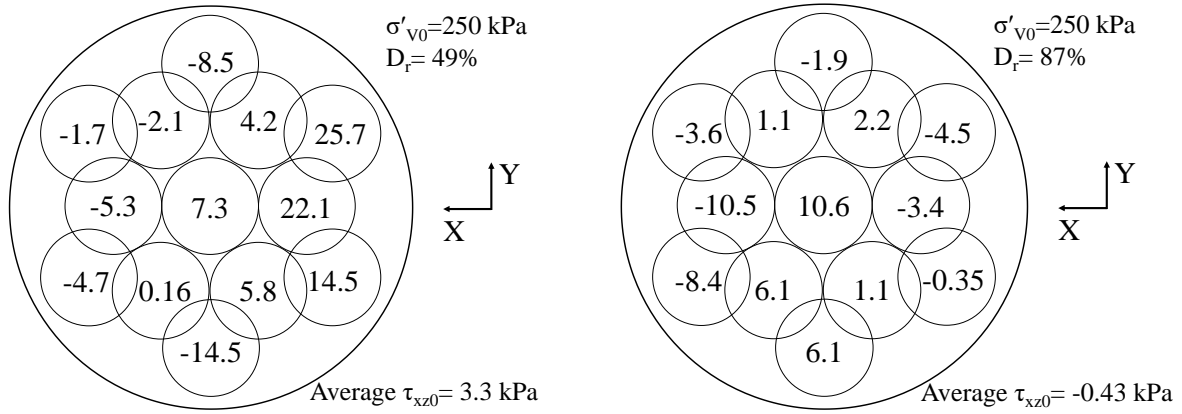


Figure 4.23 Shear stress (kPa) measured inside measurement spheres MS1-MS13 at the end of consolidation for boundary consolidated vertical stress of 250 kPa in DEM simulation of Pea gravel specimen

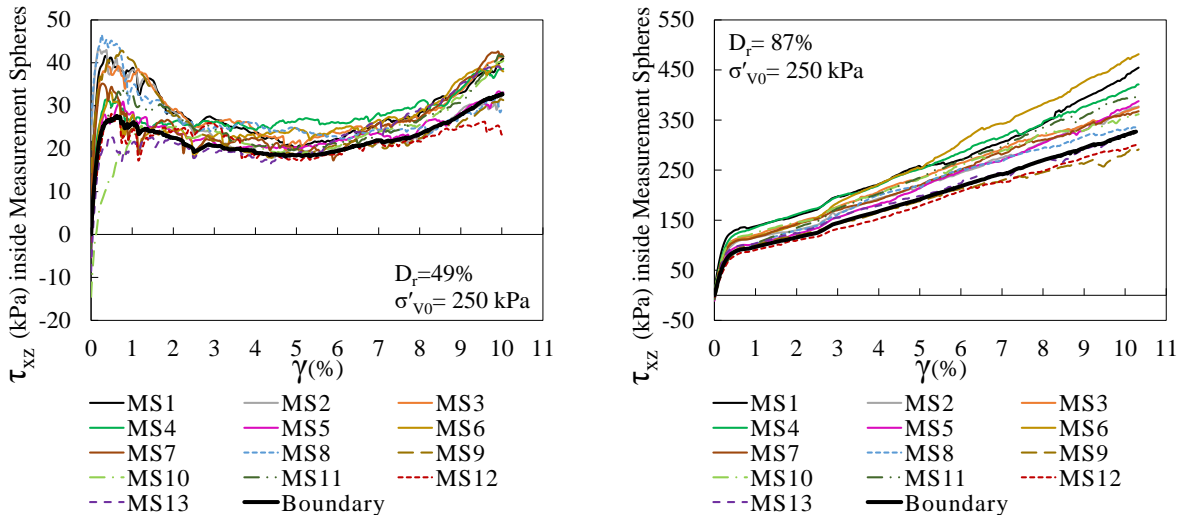


Figure 4.24 Shear stress measured inside measurement spheres MS1-MS13 during shear in DEM simulations of constant volume monotonic simple shear response of Pea gravel specimen ($\sigma'_{v0}=250$ kPa and $D_r=49\%$ (left), $D_r=87\%$ (right))

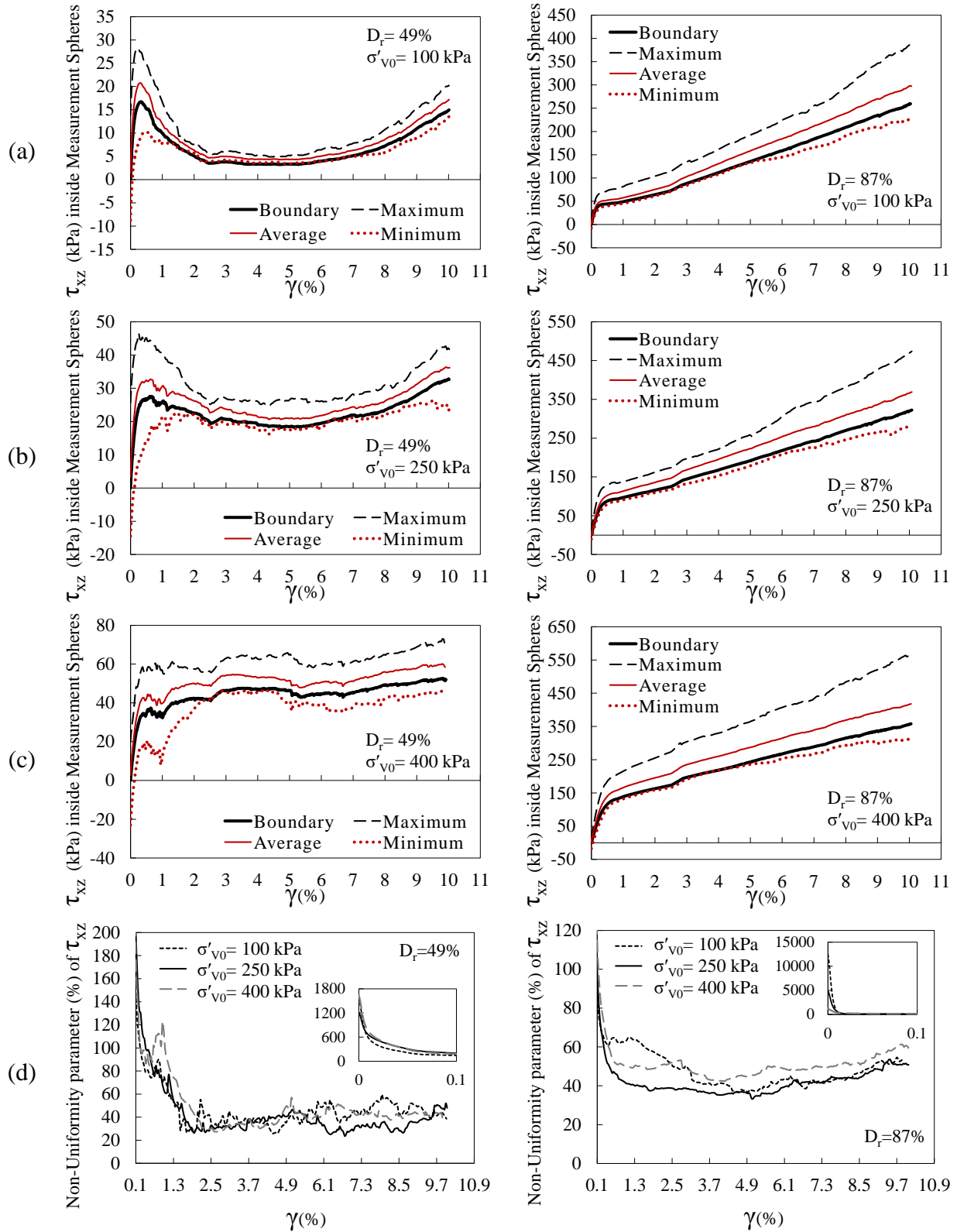


Figure 4.25 Distribution of τ_{xz} inside MS1-MS13 in DEM simulations of constant volume monotonic simple shear response of Pea gravel specimen: (a) $\sigma'_{v0}=100$ kPa, (b) $\sigma'_{v0}=250$ kPa, (c) $\sigma'_{v0}=400$ kPa, and (d) evolution of non-uniformity parameter; $D_r=49\%$ (left), $D_r=87\%$ (right)

Variation of stress ratio (τ_{xz}/σ'_{zz}) inside MS1-MS13 during shear is shown in Figure 4.26 for specimens of $\sigma'_{v0}=250$ kPa. Similar to shear stress, the value of stress ratio at the end of consolidation may be non-zero because of the induced shear stresses inside the specimen during the one dimensional consolidation. Figure 4.27 presents the range and average and non-uniformity parameter of the stress ratio values inside the specimen during shear for all cases of consolidated vertical stress and relative density. It can be observed that for all cases, the boundary measured stress ratio is between the minimum and average internal stress ratio values and approaches the average value at higher shear strains. Therefore, determining the stress ratio based on the measurement of shear and vertical stresses on the horizontal boundaries, as is done in laboratory, leads to overestimation of the actual stress ratio at some locations inside the specimen. At shear strain of about 10%, the boundary measured stress ratio overestimate the minimum local stress ratio inside the specimen by an average of 20%.

Similar to τ_{xz} , non-uniformity parameter of τ_{xz}/σ'_{zz} drops sharply from a very high value at the end of consolidation to less than 200% at shear strain of 0.1%. After the shear strain of 1.5%, the non-uniformity parameter reaches to values of 20-40% for all cases.

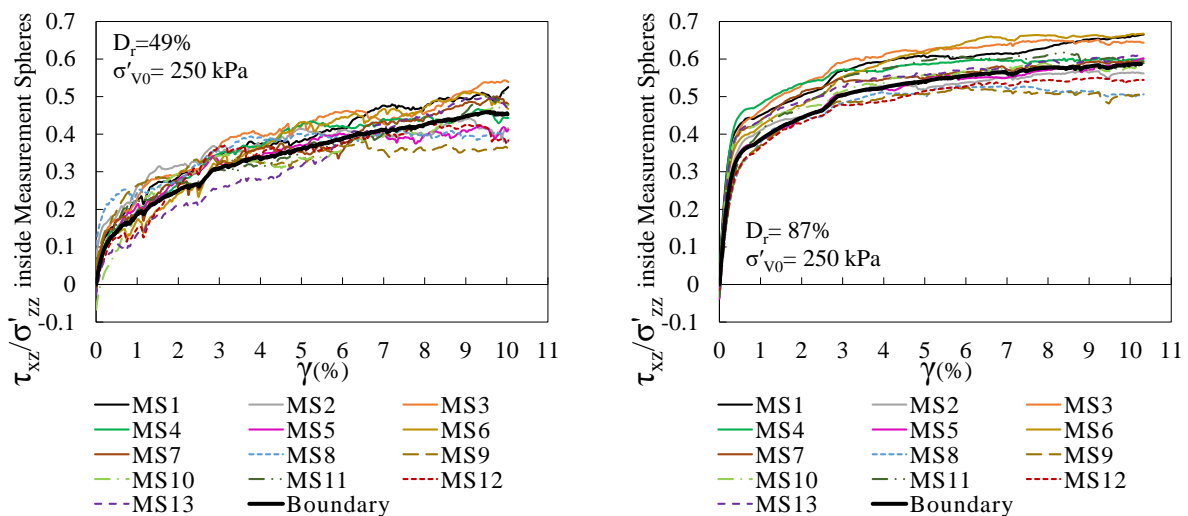


Figure 4.26 Stress ratio measured inside measurement spheres MS1-MS13 during shear in DEM simulations of constant volume monotonic simple shear response of Pea gravel specimen ($\sigma'_{v0}=250$ kPa and $D_r=49\%$ (left), $D_r=87\%$ (right))

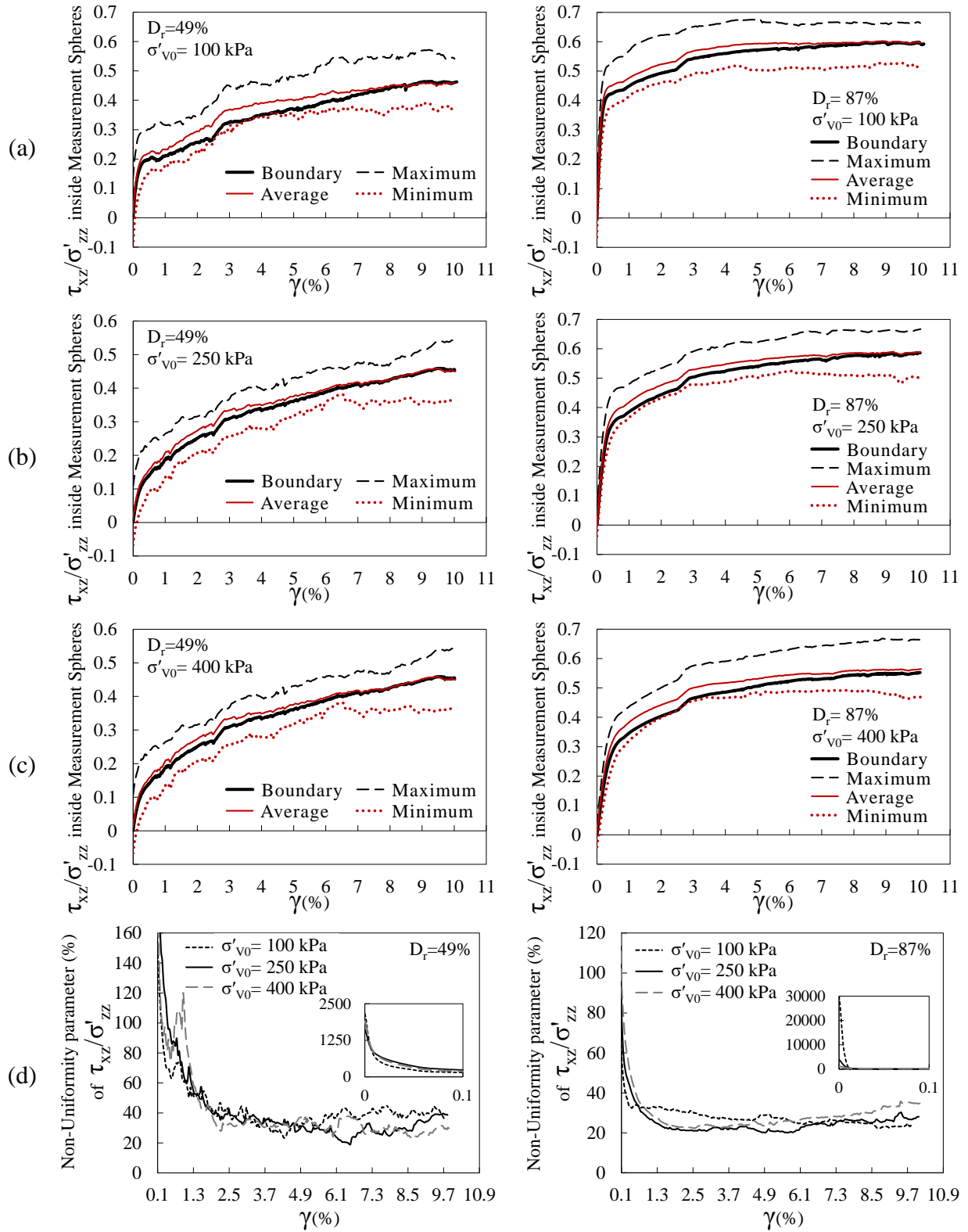


Figure 4.27 Distribution of τ_{xz}/σ'_v inside MS1-MS13 in DEM simulations of constant volume monotonic simple shear response of Pea gravel specimen: (a) $\sigma'_{v0}=100$ kPa, (b) $\sigma'_{v0}=250$ kPa, (c) $\sigma'_{v0}=400$ kPa, and (d) evolution of non-uniformity parameter; $D_r=49\%$ (left), $D_r=87\%$ (right)

The distribution of pore pressure ratio (r_u) inside the specimen is evaluated by calculating it as $(p'-p'_0)/p'_0$, in which p' is the mean effective stress inside the measurement sphere (equation 4.5). Figure 4.28 shows the variation of pore pressure ratio inside MS1-MS13 during shear for specimens of $\sigma'_{v0}=250$ kPa. For all cases of vertical stress and relative density, the range, average, and non-uniformity parameter of pore pressure ratio measured in MS1-MS13 is presented in Figure 4.29. Because of the drained consolidation, the value of pore pressure ratio inside all measurement regions is zero at the end of consolidation and the non-uniformity parameter starts from zero. Initiating the shear, the non-uniformity parameter increases sharply, which can be associated to the very small average value and relatively larger range of measured values at the beginning of the shear. This leads to a high value for the result of equation 4.10. The non-uniformity parameter then decreases to about 10-30% and 25-60% for specimens of $D_r=49\%$ and $D_r=87\%$, respectively at higher shear strains. This change in non-uniformity parameter occurs more gradually for the case of $D_r=87\%$. The non-uniform distribution of generated pore pressure inside the specimen implies that in presence of pore water in saturated specimen, there would be local migration of pore water through voids from locations of higher to lower pore pressure.

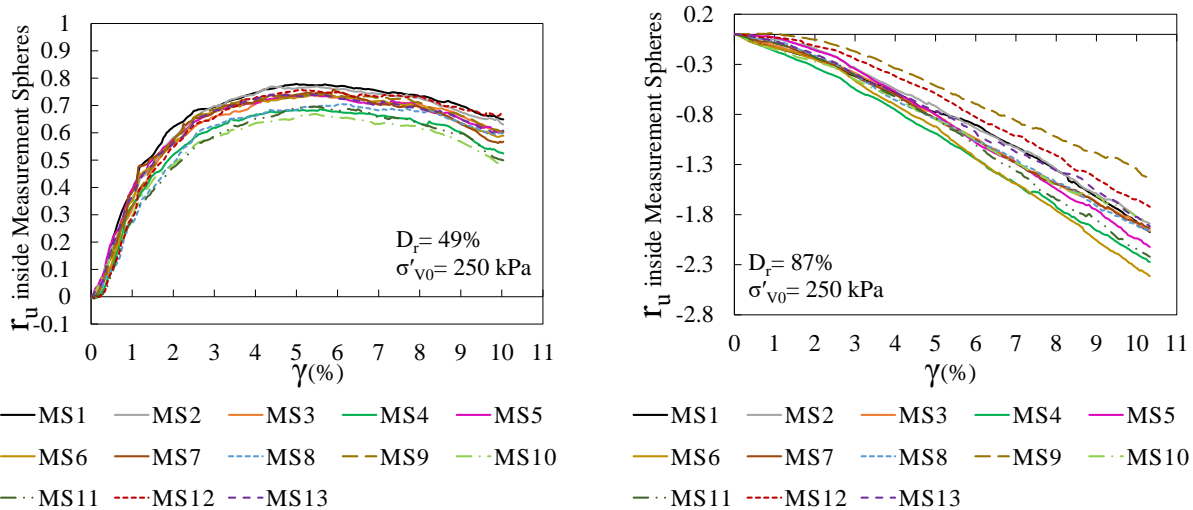


Figure 4.28 Pore pressure ratio measured inside measurement spheres MS1-MS13 during shear in DEM simulations of constant volume monotonic simple shear response of Pea gravel specimen ($\sigma'_{v0}=250$ kPa and $D_r=49\%$ (left), $D_r=87\%$ (right))

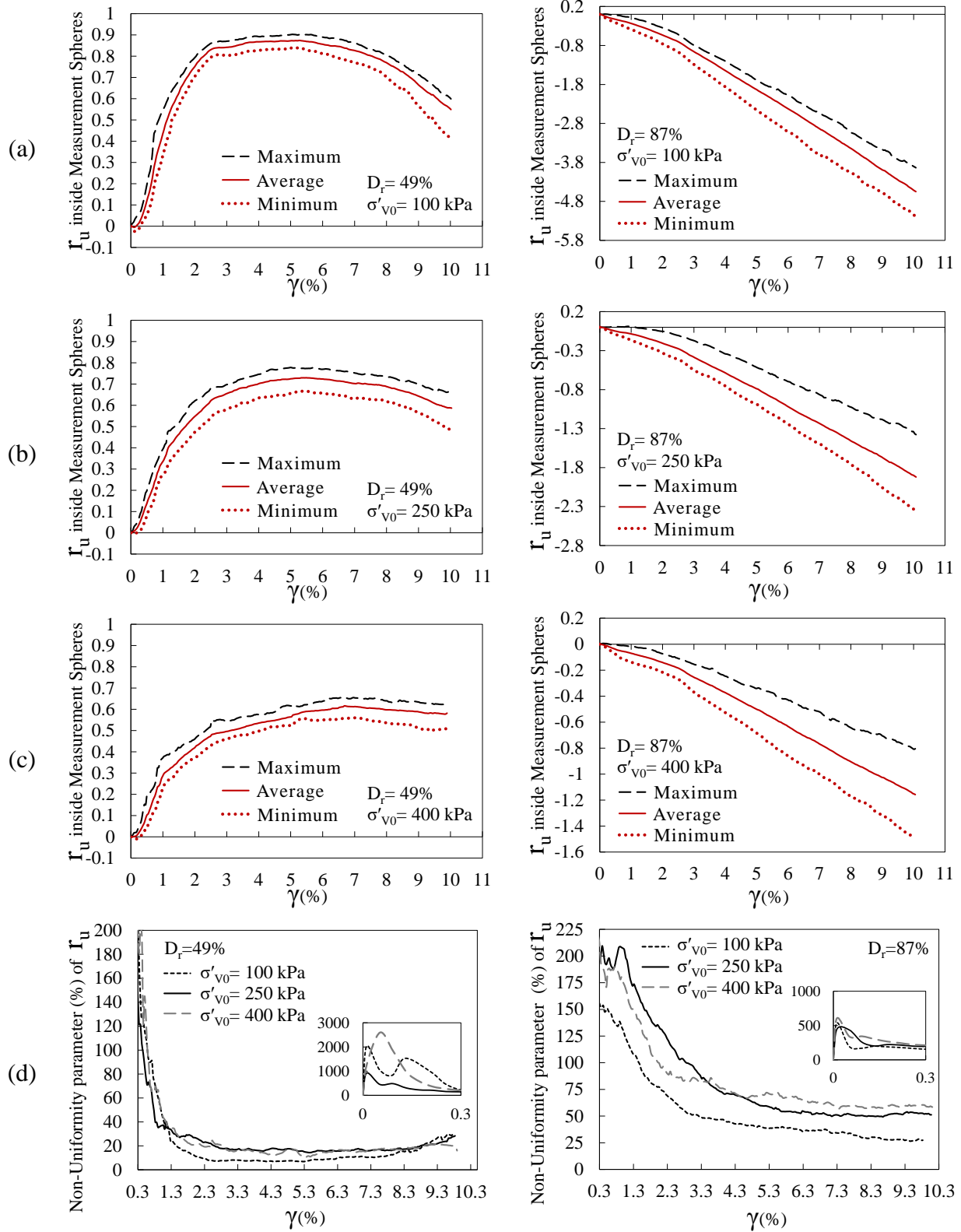


Figure 4.29 Distribution of r_u inside MS1-MS13 in DEM simulations of constant volume monotonic simple shear response of Pea gravel specimen: (a) $\sigma'_{v0}=100$ kPa, (b) $\sigma'_{v0}=250$ kPa, (c) $\sigma'_{v0}=400$ kPa, and (d) evolution of non-uniformity parameter; $D_r=49\%$ (left), $D_r=87\%$ (right)

The evolution of shear strain ($\gamma_{xz} = \varepsilon_{xz} + \varepsilon_{zx}$) inside MS1-MS13 during shear in specimens of $\sigma'_{v0} = 250$ kPa is shown in Figure 4.30, and the range, average, and non-uniformity parameter of γ_{xz} for all cases of consolidated vertical stress and relative density is presented in Figure 4.31. It can be observed that in all cases, the shear strain calculated inside the measurement spheres at the mid-height of the specimen is smaller than the boundary shear strain. It can be attributed to the local slippage of particles at the interface of the specimen and the horizontal boundaries and also the local slippage that occurs at the inter-particle contacts. These observations are in agreement with the ones reported by other researchers. For example, Dabeet et al. (2010) used DEM to investigate the non-uniformity of shear strain in simple shear device under constant load conditions. Although the slippage of particles at the horizontal boundaries was prevented and a perfect simple shear deformation was also numerically imposed on the specimen in their simulations (by assigning predefined velocities to the lateral rings), the shear strain was observed to distribute non-uniformly in the specimen and deviate from the boundary measured shear strain.

It can be concluded that the boundary measured shear strain (as done in laboratory) overestimates the induced shear strain inside the specimen, and this difference needs to be accounted for in interpretation of the experimental results. According to the simulation results, for boundary shear strains of smaller than about 0.05%, the boundary measured shear strain is by average 2.7 and 4 times larger than the average shear strain inside the specimen for specimens of $D_r = 49\%$ and 87% , respectively. For the rest of the shearing, this difference between the boundary and internally measured shear strain decreases and the boundary measured shear strain is by average 1.3 and 1.7 times larger than the average shear strain inside the specimen for specimens of $D_r = 49\%$ and 87% , respectively.

Non-uniformity parameter experiences a sharp increase from zero at the beginning of the shear for all specimen. However, after about 1% of boundary shear, the non-uniformity parameter is gradually decreases to about 20-30% and 30-40% for specimens of $D_r=49\%$ and $D_r=87\%$, respectively.

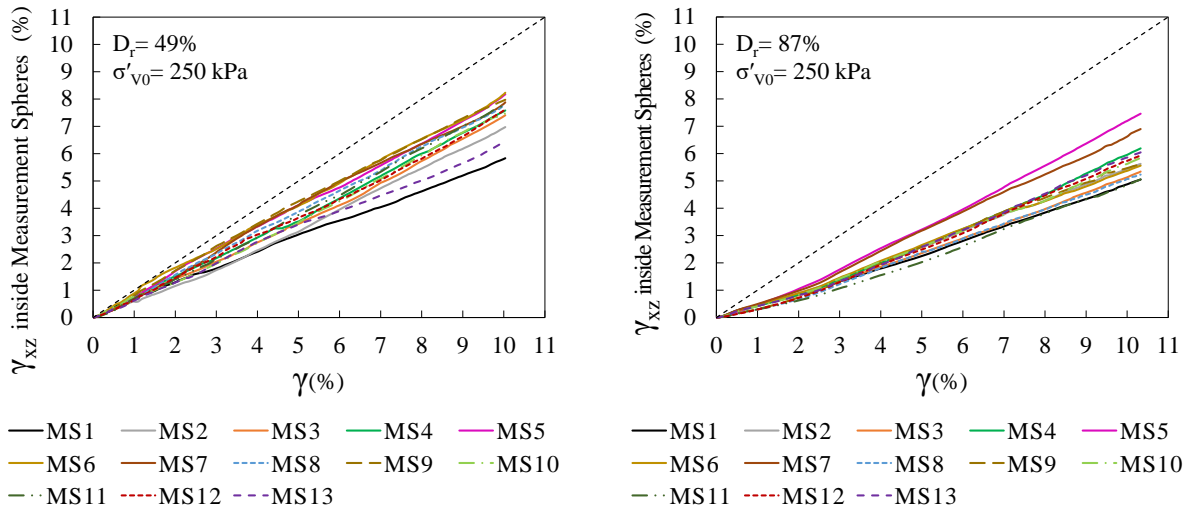


Figure 4.30 Shear strain measured inside measurement spheres MS1-MS13 during shear in DEM simulations of constant volume monotonic simple shear response of Pea gravel specimen ($\sigma'_{v0}=250$ kPa and $D_r=49\%$ (left), $D_r=87\%$ (right))

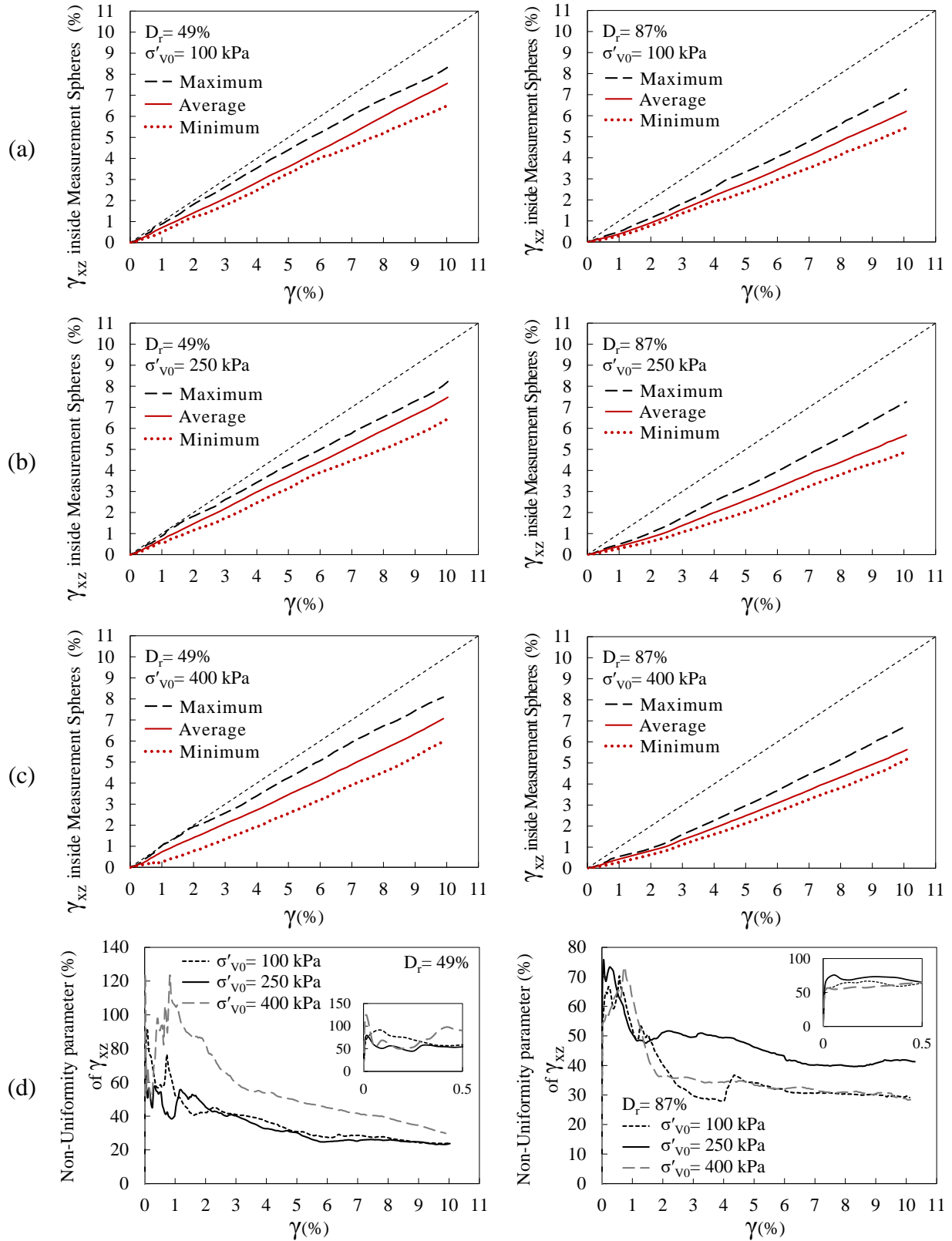


Figure 4.31 Distribution of γ_{xz} inside MS1-MS13 in DEM simulations of constant volume monotonic simple shear response of Pea gravel specimen: (a) $\sigma'_{v0}=100$ kPa, (b) $\sigma'_{v0}=250$ kPa, (c) $\sigma'_{v0}=400$ kPa, and (d) evolution of non-uniformity parameter; $D_r=49\%$ (left), $D_r=87\%$ (right)

4.7 Stress State inside the specimen

One of the limitations of simple shear test is that because of the lack of complementary shear stresses and also unavailability of stress measurement at lateral boundaries, there is not enough information available to obtain the stress state inside the specimen and draw the stress Mohr's circles. As a result, different assumptions have been made to interpret the experimental results of simple shear test to assess the mobilized friction angle in the specimen (refer to Chapter 2). In this part, these assumptions are evaluated by having a thorough information of stress state inside the specimen provided by DEM simulations.

For this purpose, the stress state at the core of the specimen (MS1) is considered in two specimens of $D_r=49\%$ and $D_r=87\%$ at boundary consolidated vertical stress of 250 kPa. It should be mentioned that although the specimen is globally under overall constant volume condition, local volume changes are observed inside the specimen because of the local rearrangement of particles. The volumetric strains observed inside MS1 during shear is presented in Figure 4.32 for all boundary consolidated vertical stresses at $D_r=49\%$ and $D_r=87\%$. Previously, it was seen that pore pressure is also generated inside MS1 (Figure 4.29). Therefore, the behavior of assembly inside MS1 is not either completely drained or completely undrained. However, the stress state at the specimen core (inside MS1) is used in this study to evaluate the stress state inside the specimen under global constant volume simple shear condition.

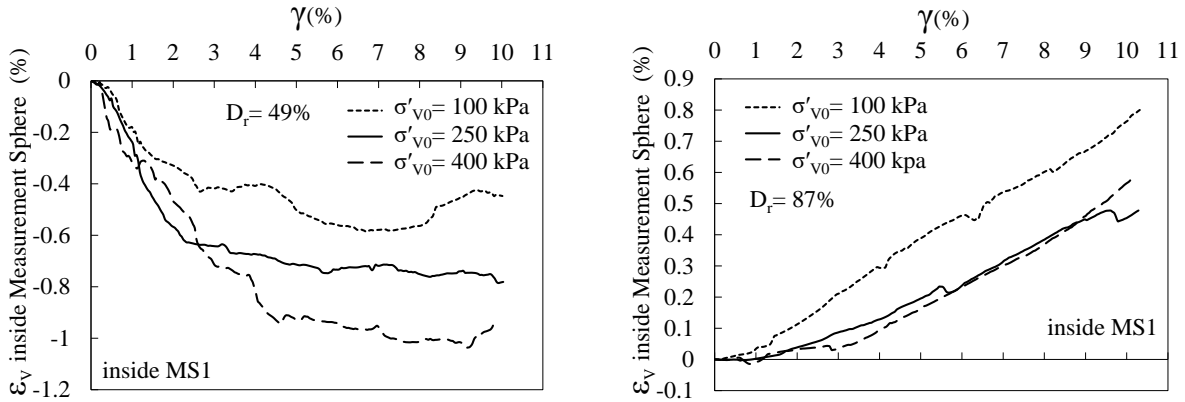
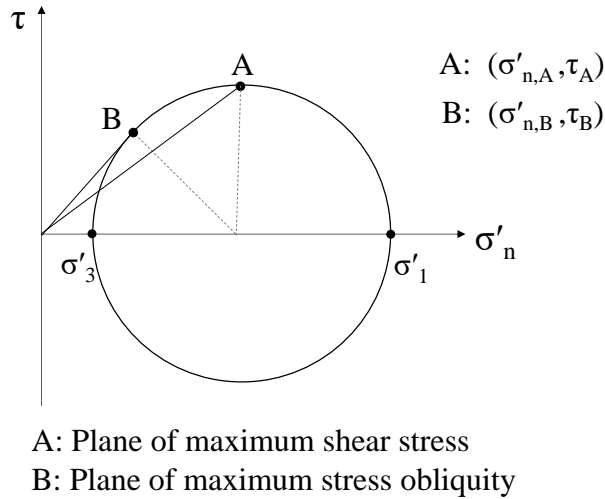


Figure 4.32 Volumetric strain inside the specimen core (MS1) in DEM simulations of constant volume monotonic simple shear response of Pea gravel specimen: $\epsilon_v < 0$ and $\epsilon_v > 0$ represents contraction and dilation, respectively.

According to Figure 4.33, mobilized friction angle can be related to the normal and shear stresses on planes of maximum shear stress and maximum stress obliquity. To assess if during shear, any of the vertical or horizontal planes is the plane of maximum shear stress or maximum shear obliquity, the following procedure is followed:



$$\varphi_{\text{mob}} = \sin^{-1}\left(\frac{\sigma'_1 - \sigma'_3}{\sigma'_1 + \sigma'_3}\right) = \sin^{-1}\left(\frac{\tau_A}{\sigma'_{n,A}}\right) = \tan^{-1}\left(\frac{\tau_B}{\sigma'_{n,B}}\right)$$

Figure 4.33 Stress Mohr circle and calculation of mobilized friction angle

If at any point during shear, the horizontal plane is the plane of maximum shear stress then the mobilized friction angle (ϕ_{mob}) will be equal to:

$$\alpha_{\text{MS1-h}} = \sin^{-1}\left(\frac{\tau_{zx}}{\sigma'_{zz}}\right) \quad (\text{Eq. 4.11})$$

in which, τ_{zx} and σ'_{zz} are the shear and normal stresses, respectively, on the horizontal plane inside MS1. The subscript “h” denotes the horizontal plane. If the horizontal plane is the plane of maximum stress obliquity at any point during shear, the mobilized friction angle will be equal to:

$$\beta_{\text{MS1-h}} = \tan^{-1}\left(\frac{\tau_{zx}}{\sigma'_{zz}}\right) \quad (\text{Eq. 4.12})$$

Similarly, in case of the vertical plane, the following angles are defined:

$$\alpha_{\text{MS1-v}} = \sin^{-1}\left(\frac{\tau_{xz}}{\sigma'_{xx}}\right) \quad (\text{Eq. 4.13})$$

$$\beta_{\text{MS1-v}} = \tan^{-1}\left(\frac{\tau_{xz}}{\sigma'_{xx}}\right) \quad (\text{Eq. 4.14})$$

in which, τ_{xz} and σ'_{xx} are the shear and normal stresses, respectively, on the vertical plane inside MS1. The subscript “v” denotes the vertical plane.

Figure 4.34 and Figure 4.35 show the evolution of mobilized friction angle and the defined angles in equations 4.11-4.14 for specimen of consolidated vertical stress of 250 kPa and relative density of 49% and 87%, respectively. For the case of $D_r=49\%$, it can be observed in Figure 4.34 that the horizontal plane is far from either the plane of maximum shear stress or the plane of maximum stress obliquity for about the first 3% of boundary shear strain. However, at boundary shear strains between 1-3%, the vertical plane is close to the plane of maximum stress obliquity. As shear proceeds, the horizontal and vertical planes gets close to the planes of maximum shear stress. It can be seen that at shear strains between about 5-10%, $\alpha_{\text{MS1-h}}$ and $\alpha_{\text{MS1-v}}$ are very close to ϕ_{mob} , which means that the horizontal and vertical planes are very close to the plane of maximum shear. For larger shear strains, $\alpha_{\text{MS1-h}}$ grows larger than ϕ_{mob} and if shear proceeds $\beta_{\text{MS1-h}}$ gets closer

to φ_{mob} , which means the horizontal plane is going toward the plane of maximum stress obliquity. For the case of $D_r=87\%$, in about 0.2% of boundary shear strain $\beta_{\text{MS1-V}}$ reaches φ_{mob} (i.e., the vertical plane reaches the plane of maximum obliquity). After that point, $\beta_{\text{MS1-V}}$ grows smaller than φ_{mob} while both $\alpha_{\text{MS1-h}}$ and $\alpha_{\text{MS1-V}}$ grow larger toward φ_{mob} , which means that the corresponding points of horizontal and vertical planes on the Mohr's circle rotates toward the point of peak shear stress. At boundary shear strain between about 2.5% to 8%, $\alpha_{\text{MS1-h}}$ and $\alpha_{\text{MS1-V}}$ are very close to φ_{mob} (i.e., closeness of the horizontal and vertical planes to the plane of maximum shear stress). As shear proceeds, $\alpha_{\text{MS1-h}}$ and $\alpha_{\text{MS1-V}}$ becomes, respectively, larger and smaller than φ_{mob} .

To assist in visualizing this evolution, the Mohr's circles in addition to the points of maximum shear stress and maximum stress obliquity and corresponding points to the horizontal and vertical planes are shown at discrete instances during shear for both specimens of $D_r=49\%$ and 87% in Appendix D. The path followed by the corresponding points to the planes of maximum shear stress, maximum stress obliquity, and the horizontal and vertical plane during shear are shown in addition to the initial stress Mohr's circles are shown in Figure 4.36 and Figure 4.37 for $D_r=49\%$ and 87%, respectively. It can be observed that the stress path for neither the horizontal plane nor the vertical plane is the same as the one for the plane of maximum shear stress or the plane of maximum stress obliquity for the whole period of shear. Therefore, it is not reasonable to make the same assumption on the state of stress at the vertical or horizontal planes regardless of the level of shear strain. The results of the discrete element simulations provided in this part also suggest that the level of density of the specimen can affect the level of shear strain at which each of the assumptions may be realistic and can be confidently used in interpretation of simple shear test data.

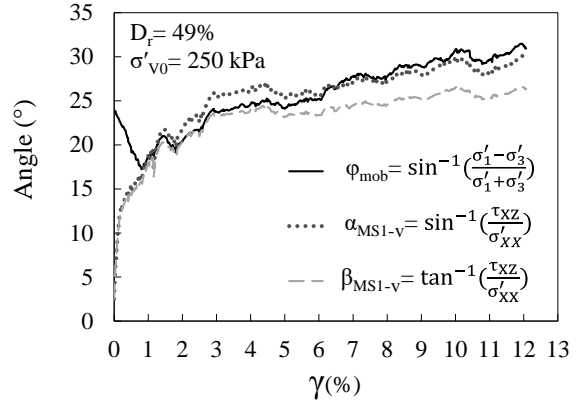
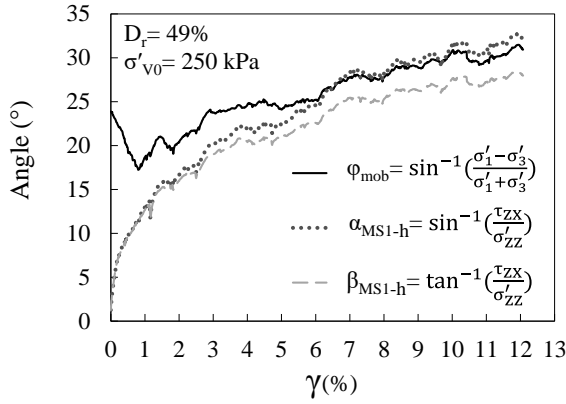


Figure 4.34 Evolution of ϕ_{mob} , α_{MS1-h} , β_{MS1-h} , α_{MS1-v} and β_{MS1-v} during shear in DEM simulations of constant volume monotonic simple shear response of Pea gravel specimen for specimen of $\sigma'_{v0}=250$ kPa and $D_r=49\%$

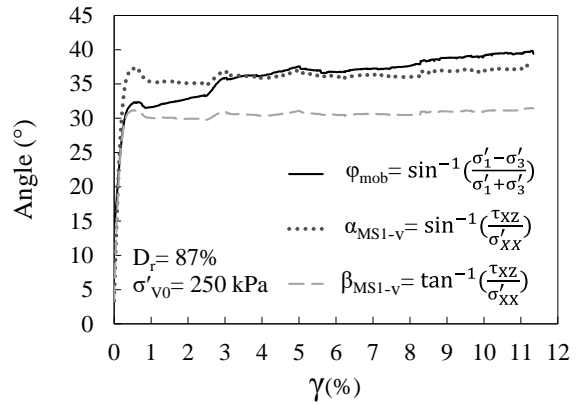
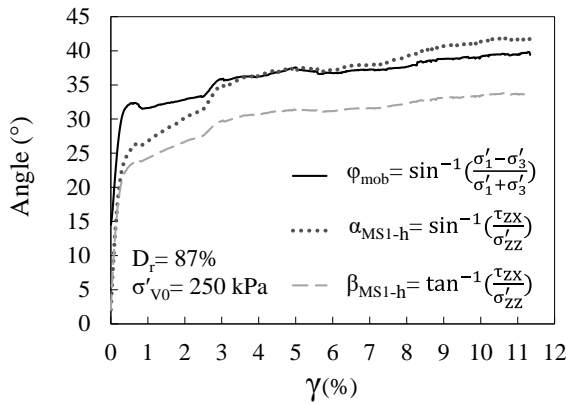


Figure 4.35 Evolution of ϕ_{mob} , α_{MS1-h} , β_{MS1-h} , α_{MS1-v} and β_{MS1-v} during shear in DEM simulations of constant volume monotonic simple shear response of Pea gravel specimen for specimen of $\sigma'_{v0}=250$ kPa and $D_r=87\%$

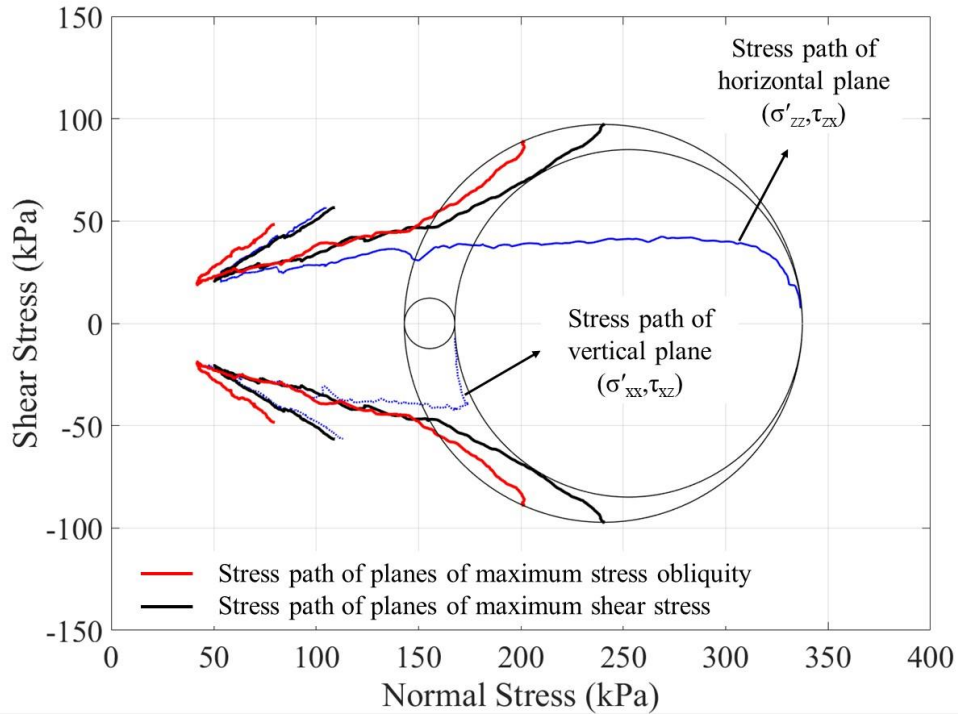


Figure 4.36 Mohr's circles of stress at the end of consolidation and the stress paths during shear in DEM simulations of constant volume monotonic simple shear response of Pea gravel specimen ($\sigma'_{v0}=250$ kPa, $D_r=49\%$)

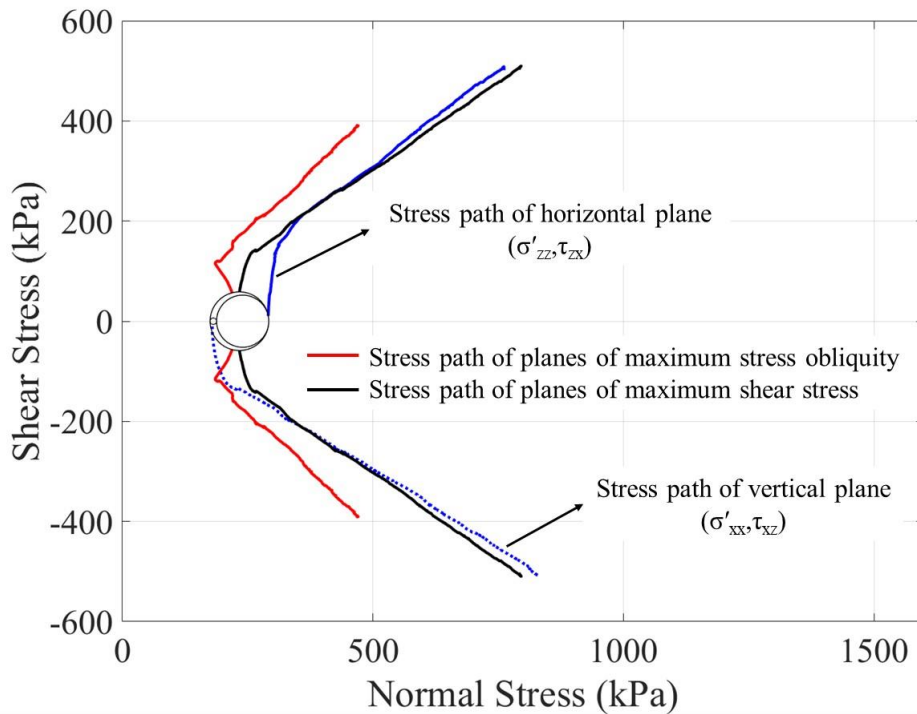


Figure 4.37 Mohr's circles of stress at the end of consolidation and the stress paths during shear in DEM simulations of constant volume monotonic simple shear response of Pea gravel specimen ($\sigma'_{v0}=250$ kPa, $D_r=87\%$)

4.8 Principal stress rotation during shear

The rotation of the direction of principal stress has been shown to take place in simple shear test (e.g., Roscoe et al., 1967; Roscoe, 1970; Oda and Konishi, 1974a). In this part, the rotation of the principal stress direction during constant volume simple shear test is evaluated in the simulated specimen consisting of spherical particles with the similar distribution of size and rolling resistance as the real Pea gravel particles.

For this purpose, the stress tensor inside the central measurement (MS1) is considered and the eigenvalues and eigenvectors are calculated for the value and direction of the principal stresses. The rotation of the principal stress during shear is shown in Figure 4.38 for all cases of consolidated vertical stress and relative density. In this figure, the angles between the direction of principal stress and three planes of XZ, XY, and YZ are shown. Plane XY is the horizontal plane parallel to the direction of shear, plane XZ and plane YZ are the vertical planes that are, respectively, parallel and perpendicular to the direction of shear. It should be mentioned that the acute angles between the major principal axis and these planes are reported in these graphs.

Because of the three dimensional granular specimen, the major principal stress axis does not necessarily lie on the XZ plane. It can be observed that the major principal axis is oriented at small angle regarding the XZ plane; however, it does not experience noticeable changes during shear. The orientation of the major principal axis regarding the YZ and XY planes changes significantly during shear. Because the acute angle between the major principal axis and YZ plane is complementary to the angle between this axis and XY plane, it can be seen that their changes occur accordingly during shear. Focusing on just the angle between the major principal axis of stress and vertical plane YZ, denoted as θ_{σ} , the evolution of this angle is shown in Figure 4.39 for all specimens. It is observed that regardless of the level of relative density and the consolidated

vertical stress, θ_σ increases from about zero at the beginning of the shear and reaches a plateau of about 45-50 degree at higher shear strains. Other interesting observation made is that this increase occurs more gradually in specimens of $D_r=49\%$.

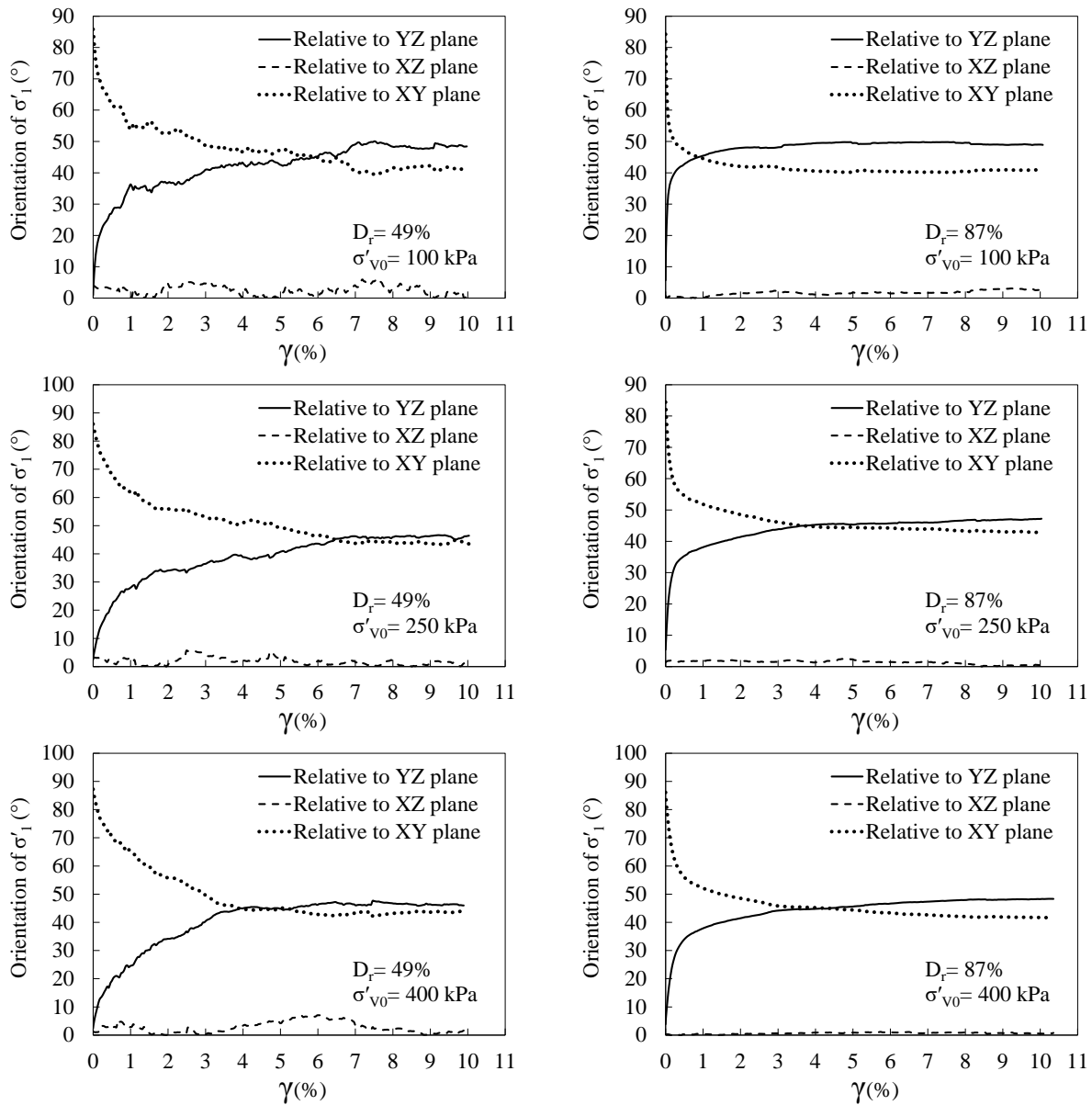


Figure 4.38 Angle between the direction of major principal stress and XZ, XY and YZ planes during shear in DEM simulations of constant volume monotonic simple shear response of Pea gravel specimen: $D_r=49\%$ (left), $D_r=87\%$ (right)

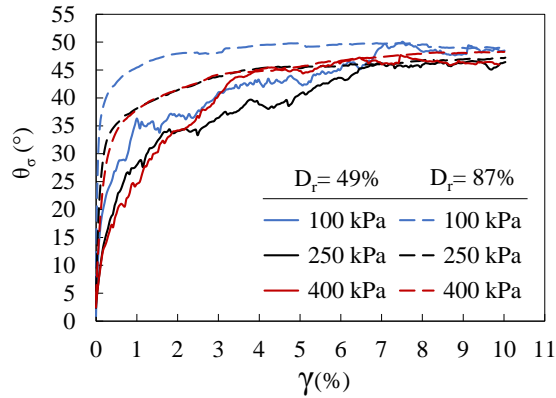


Figure 4.39 Evolution of angle θ_σ between the major principal stress axis and vertical plane YZ during shear in DEM simulations of constant volume monotonic simple shear response of Pea gravel specimen

4.9 Evolution of fabric during shear

Internal structure of granular materials has a significant role in their overall behavior. For example, it has been observed in both experimental studies and numerical simulations that granular soil behavior such as strength anisotropy, dilatancy and the level of non-coaxiality between the principal directions of stress and strain rate are influenced by fabric anisotropy (e.g., Miura et al., 1986; Gutierrez et al., 1991; Yoshimine et al., 1998; Yang et al., 2007; Yimsiri and Soga, 2011; Wang et al., 2017; Liu et al., 2019; Zheng et al., 2020). Therefore, to better understand the different aspects of granular soil behavior, it is of great importance to study the evolution of fabric, especially during simple shear loading condition that involves rotation of principal stress direction. In this section, fabric evolution is studied in constant volume simple shear condition using the DEM simulation of Pea gravel specimens.

To qualitatively demonstrate the fabric evolution, the contact force network (also known as force chain) for a simulation of a monotonic simple shear test analysis is shown in Figure 4.40 at different boundary shear strains for the specimen of $D_r=49\%$ and consolidated vertical stress of 250 kPa. Each line in this figure denotes the direction of inter-particle contact and its thickness indicates the relative magnitude of the contact force. It is observed that at the end of the

consolidation and before shearing starts ($\gamma=0\%$), the strong force chains shown by thicker lines are mostly aligned in the vertical direction. As shearing proceeds, the contact force network evolves and the strong force chains get inclined. Polar histograms in Figure 4.41 show the distribution of the orientations of contact normal in the specimen. Contact normal is the unit vector perpendicular to the plane of contact between two particles. In these histograms, only the strong contacts (those with magnitude of contact force one standard deviation above the average contact force) are considered. At $\gamma=0\%$, the majority of the contacts normal for strong contacts are oriented vertically. At higher shear strains, the predominant orientation of contacts normal deviates from vertical direction and gets more inclined by increasing shear strain.

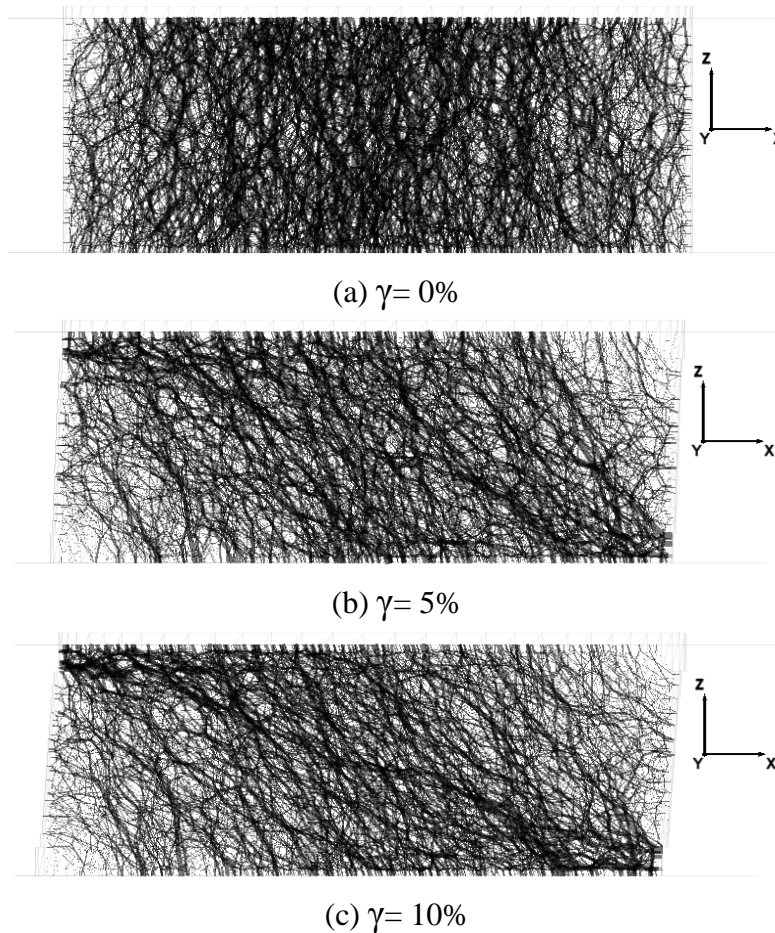


Figure 4.40 Contact force network (force chain) at different boundary shear strains in DEM simulation of constant volume monotonic simple shear response of Pea gravel specimen: $\sigma'_{v0}=250$ kPa and $D_r=49\%$

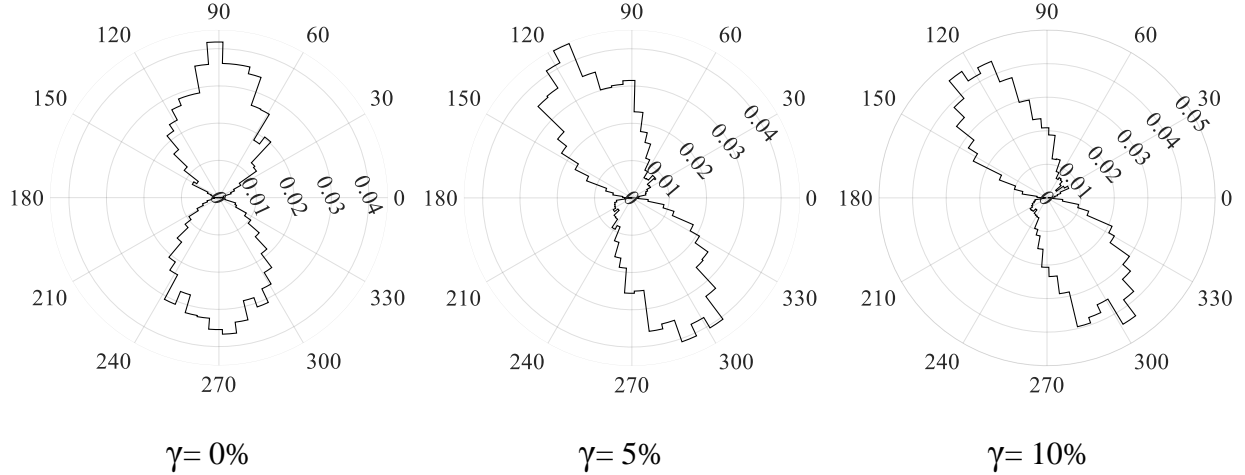


Figure 4.41 Polar histograms of contacts normal at different boundary shear strains in DEM simulation of constant volume monotonic simple shear response of Pea gravel specimen: $\sigma'_{v0}=250$ kPa and $D_r=49\%$

To quantitatively study the fabric evolution, the fabric tensor using the contact normal vector is calculated as (Satake, 1978):

$$\Phi_{ij} = \frac{1}{N_C} \sum_{k=1}^{N_C} n_i^k n_j^k \quad (\text{Eq. 4.15})$$

where N_C is the number of inter-particle contacts and n_i and n_j are the components of contact normal unit vector in i - and j -directions, respectively. All inter-particle contacts, regardless of their relative contact force, are considered here in calculating fabric tensor. The major principal direction of this tensor indicates the predominate orientation of inter-particle contacts. Figure 4.42 shows the orientation of the major principal fabric (θ_Φ) during. θ_Φ shown in this figure both for all the inter-particle contacts in the specimen (θ_Φ (the entire specimen)) and for those at the center of the specimen (θ_Φ (MS1)). The discrepancies between the orientation of major principal fabric considering all the inter-particle contacts and those inside MS1 can be attributed to the non-uniformities inside the specimen. The orientation of major principal stress (θ_σ) calculated at the center of specimen is also included in Figure 4.42. Comparing θ_σ to the corresponding θ_Φ inside MS1, it is observed that the major principal fabric direction rotates during shear to align with the direction of the major principal stress. The small differences between them is due to the fact that

in calculating the fabric tensor, all the inter-particle contacts (regardless of the relative force magnitude) are considered. As the majority of force is carried by the contacts in the strong force chains, they would be directed in the better alignment with the major principal stress direction.

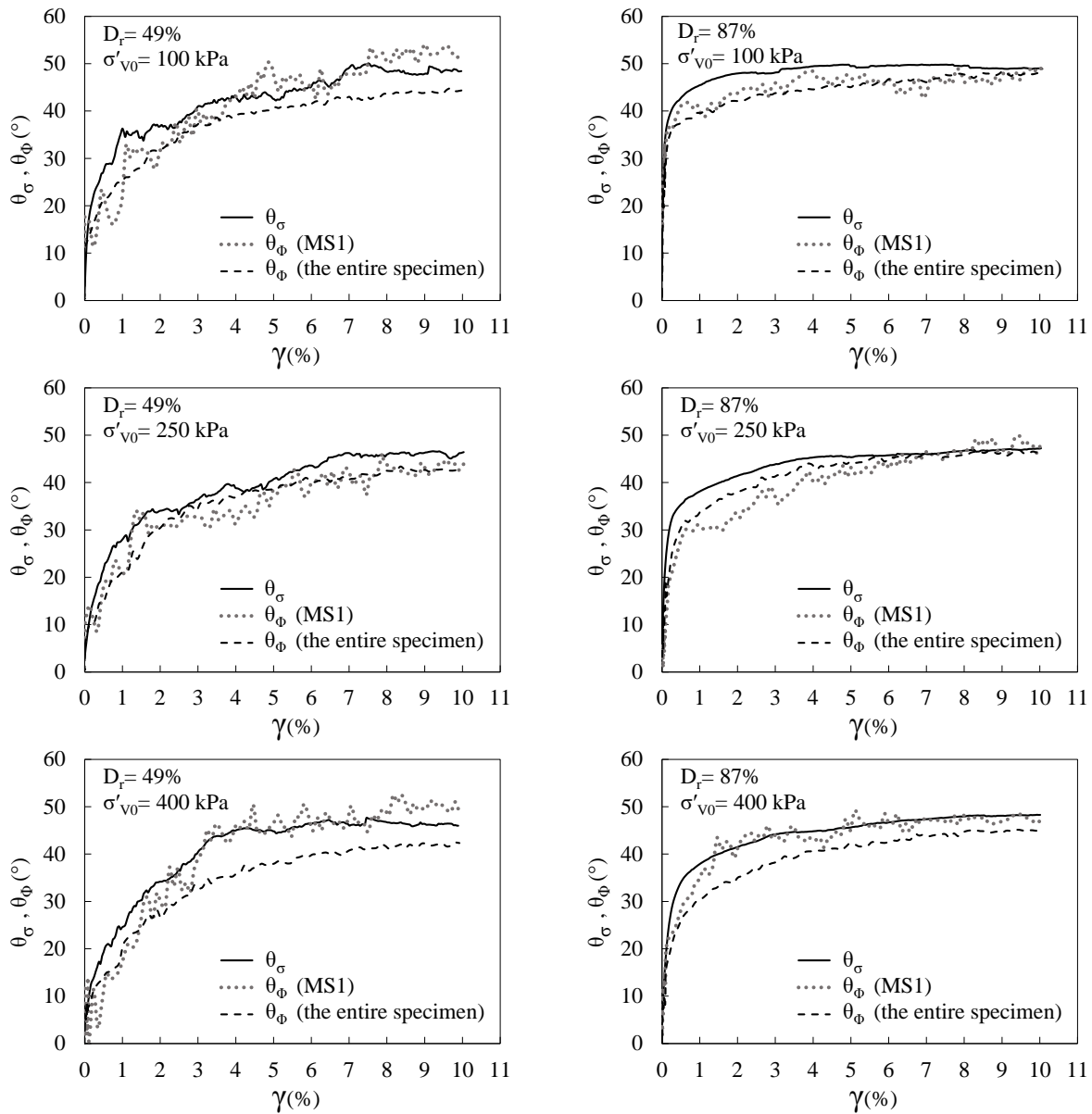


Figure 4.42 Orientation of major principal fabric (θ_ϕ) and stress (θ_σ) during shear in DEM simulations of constant volume monotonic simple shear response of Pea gravel specimen: $D_r=49\%$ (left), $D_r=87\%$ (right)

The degree of fabric anisotropy, in terms of contact normal orientations, is calculated as two definitions of $\Phi_1-\Phi_3$ (the difference between the major and minor principal values of fabric tensor (e.g., Thornton, 2000, Wang et al., 2017; Asadzadeh and Soroush, 2017) and Φ_1/Φ_3 (the ratio of major to minor principal values of fabric tensor (e.g., Maeda et al., 2006). It should be mentioned that fabric anisotropy is evaluated here by considering all the inter-particle contacts in the specimen. The fabric anisotropy at the end of the consolidation is summarized in Table 4.2 for all cases of relative density and consolidated vertical stress. A small degree of fabric anisotropy exists in all the specimens at the end of consolidation. Such fabric anisotropy can be attributed to the preferred orientation of contacts developing during deposition by gravity in specimen preparation (e.g., Yang et al., 2016) and also the one dimensional consolidation of the specimen before shearing. Wang et al. (2017) state that the fabric anisotropy generated during specimen preparation remains in the material even after isotropic consolidation. The data presented in Table 4.2 indicate that although the degree of fabric anisotropy at the end of consolidation is almost the same for all specimens, it is slightly smaller for the specimen of higher relative density, and for each level of relative density, it is slightly higher for larger consolidated vertical stress.

Table 4.2 degree of fabric anisotropy, in terms of contact normal orientations, at the end of consolidation in DEM simulations of Pea gravel specimen

	$\Phi_1-\Phi_3$		Φ_1/Φ_3	
	$D_r=49\%$	$D_r=87\%$	$D_r=49\%$	$D_r=87\%$
$\sigma'_{v0}=100$ kPa	0.023	0.012	1.07	1.04
$\sigma'_{v0}=250$ kPa	0.028	0.017	1.09	1.05
$\sigma'_{v0}=400$ kPa	0.032	0.02	1.1	1.06

The evolution of fabric anisotropy, in terms of contact normal orientations, during shear is shown in Figure 4.43. For all cases of consolidated vertical stress and relative density, the

degree of fabric anisotropy increases as shear strain increases. It is observed that consolidated vertical stress has no significant effect on the evolution of the fabric anisotropy in the simulated specimen. However, fabric anisotropy increases at a higher rate in specimen of higher relative density. At the boundary shear strain of 10%, the degree of fabric anisotropy calculated as $\Phi_1-\Phi_3$ and Φ_1/Φ_3 is, on average, 35% and 10% higher for specimen of $D_r=87\%$ comparing to those of $D_r=49\%$.

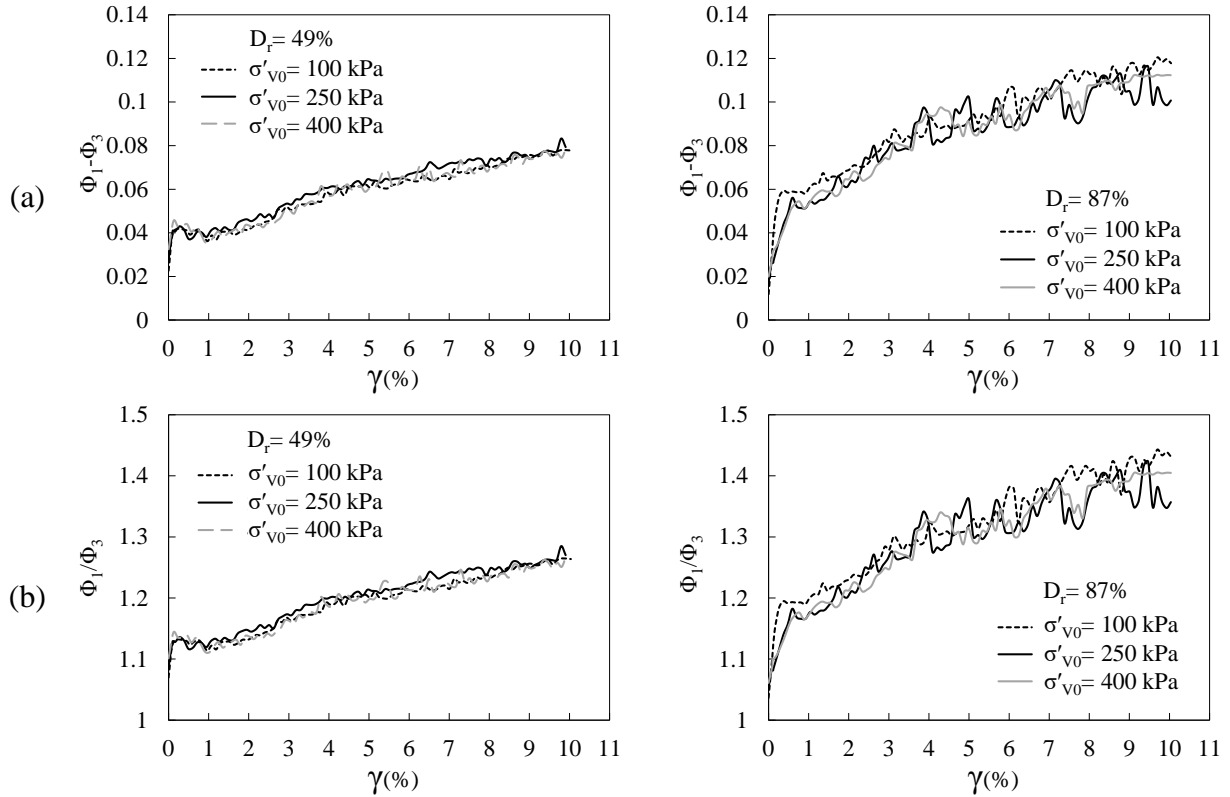


Figure 4.43 Evolution of degree of fabric anisotropy, in terms of contact normal orientations, during shear in DEM simulations of constant volume monotonic simple shear response of Pea gravel specimen: (a) $\Phi_1-\Phi_3$, (b) Φ_1/Φ_3

The evolution of internal structure or fabric can also be evaluated by monitoring the changes in the coordination number during shear. Coordination number (Z) is defined as the average number of contacts per particle as is computed as:

$$Z = \frac{2N_c}{N_p} \quad (\text{Eq. 4.16})$$

in which N_P and N_C are number of particles and contacts, respectively. This parameter is the most basic micro-scale measurement of the granular material structure. At the end consolidation, the value of Z measured inside the central measurement sphere (MS1) is 4.5 and 5.5 for specimens of $D_r=49\%$ and 87% , respectively. These values are in the range of the reported values in literature for coordination number of irregularly packed spheres. For example, in the isotopically compressed specimens of low to high densities from the DEM simulations of Barreto Gonzalez (2009), coordination number ranges from about 4.3 to 6.2.

As expected, the value of Z , which gives a measure of packing density and contact intensity at the particle scale, is higher for the more densely packed specimens in the current study. The variation of normalized coordination number to the value at the end of consolidation (Z/Z_0) during shear is shown in Figure 4.44. For comparison purposes, the changes of normalized void ratio to the consolidated value inside MS1 is also included in this figure. For specimens of $D_r=49\%$, after an initial drop in coordination number in the first 0.5% of shear strain, it keeps increasing as void ratio inside MS1 decreases during shear. At shear strain 10%, Z/Z_0 reaches to about 0.9. In case of $D_r=87\%$, coordination number decreases during shear while the void ratio increases inside MS1, and Z/Z_0 reaches to about 0.75 at shear strain of 10%. Overall, coordination number experiences more changes during shear in specimens of higher relative density. This observation is consistent with the higher level of changes in internal structure for denser specimen that is shown in terms of degree of induced anisotropy in Figure 4.43.

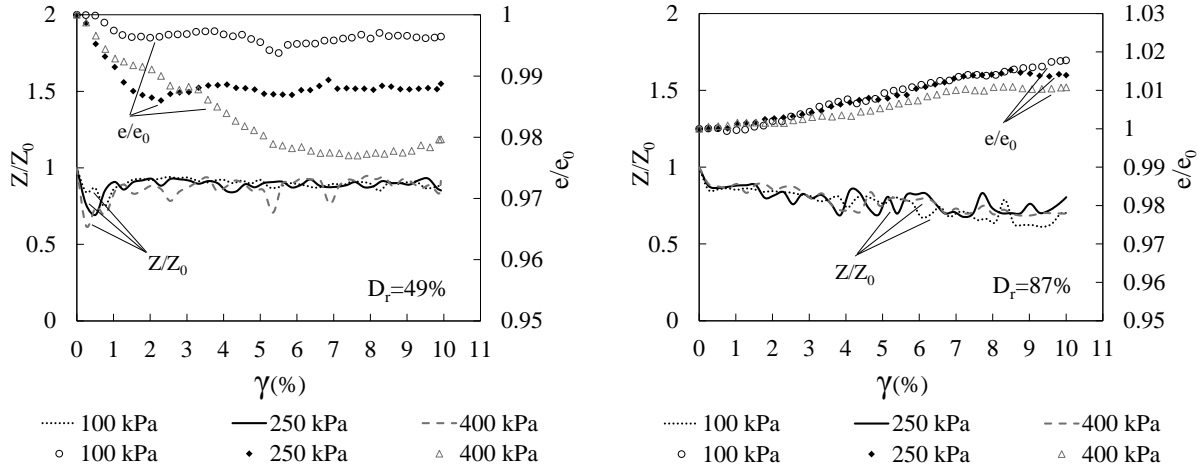


Figure 4.44 Evolution of normalized coordination number and normalized void ratio inside the central measurement sphere in DEM simulations of constant volume monotonic simple shear response of Pea gravel specimen: $D_r=49\%$ (Left), $D_r=87\%$ (Right)

4.10 Non-coaxiality of principal stress and strain increment

It has been observed in both experimental studies and numerical simulations that in granular soils during simple shear loading, the direction of the principal plastic strain increment does not follow the rotation of principal stress direction (e.g., Roscoe et al. 1967; Drescher and De Josselin De Jong 1972; Oda and Konishi 1974; Gutierrez et al. 1991; Cai et al. 2013; Ai et al. 2014; Yu et al. 2016). In this study, non-coaxiality of principal directions of stress and strain increment is evaluated for the equivalent DEM simulated specimen of Pea gravel in constant volume simple shear condition. This will provide valuable information about the non-coaxiality in simple shear response of granular soils that can help in developing more rigorous constitutive models for soil response.

For this purpose, the orientations of major principal stress (θ_σ) and strain rate (θ_ε) are monitored inside the central measurement sphere (MS1) during shear. It should be mentioned that the total strain rates are considered here. It is while in plasticity theories, the plastic component of strain rate is referred to for non-coaxiality. According to Gutierrez et al. (1991), in flow of sand

during a set of hollow cylindrical torsional tests, there is a slight difference between the total and plastic strain increment vectors at low level of shear stress, which becomes even smaller as shear stresses increases. This justifies the use of total shear strain instead of the plastic component to evaluate the non-coaxiality in this study. The same approach has been followed by other researchers such as Thornton and Zhang (2006), Qian et al. (2011), Langston et al. (2013), Ai et al. (2014) and Qian et al. (2017) among others.

Figure 4.45 shows the comparison between the orientations of major principal stress (θ_σ) and strain rate ($\theta_\dot{\epsilon}$) during shear for all cases of consolidated vertical stress and relative density. The $\theta_\dot{\epsilon}$ values reported in this figure are obtained based on the strain rate tensor measured both at the boundaries and also internally inside MS1. For the simulated specimens that are laterally constrained by stacked cylindrical walls (equivalent to the rings in the laboratory specimen) and are sheared under overall constant volume condition, the normal strain rates in horizontal and vertical directions at boundaries are zero ($\dot{\epsilon}_h = \dot{\epsilon}_v = 0$) and they are only deformed by a constant rate of shear strain ($\dot{\gamma} \neq 0$). Therefore, $\theta_\dot{\epsilon}$ measured at the boundaries is equal to 45 degree during shear. The strain rate tensor inside the specimen at location of MS1 is calculated based on the particles velocity field using least square fitting (Itasca Consulting Group Inc., 2014) as explained in Chapter 2. Fluctuations observed in the major principal strain rate direction are attributed to the local rearrangement of the particles while the whole specimen is deforming. The dissimilarity between $\theta_\dot{\epsilon}$ measured at boundaries and inside the specimen is due to the non-uniformities inside the specimen and the localized slidings that occur at the interface between specimen and horizontal boundaries. It should also be noted that although the normal strain rates in horizontal and vertical directions at boundaries are zero, the corresponding local strain rates ($\dot{\epsilon}_{xx}$ and $\dot{\epsilon}_{zz}$) inside MS1 may be non-zero during shear. Overall, significant difference between θ_σ and $\theta_\dot{\epsilon}$ is observed at

early stages of shear for all cases. As shearing continues and the principal stress direction rotates, the difference between the principal directions of stress and strain rate reduces until θ_σ grows a few degree larger than θ_ε and the difference remains about the same at higher levels of shear strain. This evolution occurs more quickly for specimen with higher relative density of 87%. It should be mentioned that these observation are only for up to 10% boundary shear strain at which the simulated specimens have not reach the critical state; therefore, coaxiality of θ_σ and θ_ε at critical state cannot be examined here.

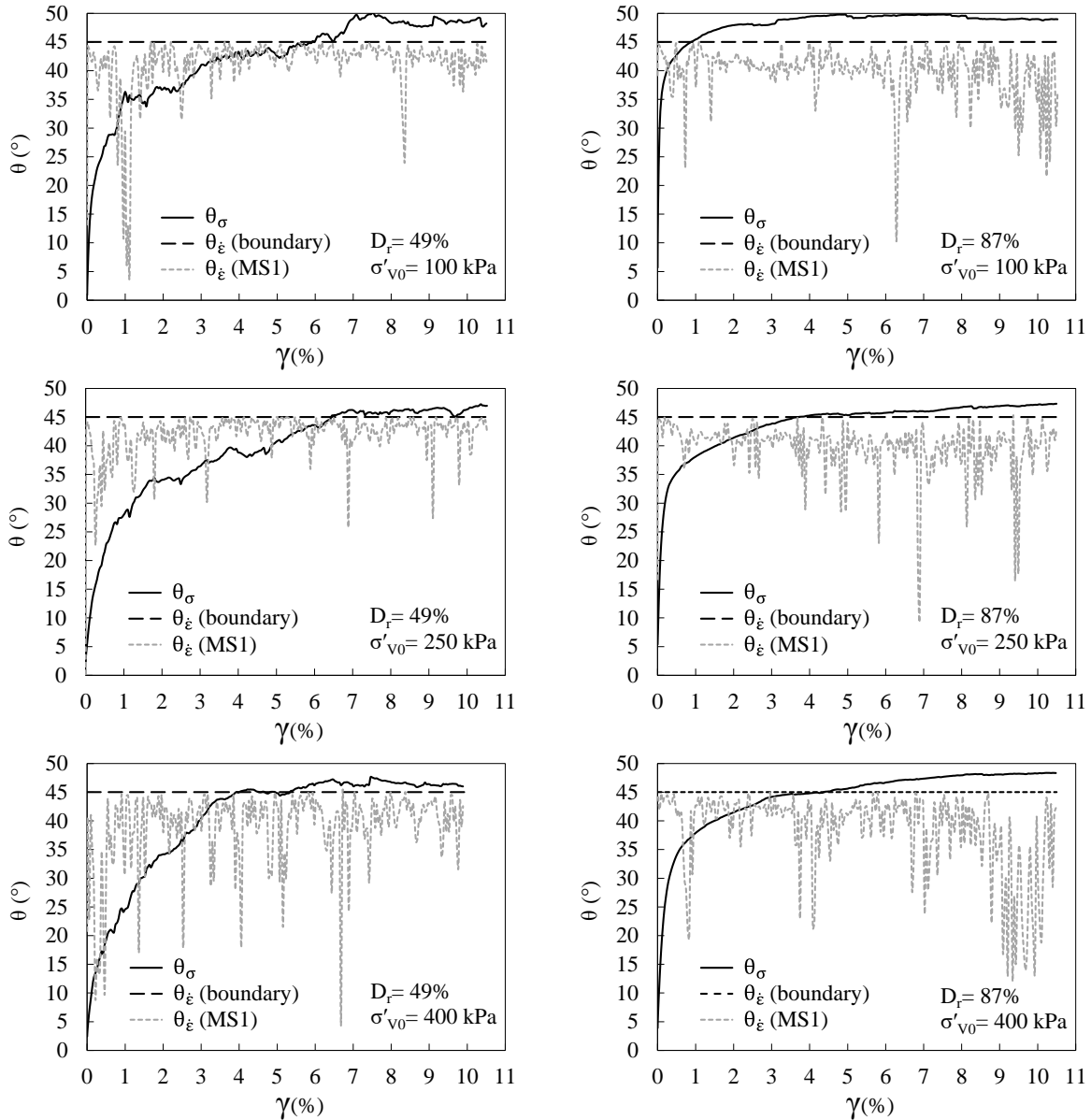


Figure 4.45 Evolution of directions of major principal stress and strain rates during shear in DEM simulations of constant volume monotonic simple shear response of Pea gravel specimen: $D_r=49\%$ (left), $D_r=87\%$ (right)

4.11 Effect of the non-uniform distribution of rolling resistance

To incorporate the effect of irregularity of particle shape in simulation of Pea gravel particles in this study, rolling resistance is added to the equivalent spherical particles. Moreover, to account for the non-uniformity of particle shapes and achieve a better representation of the real

soil assembly, a distribution of rolling resistance coefficients (estimated from the distribution of particle sphericity in the actual specimen) is considered in the simulations.

To demonstrate the necessity of considering the non-uniformity of shape particles in the simulations, the macroscopic results of simulations are compared for cases of uniform versus non-uniform distribution of rolling resistance in specimen of $\sigma'_{v0}=250$ kPa and $D_r=49\%$. For this purpose, the following procedure is followed:

Considering the same consolidated specimen with the non-uniform distribution of rolling resistance coefficients (μ_r), the uniform value of μ_r that results in the similar shear behavior is first found. All the other parameters are kept the same. Based on the probability distribution of μ_r values in the specimen shown in Figure 4.46, $\mu_r=0.105$ (which is the predominant value of rolling resistance) is assigned to all the particles during shear. As shown in Figure 4.47, it results in higher peak shear stress, less amount of strain softening, and smaller amount of pore pressure generated during shear. Overall, uniform value of $\mu_r=0.105$ generates a stronger response. However, no significant changes are observed in the stress ratio (τ/σ'_v) and the coefficient of lateral pressure. According to these observations, a smaller value of $\mu_r=0.09$ is then assigned to the spherical particles during shear. 17% and 20% of total particles in the specimen by number and volume, respectively, have rolling resistances value smaller than 0.09 (Figure 4.6). This smaller value of uniform rolling resistance coefficient during shear results in a very close simple shear response to the one with distributed value of rolling resistance. It should be mentioned again that the specimen at the beginning of the shear is the one simulated by considering a distribution of rolling resistance for the particles. It is important to investigate whether assigning this uniform value of rolling resistance to particles during all the stages of simulation, still results in the same response as the one with distributed values of rolling resistance.

Figure 4.48 shows the comparison of the response for two specimens with distributed value of rolling resistance and uniform value of $\mu_r=0.09$ through all stages of simulation. All the other parameters are the same for both specimens. Although they end up having a similar void ratio at the end of consolidation (0.675 and 0.674, respectively), they show different responses during shear. The specimen with uniform value of $\mu_r=0.09$ has a higher peak shear stress and experiences less amount of strain softening. Moreover, less positive pore pressure is generated during shear in this specimen. The stress ratio (τ/σ'_v) and the coefficient of lateral pressure does not differ noticeably between these specimens. These differences between the shear responses can be attributed to the differences in the internal structure of the specimen at the beginning of the shear. Although both specimens have the same void ratio, the different distributions of rolling resistance coefficient in them results in difference distribution of voids and contacts, which is responsible for the differences in the macroscopic response of these specimens. Further investigation at the micro scale is required to quantitatively support this claim.

The observations made in this part indicate that the internal structure of the specimen at the beginning of the shear plays a pivotal role in the subsequent behavior during shear. As the shapes of the particles, along with other properties such as particle size and roughness, affects the arrangement of particles in an assembly, it is crucial to acknowledge the non-uniformity of particle shapes and account for that in simulations. By considering a uniform value of rolling resistance for all particles, it may be still possible to obtain the close response to experiments by adjusting other material and contact parameters. However, it is as if all the real particles are assumed to have the same shape and the non-uniformity that exists in the actual soil assembly is ignored. Considering a non-uniform distribution of rolling resistance, obtained by shape characteristics of

particles, results in a more realistic representation of soil assembly and provide more reliable prediction of the micro- and macroscopic behavior of actual soil specimen.

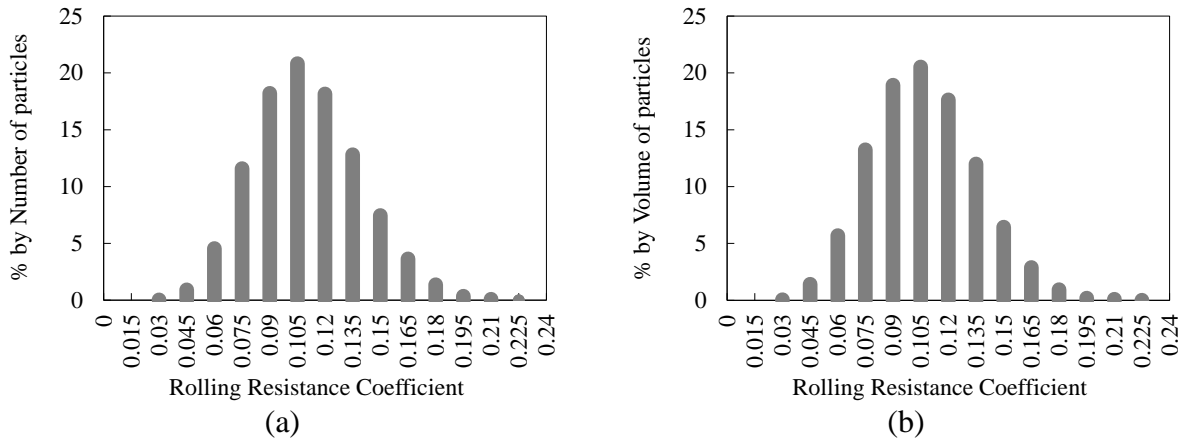


Figure 4.46 Probability distribution of rolling resistance coefficient by: (a) number of particles and (b) volume of particles in DEM simulations of Pea gravel specimen using spherical particles

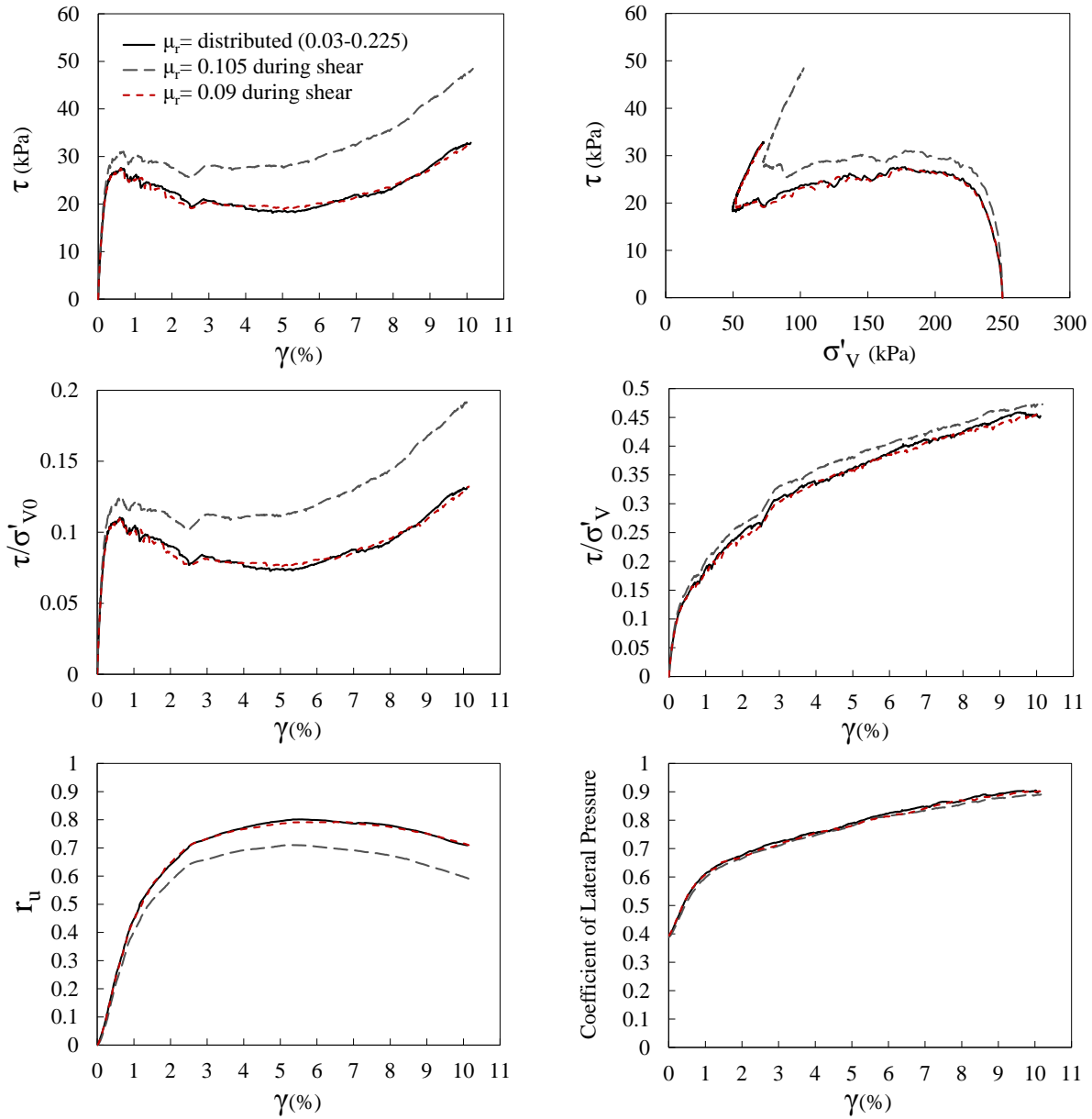


Figure 4.47 Comparison of the results from DEM simulations of constant volume monotonic simple shear response of Pea gravel specimen for the cases of distributed versus uniform rolling resistance coefficient only during shear stage ($\sigma'_{v0}=250$ kPa and $D_r=49\%$)

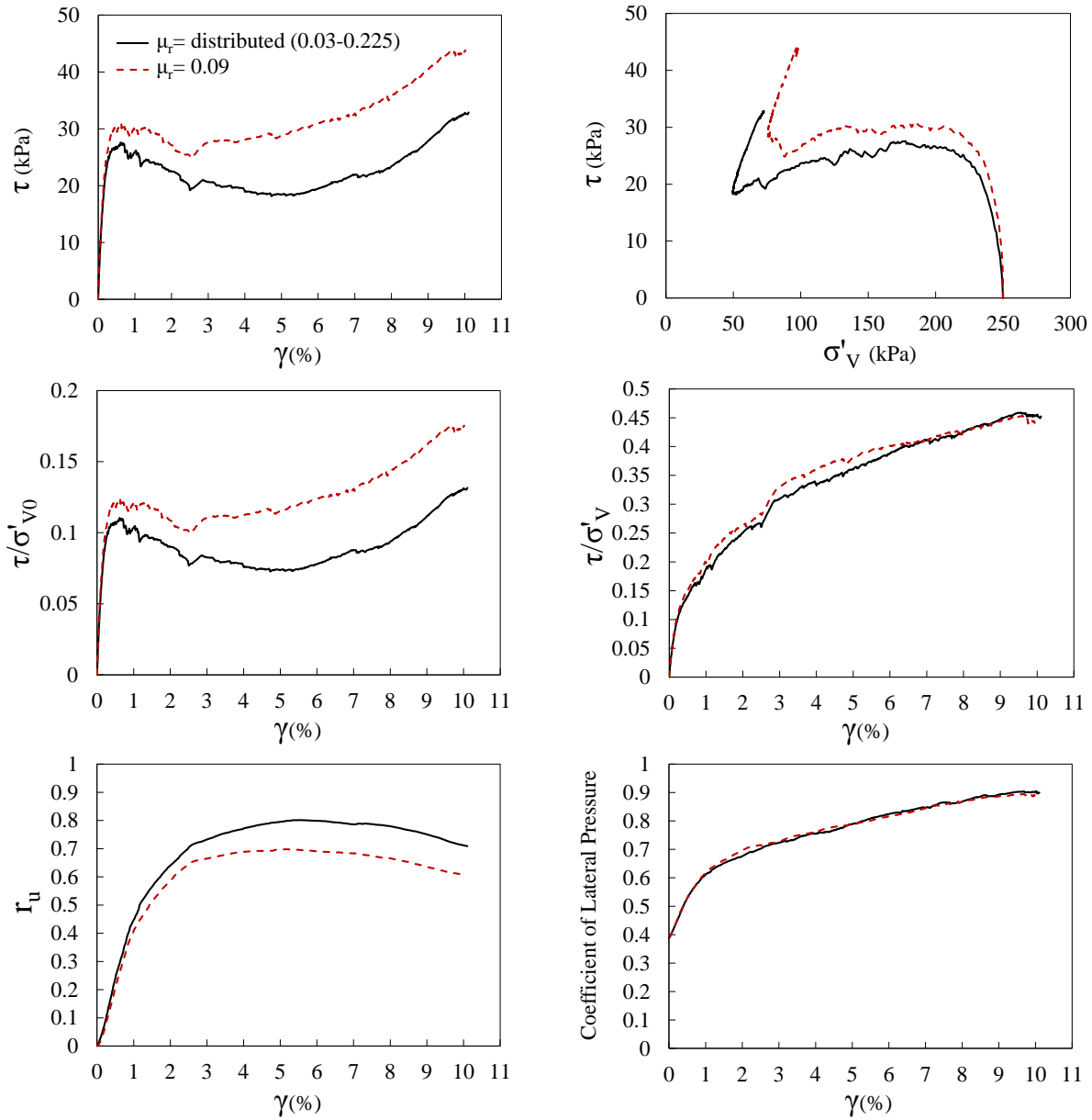


Figure 4.48 Comparison of the results from DEM simulations of constant volume monotonic simple shear response of Pea gravel specimen for the cases of distributed versus uniform rolling resistance coefficient during all simulation stages ($\sigma'_{v0}=250$ kPa and $D_r=49\%$)

4.12 Conclusions

The monotonic constant volume simple shear response of Pea gravel in stacked ring simple shear test was investigated in this chapter using the discrete element method and by simulating a

realistic representation of soil particles in terms of total number, size, and rolling resistance distribution. A summary of observations and conclusions is presented as follows:

- The discrete element model of the actual soil specimen developed and calibrated by corresponding experimental specimen in this study is capable of providing a satisfactory prediction of the macroscopic behavior of the actual specimen at different levels of relative density and consolidated vertical stress (Figure 4.8 to Figure 4.10).
- Evaluating the stress state at the specimen core, it is concluded that the planes of maximum shear stress and maximum stress obliquity continuously rotates during shear and at different points during shear, they may coincide with the horizontal or vertical planes. It is also observed that coincidence of the planes of maximum shear stress and maximum stress obliquity with either the horizontal or vertical planes does not necessarily happen at the same level of shear strain in specimens of difference relative density.
- Rotation of principal stress direction during shear is observed for all the cases of relative density and consolidated vertical stress. The angle between the major principal stress axis and the vertical plane YZ (θ_σ) increases during shear and reaches a plateau of about 45-50 degree at higher shear strains. It is also observed that the rotation of principal stress direction occurs more gradually in specimens of $D_r=49\%$.
- Non-coaxiality of principal directions of stress and strain rate is evaluated up to 10% boundary shear strain by comparing the orientation of the major principal stress (θ_σ) and strain rate ($\theta_{\dot{\epsilon}}$) inside the central measurement sphere (MS1). Significant difference of about 45° between θ_σ and $\theta_{\dot{\epsilon}}$ at the beginning of the shear gradually decreases as shear proceeds and principal direction of stress rotates until at higher shear strains, θ_σ grows slightly larger than $\theta_{\dot{\epsilon}}$ (the difference is about 5° at the most).

- The internal structure of the specimen is observed to change during shear. Considering the contact normal network inside the specimen, the predominant orientation of contact normal rotates during shear to get aligned with the major principal stress direction. The fabric anisotropy, in terms of contact normal orientations, is also increases during shear. The stress-induced fabric anisotropy increases at a higher rate for specimen of larger relative density of 87%.
- Incorporating both the irregularity and non-uniformity of particles shape by assigning a distribution of rolling resistance to the equivalent spherical particles is observed to be essential in simulating the actual soil particles. Having the same material and contact parameters except uniform versus distributed values of rolling resistance coefficients, the specimens prepared and consolidated at the same vertical stress and relative density shows difference shear responses. This observation is in consistency with the fact that internal structure or fabric of the granular material plays a key role in their response to loading. Considering a distribution of rolling resistance coefficients determined from particles shape characteristics accounts for the diversity of particle shapes in soil and provides a more realistic representation of soil assembly for the numerical simulation. The results of such simulation at micro- and micro-scales are more reliable in predicting the behavior of actual soil specimen.
- Comparing the results of stress measurements at the specimen boundaries and inside the specimen core, it was observed that there are quantitative differences between the soil specimen response measured at the boundaries and specimen core. More specifically:
 - For all cases of consolidated vertical stress and relative density, the measurements at boundaries showed lower peak shear stress (τ_p) and stress ratio τ/σ'_v than those

- measured inside the specimen core (The same comparison between the measured stress ratio at horizontal boundaries and specimen center is observed by Budhu (1979) in constant load simple shear test on Leighton Buzzard Sand). The boundary measured peak shear stress underestimated the peak shear stress at the specimen core by an average of 33%. The stress ratio measured at the boundary underestimated the stress ratio at specimen core by an average of 13%. The rate of strain hardening during shear is observed to be similar for measurements at boundaries and inside the specimen. For specimens of $D_r=49\%$, the rate of strain softening is lower for measurements at the boundaries compared to those measured at the central region of the specimen.
- The calculated pore pressure ratio (r_u) considering the changes in vertical stresses on the horizontal boundary of the specimen show more positive values than the true pore pressure ratio calculated based on the changes in mean effective stress (p') at the specimen core. For specimens of $D_r=49\%$, the calculated pore pressure ratio based on the boundary measured vertical stresses is by average 20% higher than the true pore pressure ratio at the specimen core for most of the shear (during the first 0.3% shear strain, it is higher up to even 100%). In case of $D_r=87\%$ and up to 3-4% shear strain, the calculated pore pressure ratio based on the boundary measured vertical stresses is 80-100% more positive than the true pore pressure ratio at the specimen core. For shear strains higher than about 5%, it is 25-50% higher than the true pore pressure ratio at the specimen core.
 - Overall, the simulation results indicated that the boundary measurements in constant volume simple shear test in the lab provides a conservative estimate of the soil strength and generated pore pressure at the specimen core.

- For all cases relative density and consolidated vertical stress, the coefficient of lateral pressure parallel to the direction of shearing is larger than the one in the perpendicular direction. The difference between them is larger for the higher relative density. The average value of K_x/K_y at the end of consolidation is 1.14 and 1.02 for specimens of $D_r=49\%$ and 87% , respectively. As shearing proceeds, the difference between K_x and K_y increases and at the shear strain of about 10%, the average value for K_x/K_y reaches to 1.23 and 1.48 for specimens of $D_r=49\%$ and 87% , respectively.
- Coefficient of lateral pressure determined as average value at the boundaries is mostly close to the one perpendicular to the direction of shear (k_y) measured at the specimen center for $D_r=49\%$ and is mostly close to the K_{avg} measured inside the specimen center for $D_r=87\%$. For none of the cases, the average value calculated at boundaries estimates coefficient of lateral pressure parallel to the direction of shear. Budhu (1985) also observes such dissimilarity in simple shear tests on both dense and loose Leighton Buzzard sand at constant vertical load using NGI-type wire-reinforced circular simple shear device.
- Assessing the non-uniformity of different quantities measured inside measurement spheres MS1-MS13 located across the cross sectional area and covering about the middle two third of the specimen height, the following observations are made:
 - Non-uniformities are observed in distribution of void ratio inside the specimen at the end of consolidation. Although there are differences in the evolution of void ratio inside various regions of the specimen and redistribution of void ratio is evident, the level of non-uniformity remains about the same during shear. The redistribution of the void ratio in the specimen implies that the pore spaces changes during shear. Therefore, in

- presence of pore water, there would local migration of water through the pore spaces as a result of the pore pressure redistribution that takes place by the redistribution of voids in the specimen.
- The non-uniformity parameter for distribution of vertical effective stress (σ'_{zz}) starts from a value of 20-50% at the end of consolidation and reaches to about 30% at boundary shear strain of 10% for specimens of $Dr=49\%$. This value starts from about 20-25% and reaches to about 30% % at boundary shear strain of 10% for specimens of $Dr=87\%$.
 - Comparing the vertical effective stress (σ'_v) measured at boundaries to the range of vertical effective stress (σ'_{zz}) inside the specimen, it is observed that for all cases, the boundary measured effective vertical stress is between the minimum and average measured values inside the specimen at the end of consolidation. Boundary measured vertical effective stress (as in laboratory) underestimates the actual consolidated vertical effective stress at locations inside the specimen by maximum of 18-26% for looser specimens and by maximum of 14-19% for denser specimens. No specific effect is observed of the level of applied vertical stress. As shear proceeds, this value becomes closer to the lower end of the range of the σ'_{zz} measured inside the specimen. At the shear strain of about 10%, the boundary measured value underestimates the actual vertical effective stress inside the specimen by the maximum of 23-26% in denser specimen (which is higher than that at the beginning of shear). However, the level of underestimation in looser specimen remains about the same.
 - The non-uniformity parameter values calculated as equation 4.10 are very high for the distribution of the induced shear stress (τ_{xz}) inside the specimen at the end of

- consolidation. It is because of the relatively wide range of shear stress and corresponding small average values at this point. In all cases, the non-uniformity parameter experiences a very sharp drop over less than 0.1% of shear strain at the beginning of shearing. For the specimens of $D_r = 49\%$, the non-uniformity parameter decreases to about 25% at shear strain level of 1-3% and reaches to about 40-50% at shear strain of 10%. For the case of $D_r = 87\%$, the non-uniformity parameter decreases to 35-45% at shear strain level of 4-5% and reaches to 50-60% at shear strain of 10%.
- Comparing the boundary measured shear stress (τ_h) to the range of the shear stresses (τ_{xz}) inside the specimen, it is observed that the boundary measured shear stress is between the minimum and average values of shear stress measured inside the specimen for all cases. However, for most of the shearing stage, this value is closer to the minimum value measured inside the specimens of $D_r = 87\%$.
 - Similar to the non-uniformity parameter for distribution of τ_{xz} inside the specimen, this value for distribution of stress ratio (τ_{xz}/σ'_{zz}) shows a sharp drop at the first 0.1% of shear strain. The rate of decrease becomes more gradual after that point and after the shear strain of about 1.5%, the non-uniformity parameter reaches a value of 20-40% for all cases and remains about the same for the rest of shearing.
 - The boundary measured stress ratio (τ_h/σ'_v) is observed to be between the minimum and average internal stress ratio values, approaching the average value at higher shear strains. Overall, determining the stress ratio based on the measurement of shear and vertical stresses on the horizontal boundaries, as is done in laboratory, leads to overestimation of the actual stress ratio at some locations inside the specimen. At shear

- strain of about 10%, the boundary measured stress ratio overestimate the minimum local stress ratio inside the specimen by an average of 20%.
- The non-uniformity parameter for distribution of pore pressure ratio (r_u) calculated based on the changes in the mean effective stress (p') inside the specimen starts from zero at the end of consolidation and shows a sharp peak during the first 0.3% of shear strain. This observed sharp peak can be associated to the very small average value and relatively larger range of measured r_u values at the beginning of the shear, which lead high value of non-uniformity parameter according to equation 4.10. For the rest of the shear, the non-uniformity parameter decreases to about 10-30% for specimens $D_r=49\%$ and to 25-60% for specimens of $D_r=87\%$. This change in non-uniformity parameter is more gradual for the case of $D_r=87\%$.
 - Such non-uniform distribution of generated pore pressure inside the specimen implies that in presence of pore water in saturated specimen, there would be local migration of pore water through voids from locations of higher to lower pore pressure.
 - The non-uniformity parameter for distribution of shear strain (γ_{xz}) experiences a sharp increase from zero at the beginning of the shear for all the cases of relative density and consolidated vertical stress. After the boundary shear strain of about 1%, the non-uniformity parameter gradually decreases and at boundary shear strain of 10%, it reaches to about 20-30% for specimens of $D_r=49\%$ and to about 30-40% for those of $D_r=87\%$.
 - For all cases of consolidated vertical stress and relative density, the shear strain calculated inside the measurement spheres at the mid-height of the specimen is smaller than the boundary shear strain. It can be concluded that the boundary measured shear

strain (as done in laboratory) overestimate the induced shear strain inside the specimen, and this difference needs to be accounted for in interpretation of the experimental results. According to the simulation results, for boundary shear strains of smaller than about 0.05%, the boundary measured shear strain is by average 2.7 and 4 times larger than the average shear strain inside the specimen for specimens of $D_r=49\%$ and 87% , respectively. For the rest of the shearing, this difference between the boundary and internally measured shear strain decreases and the boundary measured shear strain is by average 1.3 and 1.7 times larger than the average shear strain inside the specimen for specimens of $D_r=49\%$ and 87% , respectively.

Chapter 5

DEM Modeling of the Cyclic Simple Shear Response of Pea Gravel

5.1 Introduction

In continuation with investigating the simple shear response of gravelly soils in this study, this chapter focuses on investigating the cyclic constant volume simple shear response of Pea gravel through discrete element simulation. The undrained shear response and in particular the liquefaction of gravelly soils has not been investigated as extensively as sandy soils. It is due to the fewer well-documented case histories of field liquefaction in gravelly soils and also the lack of large scale laboratory test devices that can accommodate adequate amount of the larger particle sizes. The observed gravelly soil liquefactions during recent earthquakes (2008 Wenchuan, China, 2014 Cephalonia, Greece, and 2016 Kaikoura, New Zealand) have accentuated the necessity of more rigorous investigations of response of gravels during earthquakes. In this regard, the realistic numerical representation of Pea gravel specimen in terms of number, size, and rolling resistance of particles (as developed in chapter 4) is considered and the behavior in stacked-ring simple shear test under stress-controlled cyclic constant volume condition is studied. The outcome of the numerical simulations of this chapter, calibrated and validated by the actual experimental results, provides valuable insights into the cyclic behavior of gravelly soils at both micro- and macro-scale.

5.2 Development of the DEM Model for Constant Volume Cyclic Simple Shear Test of Pea Gravel

Numerical specimens prepared and consolidated to a specified relative density and vertical stress, as described in Chapter 4, are cyclically sheared with the same cyclic stress ratio (CSR) as the one in the experimental specimen which is used to validate the discrete element model for cyclic loading. All the material and contact model parameters are as mentioned in section 4.3 except for a small difference in value of friction coefficient during shear. Similar to the monotonic loading, this value starts from 0.5 at the initiation of shear and gradually decreases to 0.365 (equivalent to friction angle of 20°) and then for cyclic loading, it remains constant for the rest of the simulation. This gradual decrease in value of friction coefficient occurs during the first cycle of loading. To numerically simulate the stress-controlled cyclic loading in the experiment, the bottom cap (and the adjacent ring) moves horizontally following the servo control algorithm in PFC and the direction of movement is reversed whenever the shear stress ratio reaches the specified CSR value. The movements of the rest of stacked rings in the simulation are set to follow the equation of motion in the direction of shearing. To simulate the constant volume condition during shear, the movement of the top and bottom caps are prevented in the vertical direction.

The simulated specimens with relative density of 49% and consolidated vertical stresses of 100, 250 and 400 kPa are cyclically sheared with CSR of 0.095. As shown in Figure 5.1, there is a good agreement between the experimentally observed cyclic constant volume simple shear response of Pea gravel at relative density of 49% and consolidated vertical stress of 250 kPa with the corresponding simulation results. The hysteretic shear stress-strain behavior, degradation of shear modulus and accumulation of generated pore pressure ratio and shear strain observed during

cyclic shear loading of experimental specimen are captured well by the DEM simulation. This validates that the model can satisfactorily predict the cyclic behavior of the real specimen.

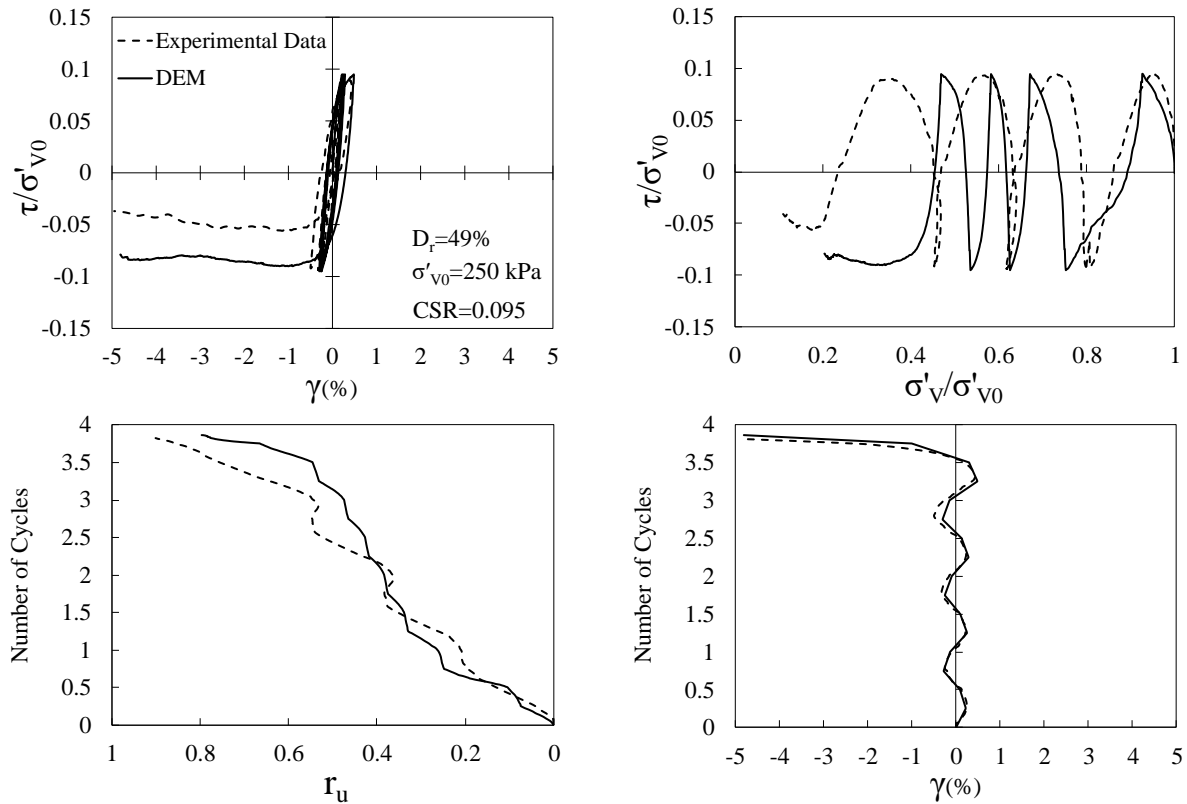


Figure 5.1 Comparison of the results from DEM simulation of constant volume cyclic simple shear test to the corresponding experimental results for Pea gravel specimen ($\sigma'_{v0}=250$ kPa, $D_r=49\%$, $CSR=0.095$)

For the case of $D_r=87\%$ and $CSR=0.095$, the simulations require very long computing times given the high resistance to liquefaction. Therefore, for investigation purposes in this study and to obtain adequate information in fewer cycles (i.e., less computational time), the cyclic behavior of such specimens is only studied for consolidated vertical stress of $\sigma'_{v0}=250$ kPa under a high CSR value of 0.475.

5.3 Macroscopic Behavior Measured at Boundaries

Results from DEM simulations of constant volume cyclic simple shear test measured at boundaries in specimens of relative densities of 49% under cyclic stress ratio of 0.095 are presented

in Figure 5.2 for all the consolidated vertical stresses. In this study, liquefaction is considered to happen when 3.75% single amplitude shear strain is reached. This is a common strain criterion that has been used as triggering point of liquefaction in a number of cyclic simple shear testing (Vaid and Sivathayalan, 1996; Sivathayalan, 2000; Wijewickreme et al., 2005; Porcino et al., 2008; Hubler et al. 2017). The hysteretic shear stress-strain behavior, degradation of shear modulus and accumulation of generated pore pressure ratio and shear strain are observed for all the specimen with different consolidated vertical stresses. For numerical specimens under different consolidated vertical stresses, liquefaction is triggered in 4 to 7 loading cycles. Accumulation of generated pore pressure ratio and shear strain happen gradually at the beginning and during the last cycle by initiation of liquefaction, an abrupt increase of pore pressure ratio and shear strain is observed. The pore pressure ratio at the initiation of liquefaction is larger than 0.7 for all cases with higher value for the lower consolidated vertical stress.

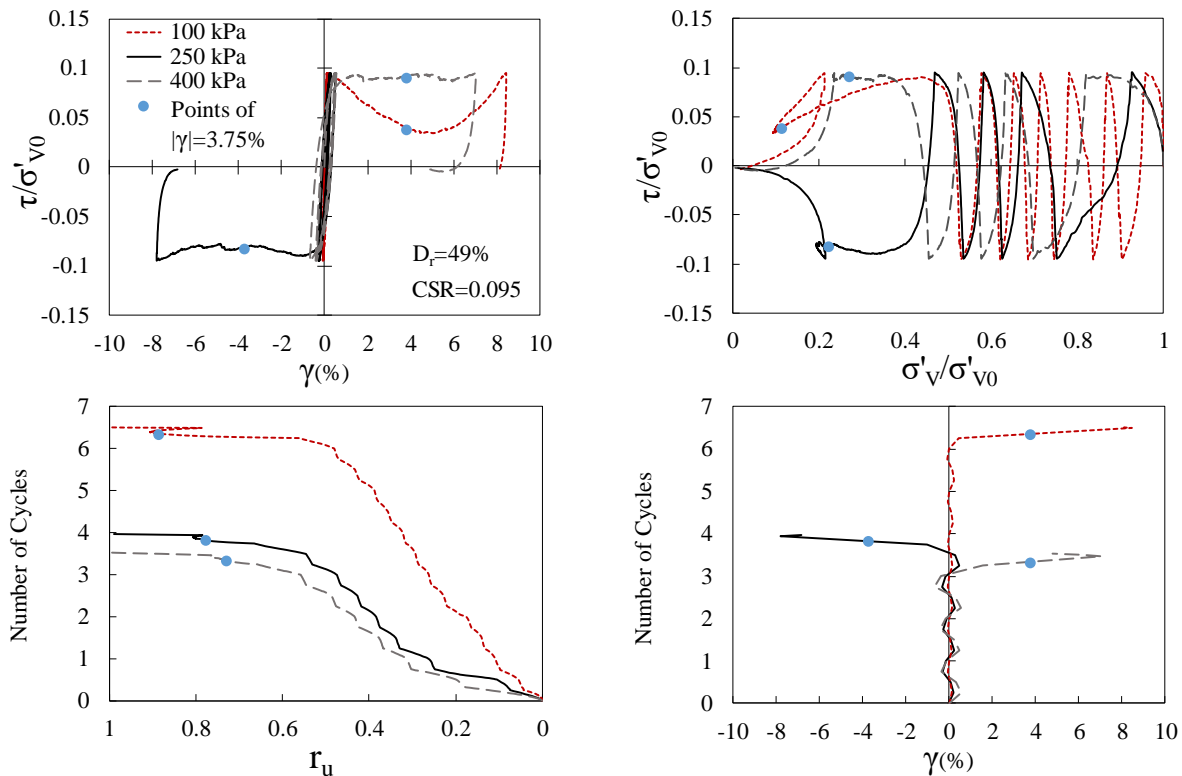


Figure 5.2 Results from DEM Simulations of constant volume cyclic simple shear response of Pea gravel specimen ($D_r=49\%$ and $CSR=0.095$)

Figure 5.3 shows the evolution of coefficient of lateral pressure measured at boundaries for specimens of $D_r=49\%$ under cyclic loading of $CSR=0.095$. By continuation of cyclic loading, coefficient of lateral pressure gradually increases until the last cycle during which liquefaction initiates and the coefficient of lateral pressure experienced a sudden increase. Although for most of the loading, coefficient of lateral pressure is larger for higher consolidated vertical stress, at initiation of liquefaction, it is larger for lower consolidated vertical stress.

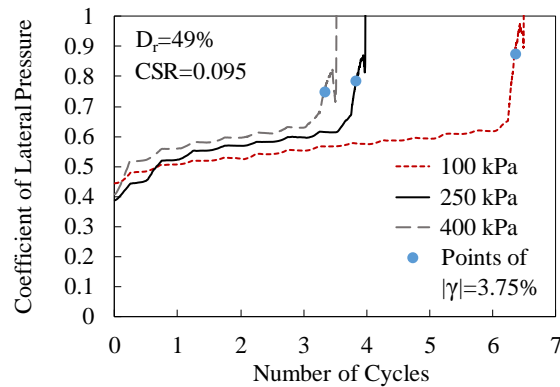


Figure 5.3 Coefficient of lateral pressure during shear in DEM simulations of constant volume cyclic simple shear response of Pea gravel specimen ($D_r=49\%$, $CSR=0.095$)

Figure 5.4 shows the cyclic simple shear responses measured at boundaries for specimen of $\sigma'_{v0}=250$ kPa and $D_r=87\%$ under cyclic stress ratio of 0.475. Cyclic mobility without limited liquefaction is observed for the specimen behavior, in which there is a gradual increase of shear strains and buildup of pore pressure without any occurrence of strain-softening (Castro, 1969; Vaid and Chern, 1985). Although the pore pressure ratio has an overall increasing trend by continuation of cyclic shear loading, it experienced relative rises and drops during each loading cycle as the specimen behavior transforms from tendency to contraction (increase of pore pressure) to tendency to dilation (decrease of pore pressure) phase. After 10 cycles of shear loading with high CSR of 0.475, the generated pore pressure ratio is about 0.5 and the maximum shear strain reaches to more than 4%. The variation of coefficient of lateral pressure for this specimen is shown in Figure 5.5.

Overall, the coefficient of lateral pressure measured at the boundaries of the specimen gradually increases during cyclic shear and after 10 loading cycles it reaches to maximum of 0.93.

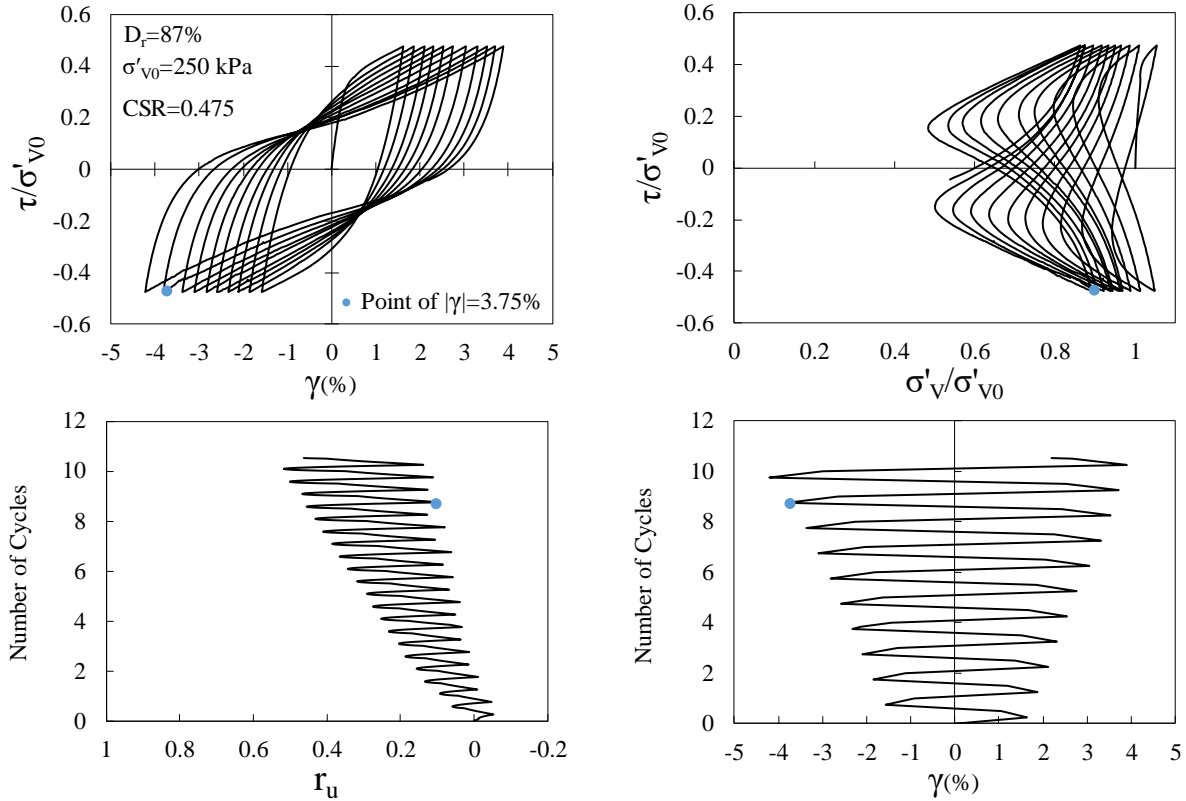


Figure 5.4 Results from DEM Simulation of constant volume cyclic simple shear response of Pea gravel specimen ($\sigma'_{v0}=250$ kPa, $D_r=87\%$ and $CSR=0.475$)

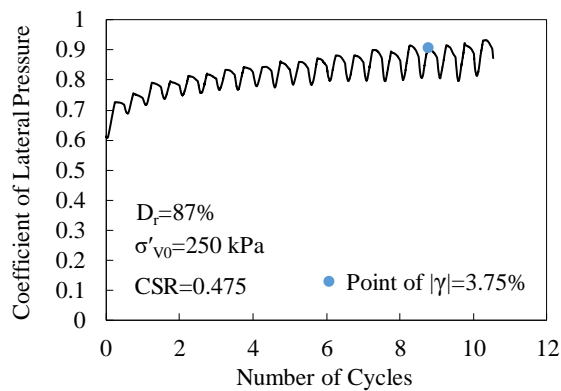


Figure 5.5 Coefficient of lateral pressure during DEM Simulation of constant volume cyclic simple shear response of Pea gravel specimen ($\sigma'_{v0}=250$ kPa, $D_r=87\%$ and $CSR=0.475$)

Figure 5.6 and Figure 5.7 show the cyclic stress paths, along with the phase transformation (PT) and ultimate state (US) lines from corresponding monotonic tests. Stress paths are bounded with the ultimate state lines obtained from corresponding monotonic loadings. Cyclic phase transformation state separating the stress path in each cycle into contractive and dilative phases is compared to the corresponding monotonic one. It can be observed that in case of $D_r=49\%$ in Figure 5.6, the PT lines for monotonic and cyclic loading are very close to each other and can be considered the same. However, for the case of $D_r=87\%$ in Figure 5.7, the PT line is not the same for monotonic and cyclic loadings and the PT line for cyclic stress path has smaller slope than the one for monotonic loading. Mao and Fahey (2003) and Porcino et al., 2008 conducted a series of monotonic and cyclic simple shear tests on calcareous and carbonated sand, respectively, and noted separated phase transformation lines for cyclic and corresponding monotonic tests.

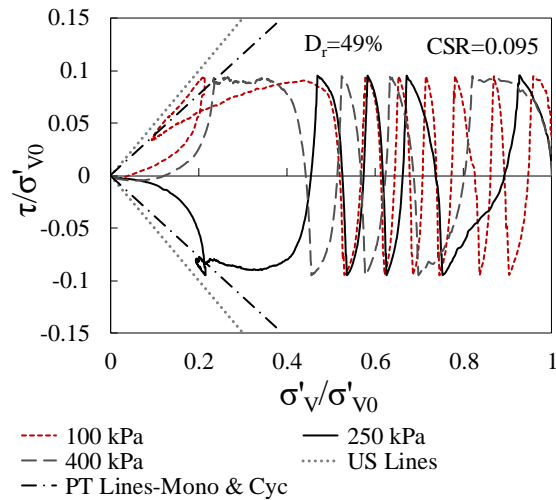


Figure 5.6 Comparison of cyclic stress paths with phase transformation (PT) and ultimate state (US) lines from monotonic stress path data from DEM simulations of Pea gravel specimen ($D_r=49\%$)

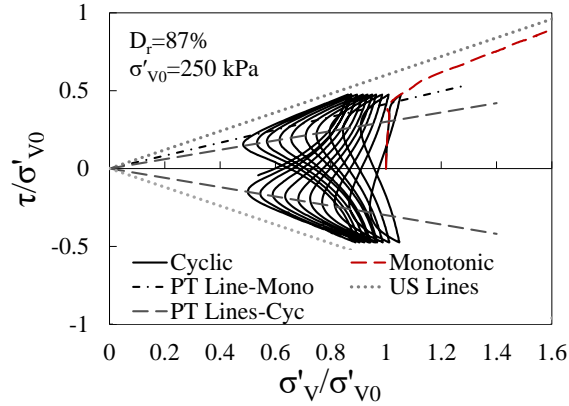


Figure 5.7 Comparison of cyclic stress paths with phase transformation (PT) and ultimate state (US) lines from monotonic stress path data from DEM simulations of Pea gravel specimen ($\sigma'_{v0}=250$ kPa and $D_r=87\%$)

Figure 5.8 and Figure 5.9 show the horizontal displacement profile of the stacked rings at boundary shear strain of 3.75% for specimens of $D_r=49\%$ and 87%, respectively. At this instance of loading (as can be seen in Figure 5.2 and Figure 5.4), noticeable pore pressure has generated that in case of the imposed constant volume loading condition also implies the weakening of contact points at the interface of horizontal boundaries and specimen. However, it can be observed that, overall, the ring displacement profiles follow the theoretical continuous simple shear deformation at lateral boundaries (shown by solid lines) reasonably well, which justifies that the simple shear condition is adequately imposed on the specimens during the cyclic loading.

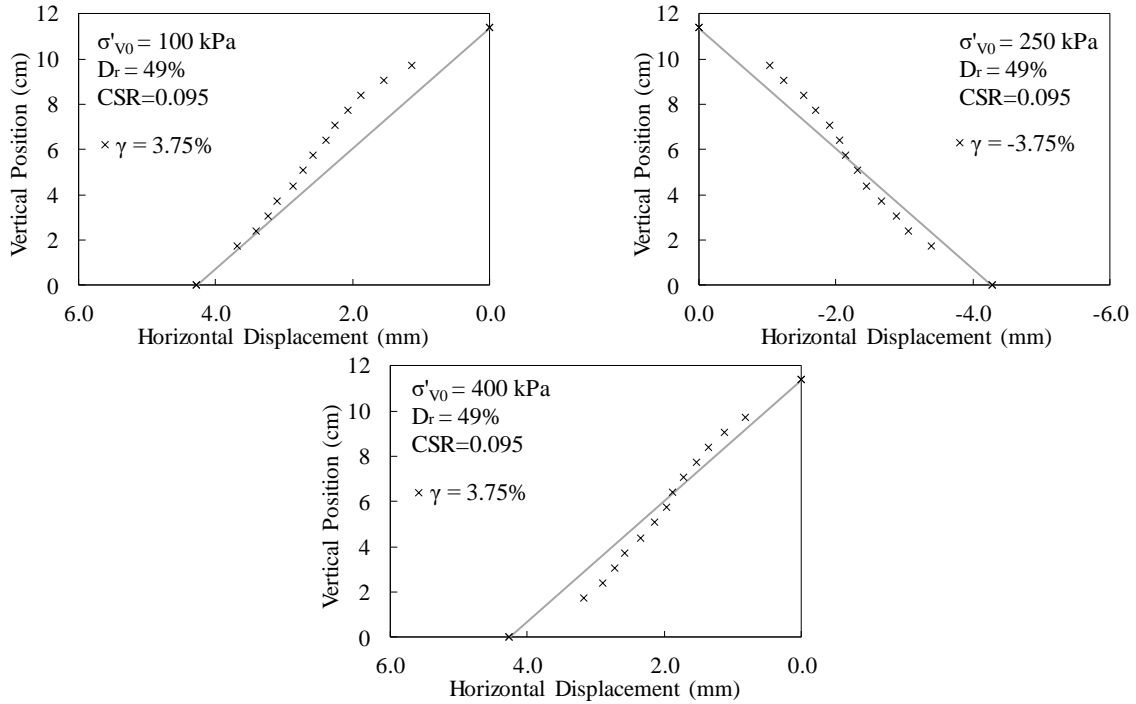


Figure 5.8 Horizontal displacement profile of stacked rings at boundary shear strain of 3.75% in DEM simulations of constant volume cyclic simple shear response of Pea gravel specimen ($D_r=49\%$)

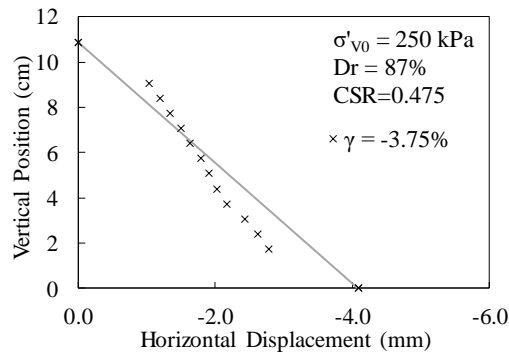


Figure 5.9 Horizontal displacement profile of stacked rings at boundary shear strain of 3.75% in DEM simulation of constant volume cyclic simple shear response of Pea gravel specimen ($\sigma'_{v0}=250$ kPa, $D_r=87\%$)

5.4 Stress measurement at boundaries versus inside specimen core

Comparison between the macroscopic cyclic shear responses of specimen obtained by stress measurements at boundaries and the specimen core (inside MS1 (refer to Figure 4.12)) is presented in this part. The differences between the two arise from the lack of complementary shear

stress at the lateral boundaries and the stress non-uniformities over the horizontal boundaries (e.g. Prevost and Høeg, 1976; Budhu, 1984) and still the stress uniformity assumption that is made in calculating the stresses on those boundaries. In this part, the consequent differences between boundaries versus central measurement (inside MS1) of stresses are qualitatively and quantitatively assessed during cyclic shear under constant volume condition.

Figure 5.10 shows the boundary and central measurement of shear stress during cyclic loading with CSR= 0.095 for specimen of σ'_{v0} =250 kPa and D_r =49%. Although the overall trend of the responses are similar, quantitative differences is observed between them. Due to the relative movement and rearrangement of particles during vertically consolidation of specimen, an initial non-zero shear stress of 7.3 kPa exists at the specimen core (inside MS1) at the beginning of the shear. At the peak of the stress cycles in both positive and negative directions, the shear stress value measured at boundaries underestimate the one exists inside MS1. The observed difference is decreasing by increasing the cycle numbers; however, the average amount of underestimation of the central shear stress by boundary measurement at the peaks is about 27%. As there are also some differences in the measured vertical stress values, the normalized shear stress to the initial consolidated vertical stress (τ/σ'_{v0}) and to the instantaneous vertical stress (τ/σ'_v) are also compared for measurements at boundaries and inside MS1. It can be observed that boundary measurements result in, respectively, underestimation and overestimation of τ/σ'_{v0} value measured inside MS1 at positive and negative peak of cycle. The average underestimation of τ/σ'_{v0} at positive cycle peaks is about 12% and the average overestimation at negative cycle peaks is about 8%. In case of τ/σ'_v , boundary measurements underestimate the internal measured value at the cycle peaks by average of 16%. Similar observations are made for vertical stresses of 100 and 400 kPa and the relevant figures are presented in Appendix E.

These results show that although a symmetric cyclic shear loading with a constant CSR is applied at the boundaries, the same is not experienced at the specimen core. It is observed that the soil at the specimen core is experiencing a non-symmetric shear cycles with variable CSR.

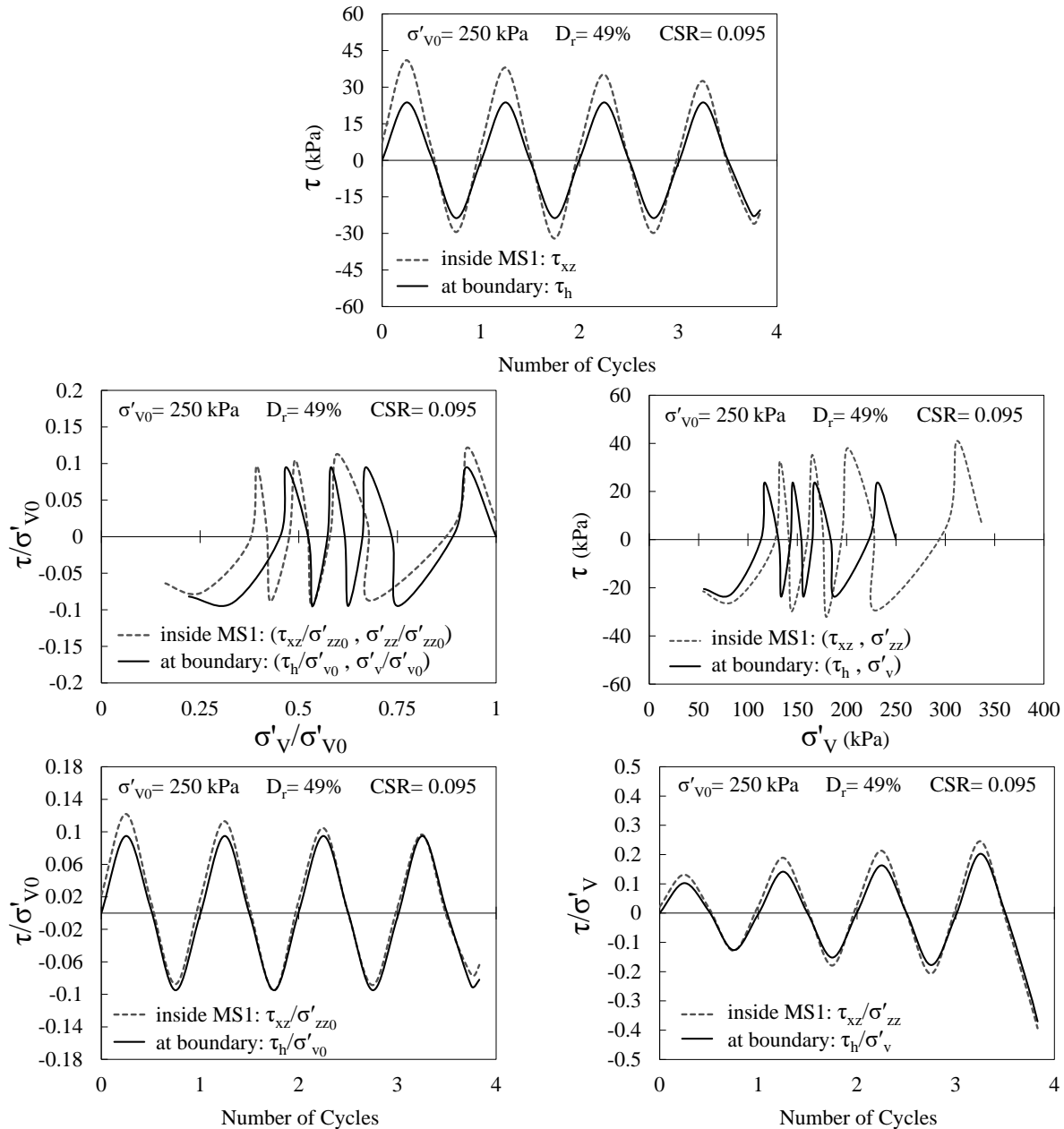


Figure 5.10 Comparison of the cyclic shear response measured at boundaries and inside the central measurement sphere in DEM simulations of constant volume cyclic simple shear response of Pea gravel specimen ($\sigma'_{v0}=250$ kPa, $D_r=49\%$, $CSR=0.095$)

Comparison of the boundary and central (inside MS1) measurements of generated pore pressure ratio and coefficient of lateral pressure for specimen of $D_r=49\%$ cyclically loaded with $CSR=0.095$ is shown in Figure 5.11 for all consolidated vertical stresses. It is observed that calculated pore pressure ratio based on the changes in vertical stress at horizontal boundaries overestimates the true pore pressure ratio calculated based on the changes in mean effective pressure inside the specimen core. Larger difference is also observed for higher consolidated vertical stress.

Moreover, the coefficient of lateral pressure calculated based on the boundary measurements (by assuming the same value in all radial directions) underestimates the ones measured inside the specimen core in both parallel (K_x) and perpendicular (K_y) to the shear direction. The difference is larger for higher consolidated vertical stress. On average for all the consolidated vertical stresses, the boundary measured coefficient of lateral pressure underestimates K_x and K_y values inside the specimen core by up to 25% and 13%, respectively. It is also observed that the coefficient of lateral pressure in the direction of shear (K_x) is larger than the one in perpendicular direction (K_y) during the whole period of cyclic loading. During the cyclic loading, K_x is, on average, 1.2 times larger than K_y .

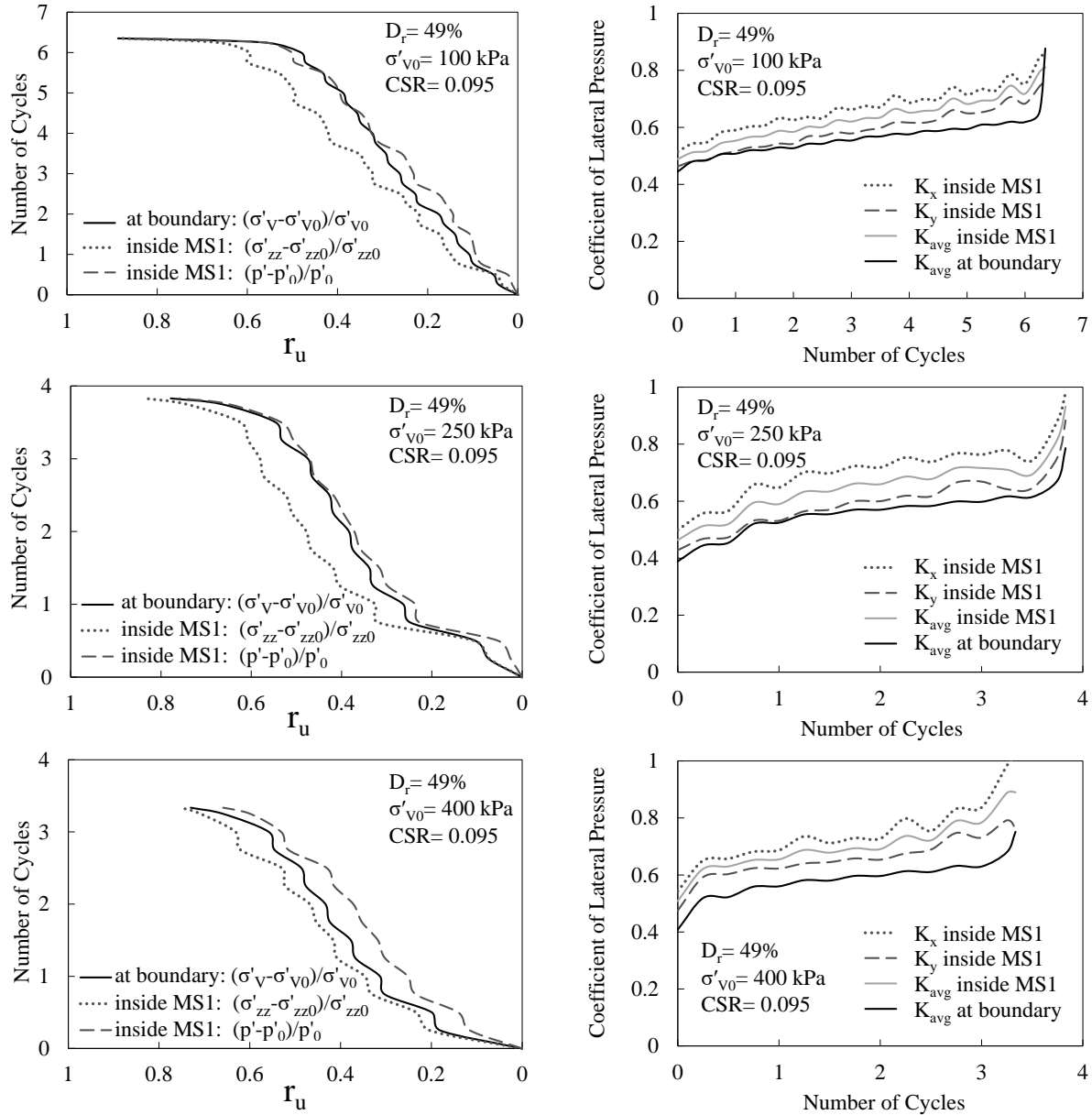


Figure 5.11 Comparison of the generated pore pressure ratio (right) and coefficient of lateral pressure (left) based on the measurements at the boundaries and inside the central measurement sphere in DEM simulations of constant volume cyclic simple shear response of Pea gravel specimen ($D_r=49\%$, $CSR=0.095$)

In case of specimen of $\sigma'_{v0}=250$ kPa, $D_r=87\%$ cyclically sheared with $CSR=0.475$, as shown in Figure 5.12, the boundary measured τ and τ/σ'_v at the loading cycle peaks underestimate the central measured values by average of 19% and 12%, respectively. For values of τ/σ'_{v0} at most of the loading cycle peaks on the negative side, boundary measured values are very close to the

ones measured at the specimen core. However, at all the positive peaks, boundary measured values overestimate the central measured ones by an average of 11%.

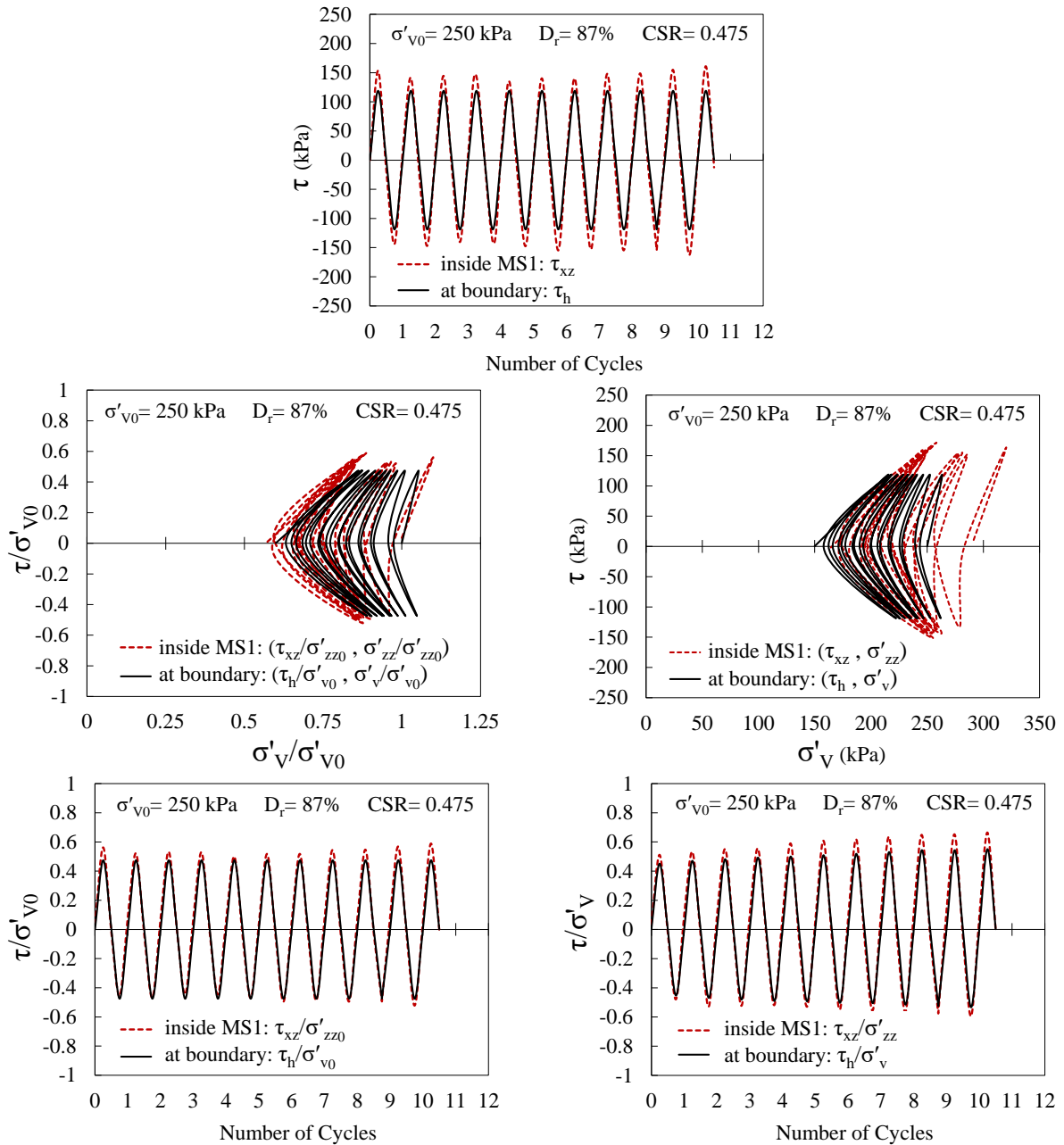


Figure 5.12 Comparison of the cyclic shear response measured at boundaries and inside the central measurement sphere in DEM simulations of constant volume cyclic simple shear response of Pea gravel specimen ($\sigma'_{v0}=250$ kPa, $D_r=87\%$, $CSR=0.475$)

It is observed in Figure 5.13 that calculated pore pressure ratio based on the changes in vertical stress at horizontal boundaries results in more positive values than the true pore pressure

ratio generated at the specimen core, which leads to conservative estimation of generated pore pressure at the specimen core.

The average value of coefficient of lateral pressure measured at boundaries is mostly between the values of coefficient of lateral pressure in perpendicular (K_y) and parallel (K_x) directions to shear. During the cyclic loading, K_x experienced larger amplitudes of fluctuations than K_y , in a way that the ratio of K_x to K_y (K_x/K_y) is, on average, 1.25 and 0.92 at instances of peak and zero shear stress, respectively.. The boundary measurements cannot capture these aspects of the behavior, and leads to underestimation of the maximum K_x values by up to 22%.

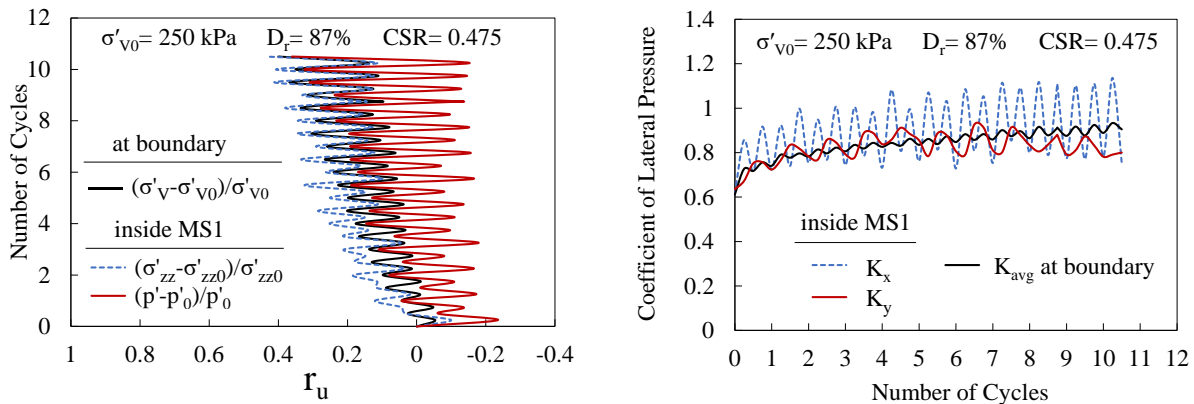


Figure 5.13 Comparison of the generated pore pressure ratio (right) and coefficient of lateral pressure (left) based on the measurements at the boundaries and inside the central measurement sphere in DEM simulations of constant volume cyclic simple shear response of Pea gravel specimen ($\sigma'_{v0}=250$ kPa, $D_r=87\%$, $CSR=0.475$)

5.5 Non-uniformities inside the specimen during cyclic simple shear loading

Non-uniformity of stress and strain distribution has been shown to exist in cyclic simple shear test specimens by different numerical studies using FEM and DEM (e.g. Shen et al., 1978; Wang et al., 2004; Asadzadeh and Soroush, 2017; Asadzadeh and Soroush, 2018). In this part, the distributions of the different measured quantities during cyclic simple shear loading are evaluated inside the simulated specimens. The more realistic simulation of boundary deformation

(displacement of the rings following the equation of motion) and representation of the real soil assembly in terms of number, size and rolling resistance distribution of particles provides more reliable information about the non-uniformities existing in actual specimen.

Measurement spheres MS1 to MS13 located at the mid-height of the specimen (Figure 5.14) are considered for measurement of different quantities and the non-uniformity parameter is calculated using Equation 4.10.

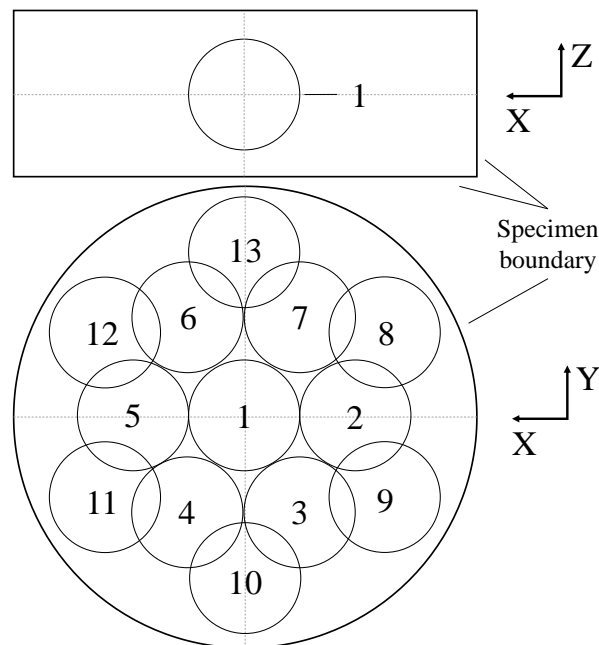


Figure 5.14 Schematic of the measurement sphere considered for evaluation of non-uniformity inside the specimen (all measurement spheres are at the same elevation as MS1)

Variation of cyclic stress ratio (τ_{xz}/σ'_{zz0}) inside MS1-MS13 during cyclic shear is shown in Figure 5.15 for specimens of $\sigma'_{v0}=250$ kPa (The relevant figures for specimens of $\sigma'_{v0}=100$ and 400 kPa and $D_r=49\%$ are presented in Appendix F). The value of stress ratio at the end of consolidation may be non-zero because of the induced shear stresses inside the specimen during the one dimensional consolidation. Consequently, nonsymmetrical loading cycles can be observed at different locations inside specimen. Similar observation is made by Shen et al. (1978) about the stress distribution in a circular soil mass subjected to cyclic testing in the NGI simple shear

apparatus. The range, average and non-uniformity parameter of the stress ratio values inside the specimen during cyclic shear for all cases of consolidated vertical stress with $D_r=49\%$ and $CSR=0.095$ are shown in Figure 5.16. It should be mentioned that non-uniformities are evaluated here at instances of maximum shear stress (in both positive and negative directions). The corresponding boundary measurements of cyclic stress ratio is also included for comparison. The boundary measured cyclic stress ratio is close to the average value inside the measurement spheres. Despite of fluctuations of non-uniformity parameter of τ_{xz}/σ'_{zz0} , an overall downtrend in its value is observed as shear cycling proceeds. The reduction in non-uniformity parameter is larger for specimen of lower consolidated vertical stress.

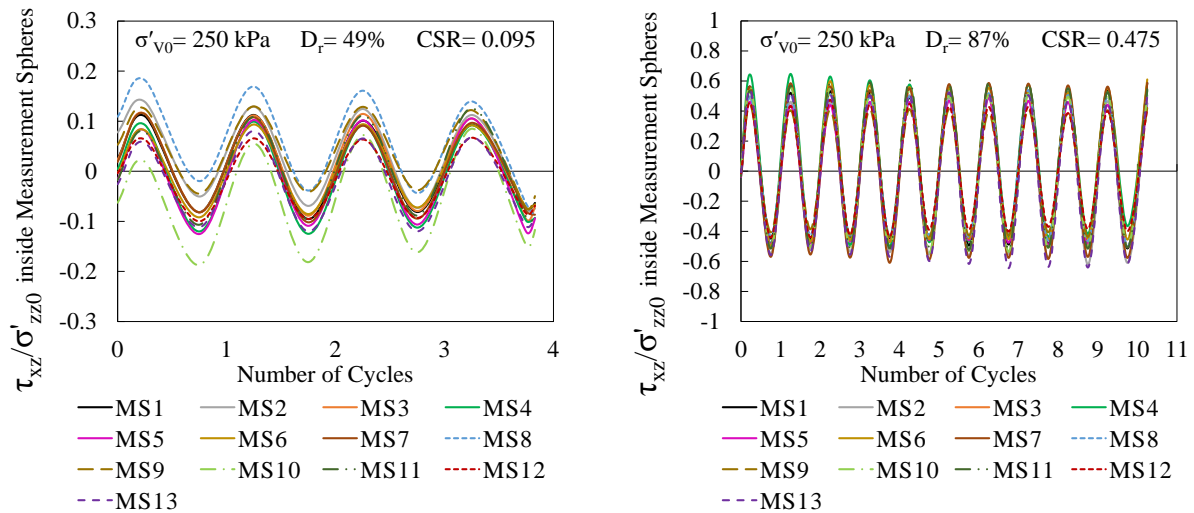


Figure 5.15 Stress ratio (τ_{xz}/σ'_{zz0}) measured inside MS1-MS13 during cyclic shear in DEM simulations of constant volume cyclic simple shear response of Pea gravel specimen: $\sigma'_{v0}=250 \text{ kPa}$ ($D_r=49\%$ and $CSR=0.095$ (left), $D_r=87\%$ and $CSR=0.475$ (right))

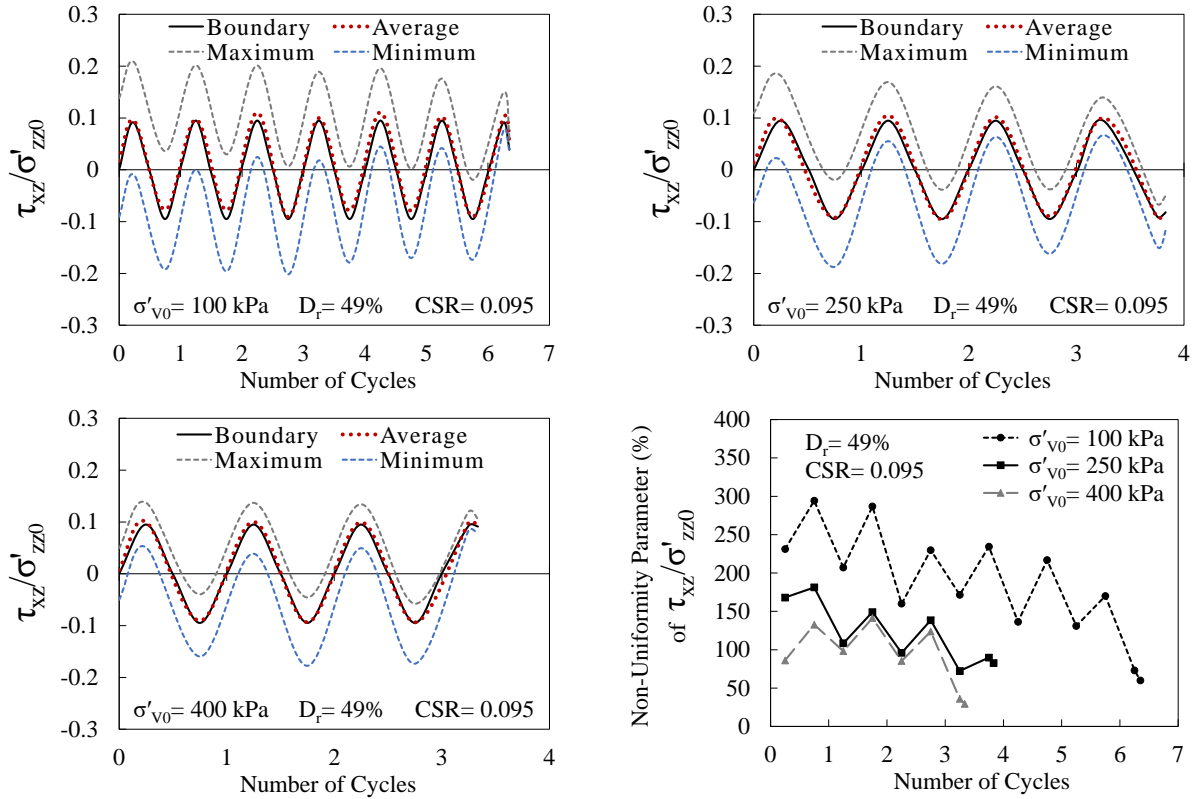


Figure 5.16 Distribution of Stress ratio (τ_{xz}/σ'_{v0}) inside MS1-MS13 and evolution of non-uniformity parameter in DEM simulations of constant volume cyclic simple shear response of Pea gravel specimen: $\sigma'_{v0}=100, 250, 400$ kPa, $D_r=49\%$ and $CSR=0.095$

In case of specimen with $D_r=87\%$ cyclically sheared with $CSR=0.475$, the non-uniformity parameter of τ_{xz}/σ'_{zz0} distribution, as shown in Figure 5.17, fluctuated between 30-55% during the applied cyclic loading. It can be observed that non-uniformity of τ_{xz}/σ'_{zz0} distribution is less in case of higher relative density.

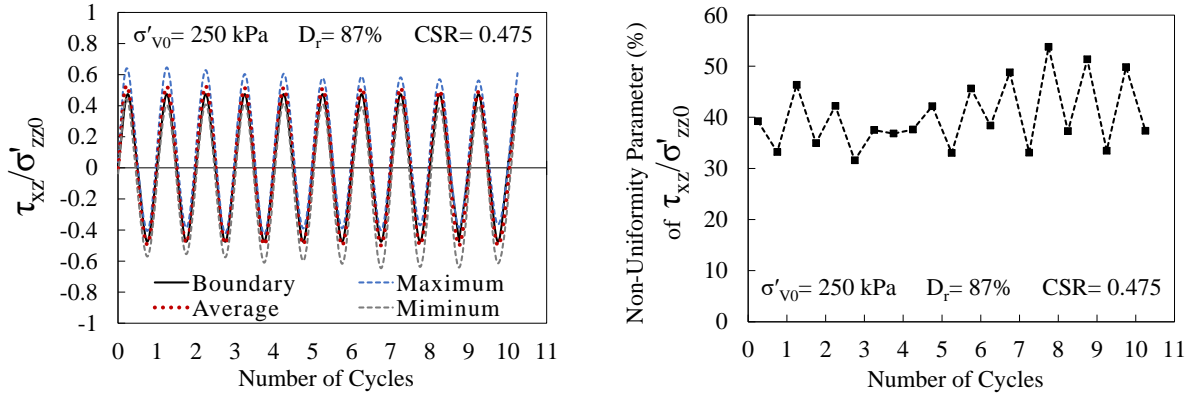


Figure 5.17 Distribution of Stress ratio (τ_{xz}/σ'_{zz0}) inside MS1-MS13 and evolution of non-uniformity parameter in DEM simulations of constant volume cyclic simple shear response of Pea gravel specimen: $\sigma'_{v0}=250$ kPa, $D_r=87\%$ and $CSR=0.475$

To assess the distribution of applied stress ratio relative to the initial state at the end of consolidation, variation of $(\tau_{xz} - \tau_{xz0})/\sigma'_{zz0}$ inside MS1-MS13 is evaluated for the specimen of $\sigma'_{v0}=250$ and $D_r=49\%$ and shown in Figure 5.18. It can be observed that the distribution of $(\tau_{xz} - \tau_{xz0})/\sigma'_{zz0}$ is not only non-uniform but also nonsymmetrical at different locations inside the specimen. Shen et al. (1978) attributed such behavior to the creation of an external moment due the horizontal displacement of horizontal boundary in the lack of complementary shear stress on the lateral boundaries, which causes the generation of additional stresses at different locations in the specimen to balance this moment. Comparing the distribution of $(\tau_{xz} - \tau_{xz0})/\sigma'_{zz0}$ inside the specimen with that applied at the boundaries, it can be observed the average value of $(\tau_{xz} - \tau_{xz0})/\sigma'_{zz0}$ over the measurement spheres at mid-height of the specimen is very close to the applied cyclic stress ratio at the boundaries.

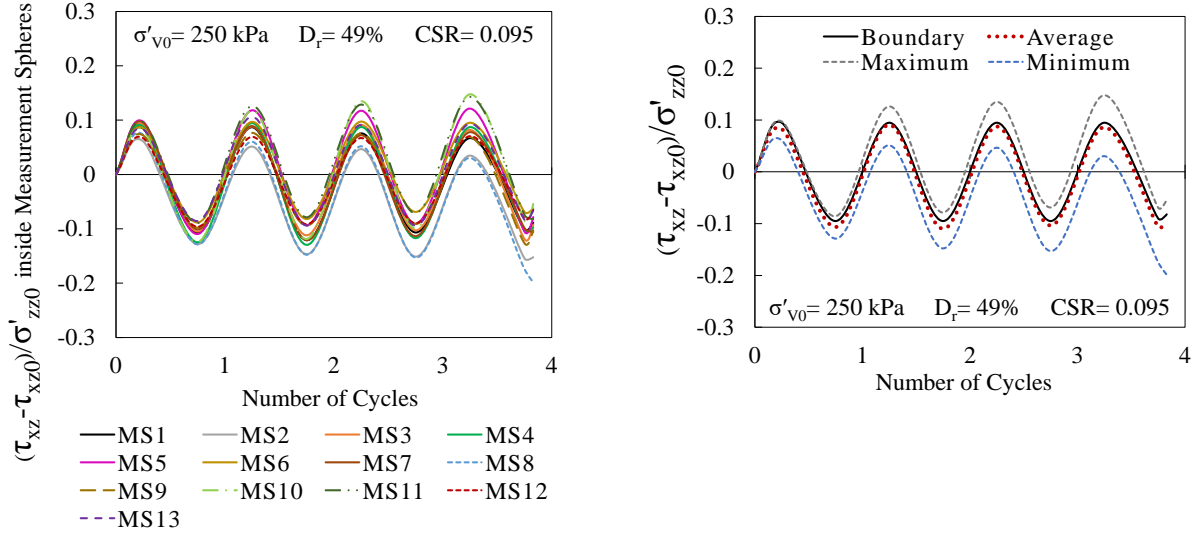


Figure 5.18 The applied stress ratio $((\tau_{xz} - \tau_{xz0}) / \sigma'_{zz0})$ measured inside MS1-MS13 in DEM simulations of constant volume cyclic simple shear response of Pea gravel specimen: $\sigma'_{v0} = 250$, $D_r = 49\%$ and $CSR = 0.095$

Overall, these results shows that despite a symmetric cyclic shear loading of constant CSR applied at the boundaries, the experienced shear cycles at different locations inside the specimen can be non-symmetric and with variable CSR. This is important to be taken into consideration for interpretation of the experimental results. To assess the liquefaction resistance in the laboratory, it is assumed that the applied cyclic loading at the boundaries is similarly experienced by the whole specimen in a uniform way. However, the DEM simulation results show that it is not a valid assumption. Although the experienced shearing cycles inside the specimen is, on average, similar to the one applied at the boundaries, different locations within the specimen experiences higher or lower shear stress ratios. This leads to a non-uniform cyclic response within the specimen that can affect the overall behavior of the specimen as a whole.

Variation of stress ratio $(\tau_{xz} / \sigma'_{zz})$ inside MS1-MS13 during shear is shown in Figure 5.19 for specimens of $\sigma'_{v0} = 250$ kPa. The relevant figures for specimens of $\sigma'_{v0} = 100$ and 400 kPa and $D_r = 49\%$ are presented in Appendix F. It is observed that the value of τ_{xz} / σ'_{zz} at the instances of peak shear stress (peaks of the shearing cycles) increases as the number of cycles increases. Figure

5.20 presents the range and average and non-uniformity parameter of the stress ratio values inside the specimen during cyclic shear for all cases of consolidated vertical stress at $D_r=49\%$ and $CSR=0.095$. Despite the non-uniformities inside the specimen, the average τ_{xz}/σ'_{zz} values inside the measurement spheres are observed to be close to the boundary measured value. The non-uniformity parameter of τ_{xz}/σ'_{zz} at the instances of peak shear stress has an overall decreasing trend by increasing the loading cycles. However, in case of specimen of $D_r=87\%$ under cyclic loading with $CSR=0.475$, as shown in Figure 5.21, the non-uniformity parameter fluctuate between 20-40% during the applied loading cycles.

Such non-uniformities in distribution of τ_{xz}/σ'_{zz} implies that at each instance during cyclic loading, the stress state is not necessarily the same at different locations within the specimen. The results show that the boundary measured value of τ_{xz}/σ'_{zz} is an estimate of the average τ_{xz}/σ'_{zz} values within the specimen.

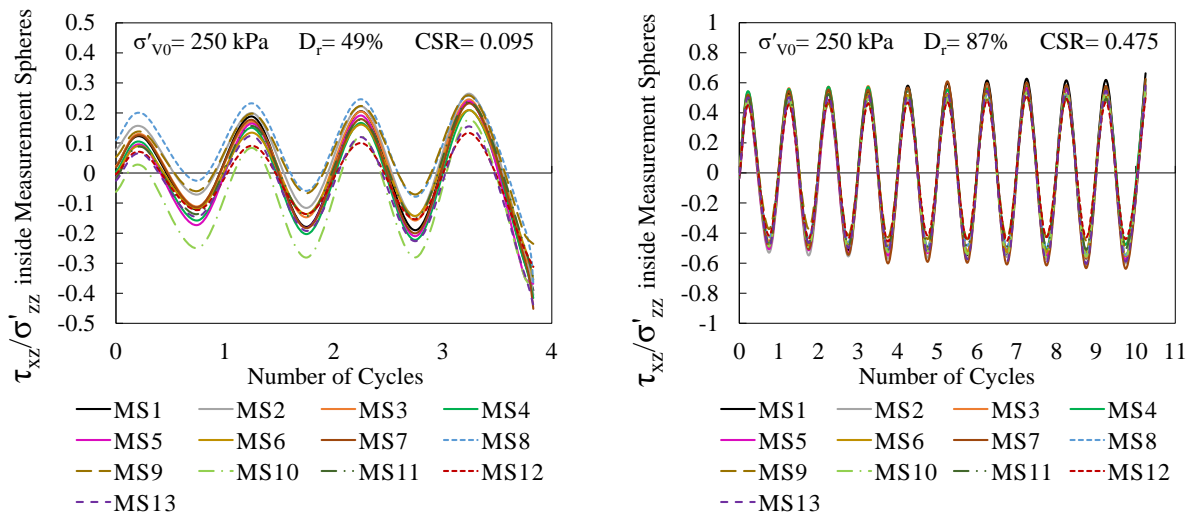


Figure 5.19 Stress ratio (τ_{xz}/σ'_{zz}) measured inside MS1-MS13 during cyclic shear in DEM simulations of constant volume cyclic simple shear response of Pea gravel specimen: $\sigma'_{v0}=250$ kPa ($D_r=49\%$ and $CSR=0.095$ (left), $D_r=87\%$ and $CSR=0.475$ (right))

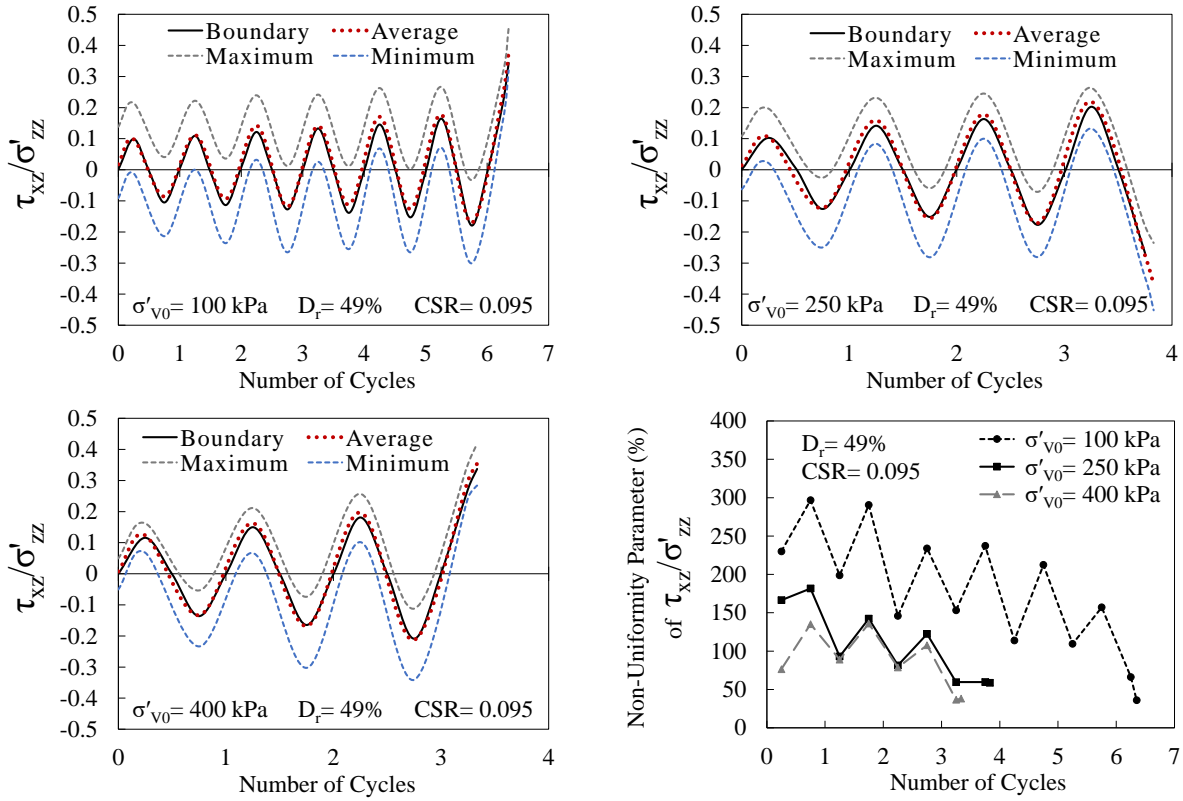


Figure 5.20 Distribution of Stress ratio (τ_{xz}/σ'_{zz}) inside MS1-MS13 and evolution of non-uniformity parameter in DEM simulations of constant volume cyclic simple shear response of Pea gravel specimen: $\sigma'_{v0}=100, 250, 400$ kPa, $D_r=49\%$ and $CSR=0.095$

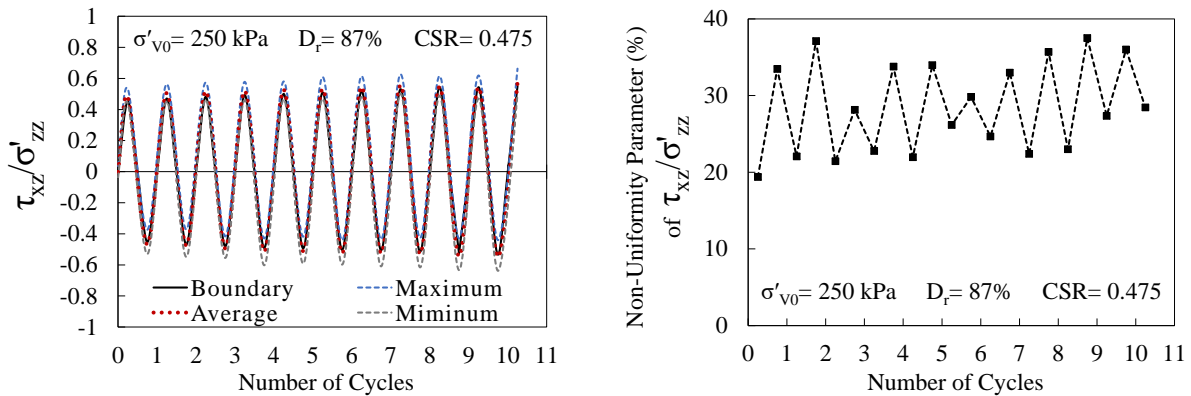


Figure 5.21 Distribution of Stress ratio (τ_{xz}/σ'_{zz}) inside MS1-MS13 and evolution of non-uniformity parameter in DEM simulations of constant volume cyclic simple shear response of Pea gravel specimen: $\sigma'_{v0}=250$ kPa, $D_r=87\%$ and $CSR=0.475$

The distribution of pore pressure ratio (r_u) inside the specimen is evaluated by calculating it as $(p'-p'_0)/p'_0$, in which p' is the mean effective stress inside the measurement sphere (equation 4.5). Figure 5.22 shows the variation of pore pressure ratio inside MS1-MS13 during cyclic shear for specimens of $\sigma'_{v0}=250$ kPa. The range, average, and non-uniformity parameter of pore pressure ratio measured inside MS1-MS13 is presented in Figure 5.23 and Figure 5.24 for specimens of $D_r=49\%$ and 87% , respectively. The non-uniformity parameter during cyclic shear is evaluated at instances of zero and maximum shear stress (negative and positive). For all specimens, the pore pressure ratio calculated based on the changes in vertical stress at horizontal boundaries is close to the maximum true positive pore pressure ratio inside MS1-MS13, and generally overestimates the positive pore pressure ratio generated inside the specimen during cyclic shearing. For specimen of $D_r=49\%$ and $CSR=0.095$, after the initial jump in non-uniformity parameter during first quarter cycle, it follows an overall decreasing trend until it reaches less than 30% when the shear strain reaches 3.75% and liquefaction initiated in the specimen. The observed non-uniformity parameter is smaller for larger consolidated vertical stress. The initial high non-uniformity parameter at the first loading peak can be attributed to the small average value and relatively wide range of pore pressure ratio at that instance, which results in high calculated value by equation 4.5. As shown in Figure 5.24 for specimen of $\sigma'_{v0}=250$ kPa, $D_r=87\%$ and $CSR=0.475$, except the local jumps in non-uniformity parameter that corresponds to the instances that average pore pressure ratio is close to zero, its value shows large variations between 50-200%.

These DEM simulation results indicate that determining pore pressure ratio based on the change of vertical effective stress on the top cap, as done in laboratory, leads to a conservative estimation of the actual pore pressure ratio generated at different locations inside the specimen.

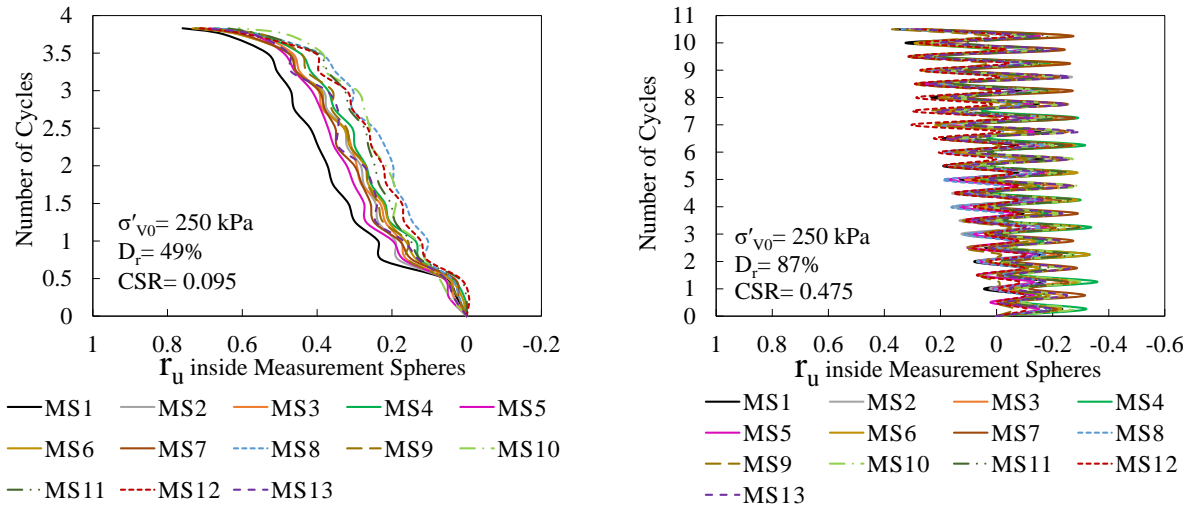


Figure 5.22 Pore pressure ratio measured inside MS1-MS13 during cyclic shear in DEM simulations of constant volume cyclic simple shear response of Pea gravel specimen: $\sigma'_{v0}=250$ kPa ($D_r=49\%$ and $CSR=0.095$ (left), $D_r=87\%$ and $CSR=0.475$ (right))

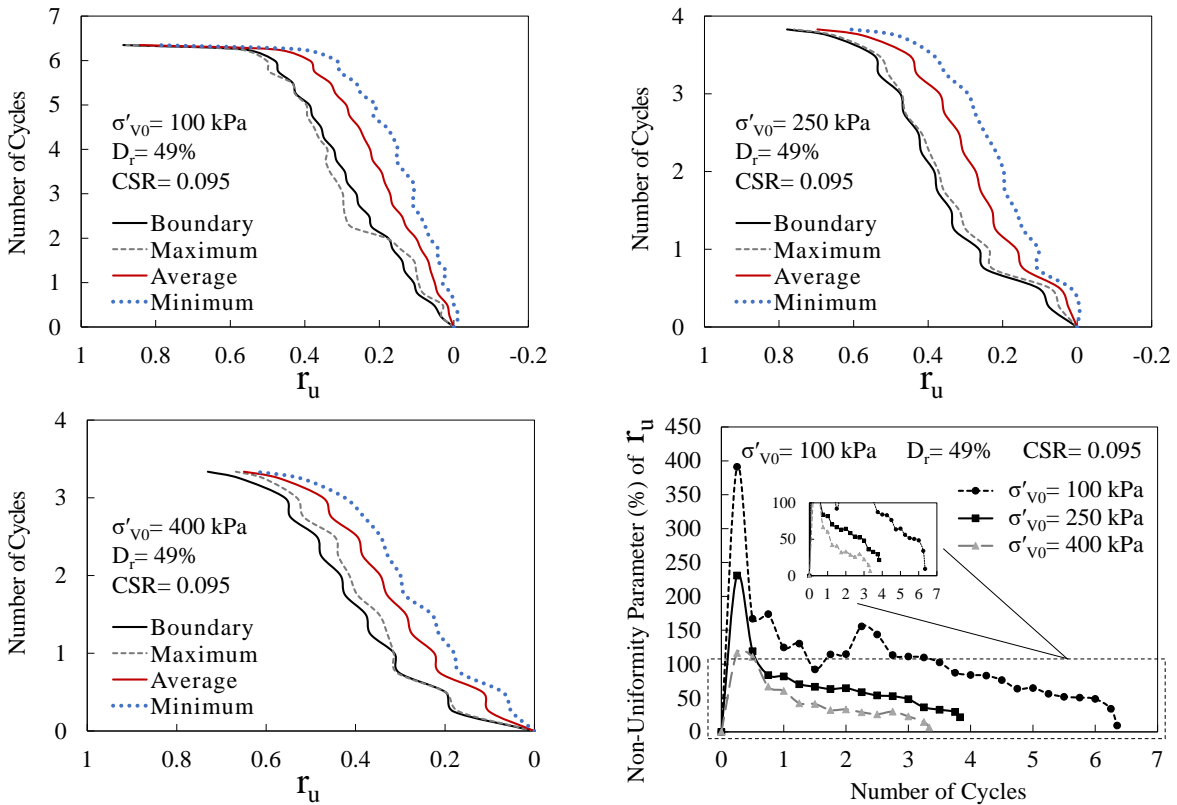


Figure 5.23 Distribution of pore pressure ratio inside MS1-MS13 and evolution of non-uniformity parameter in DEM simulations of constant volume cyclic simple shear response of Pea gravel specimen: $\sigma'_{v0}=100, 250, 400$ kPa, $D_r=49\%$ and $CSR=0.095$

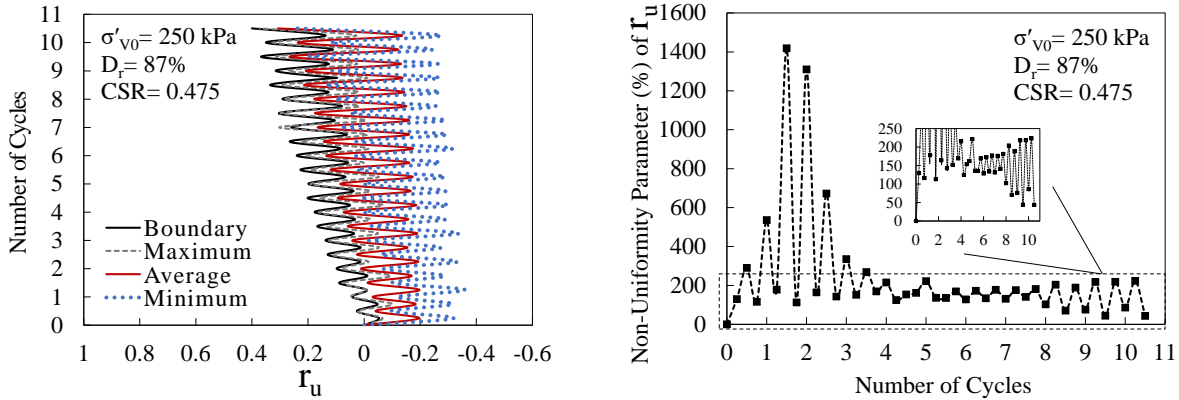


Figure 5.24 Distribution of pore pressure ratio inside MS1-MS13 and evolution of non-uniformity parameter in DEM simulations of constant volume cyclic simple shear response of Pea gravel specimen: $\sigma'_{v0}=250$ kPa, $D_r=87\%$ and $CSR=0.475$

The evolution of shear strain ($\gamma_{xz}=\epsilon_{xz}+\epsilon_{zx}$) inside MS1-MS13 during cyclic shear in specimens of $\sigma'_{v0}=250$ kPa is shown in Figure 5.25. The range, average, and non-uniformity parameter of γ_{xz} is presented in Figure 5.26 and Figure 5.27 for specimens of $D_r=49$ and 87% , respectively. Non-uniformity of shear strain and the difference between boundary shear strain and those inside the measurement spheres are evident in these figures. Overall, the boundary measured shear strain (as done in laboratory) is not representative of the induced shear strain at different locations inside the specimen. Comparing this boundary measured value to the average shear strain induced in different locations at the mid-height of the specimen shows that boundary measurements lead to shear strain values that are higher than the average value that is induced within the specimen. For specimens of $D_r=49\%$ and $CSR=0.095$, the boundary measured shear strain is, on average, 1.5 and 2.1 times larger than the average shear strain induced inside the specimen at instances of, respectively, zero and maximum shear stress. When the single amplitude shear strain reaches 3.75% (liquefaction initiation) according to the boundary measurement, the average shear strain induced within the specimens is, on average, 1.15 times smaller than that at the boundaries. For specimen of $\sigma'_{v0}=250$ kPa, $D_r=87\%$ and $CSR=0.475$, the boundary measured

shear strain is, on average, two times larger than the average shear strain induced inside the specimen at instances of zero and maximum shear stress.

It is important to account for these differences in interpretation of experimental results for analysis of the liquefaction behavior of the soil specimen.

Regarding the degree of non-uniformity of shear strain distribution, in specimens of $D_r=49\%$ and $CSR=0.095$, an overall increase in non-uniformity parameter is observed at first but this value decreases during the last cycle and at the instance of boundary shear strain of 3.75% , the non-uniformity parameter at this point is less than 50% for all consolidated vertical stresses. In specimen of $\sigma'_{v0}=250$ kPa, $D_r=87\%$ and $CSR=0.475$, the non-uniformity parameter during cyclic loading exhibits an overall increasing trend during the cyclic loading.

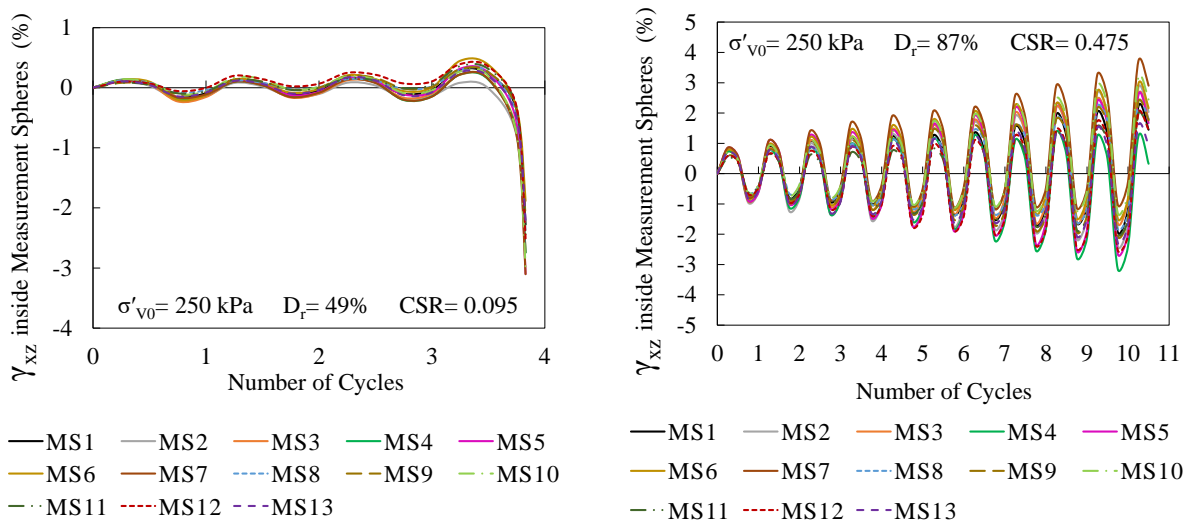


Figure 5.25 Shear strain measured inside MS1-MS13 during cyclic shear in DEM simulations of constant volume cyclic simple shear response of Pea gravel specimen: $\sigma'_{v0}=250$ kPa ($D_r=49\%$ and $CSR=0.095$ (left), $D_r=87\%$ and $CSR=0.475$ (right))

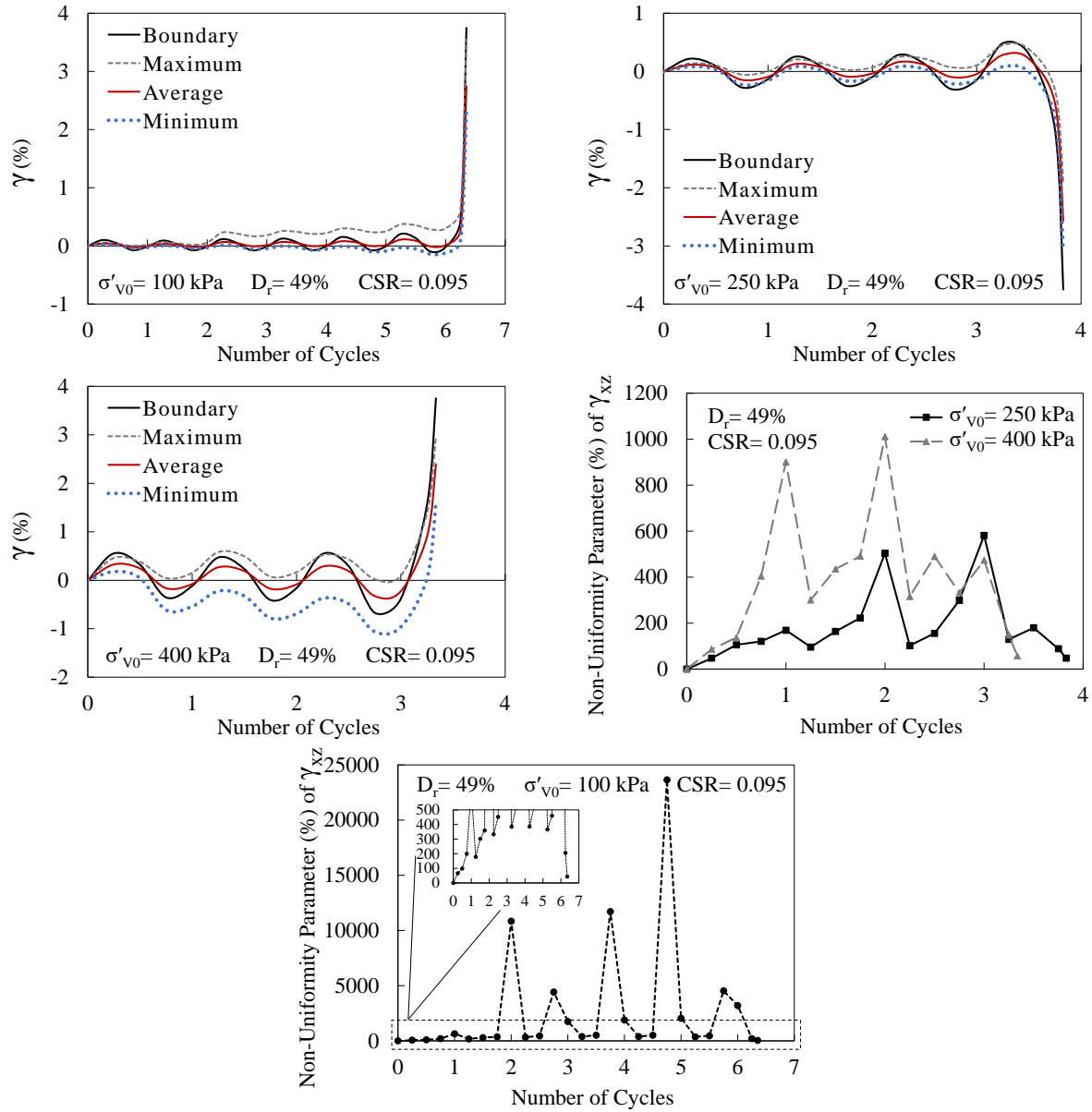


Figure 5.26 Distribution of shear strain inside MS1-MS13 and evolution of non-uniformity parameter in DEM simulations of constant volume cyclic simple shear response of Pea gravel specimen: $\sigma'_{v0} = 100, 250, 400$ kPa, $D_r = 49\%$ and $CSR = 0.095$

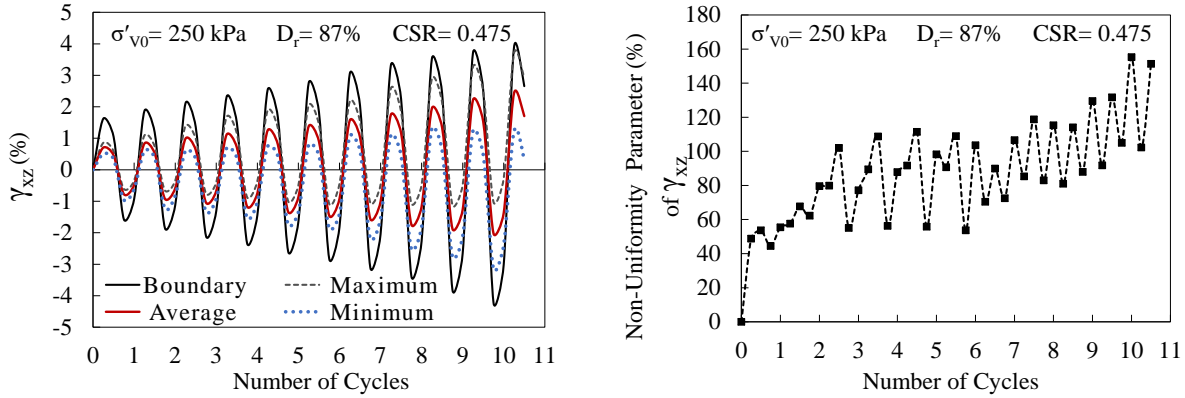


Figure 5.27 Distribution of shear strain inside MS1-MS13 and evolution of non-uniformity parameter in DEM simulations of constant volume cyclic simple shear response of Pea gravel specimen: $\sigma'_{v0}=250$ kPa, $D_r=87\%$ and $CSR=0.475$

Although a global constant volume condition is forced on the specimen by preventing the vertical displacement of horizontal boundaries, local volume changes can occur at different locations inside the specimen during shear due to the movement of particles relative to each other. The inequality of stresses and strains at different locations inside specimen can induce non-uniform distribution of volumetric changes and consequently generated excess pore pressure. Understanding the non-uniformity of volumetric changes and the associated generated pore pressure inside specimen will provide insight into better interpretation of the liquefaction strength analysis that are done by considering average measurements at the specimen boundaries in laboratory.

Figure 5.28 shows the variation of volumetric strain ($\epsilon_V = \epsilon_{xx} + \epsilon_{yy} + \epsilon_{zz}$) inside MS1-MS13 during cyclic shear in specimens of $\sigma'_{v0}=250$ kPa. The non-uniformity of volumetric strain inside specimen is evident in these figures. The variation of relative changes in volumetric strain inside the measurement spheres also implies the redistribution of voids and pore pressure inside the specimen during cyclic loading that would cause local migration of pore water through the voids in saturated specimens. The range, average, and non-uniformity parameter of ϵ_V is presented in Figure 5.29 and Figure 5.30 for specimens of $D_r=49$ and 87% , respectively. In case of $D_r=49\%$

and $CSR=0.095$, the non-uniformity parameter of ε_v at the instance of boundary shear strain of 3.75% is between 120-280% for different consolidated vertical stresses. For specimen of $\sigma'_{v0}=250$ kPa, $D_r=87\%$ and $CSR=0.475$ the non-uniformity parameter keeps increasing as load cycling proceeds.

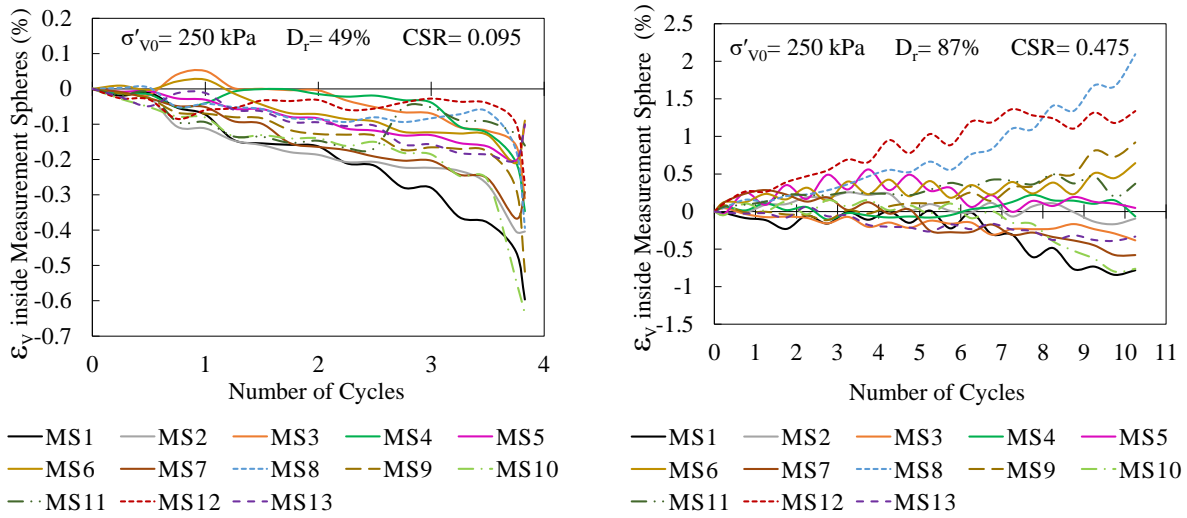


Figure 5.28 Volumetric strain measured inside MS1-MS13 during cyclic shear in DEM simulations of constant volume cyclic simple shear response of Pea gravel specimen: $\sigma'_{v0}=250$ kPa ($D_r=49\%$ and $CSR=0.095$ (left), $D_r=87\%$ and $CSR=0.475$ (right))

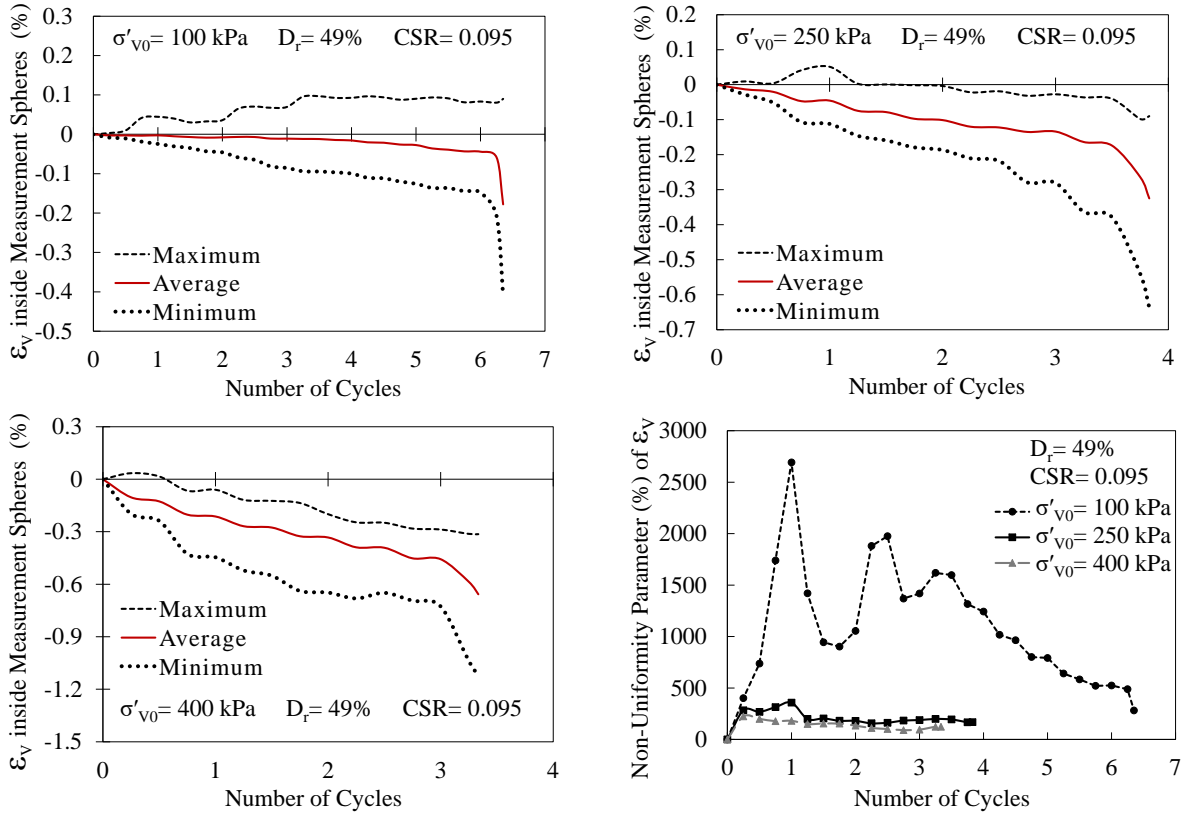


Figure 5.29 Distribution of volumetric strain inside MS1-MS13 and evolution of non-uniformity parameter in DEM simulations of constant volume cyclic simple shear response of Pea gravel specimen: $\sigma'_{v0}=100, 250, 400$ kPa, $D_r=49\%$ and $CSR=0.095$

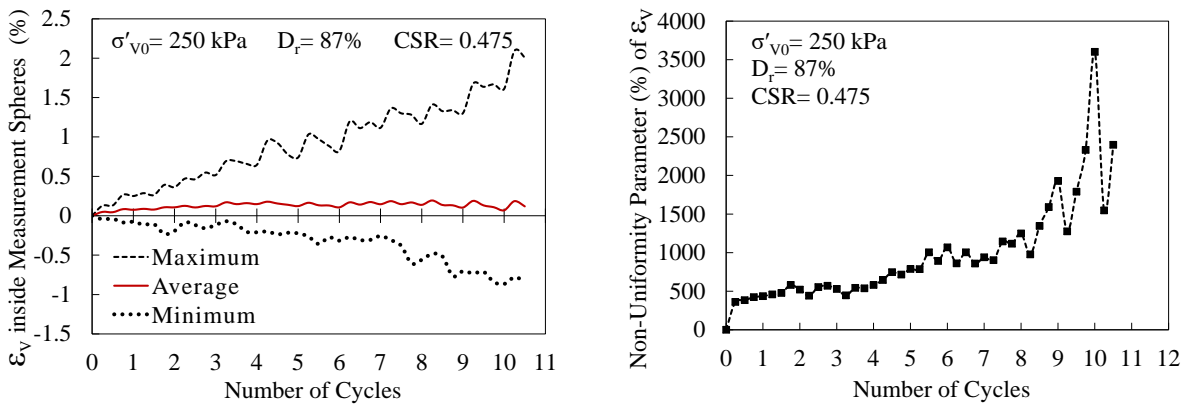


Figure 5.30 Distribution of volumetric strain inside MS1-MS13 and evolution of non-uniformity parameter in DEM simulations of constant volume cyclic simple shear response of Pea gravel specimen: $\sigma'_{v0}=250$ kPa, $D_r=87\%$ and $CSR=0.475$

5.6 Principal stress rotation during cyclic simple shear loading

Rotation of the principal stress direction during cyclic constant volume simple shear test is evaluated in this part for the simulated specimen consisting of spherical particles with the similar distribution of size and rolling resistance as the real Pea gravel particles. The stress tensor inside the central measurement (MS1) is considered and the eigenvalues and eigenvectors are calculated for the value and direction of the principal stresses. The angles between the direction of principal stress and three planes of XZ, XY, and YZ are monitored during cyclic shearing. These planes along with the positive direction of angle measurements are shown in Figure 5.31. The rotation of the principal stress during cyclic shear is shown in Figure 5.32 in term of the angles between the direction of principal stress and three planes of XZ, XY, and YZ.

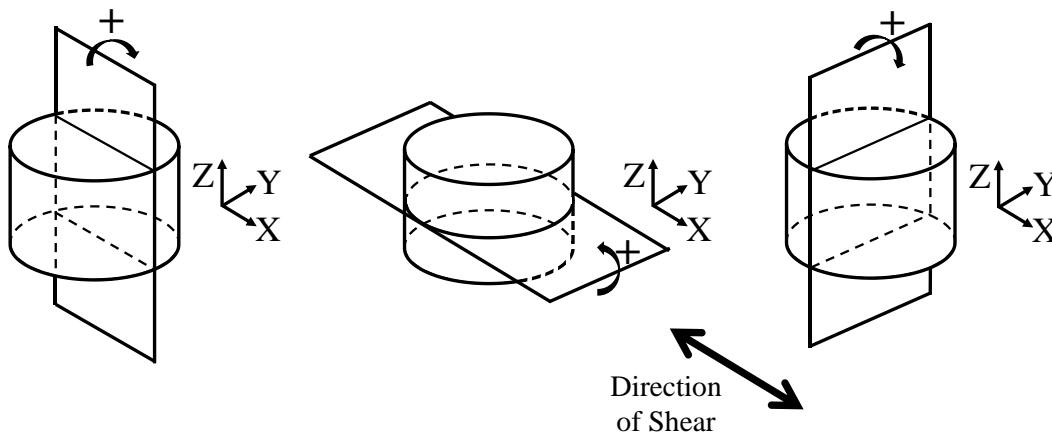


Figure 5.31 Positive direction for angle measurements regarding the XY, XZ and YZ planes

Similar to the observations of direction of principal stress during monotonic loading, due to three dimensional rearrangement and relative movement of particles, the major principal stress axis is not necessarily lies on the XZ plane and the major principal axis is oriented at a small angle from the XZ plane without any noticeable changes during shear. Figure 5.33 shows the evolution of θ_σ (the angle between the major principal axis of stress and vertical plane YZ) during cyclic

shear for all the simulated specimens. By reversal of shear direction during cyclic loading, θ_σ cycles between negative and positive values. The absolute value of θ_σ increases by increasing the number of cycles. In case of $D_r=49\%$ and $CSR=0.095$, it is observed that the increase in absolute value of θ_σ occurs more gradually for lower consolidated vertical stress. The absolute value of θ_σ reaches to about 40-50 degree at the initiation of liquefaction at the shear strain of 3.75%. In case of $D_r=87\%$ and $CSR=0.475$, the maximum absolute value of θ_σ during each cycle starts from about 40 degree during the first cycle and gradually increases toward 48 degree after 10 cycles of loading.

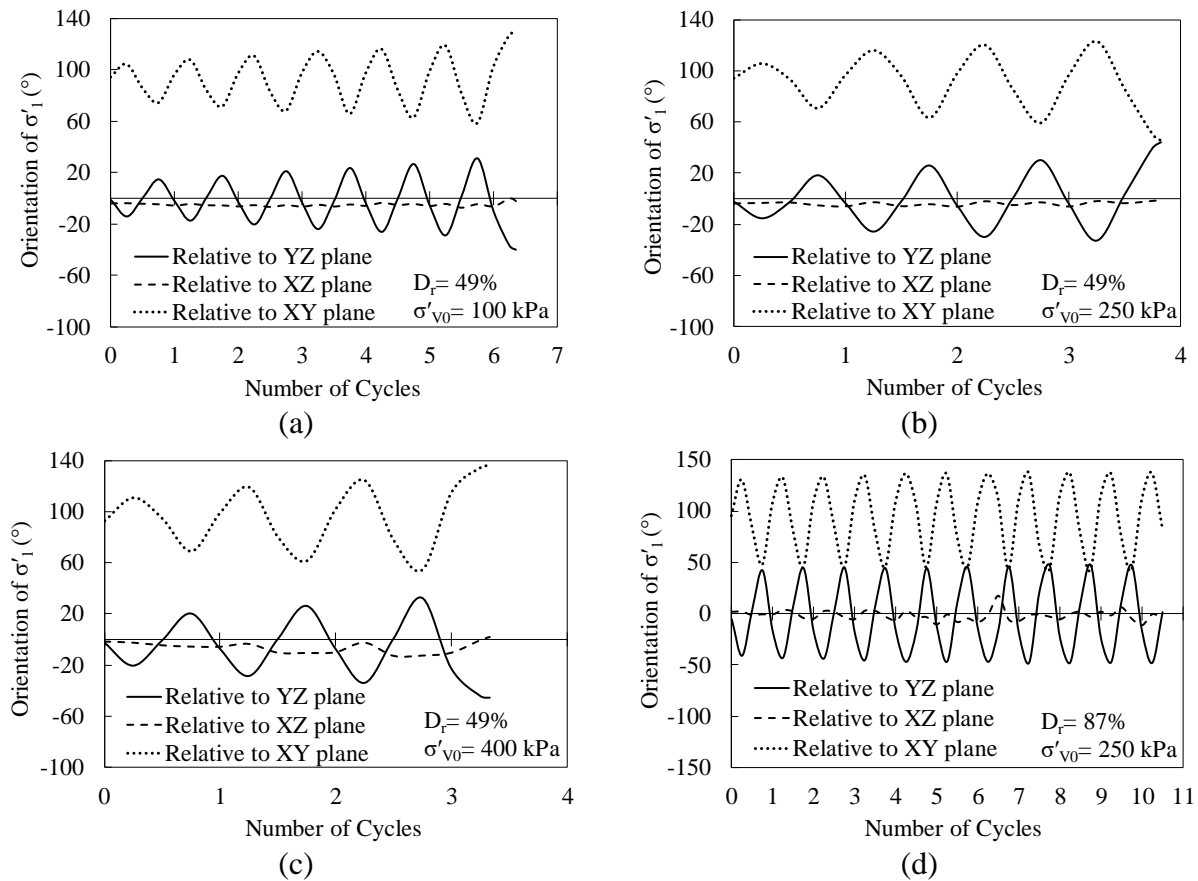


Figure 5.32 Angle between the direction of major principal stress and XZ, XY and YZ planes during cyclic shear in DEM simulations of constant volume cyclic simple shear response of Pea gravel specimen: (a), (b), (c) $\sigma'_{v0}=100, 250$ and 400 kPa, $D_r=49\%$, $CSR=0.095$, (d) $\sigma'_{v0}=250$ kPa, $D_r=87\%$, $CSR=0.475$

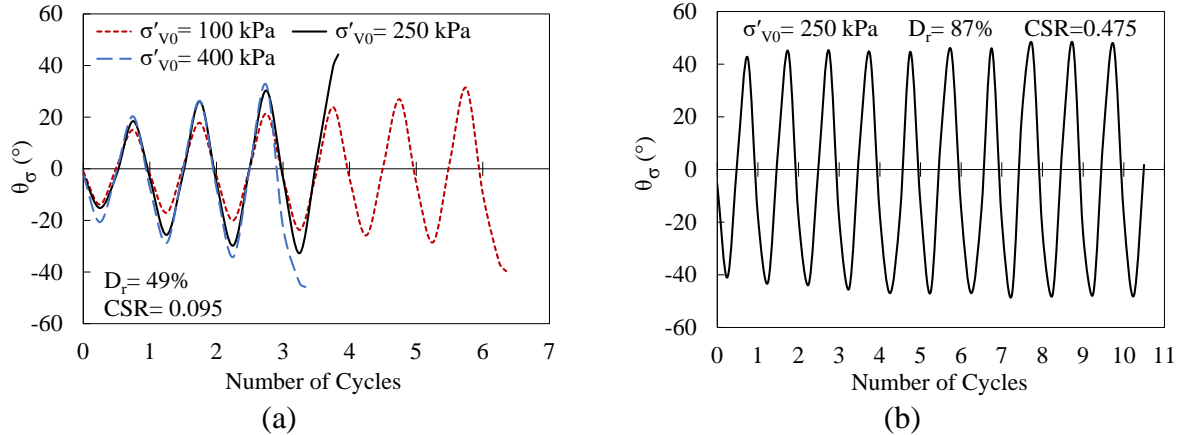


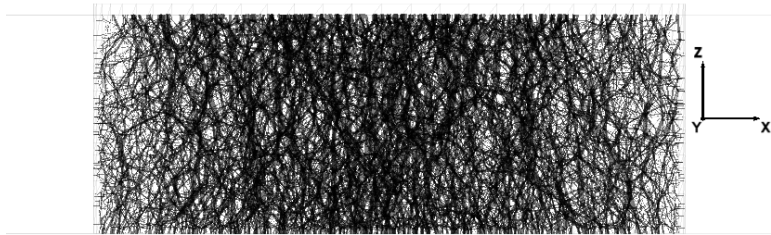
Figure 5.33 Evolution of angle θ_σ between the major principal stress axis and vertical plane YZ during cyclic shear in DEM simulations of constant volume cyclic simple shear response of Pea gravel specimen:: (a) $D_r=49\%$, $CSR=0.095$, (b) $D_r=87\%$, $CSR=0.475$

5.7 Evolution of fabric during cyclic simple shear loading

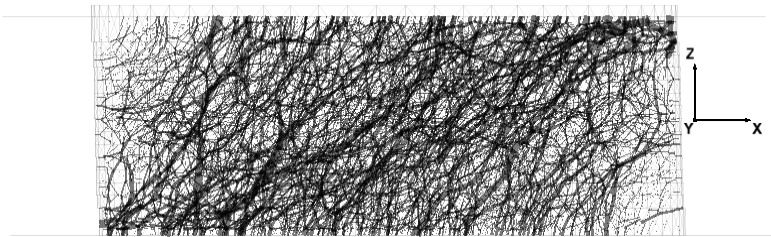
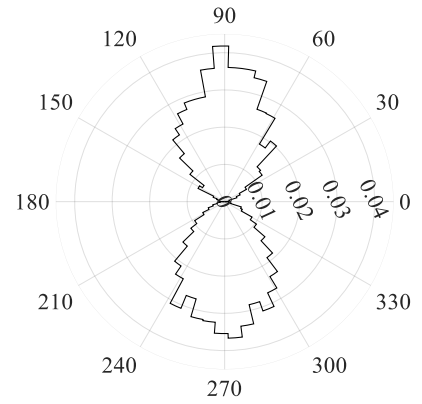
Behavior of granular materials, in particular liquefaction under cyclic loading, is significantly dependent on the internal structure (e.g., Ishibashi and Capar, 2003; Wijewickreme et al., 2005; Wei and Wang, 2016). It is also known that cyclic loading can cause changes in the internal structure of the granular materials (e.g., Sitharam, 2003; O’Sullivan et al., 2008; Sazzad and Suzuki, 2010). Therefore, to better understand the cyclic and liquefaction behavior of granular soils in order to develop robust constitutive models for soil liquefaction, it is of great importance to understand the evolution of microstructure during cyclic loading in granular soils.

Contact force network (force chain) at different instances during cyclic shear is shown in Figure 5.34 for specimen of $\sigma'_{v0}=250$ kPa and $D_r=49\%$ that is cyclically sheared with $CSR=0.095$. The corresponding polar histogram showing the distribution of contact normal directions are also included in this figure. In these histograms, only the strong contacts (those with magnitude of contact force one standard deviation above the average value) are considered. At the end of the consolidation and before shearing starts ($\gamma=0\%$), the strong force chains shown by thicker lines are mostly aligned in the vertical direction, which is also evident in the corresponding polar histogram.

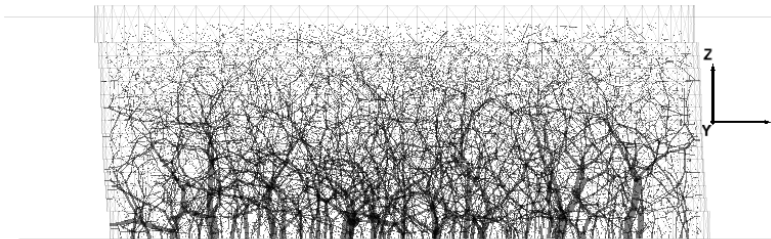
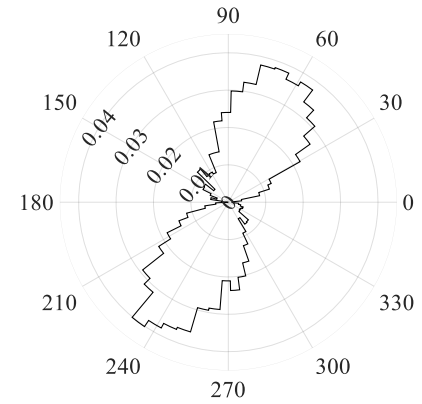
As loading cycles increase, it can be observed in Figure 5.34(b) that during the 4th loading cycle when the boundary shear strain becomes -3.75%, the strong force chains have inclined. At this instance, the generated pore pressure ratio is about 0.78 and therefore the strong force chains are smaller in number and magnitude than those at the beginning of the shear. As shearing continues during the 4th cycle after liquefaction initiated in the specimen, pore pressure ratio eventually reaches to 1 and the specimen loses its contacts with the top horizontal boundary. Only the gravitational force is now applied on the specimen and as it can be observed in Figure 5.34(c), the force chains becomes stronger at lower part of the specimen. The distribution of contact normal directions is also less anisotropic.



(a) $\gamma = 0\%$, $N = 0$, $r_u = 0$



(b) $\gamma = -3.75\%$, $N = 4$, $r_u = 0.78$



(c) $\gamma = -6.7\%$, $N = 4$, $r_u = 1$

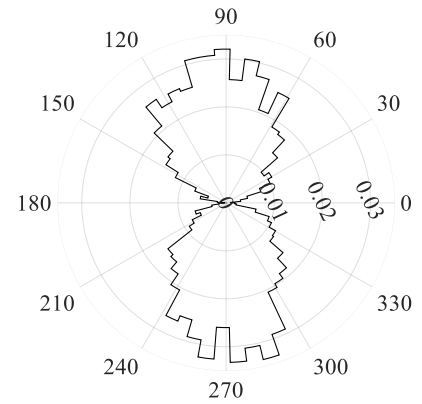
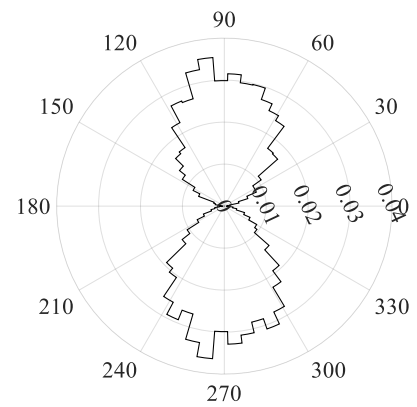
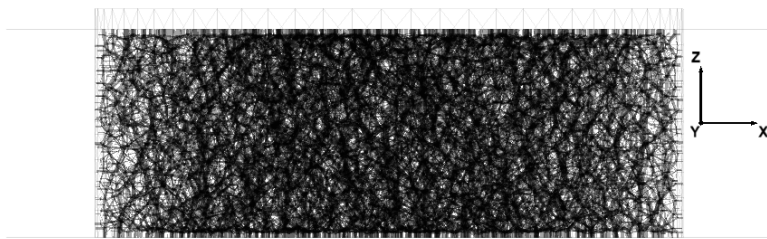
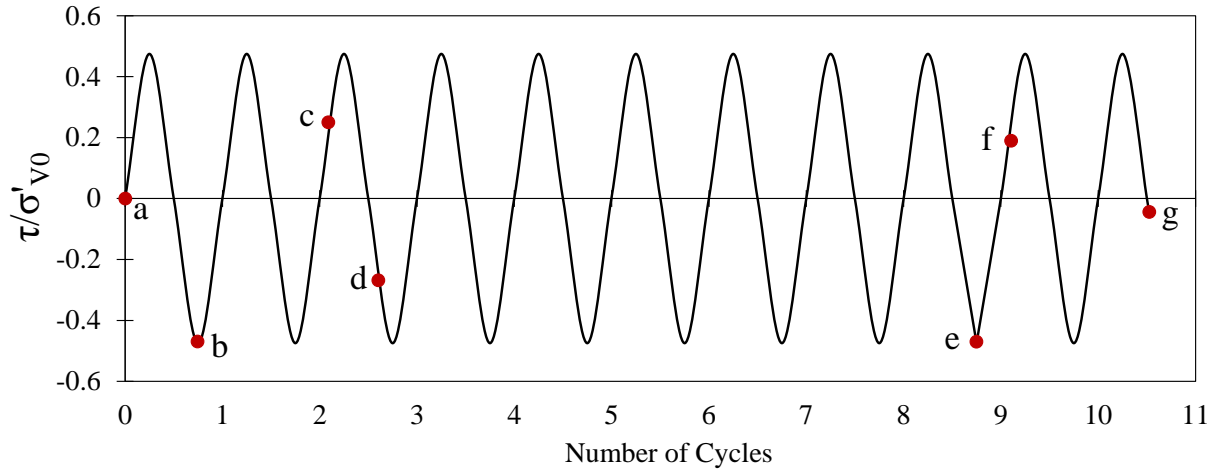
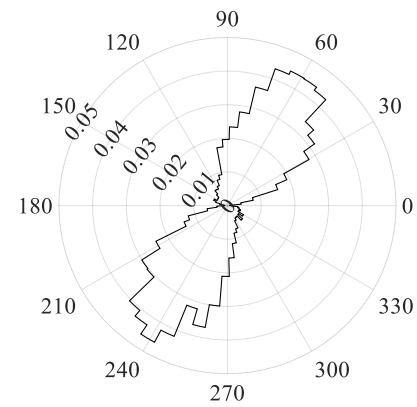
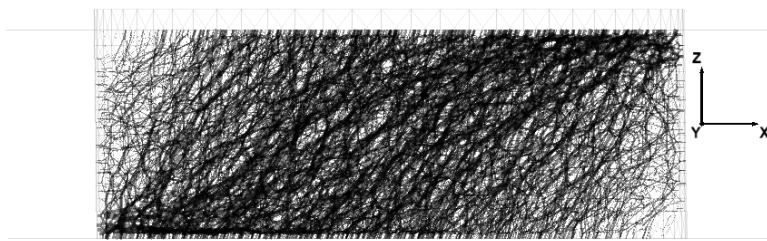


Figure 5.34 Contact force network (force chain) and corresponding polar histograms of contact normal directions at different instances during cyclic shear in DEM simulations of constant volume cyclic simple shear response of Pea gravel specimen ($\sigma'_{v0}=250$ kPa, $D_r=49\%$, and $CSR=0.095$)

For specimen of $\sigma'_{v0}=250$ kPa and $D_r=87\%$ that is cyclically sheared with $CSR= 0.475$, contact force network at different instances during cyclic shear is shown in Figure 5.35. Changes in inclination of strong force chains during cyclic shear by rotation of principal stress is evident in these figures. By accumulation of positive pore pure pressure inside the specimen, the number and magnitude of strong force chains decreases. Other interesting observation is that the hysteretic behavior during cyclic shear is also manifest in the evolution of contact force network: At points c, d and f during cyclic loading, the instantaneous boundary shear strain is about 0% while the specimen is experiencing a non-zero shear stress and consequently the strong force chains are inclined from vertical direction. At point g when shear strain is about 2.2% and the shear stress is very small (close to zero), the distribution of strong force chains are less anisotropic.

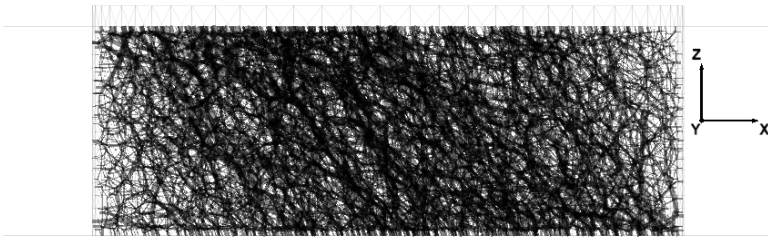


(a) $N=0$, $\gamma=0\%$, $r_u=0$

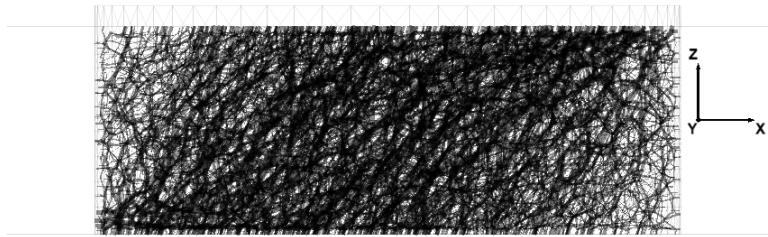
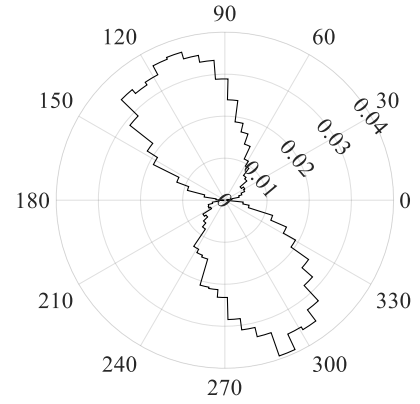


(b) $N=1$, $\gamma=-1.5\%$, $r_u=-0.04$

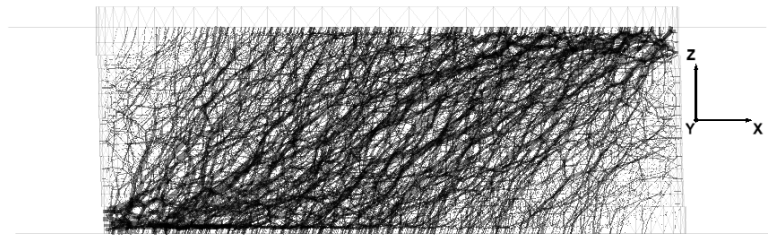
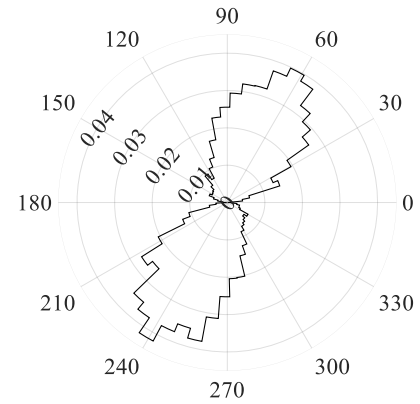
Figure 5.35 Contact force network (force chain) and corresponding polar histograms of contact normal directions at different instances during cyclic shear in DEM simulations of constant volume cyclic simple shear response of Pea gravel specimen ($\sigma'_{v0}=250$ kPa, $D_r=87\%$, and $CSR=0.475$)



(c) $N=3$, $\gamma \approx 0\%$, $r_u=0.16$



(d) $N=3$, $\gamma \approx 0\%$, $r_u=0.18$



(e) $N=9$, $\gamma = -3.75\%$, $r_u=0.1$

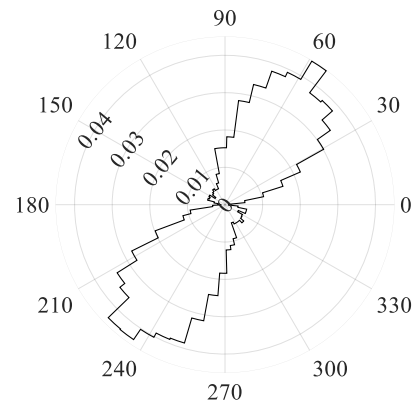
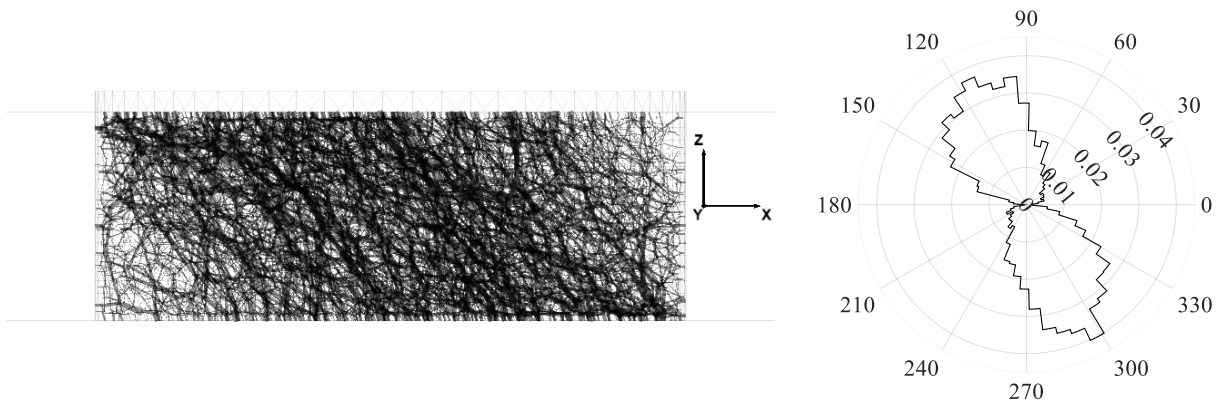
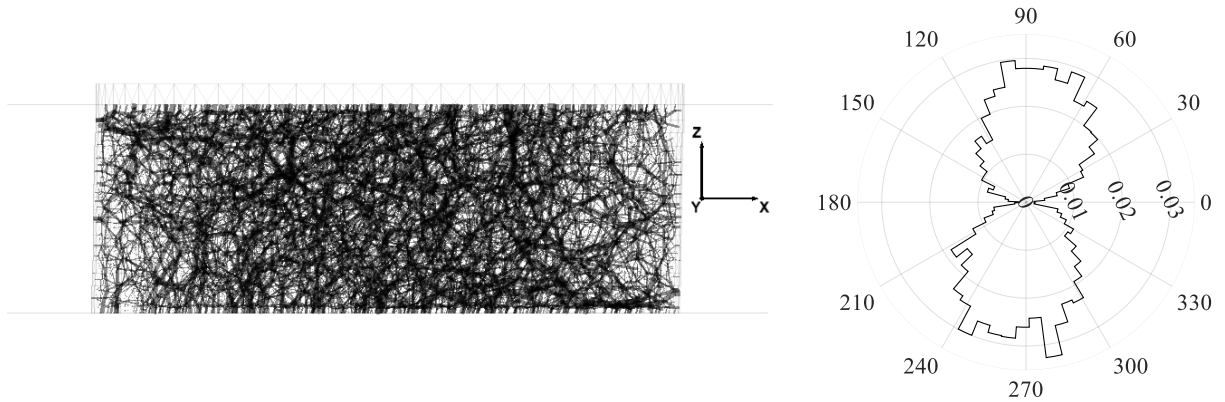


Figure 5.34 (continued).



(f) $N=10$, $\gamma \approx 0\%$, $r_u = 0.46$



(g) $N=11$, $\gamma = 2.2\%$, $r_u = 0.47$

Figure 5.34 (continued).

The evolution of fabric anisotropy, in terms of contact normal orientations, during cyclic shear is shown quantitatively in Figure 5.36 at instances of zero and maximum shear stress in both positive and negative directions. It should be mentioned that the fabric tensors are calculated here by considering all the inter-particle contacts (regardless of their relative force magnitude) in the specimen. For all cases of consolidated vertical stress with relative density=49% and CSR=0.095, fabric anisotropy at instances of zero shear stress is slightly lower than that at maximum shear stress. Overall, no substantial changes are observed in the degree of fabric anisotropy in specimen of $D_r=49\%$ and a slight decrease may be seen in fabric anisotropy as cyclic shear continues toward liquefaction. However, in specimen of $D_r=87\%$ under cyclic shear of CSR=0.475, fabric

anisotropy at instances of maximum shear stress increases as load cycling continues. Moreover, fabric anisotropy is noticeably higher at instances of maximum shear stress compared to those of zero shear stress. The changes in fabric anisotropy at instances of zero shear stress is relatively small and a slight increase is observed as number of loading cycle increases.

Changes in coordination number, as another indicator of fabric, during cyclic shear is presented in Figure 5.37. For specimens of $D_r=49\%$ sheared with $CSR=0.095$, after an initial drop in coordination number during the first quarter of first cycle, it follows an overall increasing trend with a very small rate so Z/Z_0 reaches to about 0.95 at the end of cycling. In case of $D_r=87\%$, coordination number decreases during cyclic shear with the tendency of the specimen to dilate and Z/Z_0 reaches to about 0.75 after 10 cycles of loading.

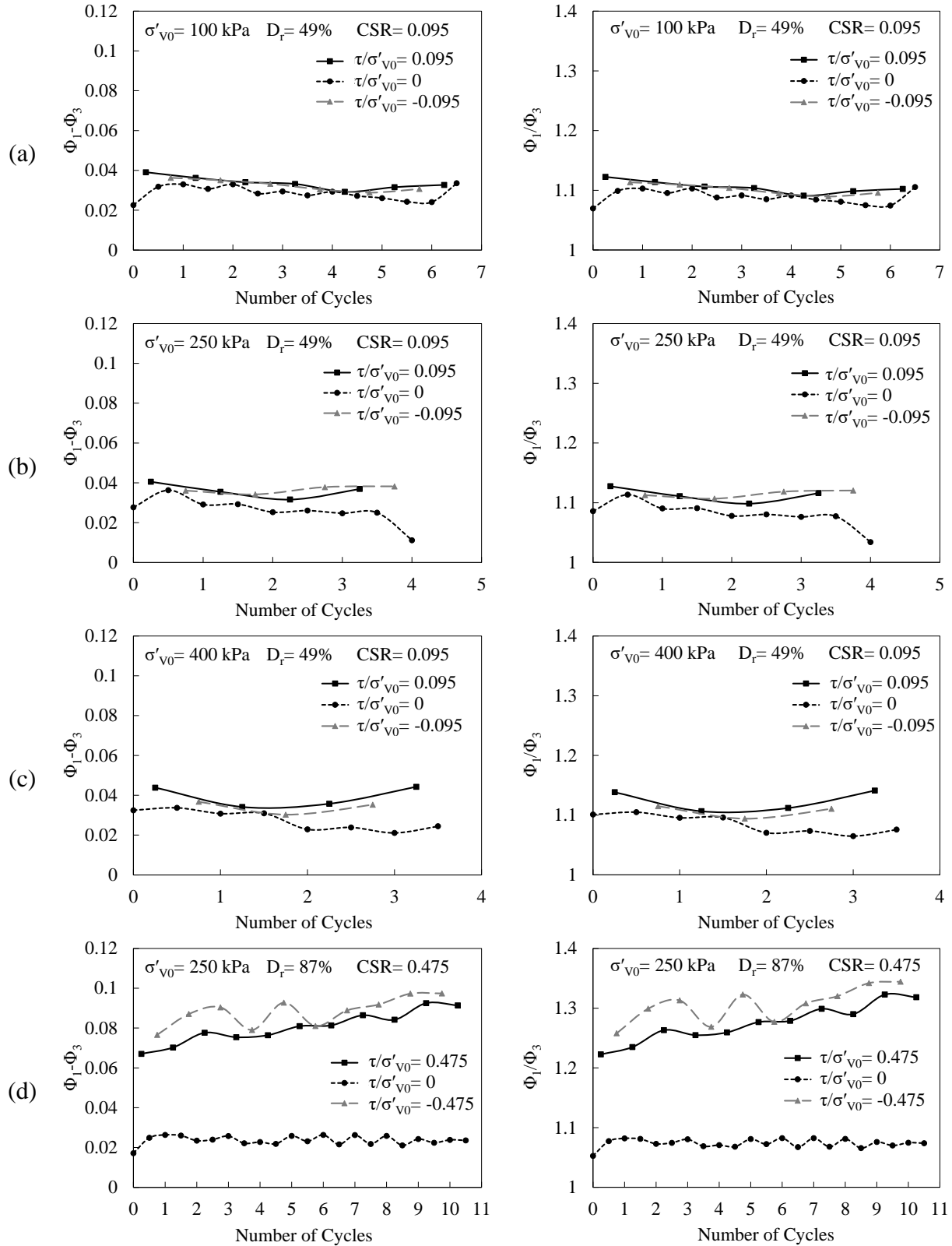


Figure 5.36 Evolution of degree of fabric anisotropy, in terms of contact normal orientations, during cyclic shear at instances of $\tau/\sigma'_{v0} = 0$ and $\pm CSR$ in DEM simulations of constant volume cyclic simple shear response of Pea gravel specimen: (a)-(c): $D_r = 49\%$, and $CSR = 0.095$, (d) $D_r = 87\%$, and $CSR = 0.475$

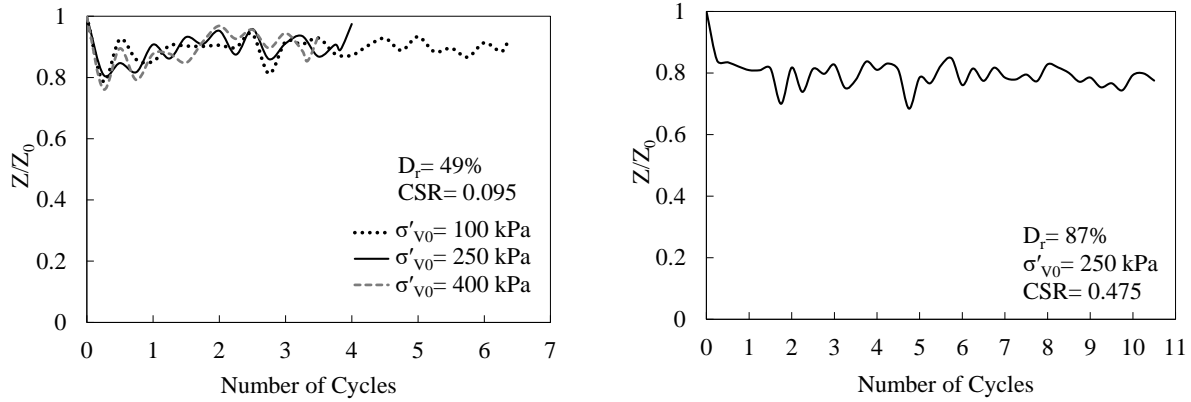


Figure 5.37 Evolution of normalized coordination number in DEM simulations of constant volume monotonic simple shear response of Pea gravel specimen: $D_r=49\%$, $CSR=0.095$ (Left), $D_r=87\%$, $CSR=0.475$ (Right)

5.8 Effect of the non-uniform distribution of rolling resistance

To demonstrate the importance of considering the non-uniformity of shape particles in simulating the cyclic shear response of actual soils, the macroscopic behavior of simulated specimens of uniform versus non-uniform distribution of rolling resistance are compared and presented for the case of $\sigma'_{v0}=250$ kPa, $D_r=49\%$ and $CSR=0.095$.

It was shown in Chapter 4.10 that having a specimen prepared and consolidated with the non-uniform distribution of rolling resistance coefficients (μ_r), setting a uniform value of $\mu_r=0.09$ during shear will result in similar macroscopic monotonic behavior. However, the specimen with this uniform value of μ_r through all stages of simulation, even though has the same void ratio, behaves quantitatively different during monotonic shear loading. The cyclic macroscopic behavior of those specimens is compared in this part. As illustrated in Figure 5.38, the specimens prepared and consolidated with the realistic non-uniform distribution of μ_r show very similar cyclic behaviors in both qualitative and quantitative ways. However, the behavior of the specimen with uniform value of $\mu_r=0.09$ through all stages of simulation deviates from those. This specimen experienced more loading cycles before reaching the single amplitude shear strain of 3.75% which

is considered in this study as the instance of liquefaction initiation. These differences between the cyclic shear responses can be attributed to the different internal structures of the specimens at the beginning of the shear. Different researchers (e.g., Ishibashi and Capar (2003), Wijewickreme et al. (2005)) conducted experimental studies to investigate the effect of the initial soil fabric on the cyclic response of sand specimens. By comparing the cyclic behavior of sand specimens prepared using different sample preparation techniques, they observed that the internal structure of the soil has a paramount effect on the mechanical response, including liquefaction susceptibility. In the DEM simulations presented in this section, despite having the same void ratio, the different distributions of rolling resistance coefficient lead to a difference in distribution of voids and contacts in the simulated specimens. Such difference in fabric at the end of the consolidation is responsible for the different subsequent behavior during cyclic shear. Further investigation at the micro scale is required to quantitatively support this claim.

These observations further corroborate the importance of incorporating the non-uniformity of shape particles by considering a non-uniform distribution of rolling resistance coefficients for the equivalent spherical particles in the simulations.

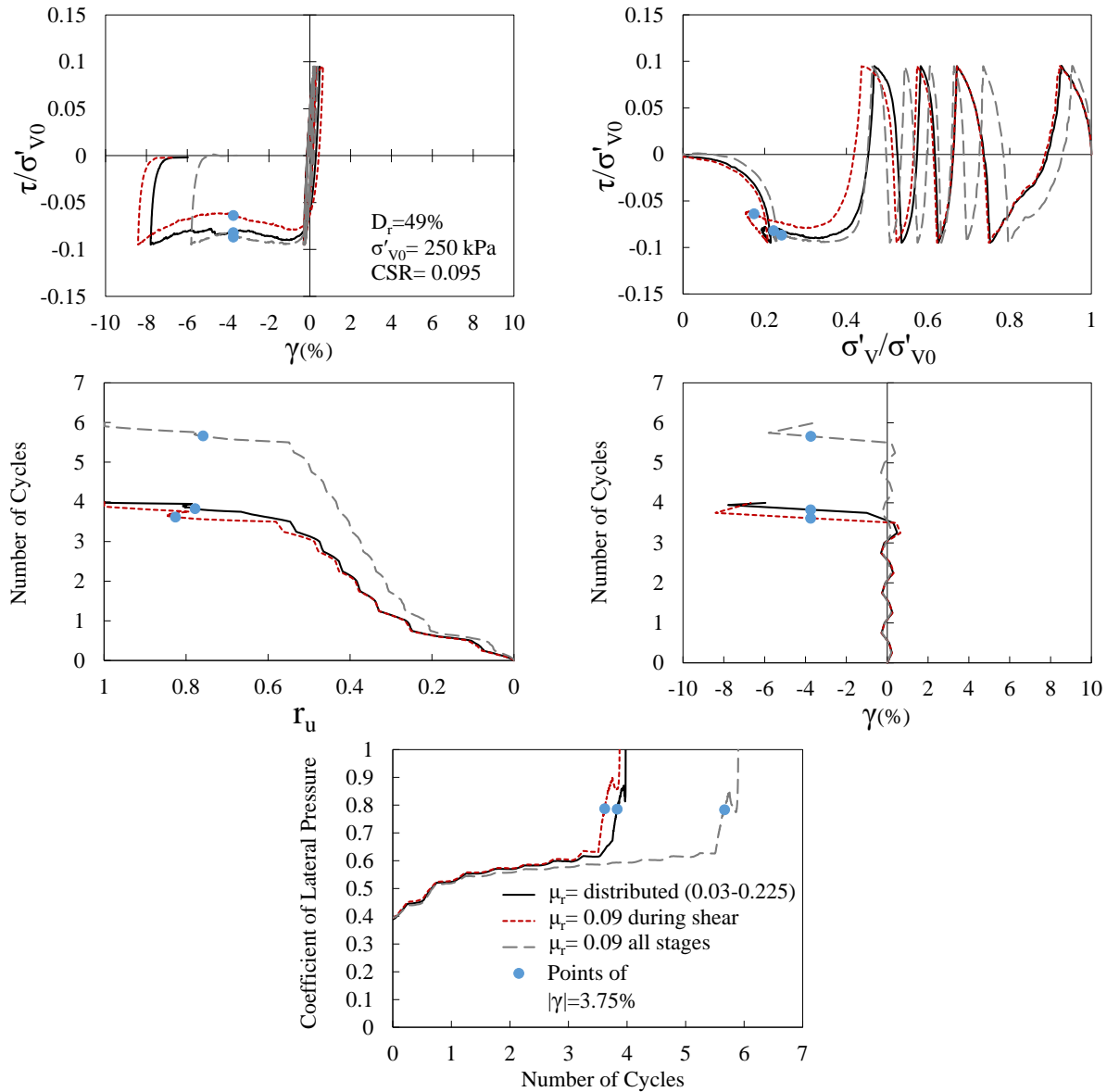


Figure 5.38 Comparison of the results from DEM simulations of constant volume cyclic simple shear response of Pea gravel specimen for the cases of distributed versus uniform rolling resistance coefficient ($\sigma'_{v0}=250$ kPa, $D_r=49\%$ and $CSR=0.095$)

5.9 Conclusions

The cyclic constant volume simple shear response of Pea gravel in stacked ring simple shear test was investigated in this chapter using discrete element method and by simulating a more realistic representation of boundary conditions and tested soil specimen. A summary of observations and conclusions is presented as follows:

- The capability of the developed discrete element model in predicting the cyclic shear response of actual soil specimen was observed. The hysteretic shear stress-strain behavior, degradation of shear modulus and accumulation of generated pore pressure ratio and shear strain observed during cyclic shear loading of experimental specimen are captured well by the DEM simulations of this study.
- Principal stresses keep rotating and oscillating during the cyclic simple shear loading. By accumulation of shear strain during stress-controlled cyclic shear, the maximum angle between the major principal axis and the vertical direction also increases. For specimens of $D_r=49\%$ and $CSR=0.095$, this value starts from $15-20^\circ$ at the first peak of shear stress and reaches to $40-45^\circ$ during the cycle that liquefaction triggers. For specimen of $\sigma'_{v0}=250$ kPa, $D_r=87\%$ with high value of $CSR=0.475$, the increase in this angle is more gradual; it starts from about 40° during the first loading cycle and reaches to 48° after 10 cycles.
- Stress-induced fabric anisotropy, in terms of contact normal orientations, in the cyclically sheared specimens was qualitatively and quantitatively investigated. Rotation and oscillation of the inclination of strong force chains are seen by proceeding of the cyclic shear and consequent rotation of principal stress direction. Quantitatively, the degree of fabric anisotropy at points of maximum shear stress (peaks of shear cycles) are higher than that at the points of zero shear stress. This difference, and generally the changes in degree of fabric anisotropy, is more evident in specimen of $D_r=87\%$ with high value of $CSR=0.475$. For this specimen, the degree of anisotropy at points of maximum shear stress increases as cyclic proceeds. The corresponding increase at the point of zero shear stress is smaller.

- The importance of incorporating the non-uniformity of particle shapes by considering a distribution of rolling resistance coefficient is confirmed again in this chapter by comparing the cyclic response of specimens with uniform and distribute values of rolling resistance coefficient. Having all the other parameters the same, these specimen with the same void ratio exhibit quantitatively different behaviors; which can be attributed to differences in their initial internal structure that arises from different distributions of rolling resistance coefficient during the preparation and consolidation stages.
- Comparing the results of stress measurements at the specimen boundaries and inside the specimen core, quantitative differences were observed between the soil specimen response measured at the boundaries and specimen core. More specifically:
 - Despite of applying a symmetric cyclic shear loading with a constant CSR at the boundaries, it was observed that the soil at the specimen core experiences a non-symmetric shear cycles with variable CSR.
 - The calculated pore pressure ratio based on the changes in vertical stress at horizontal boundaries overestimates the actual positive pore pressure ratio calculated based on the changes in mean effective pressure inside the specimen core. Therefore, determining pore pressure ratio based on boundary measurements (as done in the laboratory) provides a conservative estimation of the actual positive pore pressure ratio at the specimen core.
 - For specimen of $D_r=49\%$ cyclically sheared with $CSR=0.095$, the average value of coefficient of lateral pressure calculated based on the boundary measurements (by assuming the same value in all radial directions) underestimates the ones measured inside the specimen core in both parallel (K_x) and perpendicular (K_y) to the shear

- direction. On average for all the consolidated vertical stresses, the boundary measured coefficient of lateral pressure underestimates K_x and K_y values inside the specimen core by up to 25% and 13%, respectively.
- For specimens of $D_r=49\%$ and $CSR=0.095$, it was observed that K_x is, on average, 1.2 times larger than K_y .
 - For specimen of $\sigma'_{v0}=250$ kPa and $D_r=87\%$ cyclically sheared with $CSR=0.475$, K_x experienced larger amplitudes of fluctuations than K_y , in a way that the ratio of K_x to K_y (K_x/K_y) is, on average, 1.25 and 0.92 at instances of peak and zero shear stress, respectively. The boundary measurements leads to underestimation of the maximum K_x values by up to 22%.
- Evaluating the non-uniformity of different quantities measured inside measurement spheres MS1-MS13 located across the cross sectional area and covering about the middle two third of the specimen height, the following observations are made:
 - Non-uniformity in distribution of stress ratio τ_{xz}/σ'_{zz0} follows an overall decreasing trend as the specimens of $D_r=49\%$ are cyclically sheared toward liquefaction. Higher rate of decrease is also observed for lower consolidated vertical stress. In case of specimen of $\sigma'_{v0}=250$ kPa and $D_r=87\%$ cyclically sheared with $CSR=0.475$, the non-uniformity parameter for distribution of stress ratio τ_{xz}/σ'_{zz0} remains in the same level and fluctuates between 30-50% during 10 cycles of shear.
 - The variation of $(\tau_{xz} - \tau_{xz0})/\sigma'_{zz0}$ inside MS1-MS13 is monitored for the specimen of $\sigma'_{v0}= 250$ and $D_r=49\%$ to evaluate the distribution of applied stress ratio respect to the initial state at the end of consolidation. In addition to the non-uniform distribution of stress ratio, non-symmetrical cycles of stress ratio are observed at these locations.

Overall, despite a symmetric cyclic shear loading of constant CSR applied at the boundaries, the experienced shear cycles at different locations inside the specimen can be non-symmetric and with variable CSR. Although the experienced shearing cycles inside the specimen is, on average, similar to the one applied at the boundaries, different locations within the specimen experiences higher or lower shear stress ratios. This leads to a non-uniform cyclic response within the specimen that can affect the overall behavior of the specimen as a whole. According to Shen et al. (1978), creation of an external moment in the lack of complementary shear stress on the lateral boundaries during shear generates additional stresses at different locations in the specimen to balance this moment; which causes the observed non-symmetrical cycles of stress ratio at difference points in the specimen.

- Non-uniform distribution of τ_{xz}/σ'_{zz} within the specimen was also observed. Although the values of τ_{xz}/σ'_{zz} at the instances of peak shear stress (peaks of the shearing cycles) inside all the measurement spheres increase as the number of cycles increases, there were quantitative differences among them. The results show that the boundary measured value of τ_{xz}/σ'_{zz} is a good estimate of the average τ_{xz}/σ'_{zz} values within the specimen.
- The existing non-uniformities in distribution of τ_{xz}/σ'_{zz} implies that at each instance during cyclic loading, the stress state is not necessarily the same at different locations within the specimen.
- Generated pore pressure ratio is also distributed non-uniformly inside the specimen for all cases of σ'_{v0} , D_r and CSR. For all specimens, the pore pressure ratio calculated based on the changes in vertical stress at horizontal boundaries is close to the maximum

- true positive pore pressure ratio inside MS1-MS13, and generally overestimates the positive pore pressure ratio generated inside the specimen during cyclic shearing. It can be concluded that determining pore pressure ratio based on the change of vertical effective stress on the top cap, as done in laboratory, leads to a conservative estimation of the actual pore pressure ratio generated at different locations inside the specimen.
- It is observed that shear strain is developed non-uniformly inside the specimen. The boundary measured shear strain value for specimens of $D_r=49\%$ and $CSR=0.095$ is in the range of shear strain values at MS1-MS13 and is, on average, 1.5 and 2.1 times

Chapter 6

Conclusions and Recommendations for Future Research

The major findings of this dissertation are summarized in this chapter, followed by suggestions for future research.

6.1 Development of the DEM Model for Constant Volume Simple Shear Test

- 3D DEM simulations of constant volume monotonic simple shear test of uniform and rounded particles, by considering a realistic algorithm for modeling the movement of stacked rings, indicated that sliding and/or rolling of the particles at the interface between the specimen and horizontal boundaries reduces the level of shear transferred into the specimen. Consequently, the true simple shear deformation may not be imposed on the specimen, and the experimental data of shear displacements and forces cannot be confidently used to reliably evaluate the simple shear behavior. Therefore, extra caution should be taken and necessary modifications should be applied for testing granular material with particles of low rolling resistance (e.g. rounded particles) and/or low friction to ensure proper imposition of simple shear deformation on the specimen.
- Several modifications were numerically examined to ensure the complete transfer of shear from the moving boundary into the steel spheres specimen with particles of low friction and no rolling resistance. It is concluded that steel spheres in contact with planar boundaries

should be attached to them (e.g. by using glue) in order to avoid any slippage and rolling at these boundaries and obtaining reliable data from the experiments.

- Numerically increasing the friction and rolling resistance of the spheres in order to preliminary mimic the soil particles, it was observed that fixing the movement of the very top and bottom rings to their adjacent caps can ensure a decent imposition of simple shear deformation on the specimen.
- According to these findings and to obtain reliable data from the laboratory simple shear tests of Pea gravel for validation of 3D DEM simulations of this study, relatively thicker rings (about 3 times as thick as the other ones) fixed to the upper and lower caps were used at the most ends of the specimen. The same configuration of the rings was then modelled in the DEM simulations.
- Incorporating both the irregularity and non-uniformity of actual soil particle shapes by assigning a distribution of rolling resistance to the equivalent spherical particles was shown to be crucial in simulating the actual soil assembly. Despite the simplification of representing the soil particles by spheres in order to reduce the computational effort, considering a distribution of rolling resistance coefficients (determined from particles shape characteristics) accounts for the diversity of particle shapes in soil and provides a more realistic representation of soil assembly for the numerical simulation. The results of such simulations at micro- and micro-scales are more reliable in predicting the behavior of actual soil specimen.

6.2 Constant Volume Monotonic Simple Shear Response of Pea Gravel at the Micro- and Meso-scale

A realistic representation of soil assembly in terms of total number, size, and rolling resistance distribution was used in the DEM simulations to study the constant volume simple shear response of Pea gravel. Different aspects of the soil behavior in constant volume monotonic simple shear conditions were investigated at micro-and meso-scale: stress state inside the specimen, rotation of principal stresses, non-coaxiality and fabric evolution. Non-uniformities in distribution of stress and strain inside the specimen and their comparison with the boundary measured values were also investigated. A summary of the findings is presented as follows:

- Experimentally validated 3D DEM model of this study was shown to be capable of providing a satisfactory prediction of the constant volume monotonic simple shear response of actual specimen at different levels of relative density and consolidated vertical stress. The good agreement between the DEM simulation and the corresponding experimental results can be seen in Figure 6.1. The effects of vertical stress and relative density on the macroscopic response were also captured well by the DEM model and were consistent with the laboratory results shown by Hubler (2017).

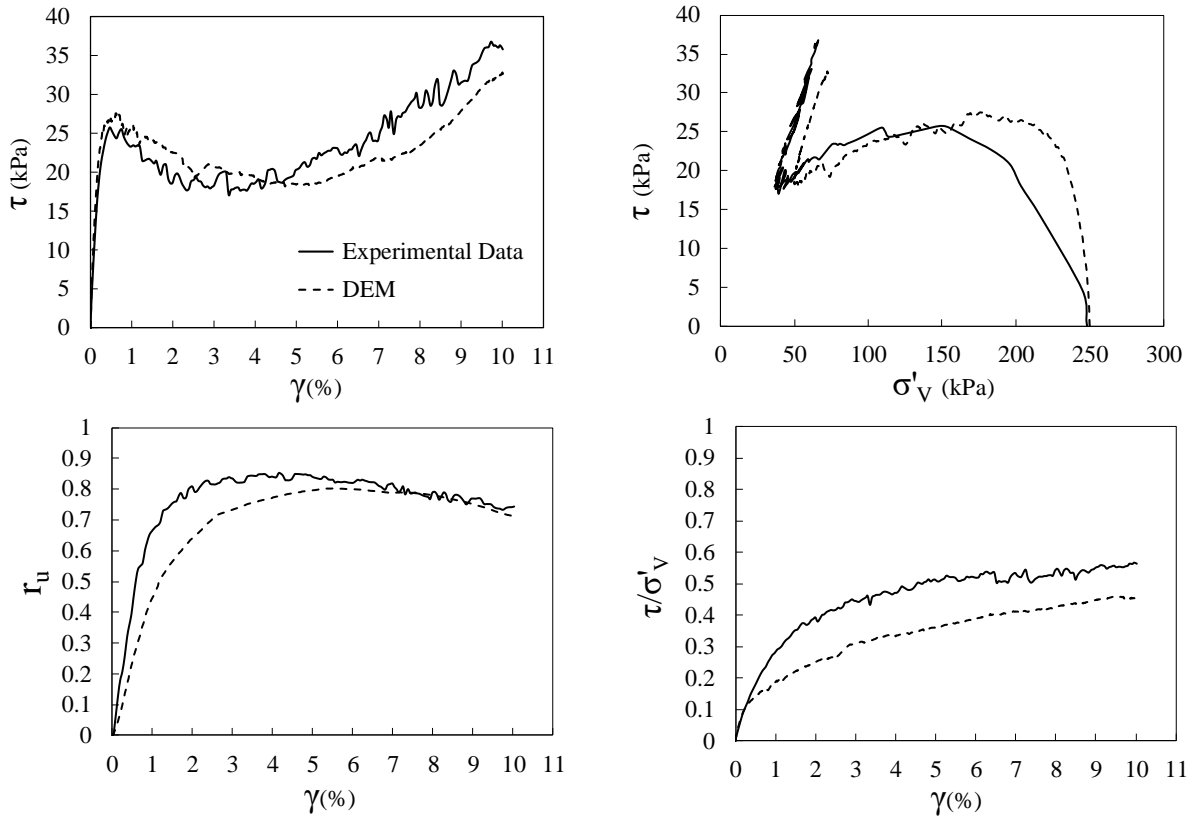


Figure 6.1 Comparison of the results from DEM simulation of constant volume monotonic simple shear test to the corresponding experimental results for Pea gravel specimen ($\sigma'_{v0}=250$ kPa, $D_r=49\%$)

- For all cases of consolidated vertical stress and relative density, boundary measured peak shear stress (τ_p) and stress ratio (τ/σ'_v) are lower than those measured inside the specimen core. The boundary measured peak shear stress and stress ratio underestimate the peak shear stress and stress ratio at the specimen core by an average of 33% and 13%, respectively. The rate of strain hardening during shear is observed to be similar for measurements at boundaries and inside the specimen. For specimens of $D_r=49\%$, the rate of strain softening is lower for measurements at the boundaries compared to those measured at the central region of the specimen.

- Determining pore pressure ratio based on the changes in the vertical stresses measured either at boundaries or at the specimen core leads to a more positive value than the true pore pressure ratio that generated inside the central part of the specimen.
- Based on the DEM simulation results, it is concluded that the boundary measurements in constant volume monotonic simple shear test in the lab provides a conservative estimate of the soil strength and generated pore pressure at the specimen core.
- The coefficient of lateral pressure (measured at the specimen core) parallel to the shearing direction (K_x) is larger than the one in the perpendicular direction (K_y). The difference between them during shear is larger for the higher relative density. The average value of K_x/K_y at the end of consolidation is 1.14 and 1.02 for specimens of $D_r=49\%$ and 87% , respectively. As shearing proceeds, the difference between K_x and K_y increases and at the shear strain of about 10%, the average value for K_x/K_y reaches to 1.23 and 1.48 for specimens of $D_r=49\%$ and 87% , respectively.
- Coefficient of lateral pressure determined as average value at the boundaries is mostly close to the one perpendicular to the direction of shear (k_y) measured at the specimen center for $D_r=49\%$ and is mostly close to the K_{avg} measured at the specimen core for $D_r=87\%$.
- Evaluating the stress state at the specimen core during the monotonic constant volume simple shear loading, it was shown that the stress path for neither the horizontal plane nor the vertical plane is the same as the one for the plane of maximum shear stress or the plane of maximum stress obliquity during the whole period of shear (These stress paths are shown in Figure 6.2 as an example for specimen of $\sigma'_{v0}=250$ kPa, $D_r=49\%$). Therefore, it is not reasonable to make the same assumption on the state of stress at the vertical or horizontal planes regardless of the level of shear strain. The DEM simulation results also

suggest that the level of density of the specimen can affect the level of shear strain at which each of the assumptions may be realistic and can be confidently used in interpretation of simple shear test data.

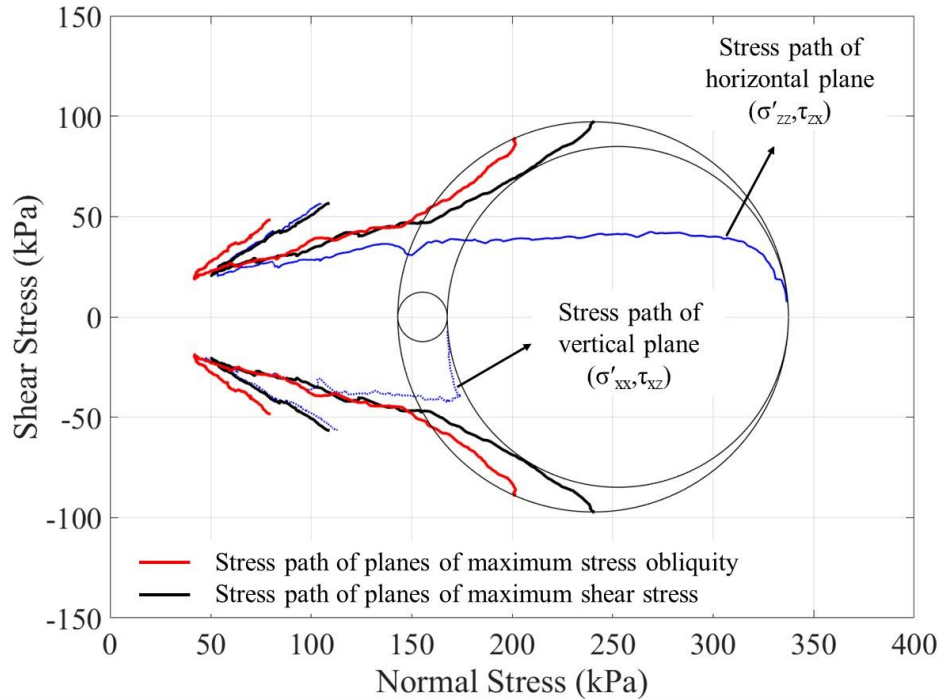


Figure 6.2 Mohr's circles of stress at the end of consolidation and the stress paths during shear in DEM simulations of constant volume monotonic simple shear response of Pea gravel specimen ($\sigma'_{v0}=250$ kPa, $D_r=49\%$)

- Principal stresses rotate during shear in a way that the orientation of the major principal direction gradually deviates from vertical direction and get inclined at about $45-50^\circ$ from vertical direction at higher shear strains. The rotation of principal stress directions happens more gradually in specimens of lower relative density (Figure 6.3).

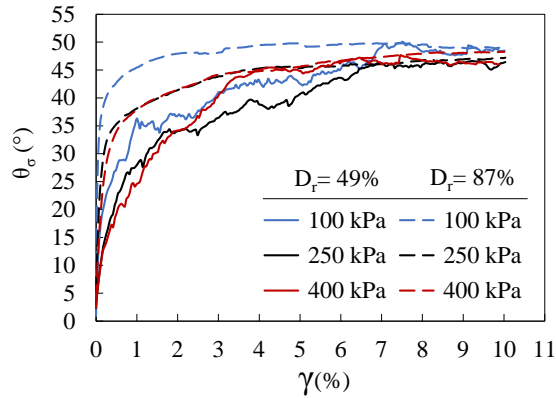


Figure 6.3 Evolution of angle θ_σ between the major principal stress axis and vertical direction during shear in DEM simulations of constant volume monotonic simple shear response of Pea gravel specimen

- Non-coaxiality of principal directions of stress and strain rate was evaluated during monotonic loading up to 10% boundary shear strain and by comparing the orientation of the major principal stress (θ_σ) and strain rate (θ_ε) inside the specimen core. Significant difference of about 45° between θ_σ and θ_ε at the beginning of the shear gradually decreases as shear proceeds, and principal direction of stress rotates until at higher shear strains, θ_σ grows slightly larger than θ_ε (the difference is about 5° at the most).
- The internal structure (fabric) of the specimen changes during the monotonic shear. The orientation of strong force chains rotates to get aligned with the direction of the major principal stress. At the end of consolidation and before any shearing, the degree of fabric anisotropy, in terms of contact normal orientations, is almost the same in all specimens of different relative density and vertical stress; it is slightly smaller for the specimen of higher relative density, and for each level of relative density, it is slightly higher for larger consolidated vertical stress. However, the degree of fabric anisotropy increases by continuation of shear, with greater values and higher rate of increase in specimen of larger relative density.

- Comparing the different measurement quantities at various locations across the cross sectional area and covering about the middle two third of the specimen height, the results of DEM simulations showed non-uniform distributions of these quantities inside the specimen during shear. The range of the measured values inside the specimen was also compared with the corresponding boundary measured values to assess how reliable the boundary measurements (as done in the laboratory) are in determining the response of the specimen. Summary of the major findings are as follows:
 - Despite the differences in the evolution of void ratio inside various regions within the specimen which leads to redistribution of void ratio, the level of non-uniformity remains about the same during shear. The redistribution of the void ratio within the specimen implies that pore spaces changes during shear. In presence of pore water, this would lead to local migration of water through the pore spaces as a result of the pore pressure redistribution that takes place by the redistribution of voids in the specimen.
 - For all cases of consolidated vertical stress and relative density, boundary measured vertical effective stress (σ'_v) is between the minimum and average measured values inside the specimen at the end of consolidation. Boundary measured vertical effective stress (as done in laboratory) underestimates the actual consolidated vertical effective stress at various locations inside the specimen by maximum of 18-26% for looser specimens and by maximum of 14-19% for denser specimens. No specific effect is observed of the level of applied vertical stress. As shear proceeds, boundary measured vertical effective stress (σ'_v) becomes closer to the lower bound of the σ'_{zz} measured inside the specimen. At the shear strain of about 10%, the boundary measured value underestimates the actual vertical effective stress inside the specimen by the maximum

- of 23-26% in denser specimen; which is higher than that at the beginning of shear. The level of underestimation in looser specimen does not change significantly during shear and remains about the same as that at the end of consolidation.
- The boundary measured stress ratio (τ_h/σ'_v) is observed to be between the minimum and average values of internal stress ratio (τ_{xz}/σ'_{zz}), approaching the average value at higher shear strains. Overall, determining the stress ratio based on the measurement of shear and vertical stresses on the horizontal boundaries, as is done in laboratory, leads to overestimation of the actual stress ratio at some locations inside the specimen. At shear strain of about 10%, the boundary measured stress ratio overestimate the minimum local stress ratio inside the specimen by an average of 20%.
 - Generated pore pressure distributed non-uniformly inside the specimen, which implies that in presence of pore water in saturated specimen, there would be local migration of pore water through voids from locations of higher to lower pore pressure.
 - Non-uniform distribution of shear strain (γ_{xz}) was observed inside the specimen. For all cases of consolidated vertical stress and relative density, the induced shear strain at various locations within the specimen is smaller than the boundary shear strain. It can be concluded that the boundary measured shear strain (as done in laboratory) overestimate the induced shear strain inside the specimen, and this difference needs to be accounted for in interpretation of the experimental results.

6.3 Constant Volume Cyclic Simple Shear Response of Pea Gravel at the Micro- and Meso-scale

- Experimentally validated 3D DEM model of this study, which is essentially the same for monotonic and cyclic loading conditions, was shown to be capable of predicting the cyclic shear response at different levels of consolidated vertical stress and relative density. The good agreement between the DEM simulation and the corresponding experimental results can be seen in Figure 6.4. The hysteretic shear stress-strain behavior, degradation of shear modulus and accumulation of generated pore pressure ratio and shear strain during cyclic shear loading of experimental specimen are captured well by the DEM simulations.

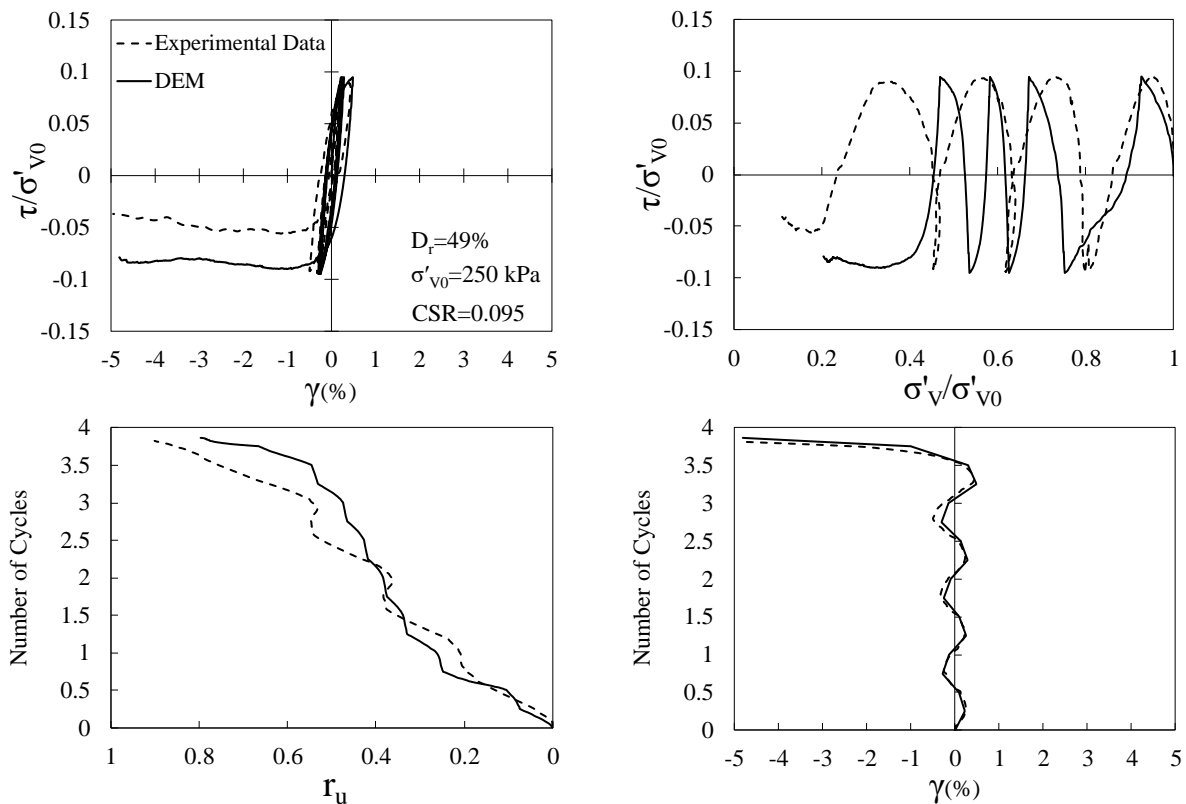


Figure 6.4 Comparison of the results from DEM simulation of constant volume cyclic simple shear test to the corresponding experimental results for Pea gravel specimen ($\sigma'_{v0}=250$ kPa, $D_r=49\%$, $CSR=0.095$)

- Comparing the stress paths of cyclic loading with the corresponding monotonic ones along with the relevant phase transformation (PT) and ultimate state (US) lines, it is observed that cyclic stress paths are bounded within the ultimate state lines obtained from corresponding monotonic loadings. In case of $D_r=49\%$, the PT lines for monotonic and cyclic (with $CSR=0.095$) loading are very close to each other and can be considered the same. However, for the case of $\sigma'_{v0}=250$ kPa, $D_r=87\%$ and $CSR=0.475$, different PT lines are observed for monotonic and cyclic loadings and the PT line for cyclic loading has smaller slope than the one for monotonic loading (Figure 6.5).

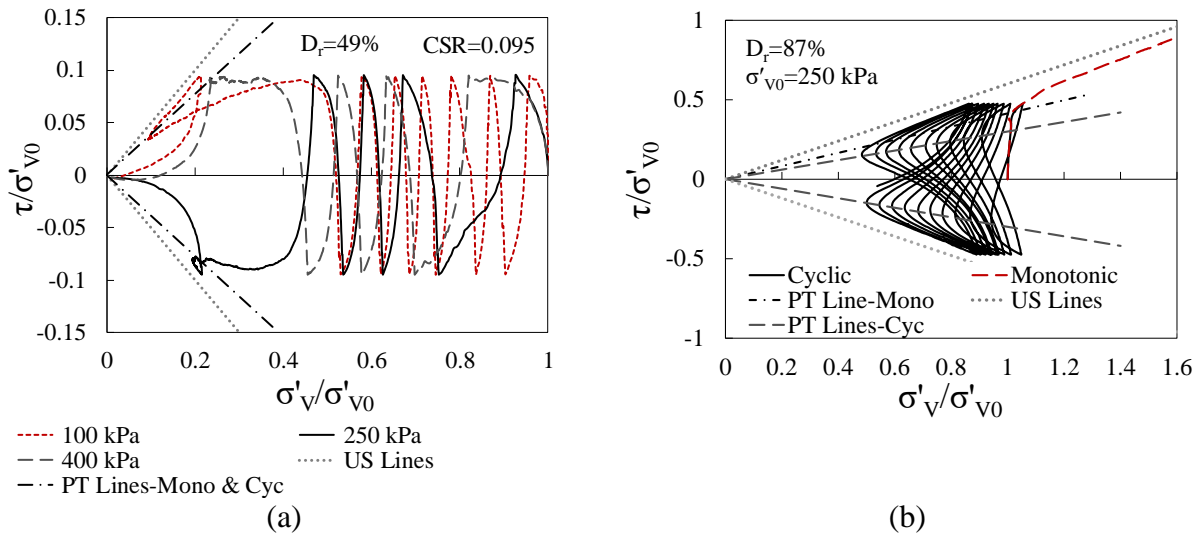


Figure 6.5 Comparison of cyclic stress paths with phase transformation (PT) and ultimate state (US) lines from monotonic stress path data from DEM simulations of Pea gravel specimen: (a) $D_r=49\%$, $CSR=0.095$, (b) $D_r=87\%$, $CSR=0.475$

- Despite the symmetric boundary applied cyclic shear loading with a constant CSR , the soil at the specimen core experiences a non-symmetric shear cycles with variable CSR during the period of loading.
- The generated pore pressure ratio calculated based on the changes in vertical stress at horizontal boundaries (as done in the lab) is a conservative estimation of the actual pore

pressure ratio at the specimen core. The boundary-based determination of pore pressure ratio leads to more positive values than the actual one generated at the specimen core.

- During the constant volume simple shear loading, it was observed that the coefficients of lateral pressure in directions parallel (K_x) and perpendicular (K_y) to shear direction are different. For specimens of $D_r=49\%$ and $CSR=0.095$, K_x is, on average, 1.2 times larger than K_y . For specimen of $\sigma'_{v0}=250$ kPa, $D_r=87\%$ and $CSR=0.475$, K_x experienced larger amplitudes of fluctuations than K_y , in a way that the ratio of K_x to K_y (K_x/K_y) is, on average, 1.25 and 0.92 at instances of peak and zero shear stress, respectively. Boundary measurement of average coefficient of lateral pressure, by assuming the same value in all radial directions, cannot capture this aspect of the behavior. In case of $D_r=49\%$ and $CSR=0.095$ and on average for all the consolidated vertical stresses, the boundary measured coefficient of lateral pressure underestimates K_x and K_y values inside the specimen core by up to 25% and 13%, respectively. For specimen of $\sigma'_{v0}=250$ kPa, $D_r=87\%$ and $CSR=0.475$, the boundary measurements lead to underestimation of the maximum K_x values by up to 22%.
- During cyclic loading, direction of principal stresses rotates and oscillates and the maximum angle between major principal axis and the vertical direction increases as cycling proceeds. For specimens of $D_r=49\%$ and $CSR=0.095$, this value starts from 15-20° at the first peak of shear stress and reaches to 40-45° during the cycle of liquefaction initiation. For specimen of $\sigma'_{v0}=250$ kPa, $D_r=87\%$ and $CSR=0.475$, it starts from about 40° at the first peak of shear stress and reaches to about 48° after 10 cycles.
- Stress-induced fabric anisotropy, in terms of contact normal orientations, in the cyclically sheared specimens was qualitatively and quantitatively investigated. The orientation of

strong force chains rotates and oscillates following the rotation and oscillation of the major principal axis. The degree of stress-induced fabric anisotropy at points of maximum shear stress are higher than that at the points of zero shear stress. This difference and generally the changes in degree of fabric anisotropy is more evident in specimen of $D_r=87\%$ and $CSR=0.475$. For this specimen, the degree of anisotropy at points of maximum shear stress increases as cyclic loading proceeds. The corresponding increase at the point of zero shear stress is smaller.

- Evaluating the non-uniformities inside the specimen and comparing the range of the measured values of different stress and strain quantities inside the specimen with those measured at the boundaries, the following observations and conclusions are made:
 - Despite a symmetric cyclic shear loading of constant CSR applied at the boundaries, the experienced shear cycles at different locations inside the specimen can be non-symmetric and with variable CSR. Although the experienced shearing cycles inside the specimen is, on average, similar to the one applied at the boundaries, different locations within the specimen experiences higher or lower shear stress ratios. This leads to a non-uniform cyclic response within the specimen that can affect the overall behavior of the specimen as a whole and should be taken into consideration for interpretation of experimental results.
 - Although the values of τ_{xz}/σ'_{zz} at the instances of peak shear stress (peaks of the shearing cycles) at various locations inside the specimen increase as the number of cycles increases, there are quantitative differences among them. The non-uniformities in distribution of τ_{xz}/σ'_{zz} implies that at each instance during cyclic loading, the stress state is not necessarily the same at different locations within the specimen. However,

- the simulation results showed that the boundary measured value of stress ratio (τ_h/σ'_v) is a good estimate of the average τ_{xz}/σ'_{zz} values within the specimen.
- Generated pore pressure ratio is distributed non-uniformly inside the specimen. For all specimens, the pore pressure ratio calculated based on the changes in vertical stress at horizontal boundaries generally overestimates the positive pore pressure ratio generated inside the specimen during cyclic shearing. Therefore, determining pore pressure ratio based on the change of vertical effective stress on the top cap, as done in laboratory, leads to a conservative estimation of the actual pore pressure ratio generated inside the specimen.
 - Shear strain (γ_{xz}) is developed non-uniformly inside the specimen during cyclic loading. For specimens of $D_r=49\%$ and $CSR=0.095$, the boundary measured shear strain value is in the range of shear strain values developed within the specimen and is, on average, 1.5 and 2.1 times larger than the average shear strain induced inside the specimen at instances of, respectively, zero and maximum shear stress. When the single amplitude boundary shear strain reaches 3.75% (liquefaction initiation), the average shear strain induced within the specimens is, on average, 1.15 times smaller than that at the boundaries. In specimen of $\sigma'_{v0}=250$ kPa, $D_r=87\%$ and $CSR=0.475$, the boundary measured shear strain is larger than the internally developed shear strains within the specimen, and is, on average, two times larger than the average value of γ_{xz} .
 - Despite the overall constant volume condition during shear, local volume changes can occur at different locations inside the specimen due to the local movement of particles relative to each other. It was observed that volumetric changes are distributed non-uniformly within the specimen during cyclic shear. Variable and non-uniformly

distribution of volumetric changes within the specimen implies the redistribution of voids and pore pressure during cyclic loading that would cause local migration of pore water through the voids in saturated specimens.

- All in all, these observations provide a deeper insight into the existing non-uniformities of stress and strain inside the specimen and into how they compare with the boundary measured ones. It is very important to account for them in experimental results interpretation for analysis of the cyclic and liquefaction behavior of the soil specimen.

6.4 Recommendations for future research

This study has made several contributions and provides valuable insight into different aspects of gravelly soil behavior at the micro- and meso-scale; however, there is more to be considered and investigated. In this regard, the following directions are recommended for future research:

- Using other contact models available in PFC software such as non-linear Hertz contact model and modify it to account for rolling resistance of the equivalent spherical particles in the simulations, to examine the potential benefits of using more complex contact models.
- Representing the soil particles as simple clumps of 2-3 spheres with the range of size and aspect ratio obtained from TST test for the Pea gravel specimen. In this case, there is no need to numerically add any rolling resistance as the non-spherical shape of the clumps prevents the free rolling and rotation.
- Using more complex clumps composed of larger number of spheres in more irregular configuration in order to obtain closer representation of real soil particles. For this purpose, more information from TST tests is simultaneously be accounted for. The multidimensional

probability of shape features of the Pea gravel sample obtained from TST test is used to select the representative particle size and shape combinations to be modelled in the simulation. The third dimension of particle size is also accounted for (not assumed to be equal to the intermediate dimension). Example shapes for such clumps can be seen in Figure 6.6.

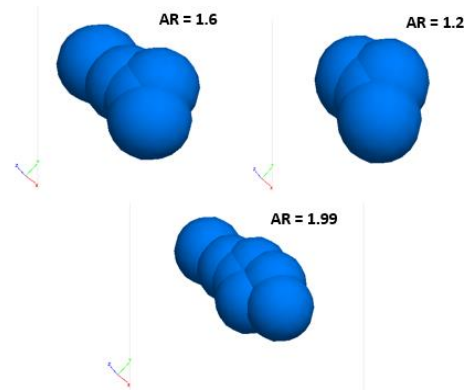


Figure 6.6 Example of complex clumps as numerical representation of soil particles

Comparing the results of these recommended approaches in simulating the soil particles size and morphology with the results of this study will reveal the amount of the complexity and accuracy required for numerically replicating the particles in order to capture the monotonic and cyclic response of gravels in constant volume simple shear loading at a satisfactory level.

- In this study, the behavior of dry particle assembly under constant volume condition was studied as equivalent to undrained behavior of the saturated soil. Although this is an acceptable approach to deal with complexities associated with undrained testing of saturated specimens, and has been shown to provide similar results, such DEM simulations are not able to investigate some of the important phenomena such as possible upward water flow and/or water film formation during cyclic loading and liquefaction of saturated soils. In this regard, it is recommended to incorporate the presence of pore water in simulations and investigate the truly undrained response of saturated assemblies. To achieve this, the Computational Fluid Dynamics Module (CFD Module) for PFC3D can be used.

Appendices

Appendix A

Selection of the size of Measurement Spheres

The results of the sensitivity analysis of different measured quantities to the size of the central measurement sphere at different vertical stresses and relative densities are presented here. The effect of the measurement sphere size on the void ratio, shear strain (γ_{xz}), vertical stress (σ'_{zz}) and shear stress (τ_{xz}) measured at the central part of the specimen is presented in Figure A.1, Figure A.2, Figure A.3 and Figure A.4, respectively.

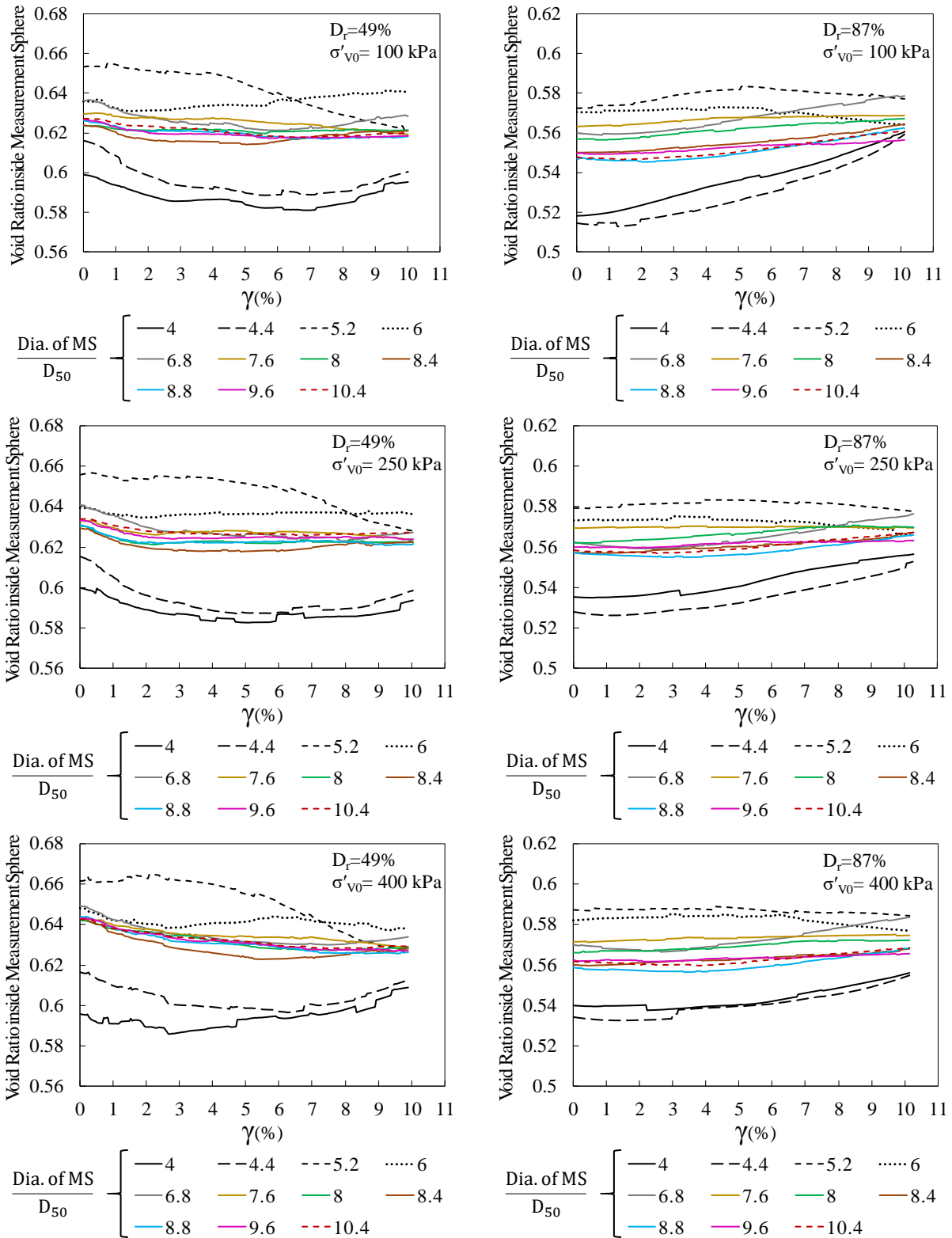


Figure A.1 Void ratio measured inside the central measurement sphere with different diameters: $D_r=49\%$ (left) and $D_r=87\%$ (right)

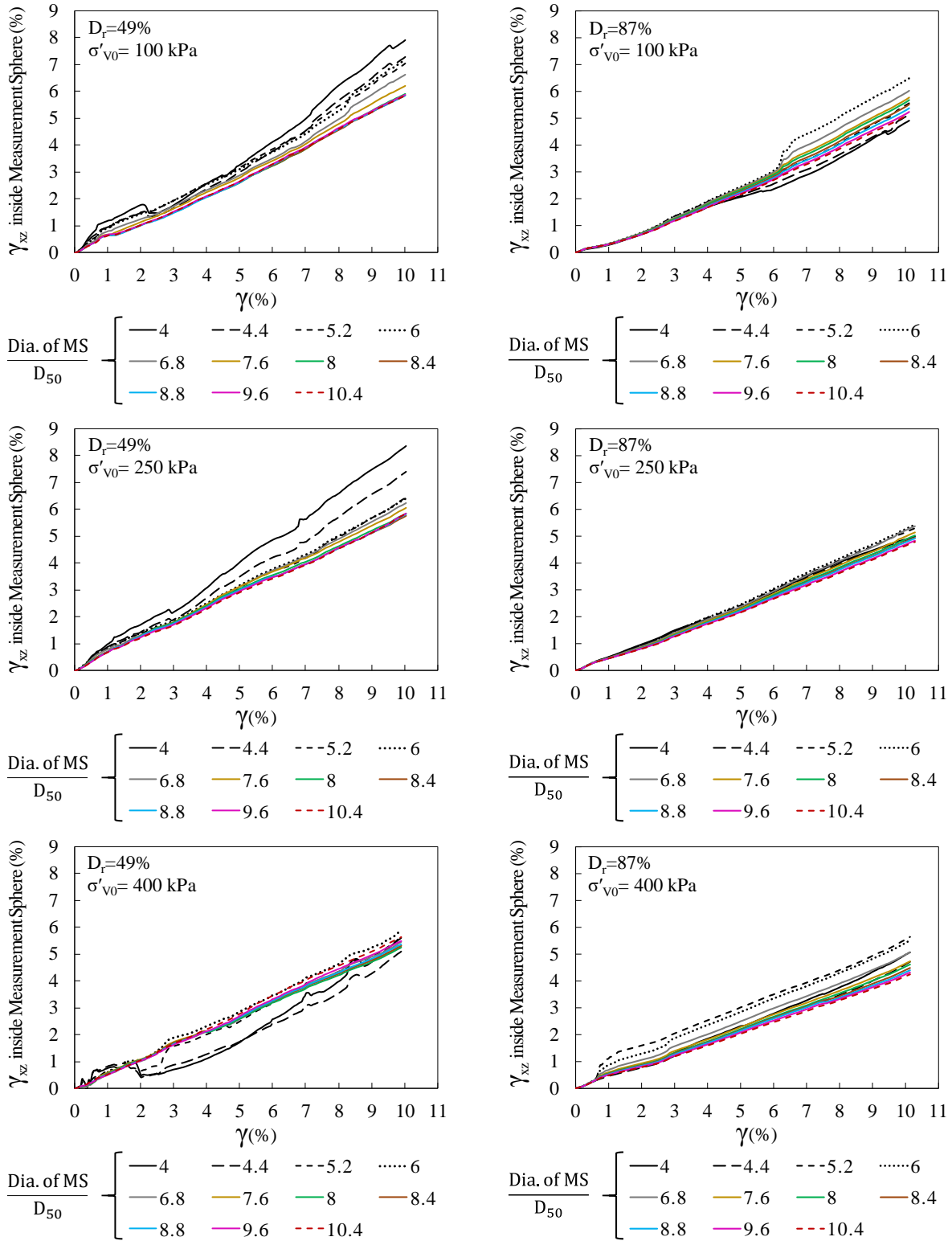


Figure A.2 Shear strain measured inside the central measurement sphere with different diameters: $D_r=49\%$ (left) and $D_r=87\%$ (right)

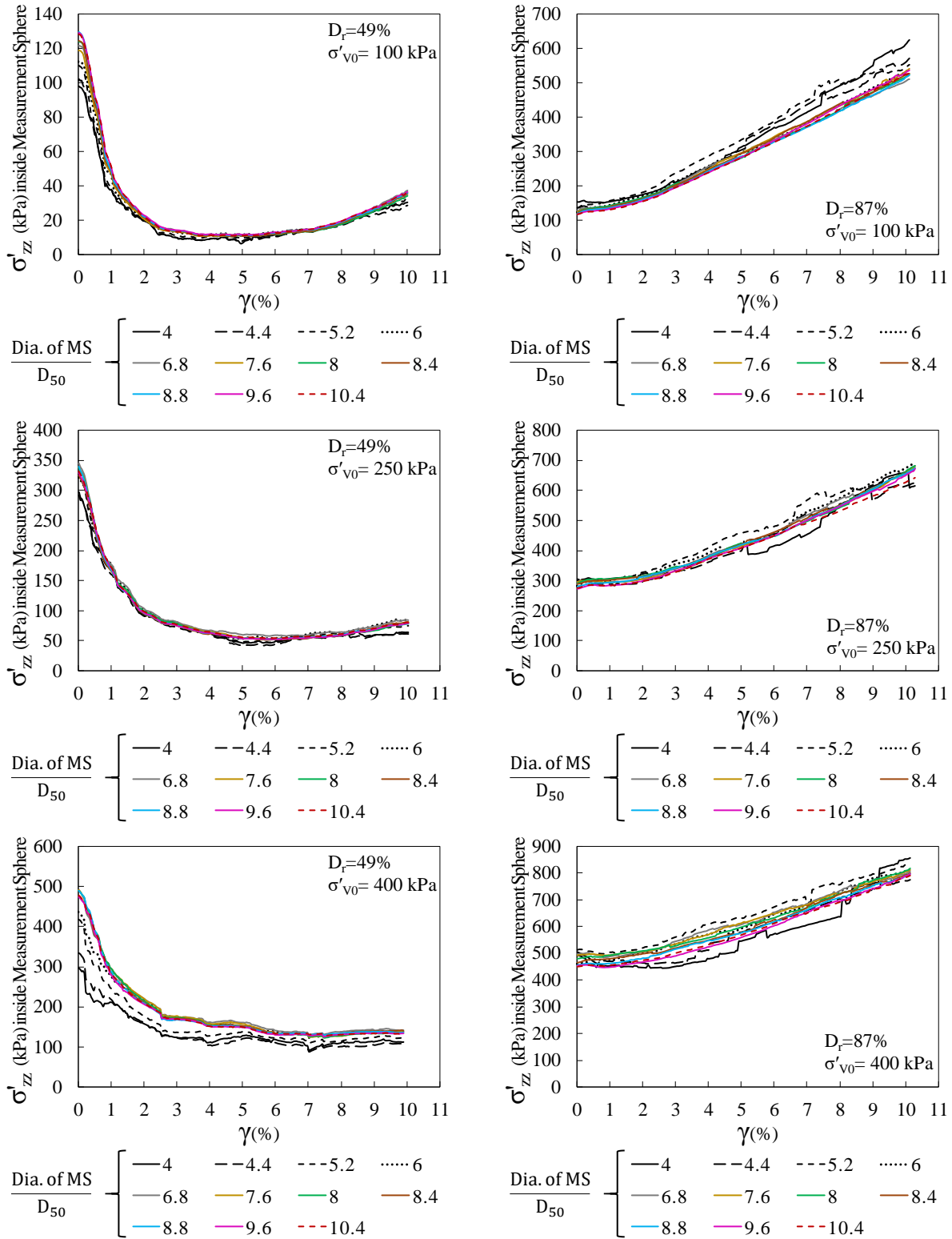


Figure A.3 Vertical stress measured inside the central measurement sphere with different diameters: $D_r=49\%$ (left) and $D_r=87\%$ (right)

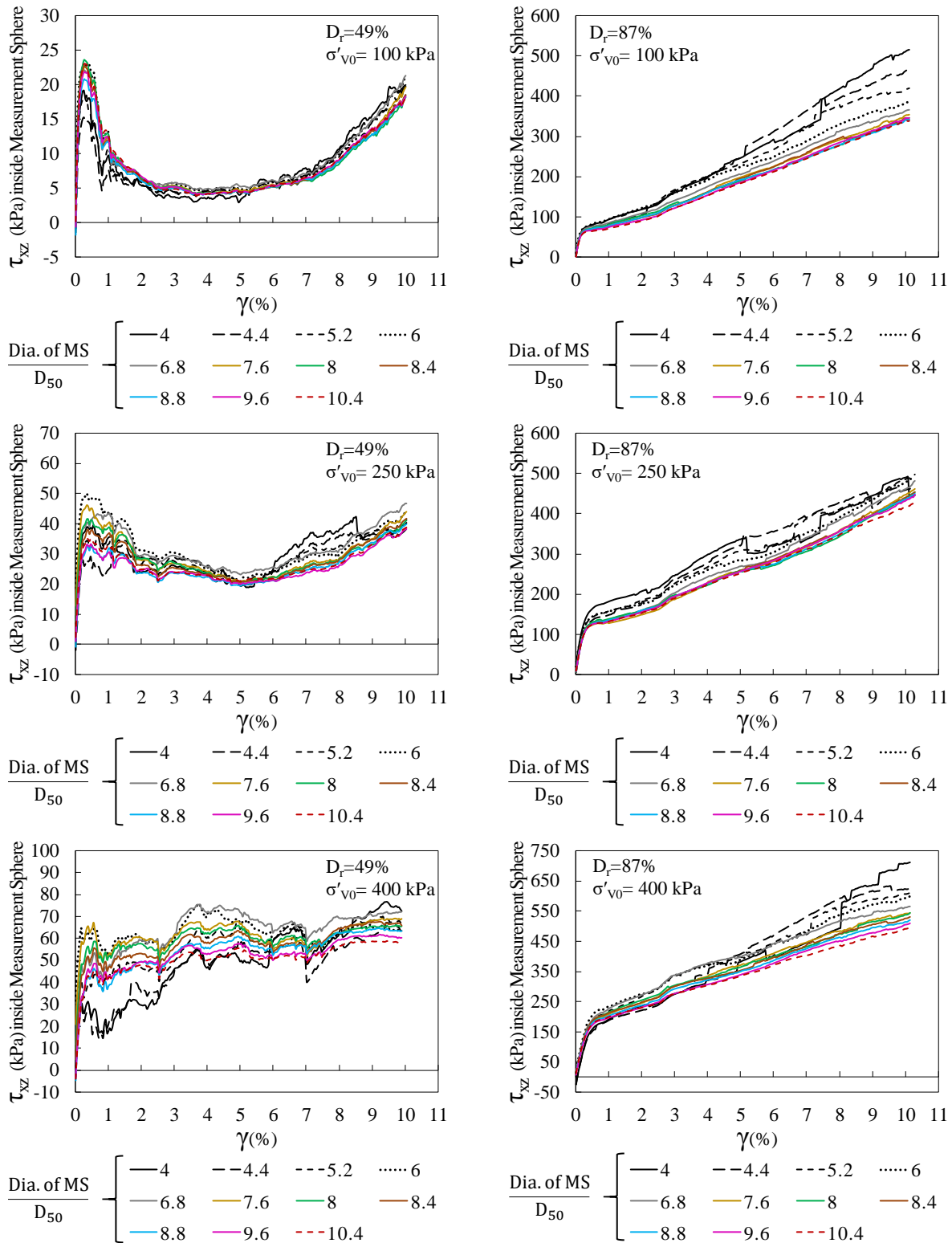


Figure A.4 Shear stress measured inside the central measurement sphere with different diameters: $D_r=49\%$ (left) and $D_r=87\%$ (right)

Appendix B

Comparison of the monotonic simple shear response measured at boundaries and inside the central measurement spheres for consolidated vertical stresses of 100 and 400 kPa

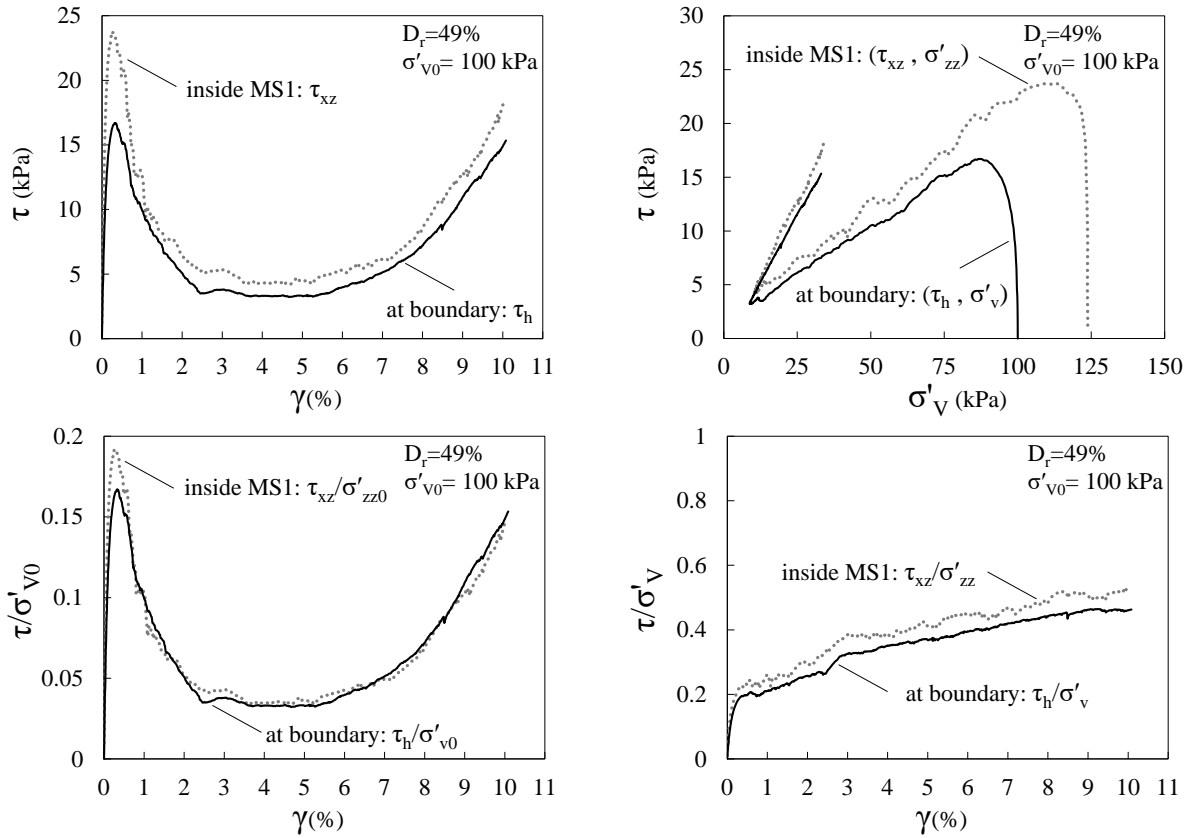


Figure B.1 Comparison of the monotonic shear response measured at boundaries and inside the central measurement sphere in DEM simulation of constant volume monotonic simple shear response of Pea gravel specimen ($\sigma'_{v0}=100$ kPa, $D_r=49\%$)

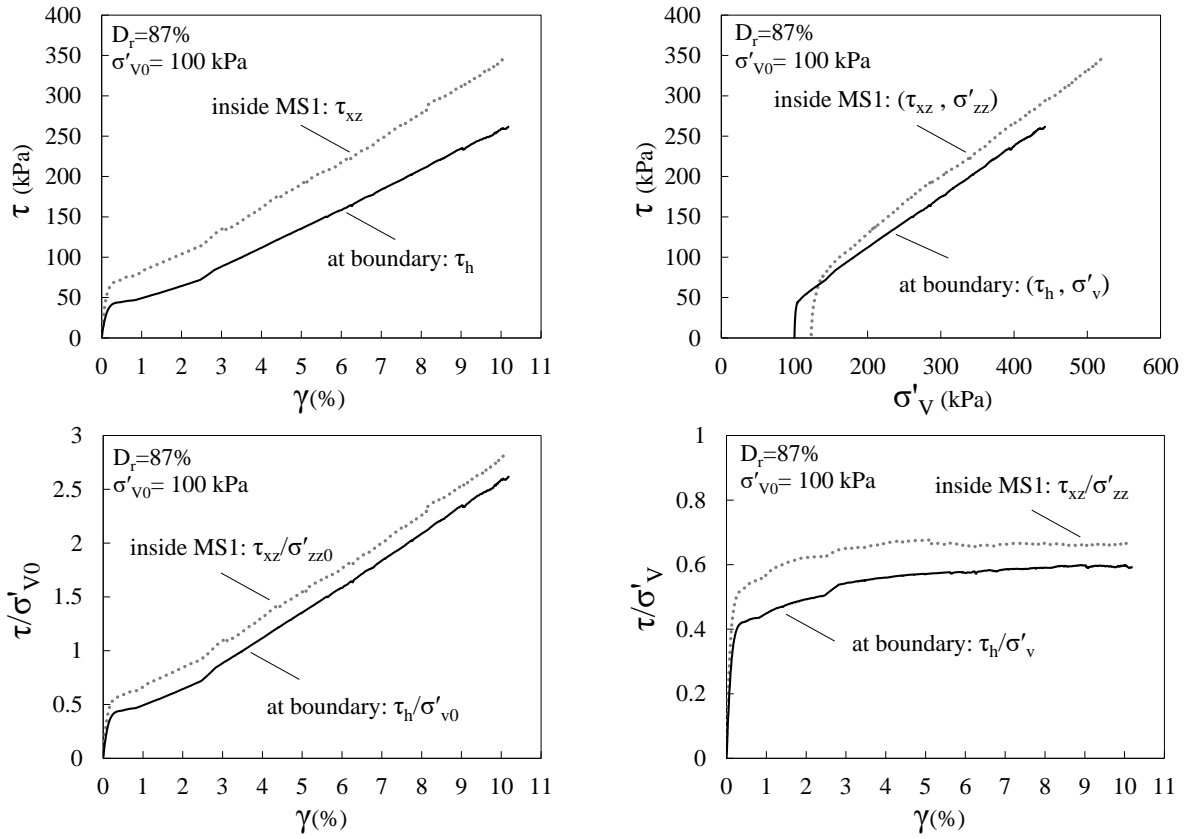


Figure B.2 Comparison of the monotonic shear response measured at boundaries and inside the central measurement sphere in DEM simulation of constant volume monotonic simple shear response of Pea gravel specimen ($\sigma'_{v0} = 100$ kPa, $D_r = 87\%$)

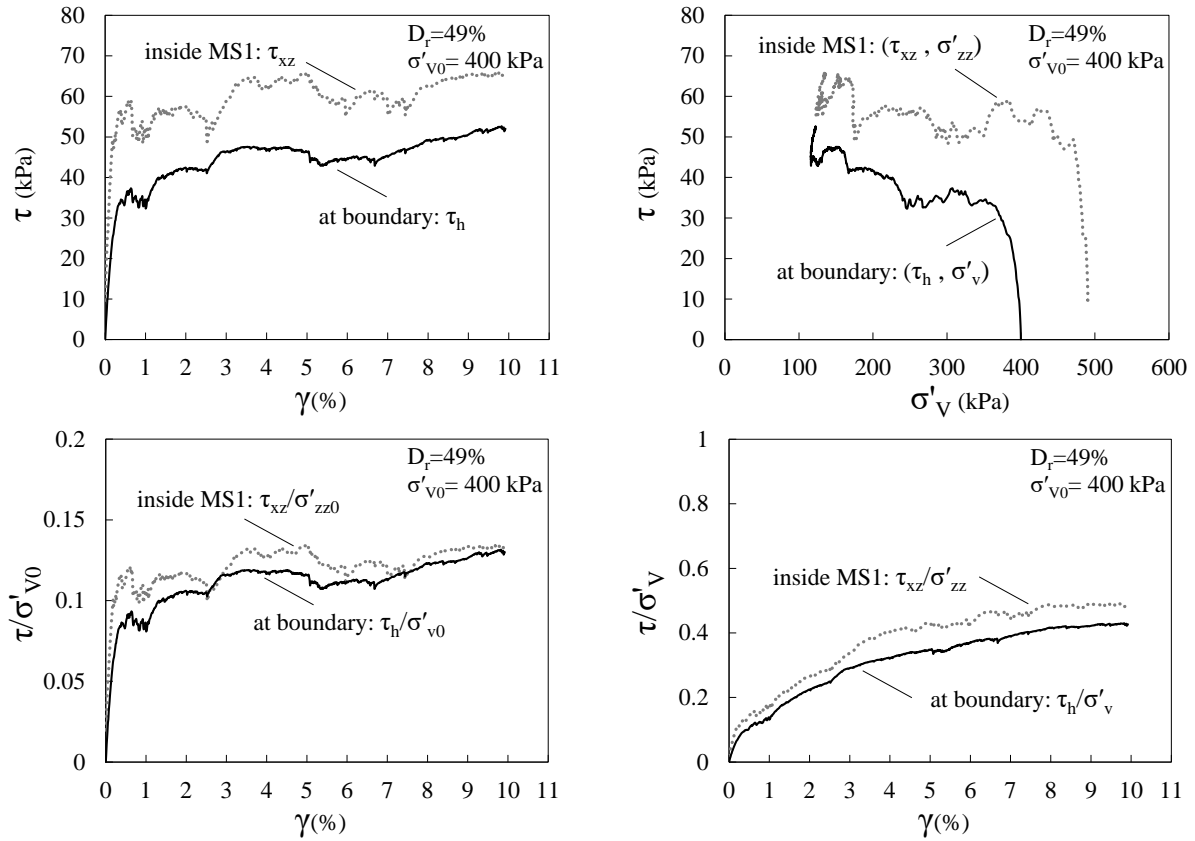


Figure B.3 Comparison of monotonic shear response measured at boundaries and inside the central measurement sphere in DEM simulation of constant volume monotonic simple shear response of Pea gravel specimen ($\sigma'_{v0}=400$ kPa, $D_r=49\%$)

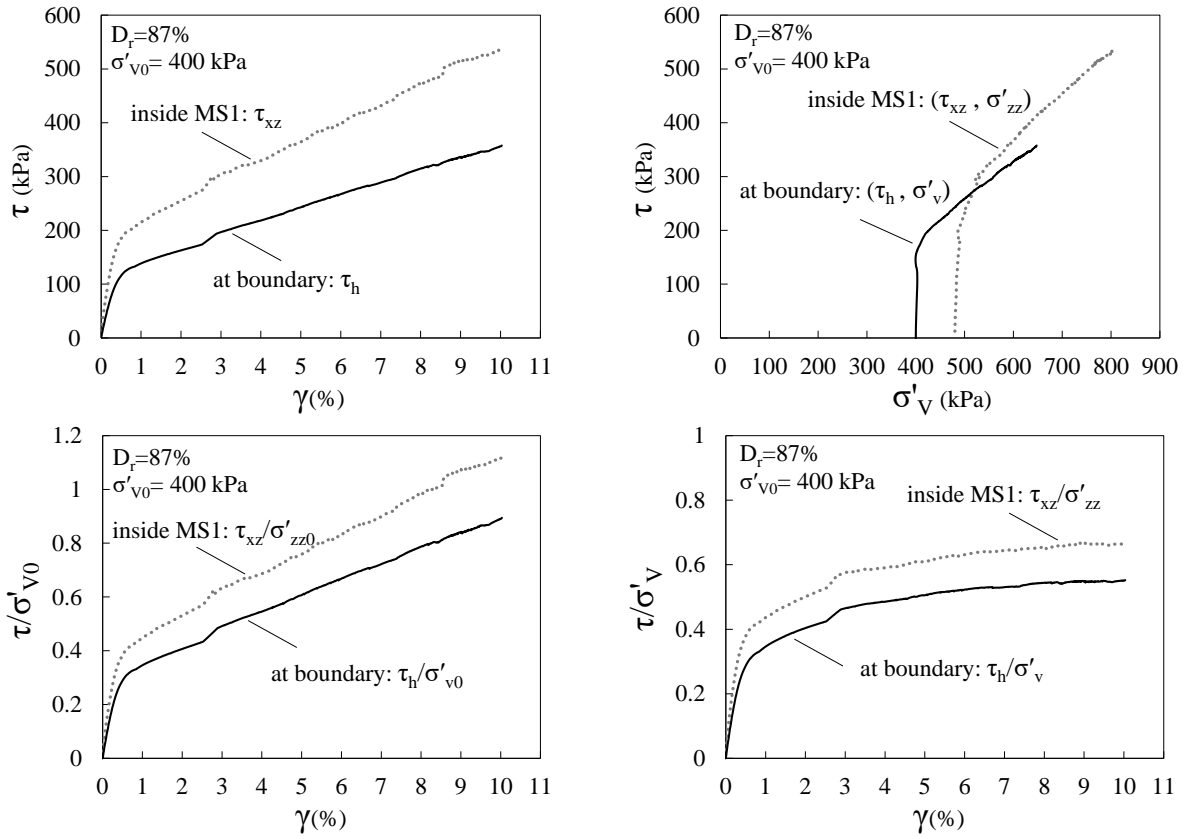


Figure B.4 Comparison of the monotonic shear response measured at boundaries and inside the central measurement sphere in DEM simulation of constant volume monotonic simple shear response of Pea gravel specimen (σ'_{v0}=400 kPa, D_r=87%)

Appendix C

Variation of different measurement quantities inside MS1-MS13 during monotonic shear for consolidated vertical stresses of 100 and 400 kPa

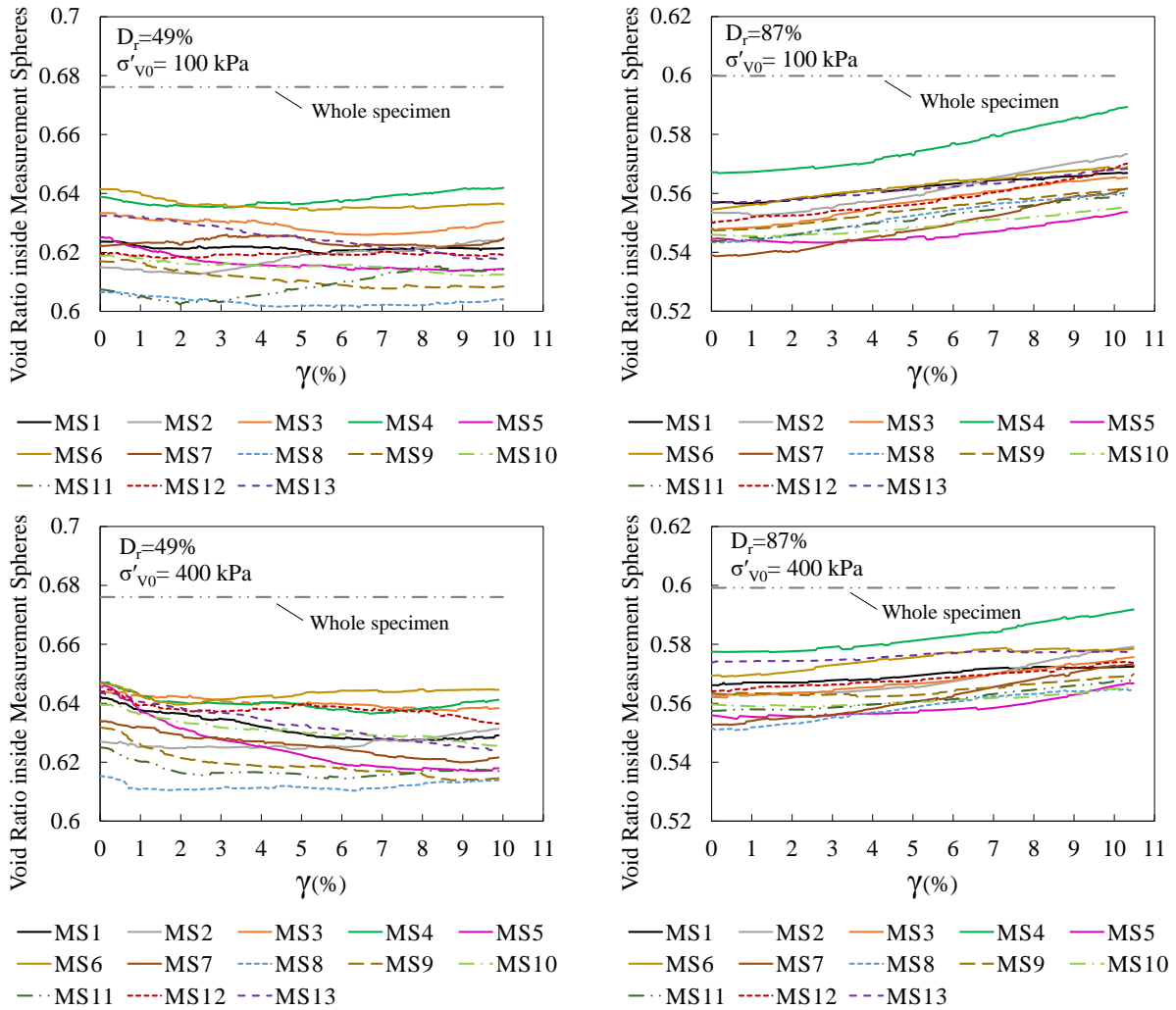


Figure C.1 Void ratio measured inside measurement spheres MS1-MS13 during shear in DEM simulations of constant volume monotonic simple shear response of Pea gravel specimen for $\sigma'_{v0}=100$ and 400 kPa: $D_r=49\%$ (left), $D_r=87\%$ (right)

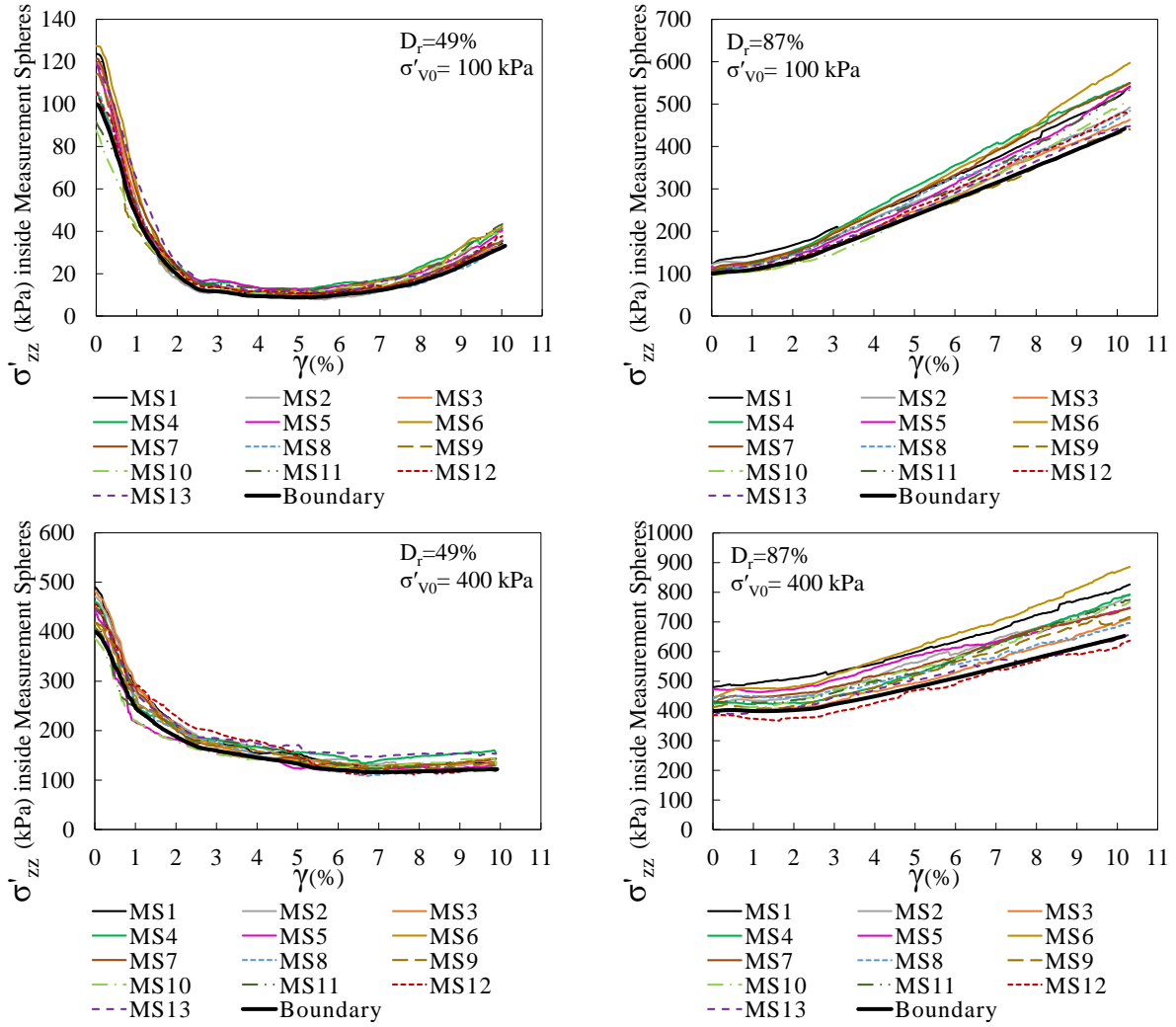


Figure C.2 Effective vertical stress measured inside measurement spheres MS1-MS13 during shear in DEM simulations of constant volume monotonic simple shear response of Pea gravel specimen for $\sigma'_{v0}=100$ and 400 kPa: $D_r=49\%$ (left), $D_r=87\%$ (right)

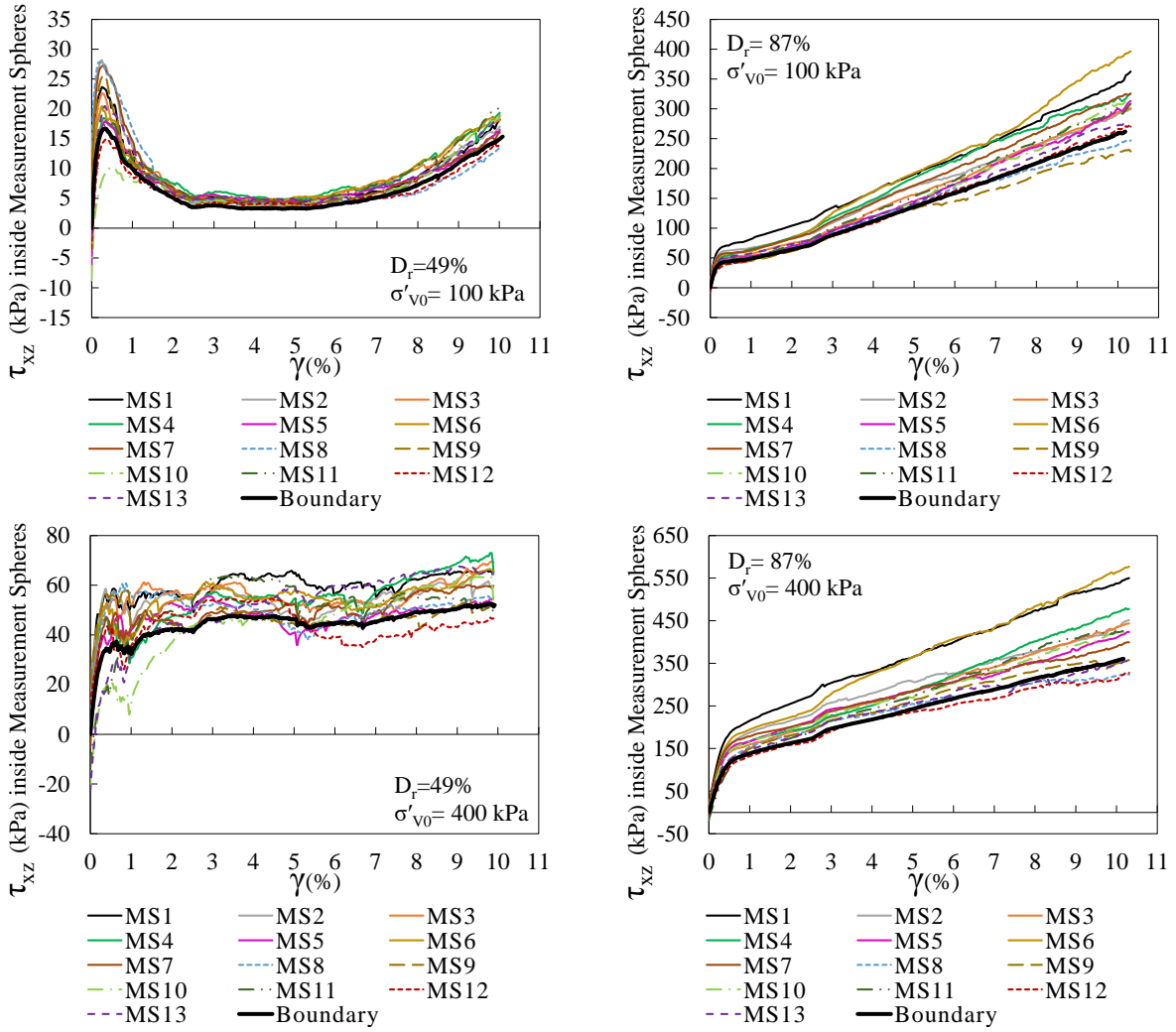


Figure C.3 Shear stress measured inside measurement spheres MS1-MS13 during shear in DEM simulations of constant volume monotonic simple shear response of Pea gravel specimen for $\sigma'_{v0}=100$ and 400 kPa: $D_r=49\%$ (left), $D_r=87\%$ (right)

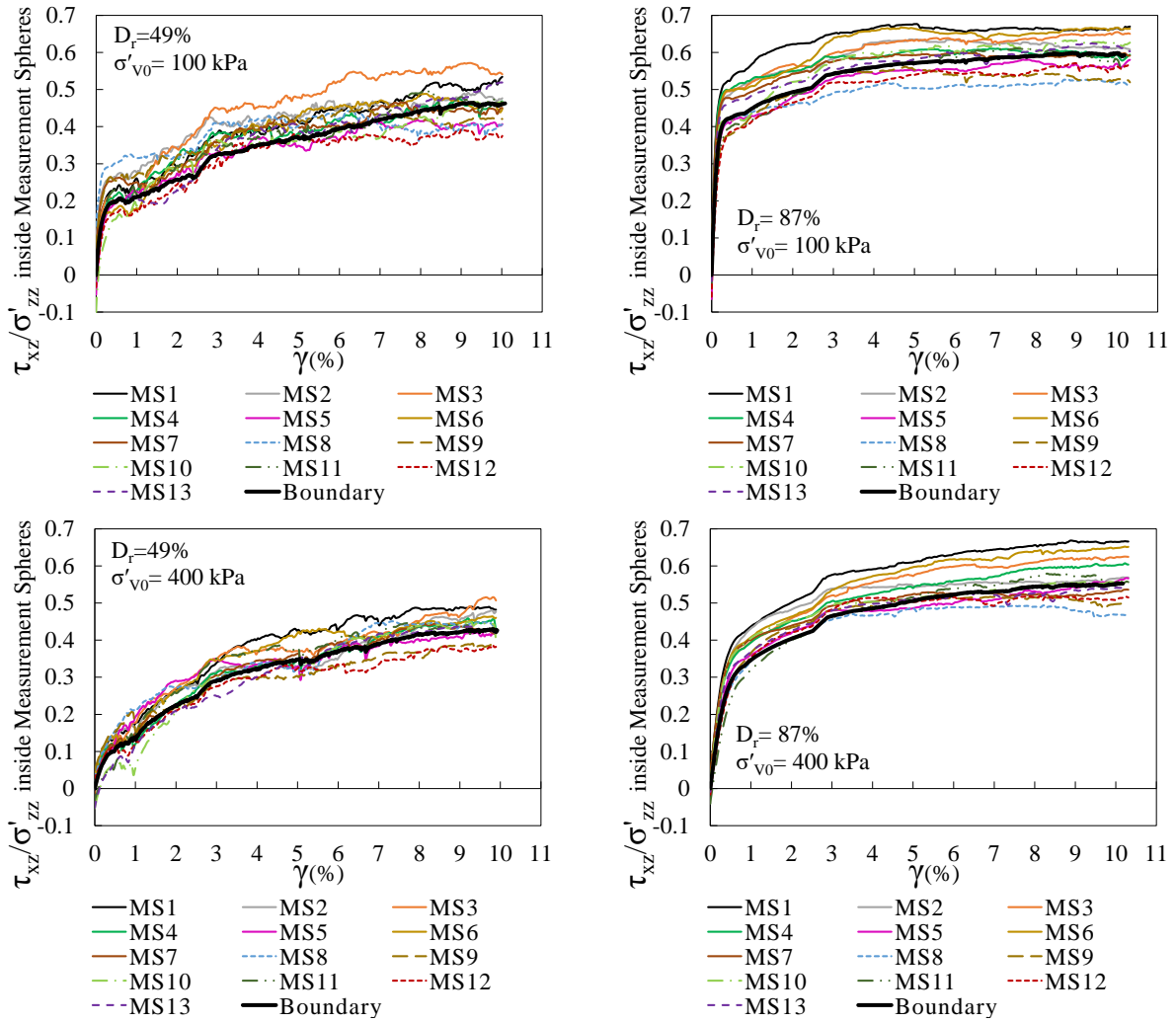
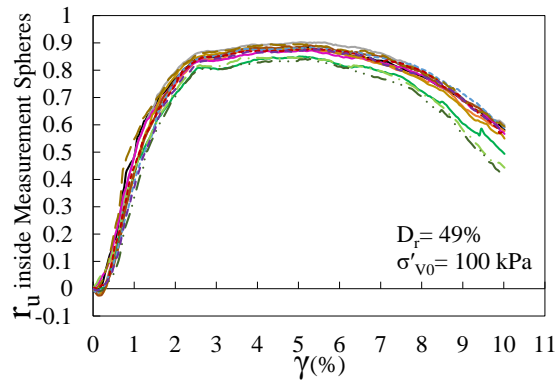
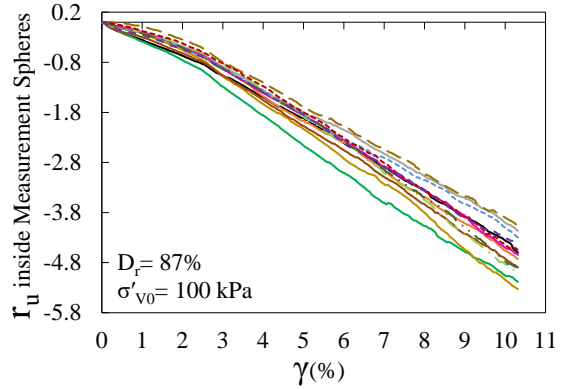


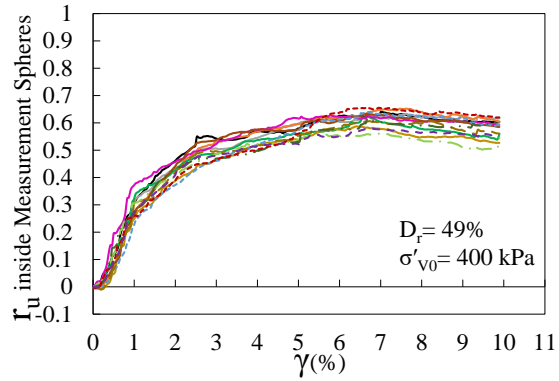
Figure C.4 Stress ratio measured inside measurement spheres MS1-MS13 during shear in DEM simulations of constant volume monotonic simple shear response of Pea gravel specimen for $\sigma'_{v0}=100$ and 400 kPa: $D_r=49\%$ (left), $D_r=87\%$ (right)



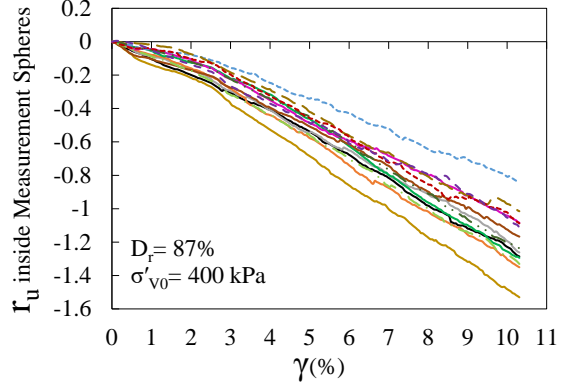
— MS1 — MS2 — MS3 — MS4 — MS5
 — MS6 — MS7 - - MS8 - - MS9 - - MS10
 - - MS11 - - MS12 - - MS13



— MS1 — MS2 — MS3 — MS4 — MS5
 — MS6 — MS7 - - MS8 - - MS9 - - MS10
 - - MS11 - - MS12 - - MS13



— MS1 — MS2 — MS3 — MS4 — MS5
 — MS6 — MS7 - - MS8 - - MS9 - - MS10
 - - MS11 - - MS12 - - MS13



— MS1 — MS2 — MS3 — MS4 — MS5
 — MS6 — MS7 - - MS8 - - MS9 - - MS10
 - - MS11 - - MS12 - - MS13

Figure C.5 Pore pressure ratio measured inside measurement spheres MS1-MS13 during shear in DEM simulations of constant volume monotonic simple shear response of Pea gravel specimen for $\sigma'_{v0}=100$ and 400 kPa: $D_r=49\%$ (left), $D_r=87\%$ (right)

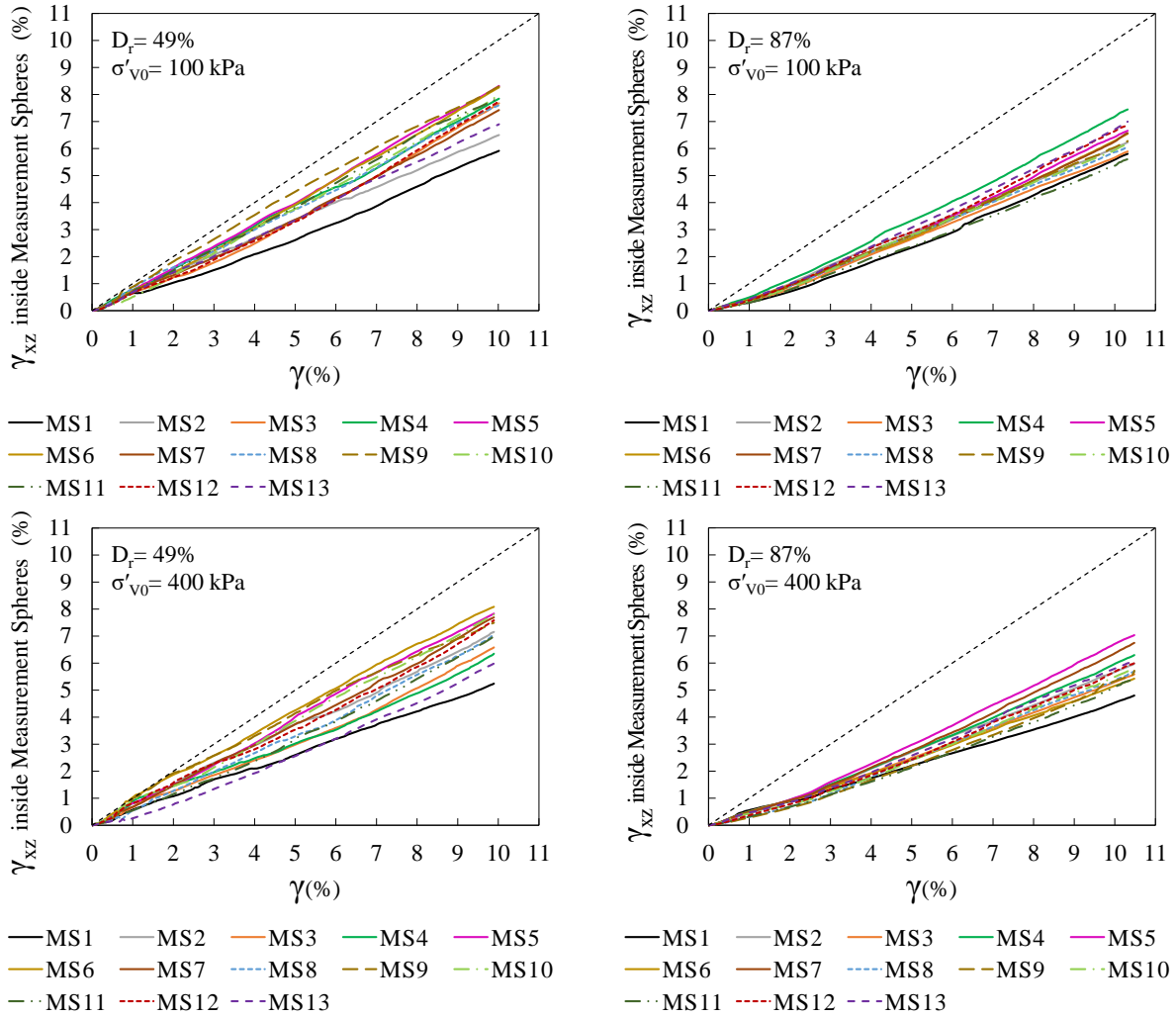


Figure C.6 Shear strain measured inside measurement spheres MS1-MS13 during shear in DEM simulations of constant volume monotonic simple shear response of Pea gravel specimen for $\sigma'_{v0}=100$ and 400 kPa: $D_r=49\%$ (left), $D_r=87\%$ (right)

Appendix D

Evolution of Mohr's circles of stress during constant volume monotonic simple shear for specimens of $\sigma'_{v0}=250$ kPa and $D_r=49\%$ and 87%

- * Horizontal plane (σ'_{zz}, τ_{zx})
- × Vertical plane (σ'_{xx}, τ_{xz})
- ◇ Planes of maximum plane stress
- Planes of maximum stress obliquity

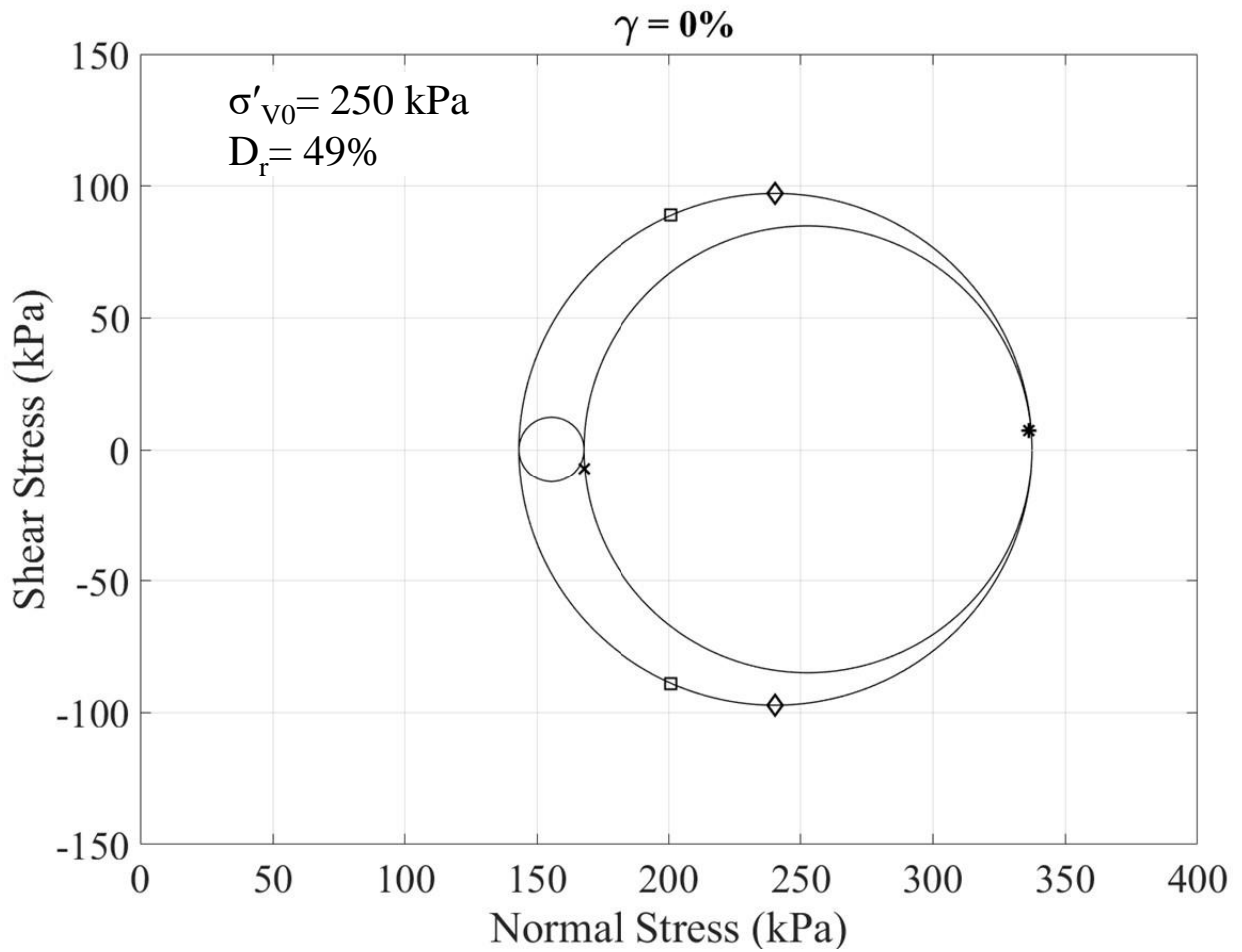


Figure D.1 Mohr's circles of stress at boundary shear strain of 0% ($\sigma'_{v0}=250$ kPa and $D_r=49\%$)

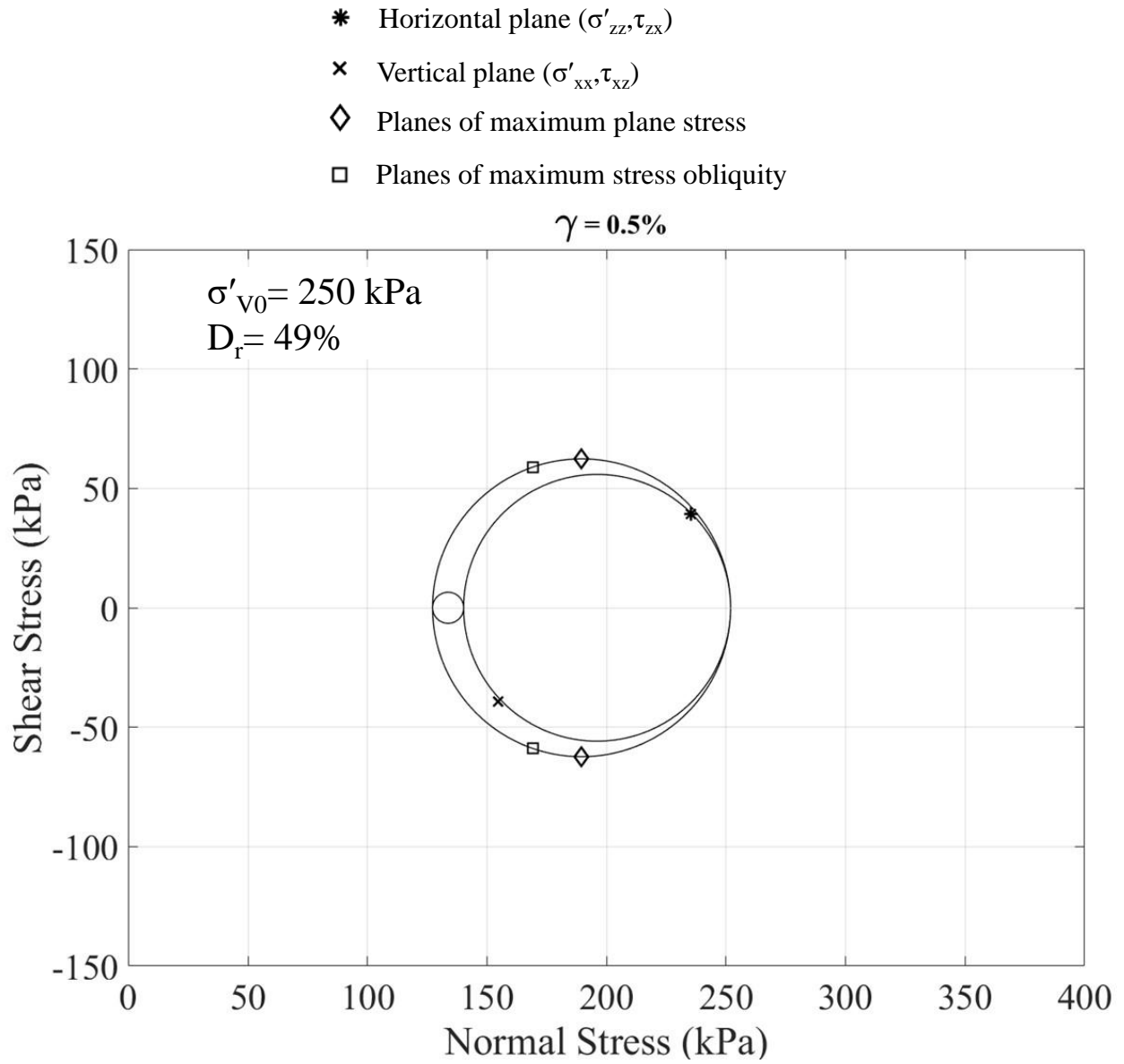


Figure D.2 Mohr's circles of stress at boundary shear strain of 0.5% ($\sigma'_{v0}=250 \text{ kPa}$ and $D_r=49\%$)

- * Horizontal plane (σ'_{zz}, τ_{zx})
- × Vertical plane (σ'_{xx}, τ_{xz})
- ◇ Planes of maximum plane stress
- Planes of maximum stress obliquity

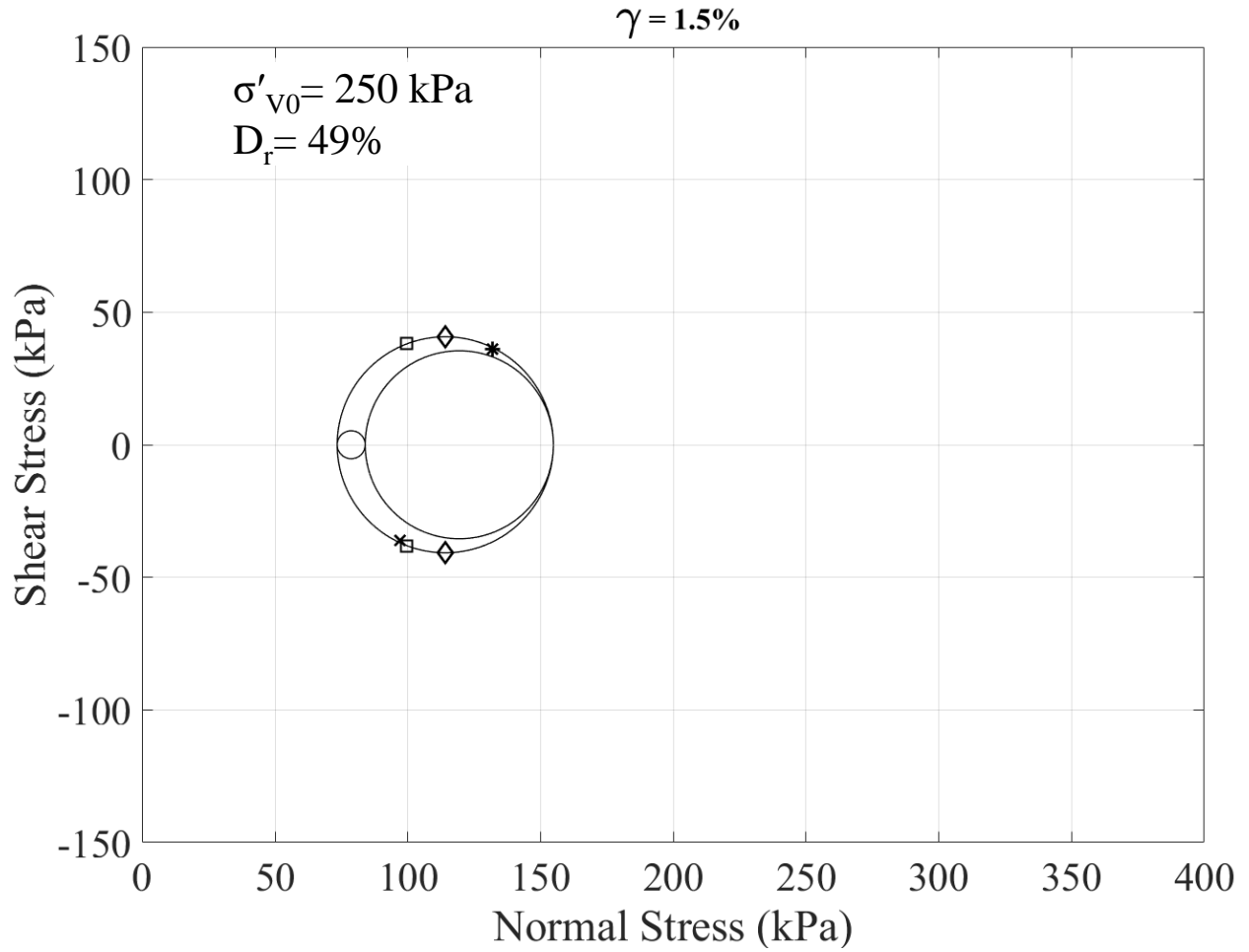


Figure D.3 Mohr's circles of stress at boundary shear strain of 1.5% ($\sigma'_{v0}=250 \text{ kPa}$ and $D_r=49\%$)

- * Horizontal plane (σ'_{zz}, τ_{zx})
- × Vertical plane (σ'_{xx}, τ_{xz})
- ◇ Planes of maximum plane stress
- Planes of maximum stress obliquity

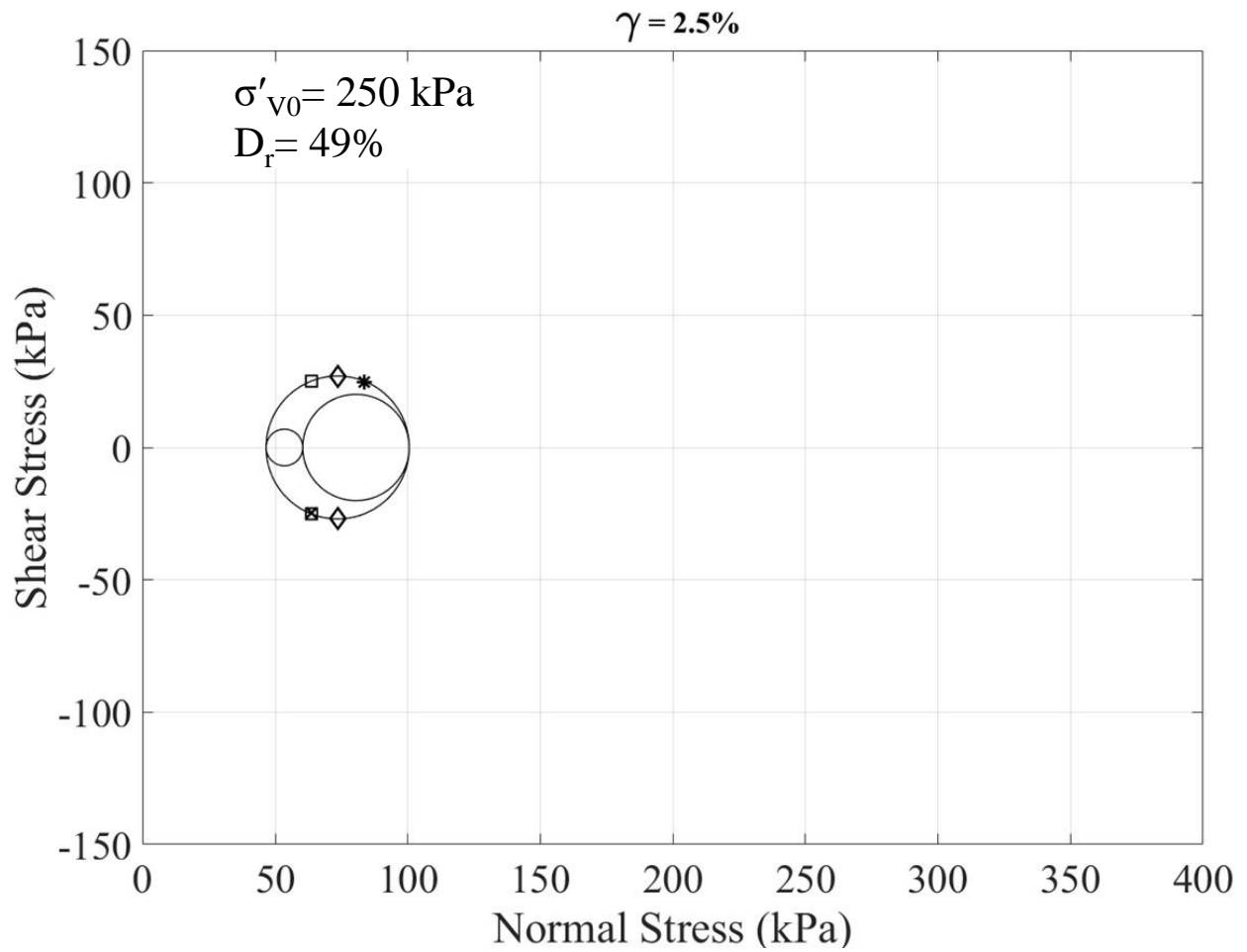


Figure D.4 Mohr's circles of stress at boundary shear strain of 2.5% ($\sigma'_{v0}=250$ kPa and $D_r=49\%$)

- * Horizontal plane (σ'_{zz}, τ_{zx})
- × Vertical plane (σ'_{xx}, τ_{xz})
- ◇ Planes of maximum plane stress
- Planes of maximum stress obliquity

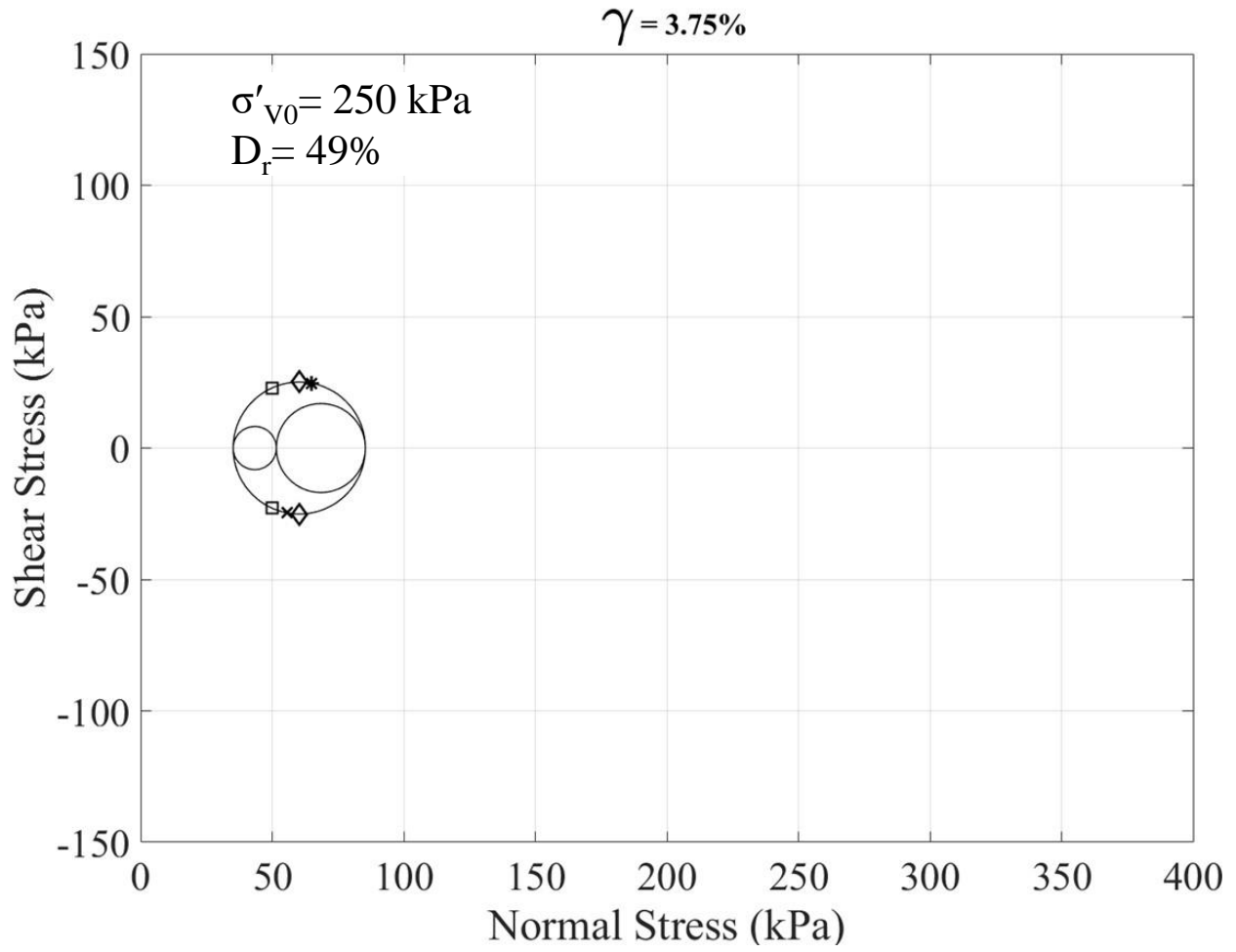


Figure D.5 Mohr's circles of stress at boundary shear strain of 3.75% ($\sigma'_{v0}=250 \text{ kPa}$ and $D_r=49\%$)

- * Horizontal plane (σ'_{zz}, τ_{zx})
- × Vertical plane (σ'_{xx}, τ_{xz})
- ◇ Planes of maximum plane stress
- Planes of maximum stress obliquity

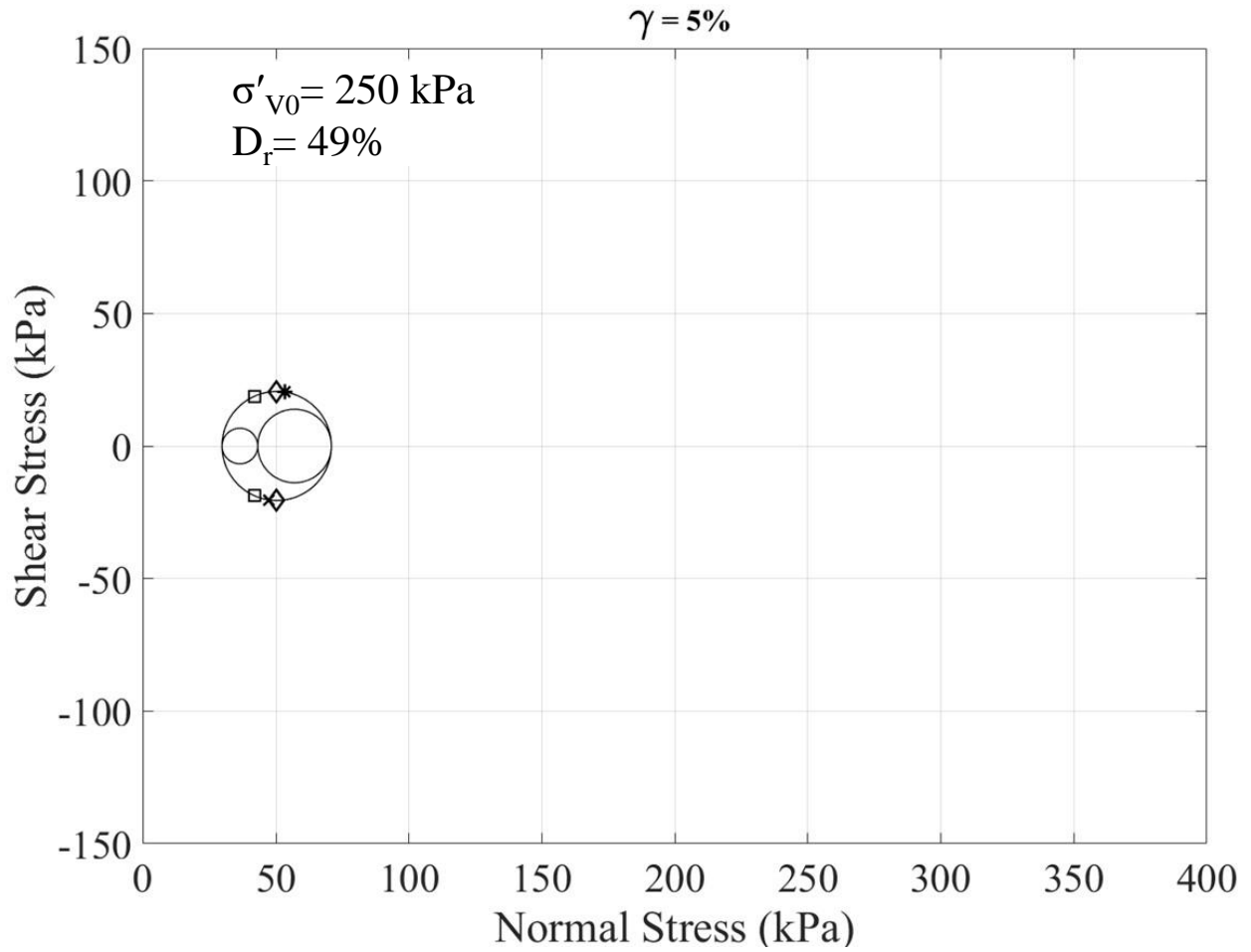


Figure D.6 Mohr's circles of stress at boundary shear strain of 5% ($\sigma'_{v0}=250$ kPa and $D_r=49\%$)

- * Horizontal plane (σ'_{zz}, τ_{zx})
- × Vertical plane (σ'_{xx}, τ_{xz})
- ◇ Planes of maximum plane stress
- Planes of maximum stress obliquity

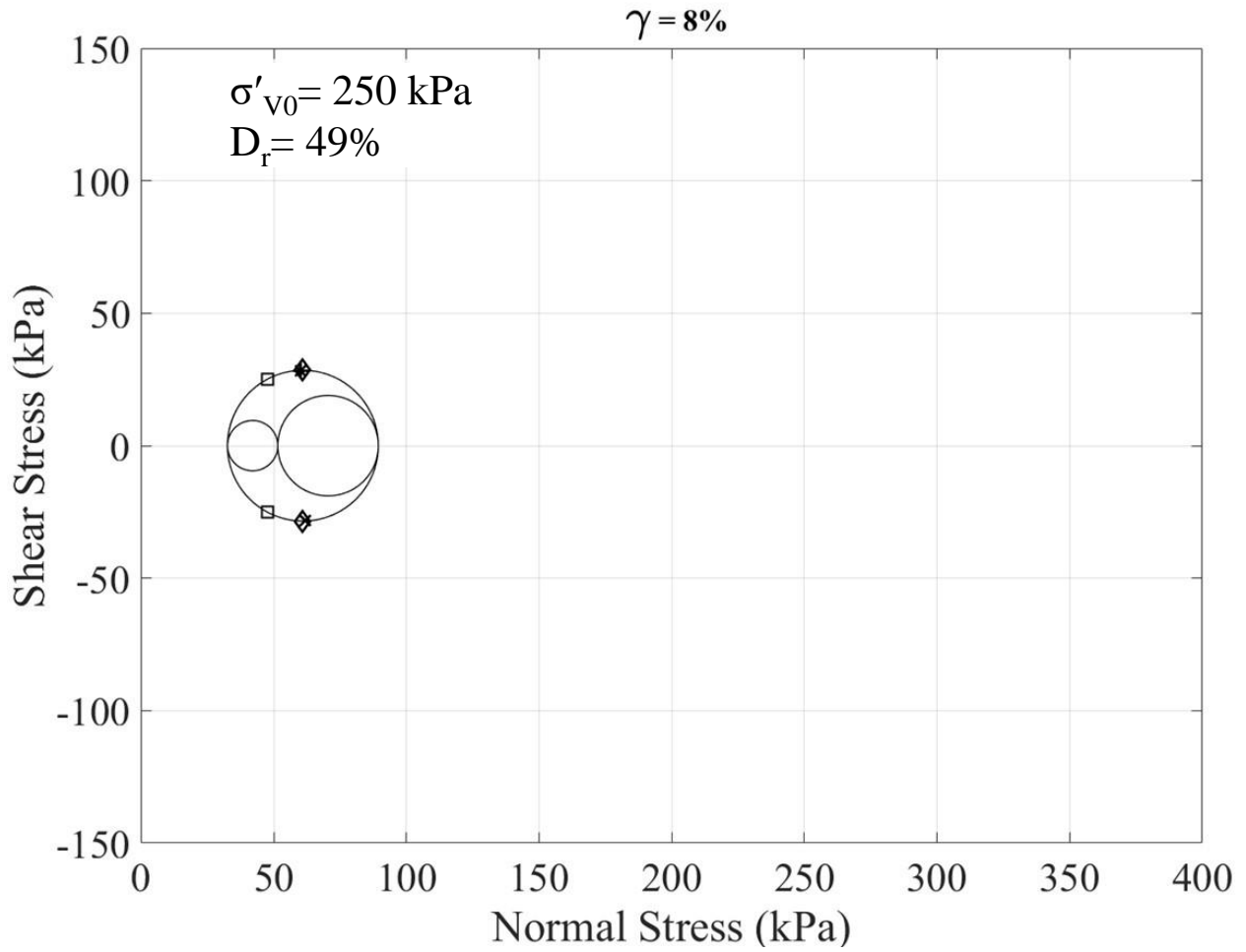


Figure D.7 Mohr's circles of stress at boundary shear strain of 8% ($\sigma'_{v0}=250$ kPa and $D_r=49\%$)

- * Horizontal plane (σ'_{zz}, τ_{zx})
- × Vertical plane (σ'_{xx}, τ_{xz})
- ◇ Planes of maximum plane stress
- Planes of maximum stress obliquity

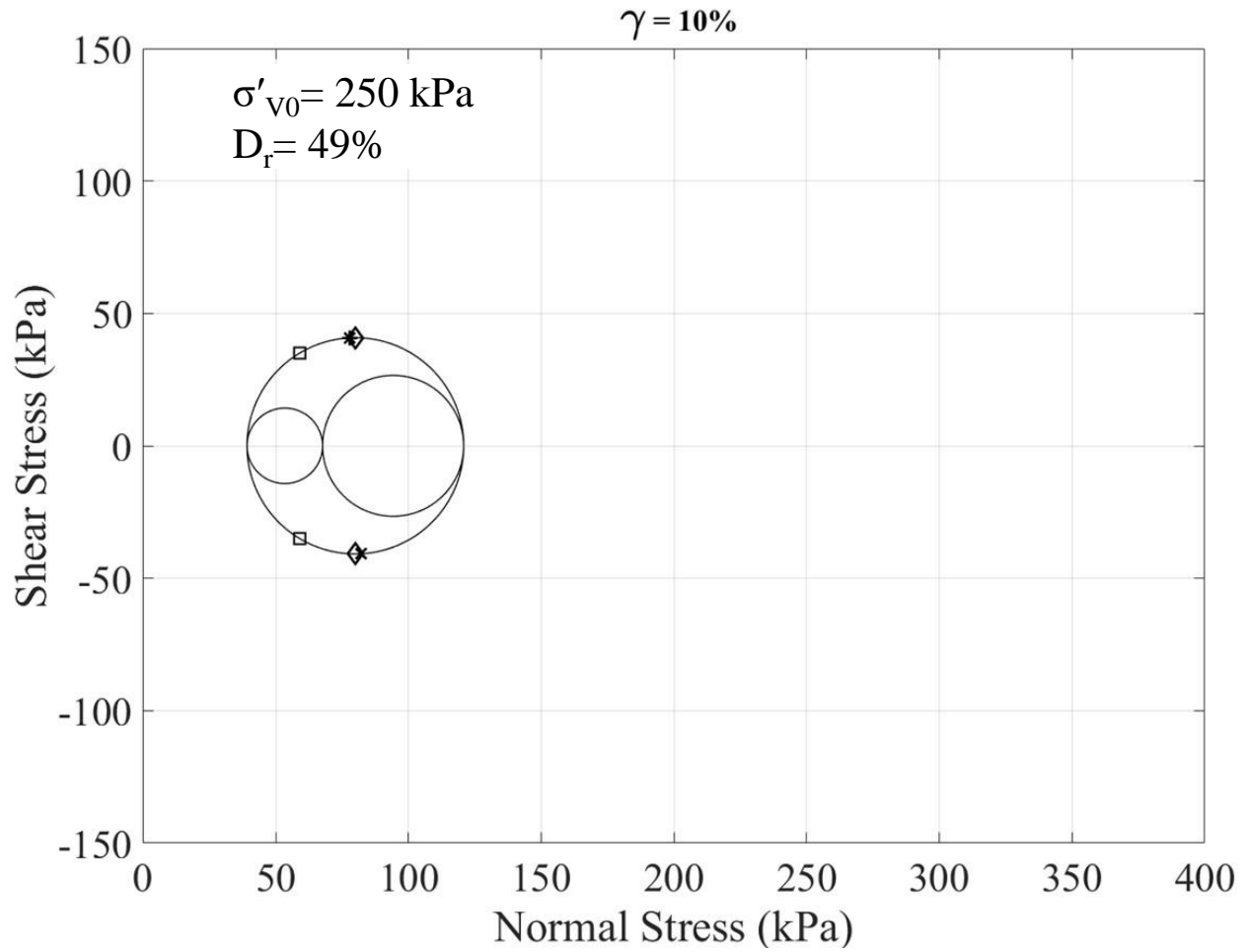


Figure D.8 Mohr's circles of stress at boundary shear strain of 10% ($\sigma'_{v0}=250 \text{ kPa}$ and $D_r=49\%$)

- * Horizontal plane (σ'_{zz}, τ_{zx})
- × Vertical plane (σ'_{xx}, τ_{xz})
- ◇ Planes of maximum plane stress
- Planes of maximum stress obliquity

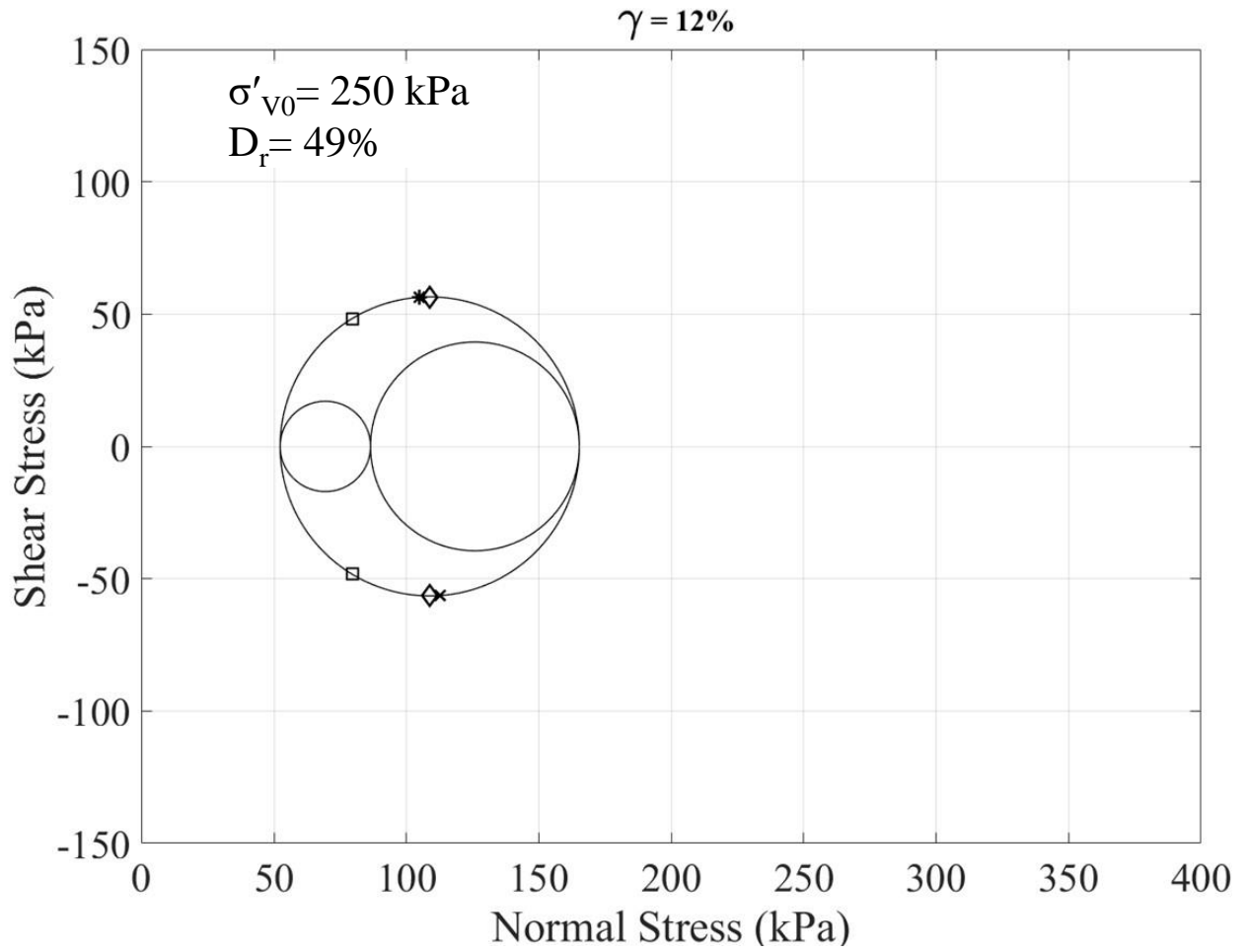


Figure D.9 Mohr's circles of stress at boundary shear strain of 12% ($\sigma'_{v0}=250 \text{ kPa}$ and $D_r=49\%$)

- * Horizontal plane (σ'_{zz}, τ_{zx})
- × Vertical plane (σ'_{xx}, τ_{xz})
- ◇ Planes of maximum plane stress
- Planes of maximum stress obliquity

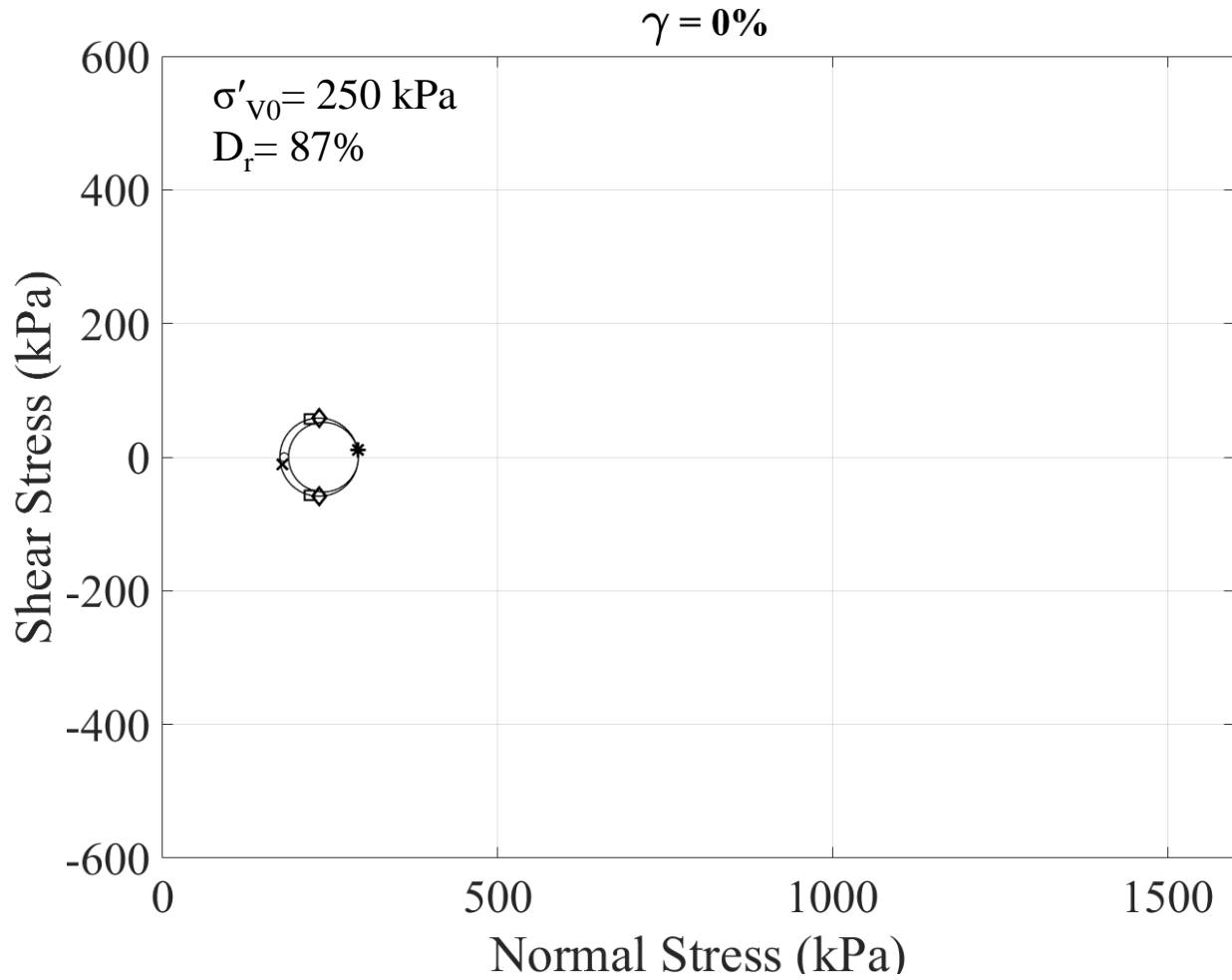


Figure D.10 Mohr's circles of stress at boundary shear strain of 0% ($\sigma'_{v0}=250$ kPa and $D_r=87\%$)

- * Horizontal plane (σ'_{zz}, τ_{zx})
- × Vertical plane (σ'_{xx}, τ_{xz})
- ◇ Planes of maximum plane stress
- Planes of maximum stress obliquity

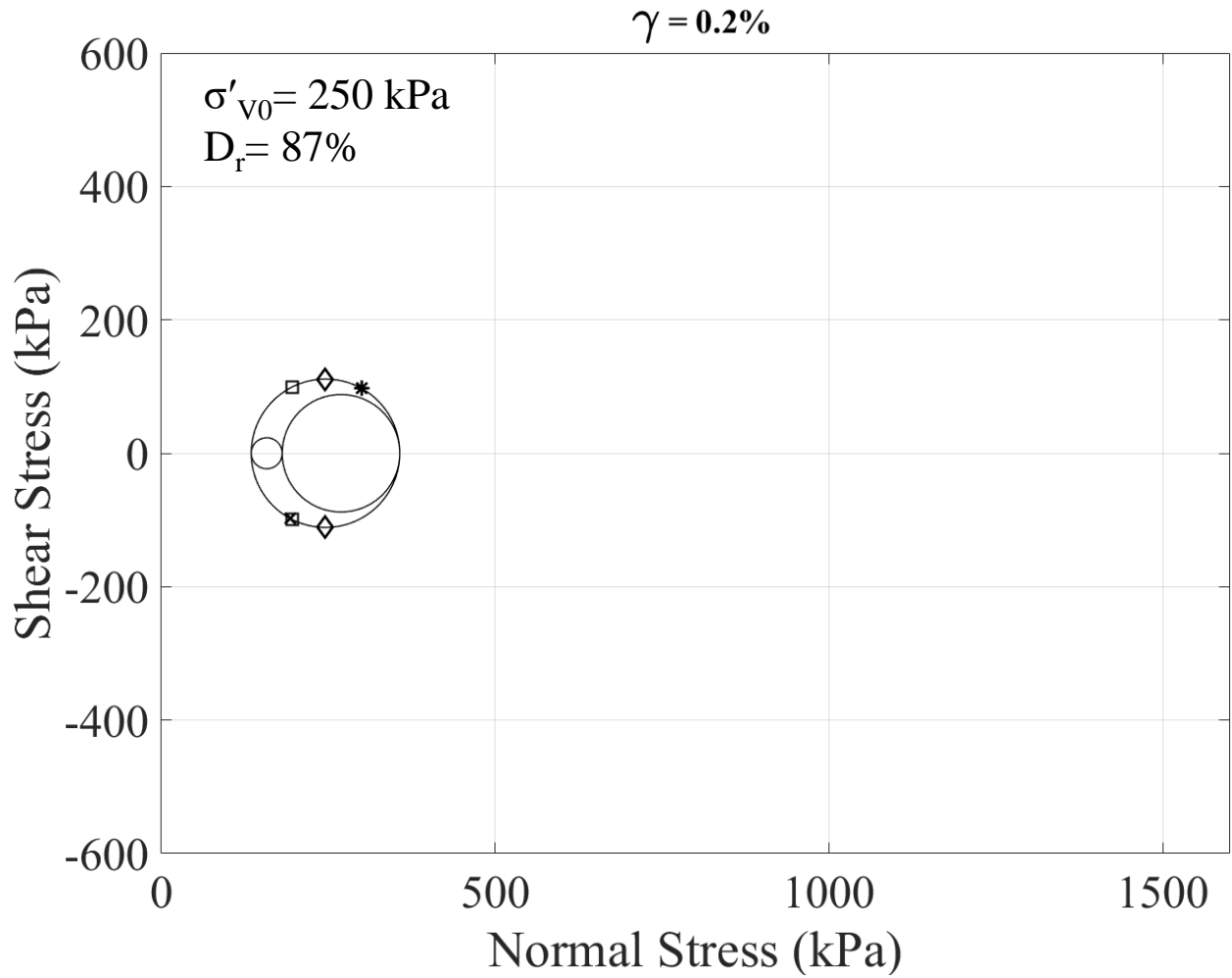


Figure D.11 Mohr's circles of stress at boundary shear strain of 0.2% ($\sigma'_{v0}=250 \text{ kPa}$ and $D_r=87\%$)

- * Horizontal plane (σ'_{zz}, τ_{zx})
- × Vertical plane (σ'_{xx}, τ_{xz})
- ◇ Planes of maximum plane stress
- Planes of maximum stress obliquity

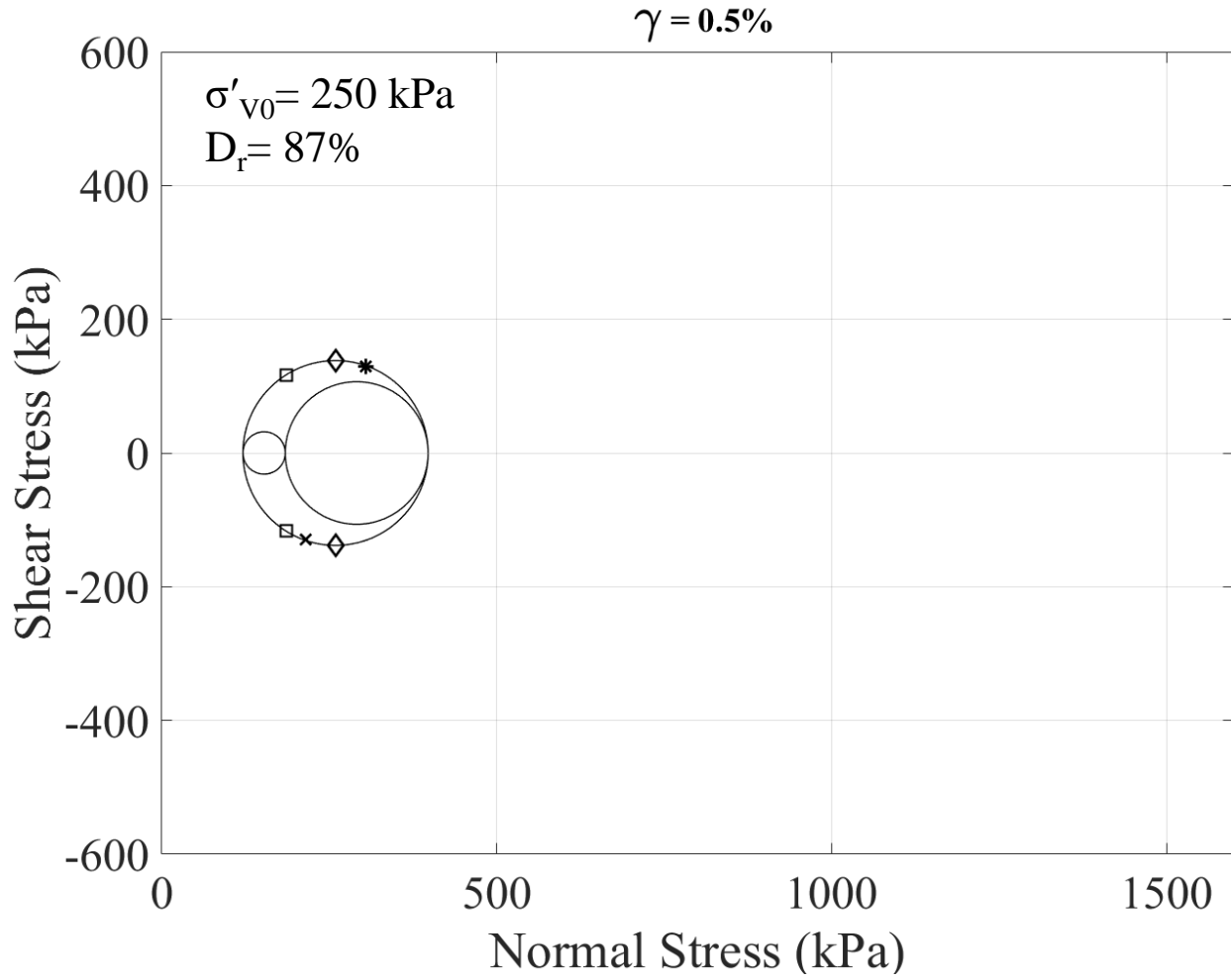


Figure D.12 Mohr's circles of stress at boundary shear strain of 0.5% ($\sigma'_{v0}=250 \text{ kPa}$ and $D_r=87\%$)

- * Horizontal plane (σ'_{zz}, τ_{zx})
- × Vertical plane (σ'_{xx}, τ_{xz})
- ◇ Planes of maximum plane stress
- Planes of maximum stress obliquity

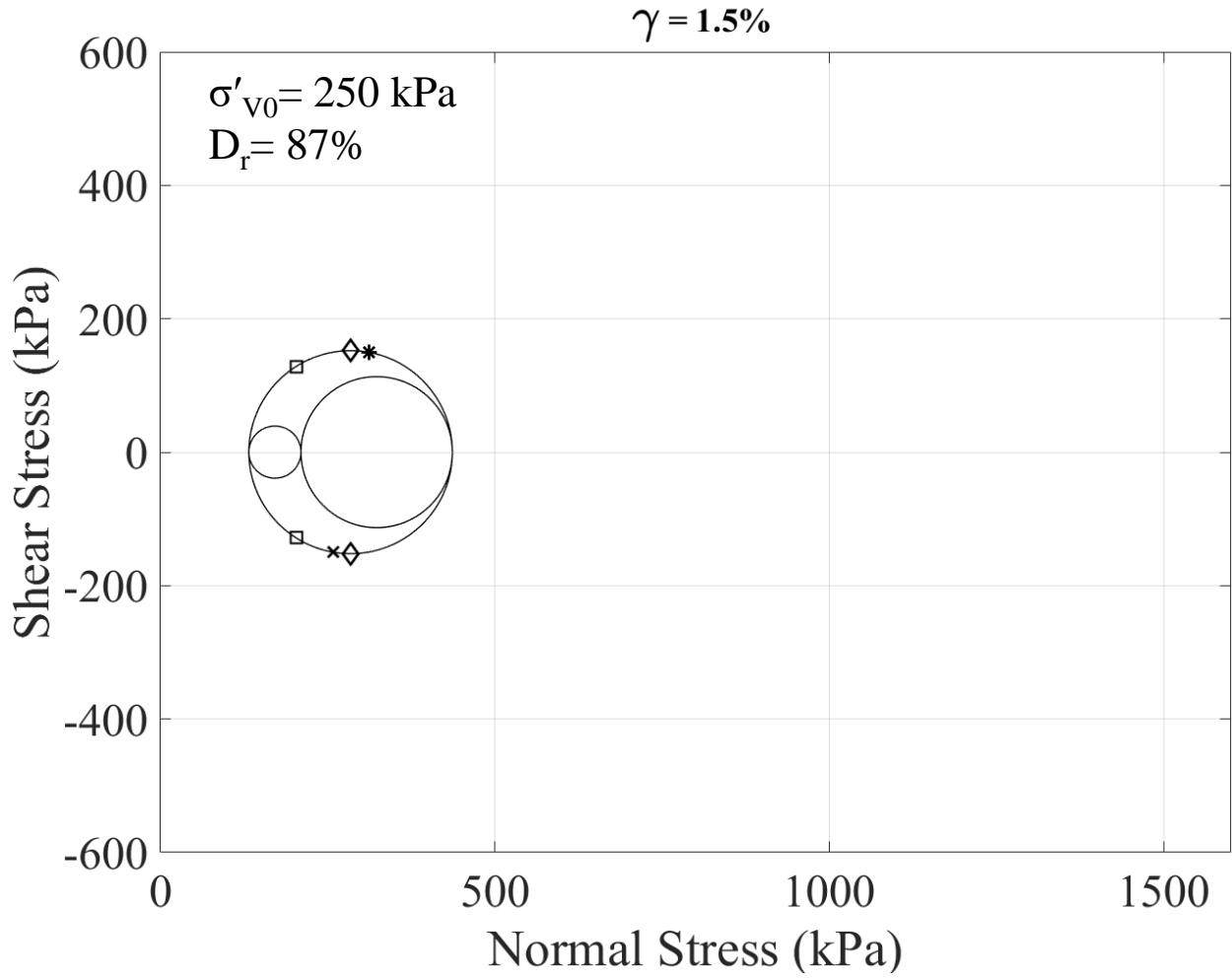


Figure D.13 Mohr's circles of stress at boundary shear strain of 1.5% ($\sigma'_{v0}=250 \text{ kPa}$ and $D_r=87\%$)

- * Horizontal plane (σ'_{zz}, τ_{zx})
- × Vertical plane (σ'_{xx}, τ_{xz})
- ◇ Planes of maximum plane stress
- Planes of maximum stress obliquity

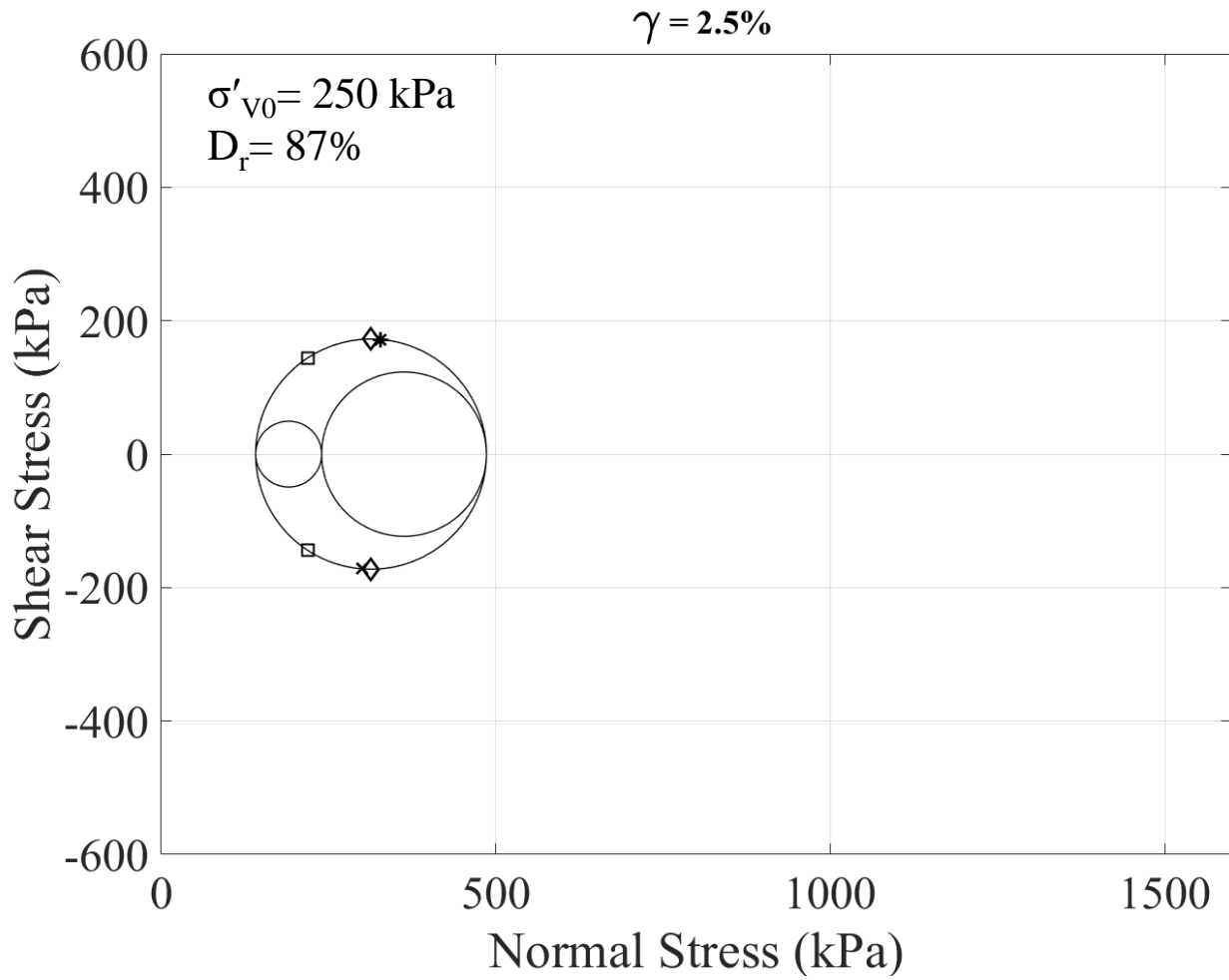


Figure D.14 Mohr's circles of stress at boundary shear strain of 2.5% ($\sigma'_{v0}=250 \text{ kPa}$ and $D_r=87\%$)

- * Horizontal plane (σ'_{zz}, τ_{zx})
- × Vertical plane (σ'_{xx}, τ_{xz})
- ◇ Planes of maximum plane stress
- Planes of maximum stress obliquity

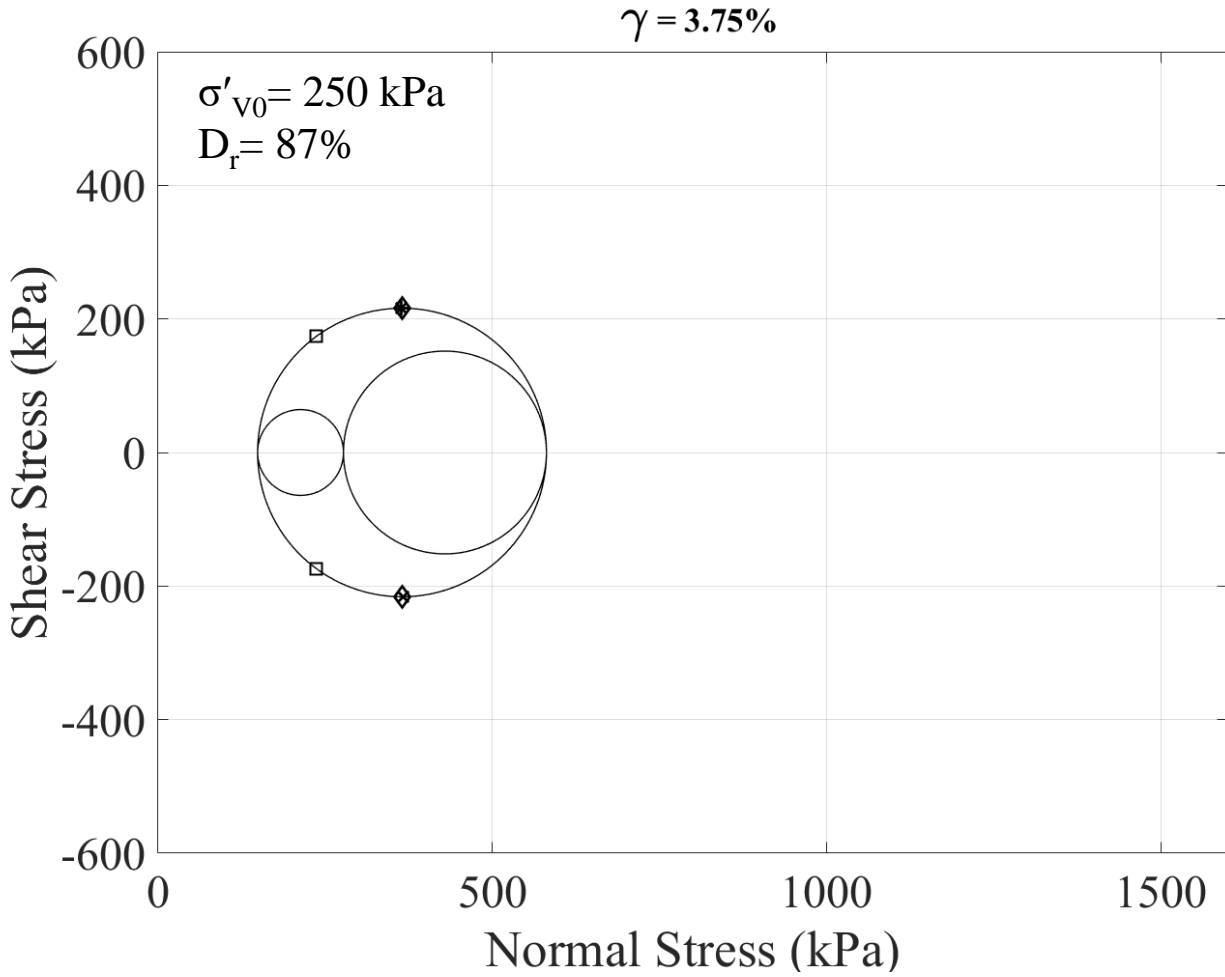


Figure D.15 Mohr's circles of stress at boundary shear strain of 3.75% ($\sigma'_{v0}=250 \text{ kPa}$ and $D_r=87\%$)

- * Horizontal plane (σ'_{zz}, τ_{zx})
- × Vertical plane (σ'_{xx}, τ_{xz})
- ◇ Planes of maximum plane stress
- Planes of maximum stress obliquity

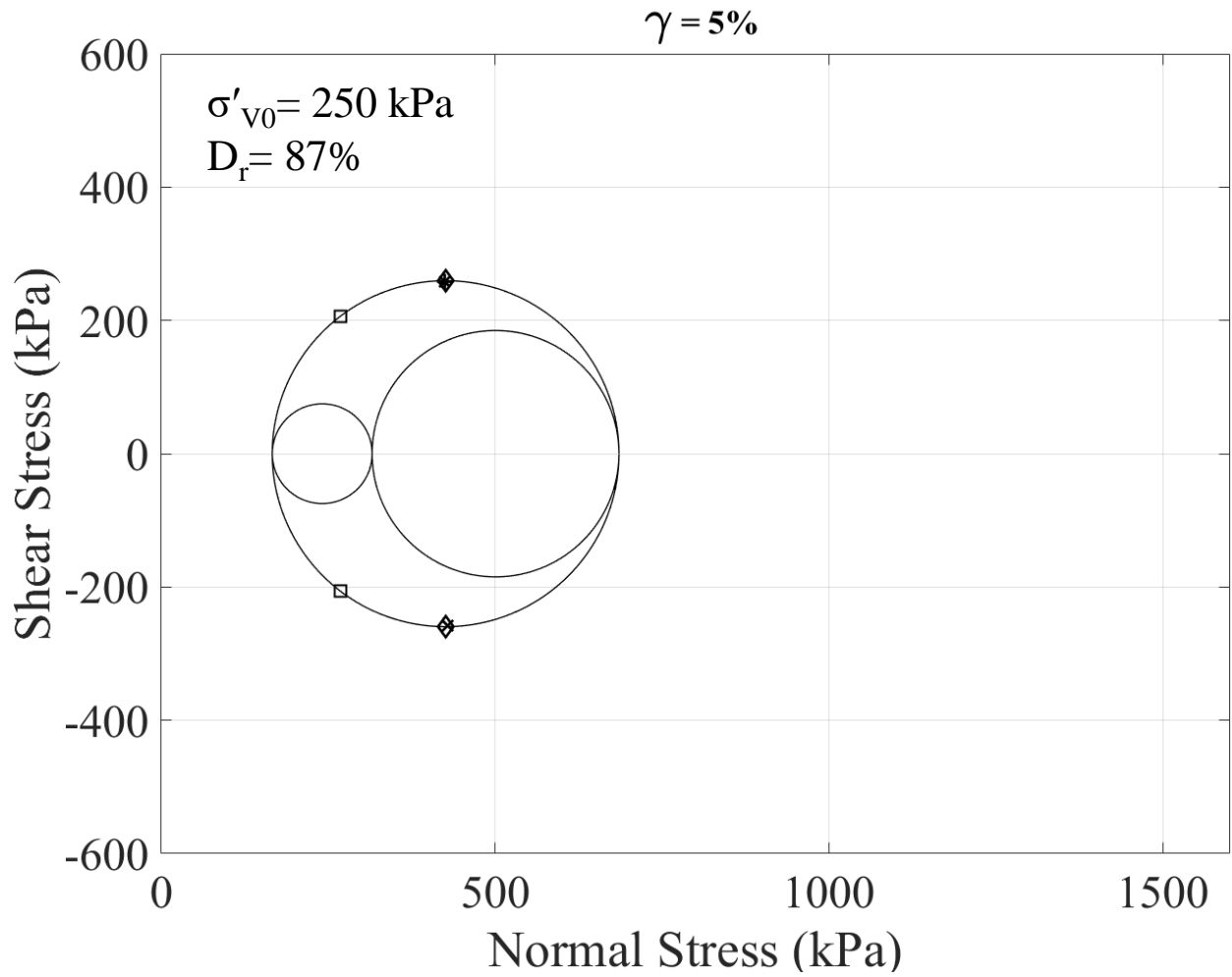


Figure D.16 Mohr's circles of stress at boundary shear strain of 5% ($\sigma'_{v0}=250$ kPa and $D_r=87\%$)

- * Horizontal plane (σ'_{zz}, τ_{zx})
- × Vertical plane (σ'_{xx}, τ_{xz})
- ◇ Planes of maximum plane stress
- Planes of maximum stress obliquity

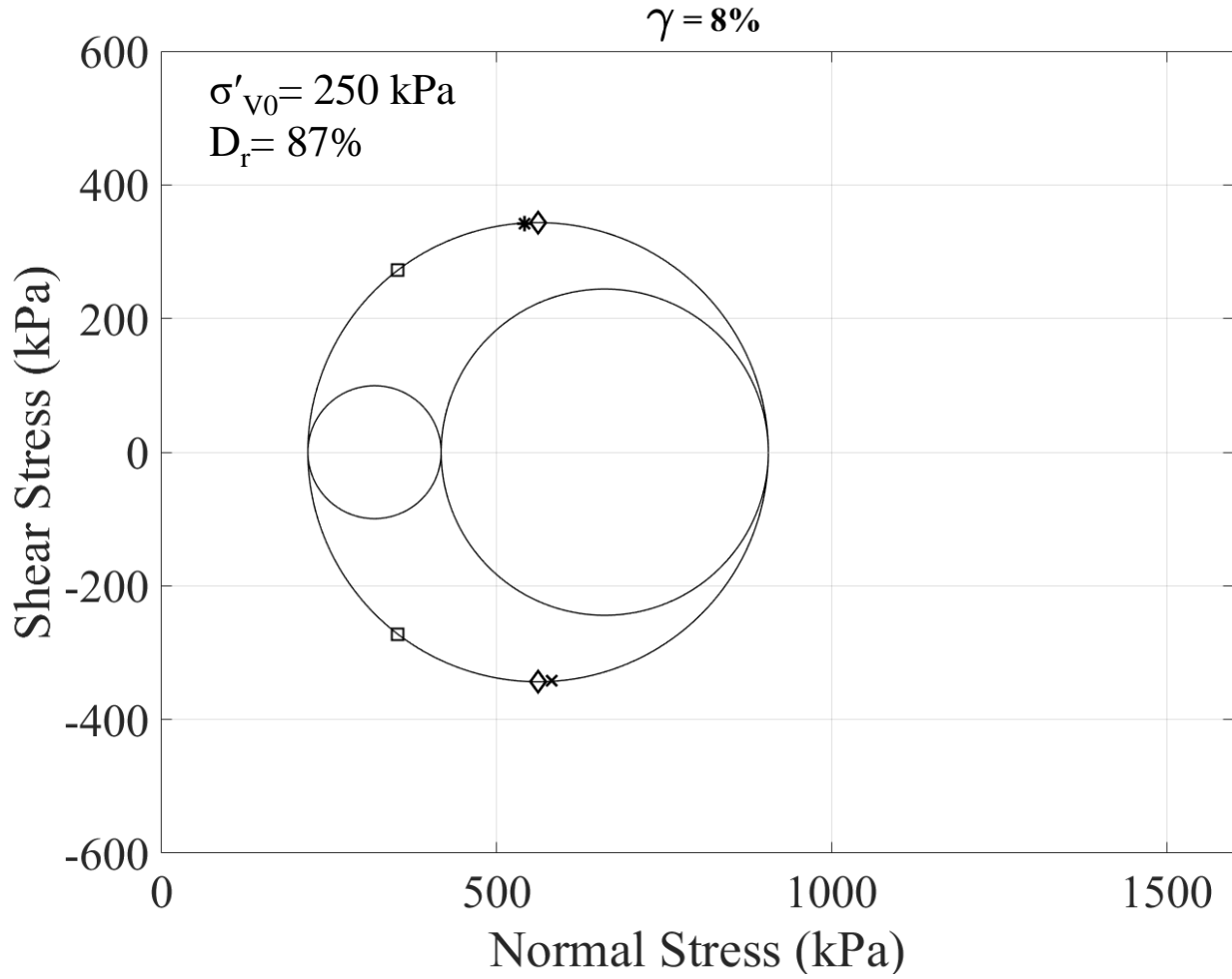


Figure D.17 Mohr's circles of stress at boundary shear strain of 8% ($\sigma'_{v0}=250$ kPa and $D_r=87\%$)

- * Horizontal plane (σ'_{zz}, τ_{zx})
- × Vertical plane (σ'_{xx}, τ_{xz})
- ◇ Planes of maximum plane stress
- Planes of maximum stress obliquity

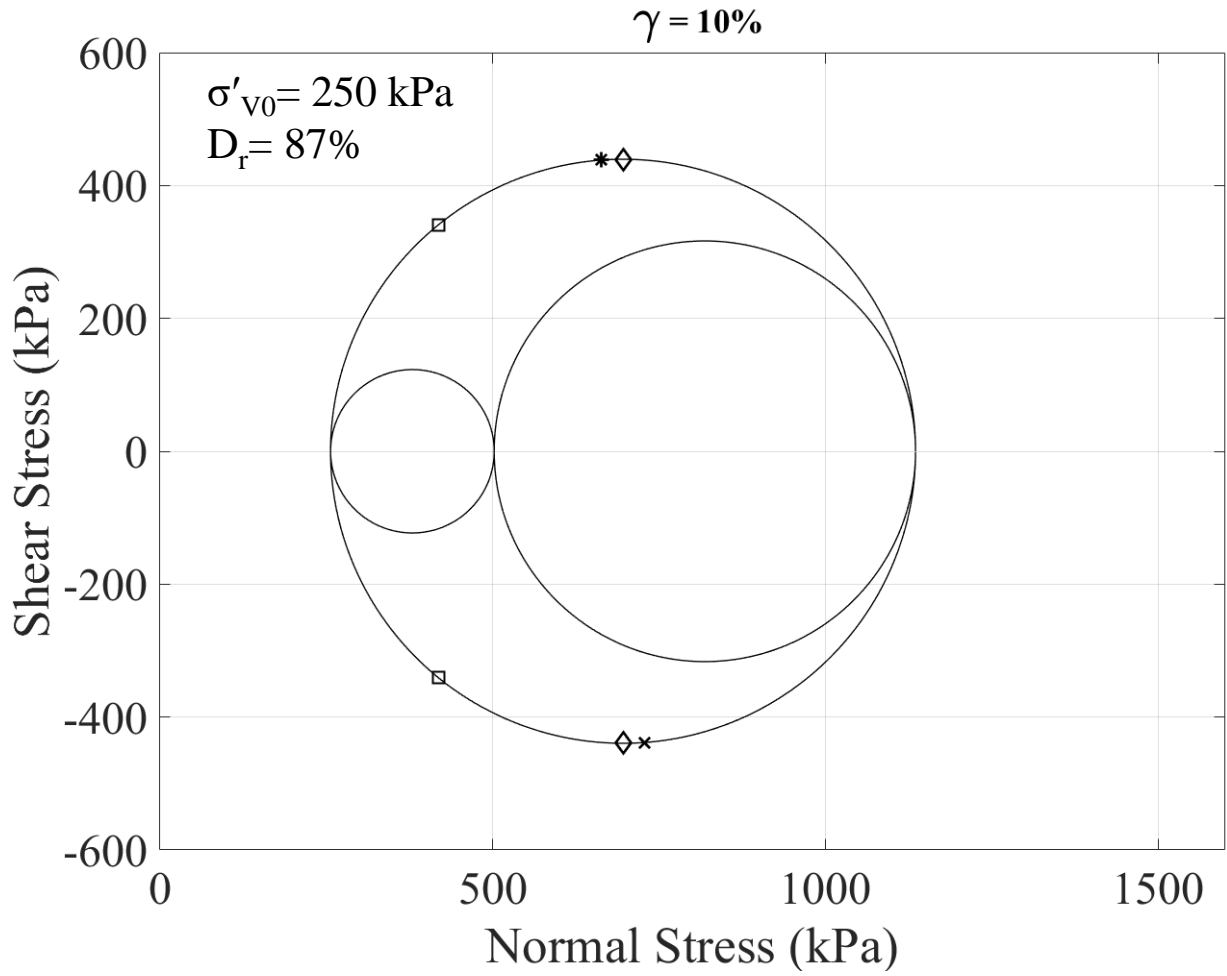


Figure D.18 Mohr's circles of stress at boundary shear strain of 10% ($\sigma'_{v0}=250 \text{ kPa}$ and $D_r=87\%$)

- * Horizontal plane (σ'_{zz}, τ_{zx})
- × Vertical plane (σ'_{xx}, τ_{xz})
- ◇ Planes of maximum plane stress
- Planes of maximum stress obliquity

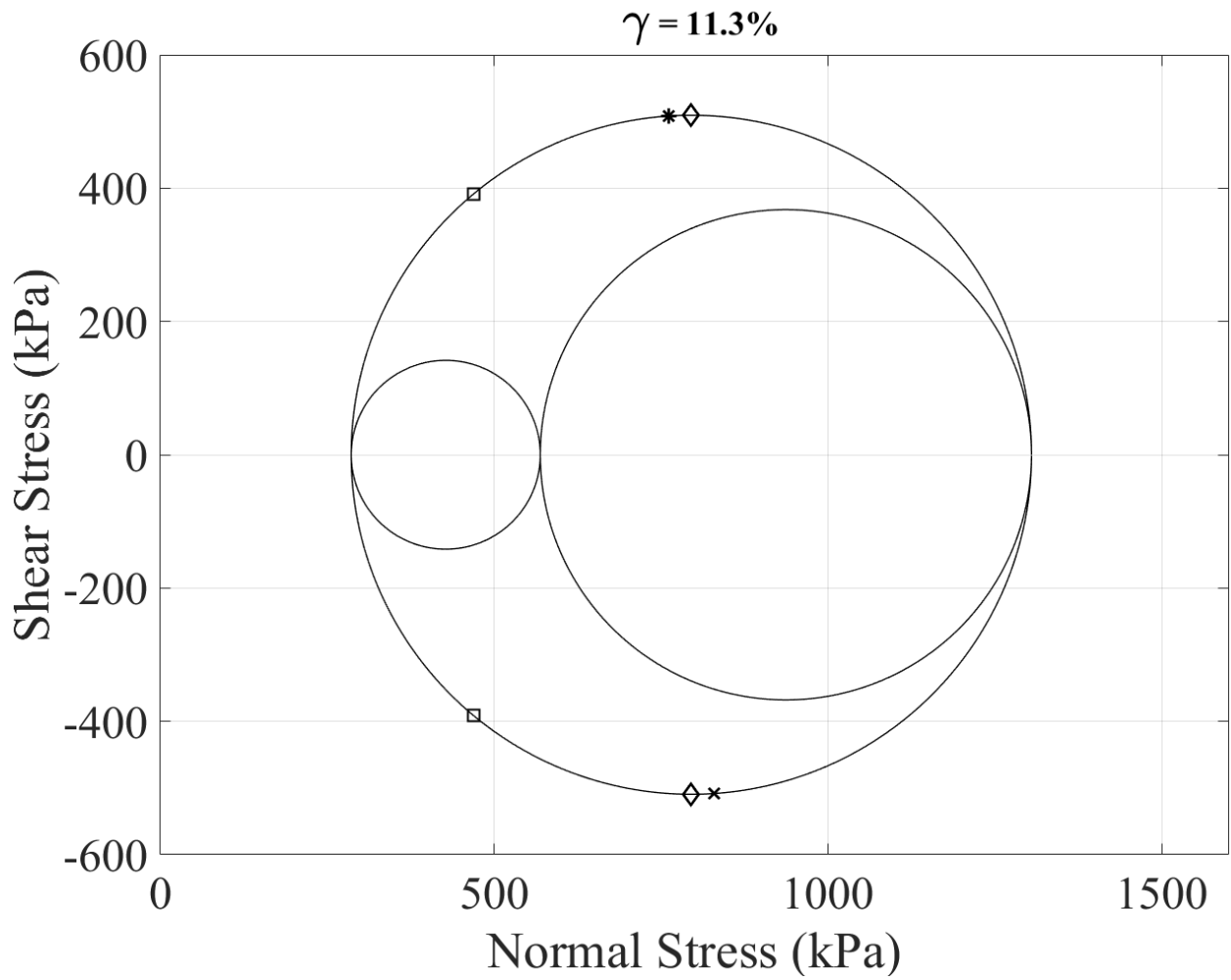


Figure D.19 Mohr's circles of stress at boundary shear strain of 11.3% ($\sigma'_{v0}=250$ kPa and $D_r=87\%$)

Appendix E

Comparison of the cyclic simple shear response measured at boundaries and inside the central measurement spheres for consolidated vertical stresses of 100 and 400 kPa at relative density of 49%

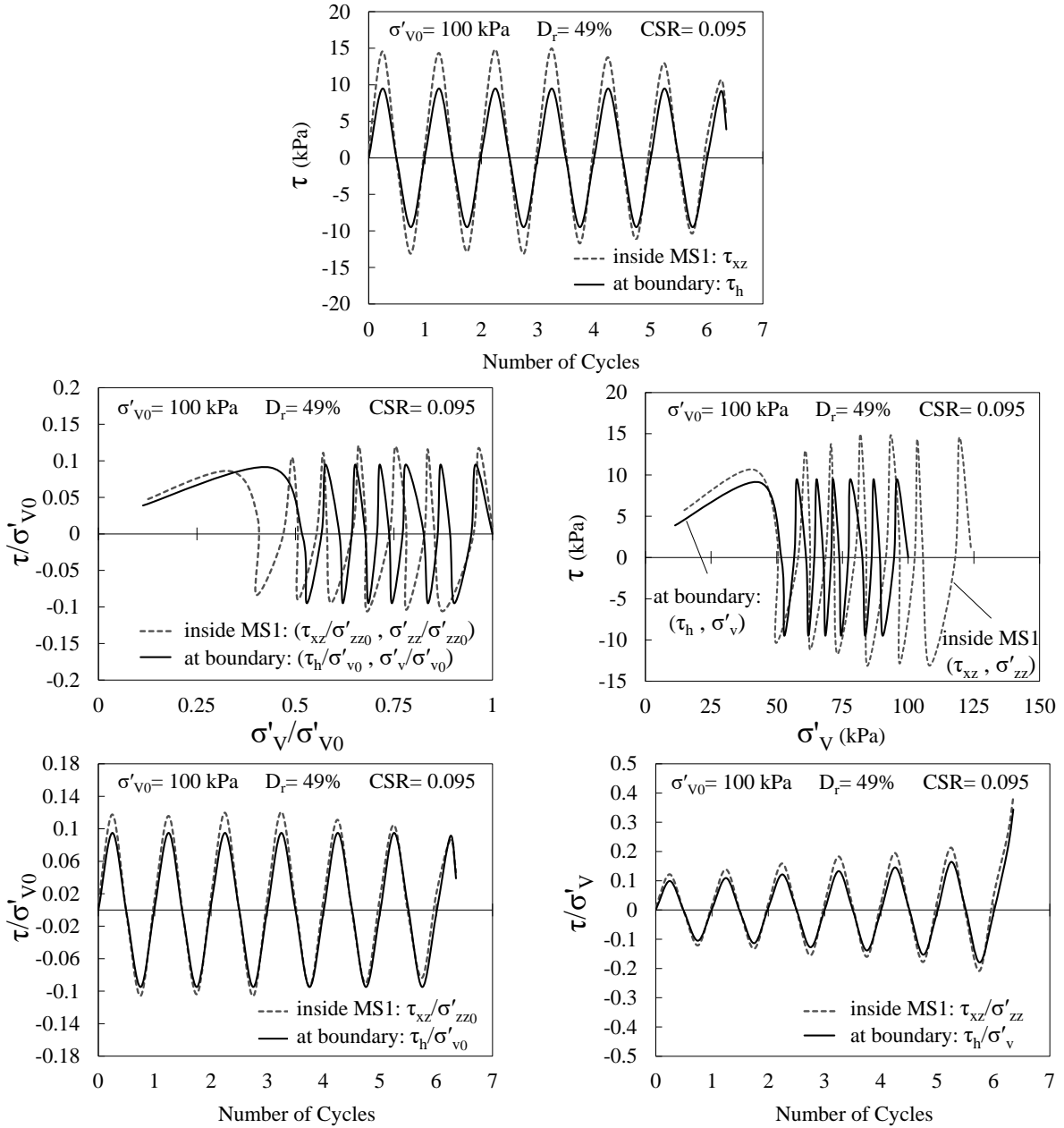


Figure E.1 Comparison of the cyclic shear response measured at boundaries and inside the central measurement sphere in DEM simulations of constant volume cyclic simple shear response of Pea gravel specimen ($\sigma'_{v0} = 100$ kPa, $D_r = 49\%$, $CSR = 0.095$)

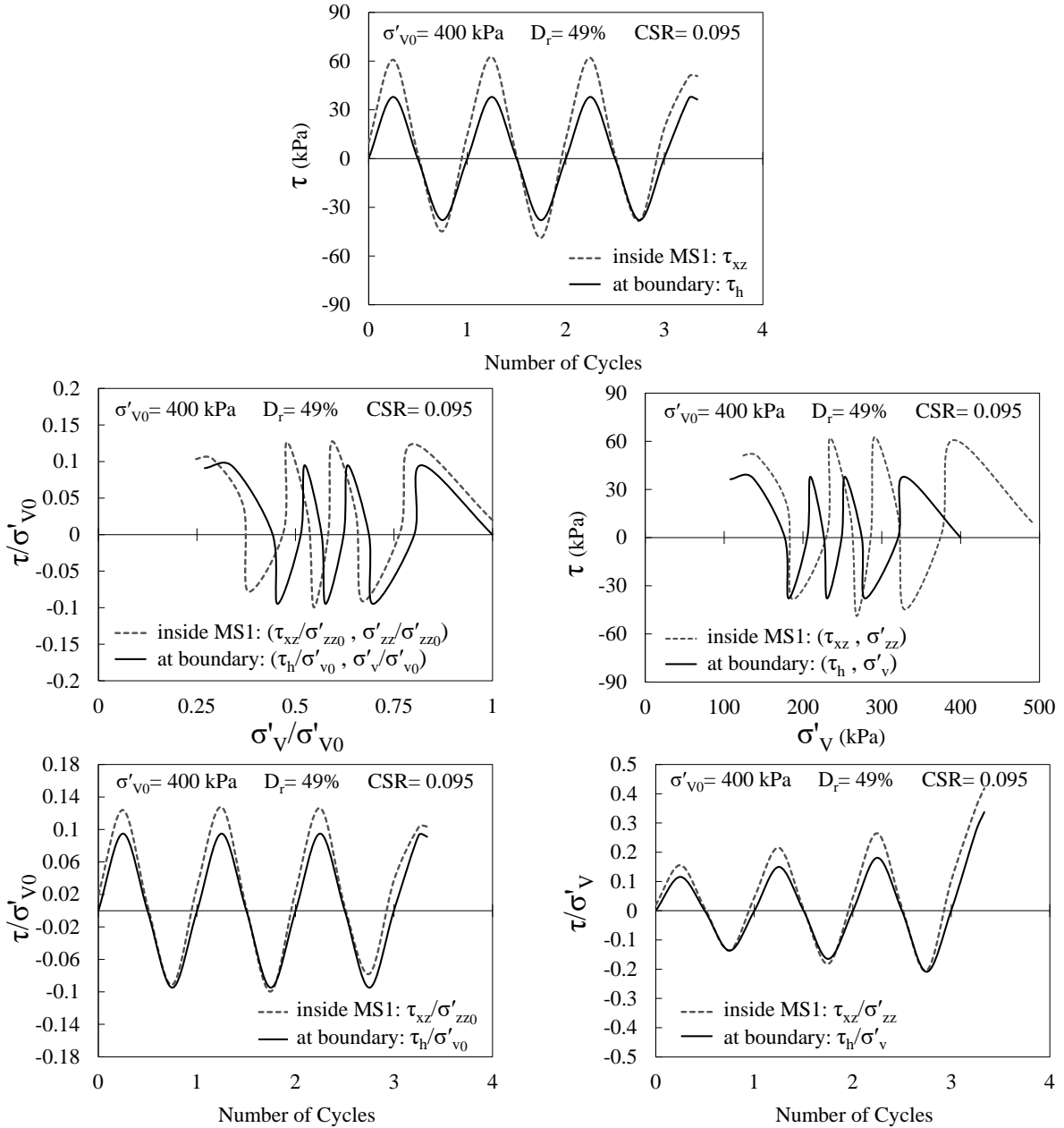


Figure E.2 Comparison of the cyclic shear response measured at boundaries and inside the central measurement sphere in DEM simulations of constant volume cyclic simple shear response of Pea gravel specimen ($\sigma'_{v0}=400$ kPa, $D_r=49\%$, $CSR=0.095$)

Appendix F

Variation of different measurement quantities inside MS1-MS13 during cyclic shear for consolidated vertical stresses of 100 and 400 kPa at relative density of 49%

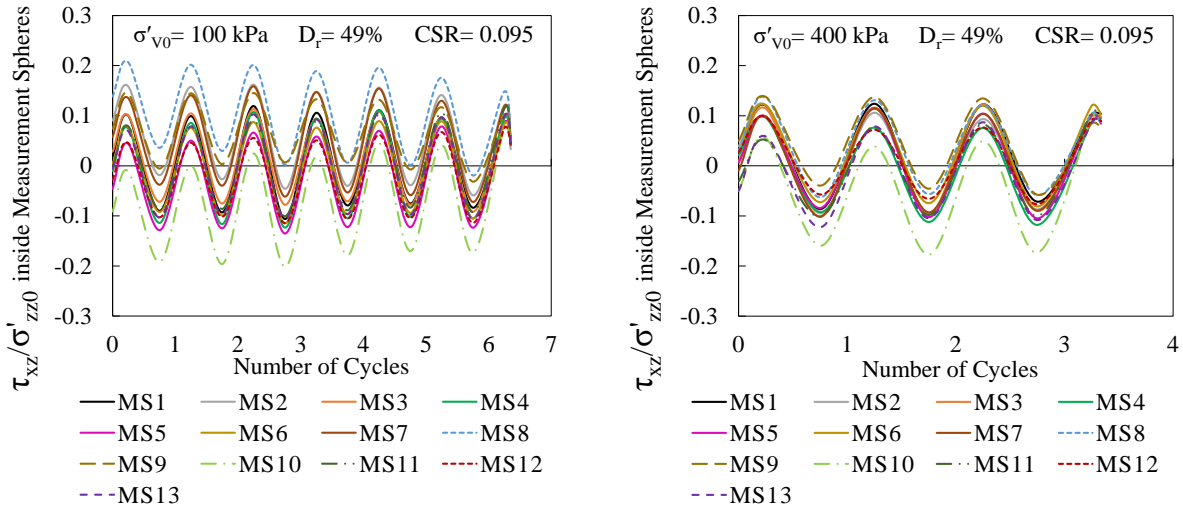


Figure F. Stress ratio (τ_{xz}/σ'_{zz0}) measured inside MS1-MS13 during cyclic shear in DEM simulations of constant volume cyclic simple shear response of Pea gravel specimen $\sigma'_{v0}=100$ and 400 kPa, $D_r=49\%$ and $\text{CSR}=0.095$

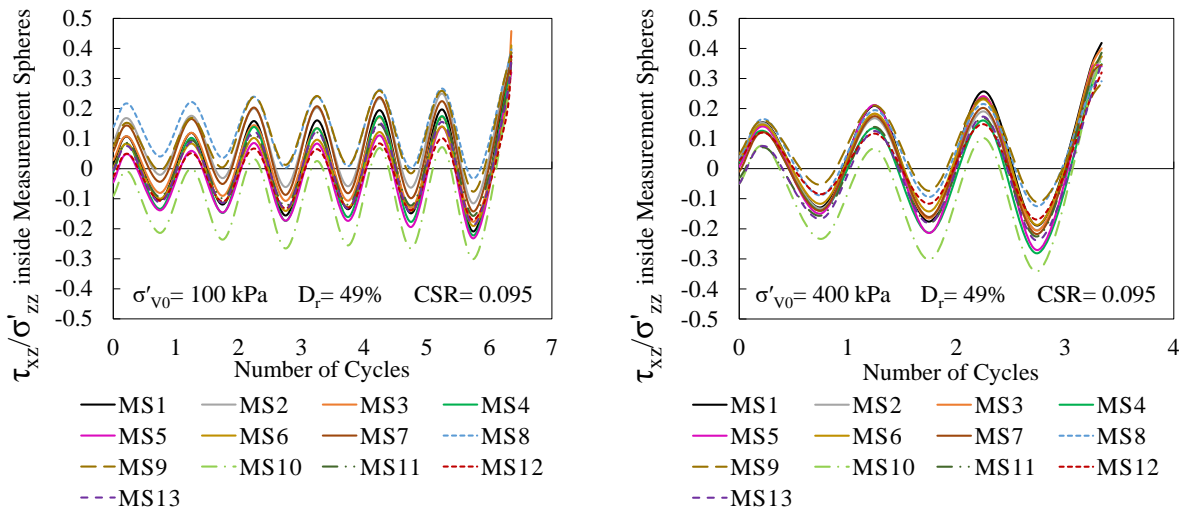


Figure F.1 Stress ratio (τ_{xz}/σ'_{zz}) measured inside MS1-MS13 during cyclic shear in DEM simulations of constant volume cyclic simple shear response of Pea gravel specimen for $\sigma'_{v0}=100$ and 400 kPa, $D_r=49\%$ and $\text{CSR}=0.095$

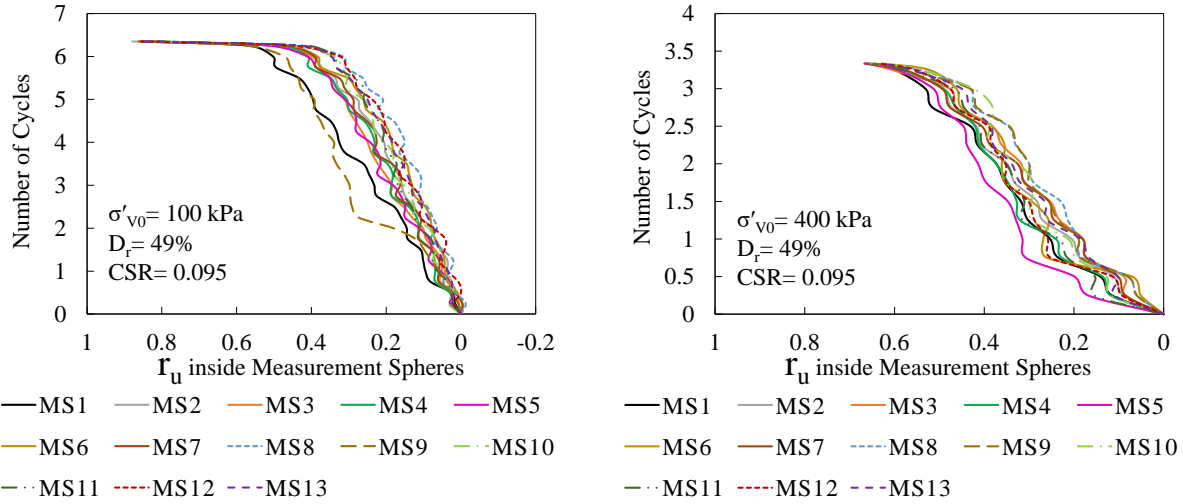


Figure F.2 Pore pressure ratio measured inside MS1-MS13 during cyclic shear in DEM simulations of constant volume cyclic simple shear response of Pea gravel specimen for $\sigma'_{v0}=100$ and 400 kPa, $D_r=49\%$ and $CSR=0.095$

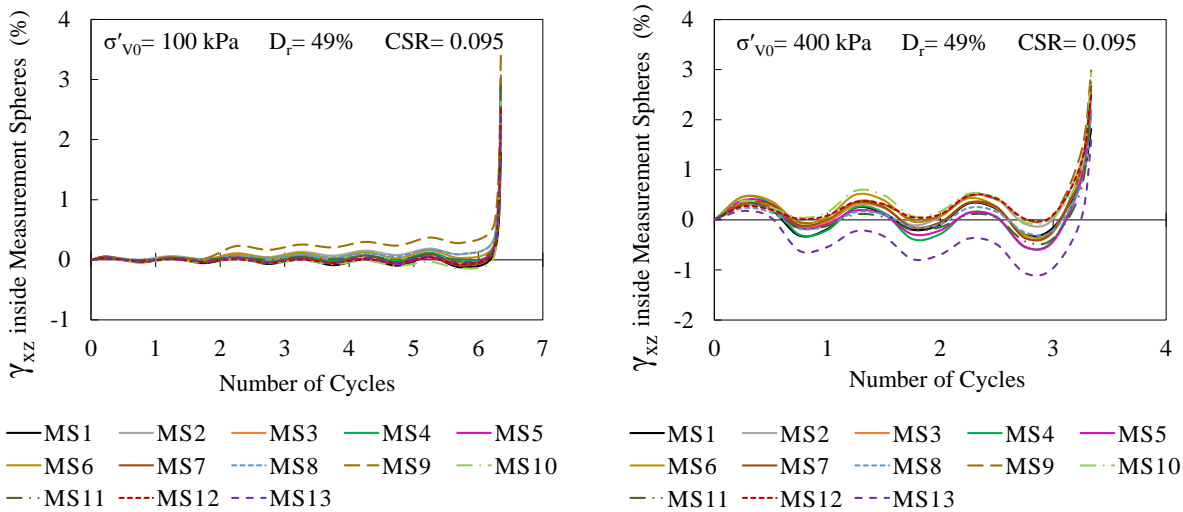
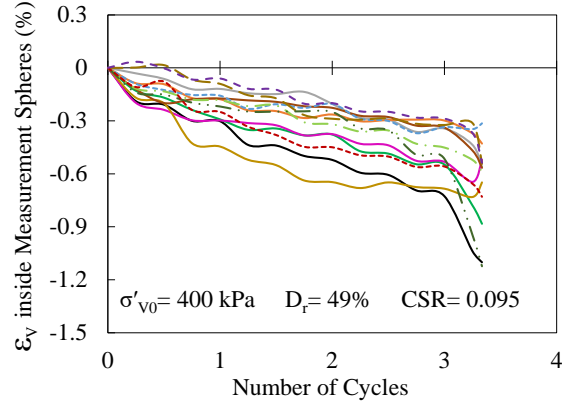
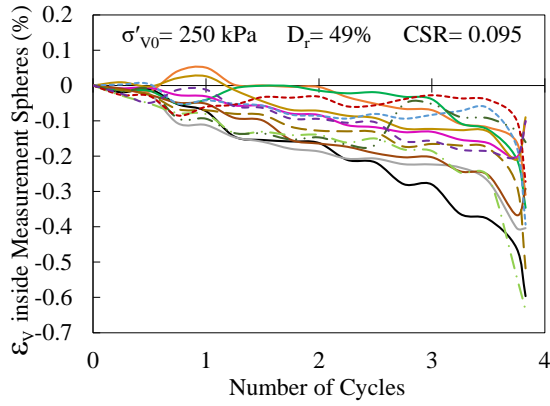


Figure F.3 Shear strain measured inside MS1-MS13 during cyclic shear in DEM simulations of constant volume cyclic simple shear response of Pea gravel specimen for $\sigma'_{v0}=100$ and 400 kPa, $D_r=49\%$ and $CSR=0.095$



— MS1 — MS2 — MS3 — MS4 — MS5
 — MS6 — MS7 - - MS8 - - MS9 - - MS10
 - · MS11 - · MS12 - · MS13

— MS1 — MS2 — MS3 — MS4 — MS5
 — MS6 — MS7 - - MS8 - - MS9 - - MS10
 - · MS11 - · MS12 - · MS13

Figure F.4 Volumetric strain measured inside MS1-MS13 during cyclic shear in DEM simulations of constant volume cyclic simple shear response of Pea gravel specimen for $\sigma'_{v0}=100$ and 400 kPa, $D_r=49\%$ and $CSR=0.095$

Bibliography

- Ai, J., Langston, P. A., and Yu, H. S. (2014). "Discrete element modelling of material non-coaxiality in simple shear flow." *International Journal for Numerical and Analytical Methods in Geomechanics*, 38, 615–635.
- Airey, D. W., and Wood, D. M. (1987). "An evaluation of direct simple shear tests on clay." *Geotechnique*, 37(1), 25–35.
- Altuhafi, F., O'Sullivan, C., and Cavarretta, I. (2012). "Analysis of an Image-Based Method to Quantify the Size and Shape of Sand Particles." *Journal of Geotechnical and Geoenvironmental Engineering*, 139(8), 1290–1307.
- Andrus, R., Stokoe, K., Bray, J., and Youd, T. (1992). "In situ VS of gravelly soils which liquefied, in Proceedings of the 10th World Conference on Earthquake Engineering." *Proceedings of the 10th World Conference on Earthquake Engineering*.
- Asadzadeh, M., and Soroush, A. (2016). "Fundamental investigation of constant stress simple shear test using DEM." *Powder Technology*, Elsevier B.V., 292, 129–139.
- Asadzadeh, M., and Soroush, A. (2017). "Macro- and micromechanical evaluation of cyclic simple shear test by discrete element method." *Particuology*, Chinese Society of Particuology, 31, 129–139.
- Asadzadeh, M., and Soroush, A. (2018). "Evaluation of stress and strain non-uniformity during cyclic simple shear test using DEM: effect of the horizontal platen asperities." *Granular Matter*, Springer Berlin Heidelberg, 20(3), 1–11.
- Ashmawy, A. K., Sukumaran, B., and Hoang, V. V. (2003). "Evaluating The Influence of Particle Shape on Liquefaction Behavior Using Discrete Element Modeling." *Paper No. 2003-PCW-05*.
- ASTM D6528-07. (2007). "Standard Test Method for Consolidated Undrained Direct Simple Shear Testing of Cohesive Soils." *ASTM International*.
- Azzouz, A. S., Malek, A. M., and Baligh, M. M. (1989). "Cyclic behavior of clays in undrained simple shear." *Journal of Geotechnical Engineering*, 115(5), 637–657.
- Barreto Gonzalez, D. (2009). "Numerical and experimental investigation into the behaviour of granular materials under generalised stress states." PhD Dissertation, Imperial College, London.

- Basham, M., Zekkos, A., and Zekkos, D. (2019). "The importance of vertical displacement control during constant volume cyclic direct simple shear testing." *7th International Conference on Earthquake Geotechnical Engineering*, Rome, Italy.
- Bathurst, R. J., and Rothenburg, L. (1990). "Observations on stress-force-fabric relationships in idealized granular materials." *Mechanics of Materials*, 9(1), 65–80.
- Belheine, N., Plassiard, J. P., Donzé, F. V., Darve, F., and Seridi, A. (2009). "Numerical simulation of drained triaxial test using 3D discrete element modeling." *Computers and Geotechnics*, 36(1–2), 320–331.
- Bernhardt, M. L., Biscontin, G., and O’Sullivan, C. (2014). "3D Discrete Element Method Simulations of a Laminar-Type Simple Shear Apparatus." *Geo-Congress 2014 Technical Papers*, (234 GSP), 614–623.
- Bernhardt, M. L., Biscontin, G., and O’Sullivan, C. (2016). "Experimental validation study of 3D direct simple shear DEM simulations." *Soils and Foundations*, Elsevier, 56(3), 336–347.
- Beucher, S., and Lantuejoul, C. (1979). "Use of Watersheds in Contour Detection." *International Workshop on Image Processing: Real-time Edge and Motion Detection/Estimation*.
- Bjerrum, L., and Landva, A. (1966). "Direct Simple-Shear Tests on a Norwegian Quick Clay." *Géotechnique*, 16(1), 1–20.
- Boulanger, R., Chan, C. K., Seed, H. B., Seed, R. B., and Sousa, J. B. (1993). "A Low-Compliance Bi-Directional Cyclic Simple Shear Apparatus." *Geotechnical Testing Journal*, 16(1), 36–45.
- Budhu, M. (1979). "Simple shear deformation of sands." PhD Dissertation, University of Cambridge, United Kingdom.
- Budhu, M. (1984). "Nonuniformities imposed by simple shear apparatus." *Canadian Geotechnical Journal*, 21(1), 125–137.
- Budhu, M. (1985). "Lateral stresses observed in two simple shear apparatus." *Journal of Geotechnical Engineering*, 111(6), 698–711.
- Budhu, M. (1988). "Failure state of a sand in simple shear." *Canadian Geotechnical Journal*, 25(2), 395–400.
- Budhu, M., and Britto, A. (1987). "Numerical Analysis of Soils in Simple Shear Devices." *Soils and Foundations*, 27(2), 31–41.
- Cai, Y., Yu, H. S., Wanatowski, D., and Li, X. (2013). "Noncoaxial behavior of sand under various stress paths." *Journal of Geotechnical and Geoenvironmental Engineering*, 139(8), 1381–1395.
- Cao, Z., Leslie Youd, T., and Yuan, X. (2011). "Gravelly soils that liquefied during 2008

- Wenchuan, China earthquake, Ms=8.0.” *Soil Dynamics and Earthquake Engineering*, Elsevier, 31(8), 1132–1143.
- Castro, G. (1969). “Liquefaction of Sands.” PhD Dissertation, Harvard Soil Mech. Series, No. 81, Harvard University.
- Chang, W. J., Chang, C. W., and Zeng, J. K. (2014). “Liquefaction characteristics of gap-graded gravelly soils in K0 condition.” *Soil Dynamics and Earthquake Engineering*, Elsevier, 56, 74–85.
- Charles, J. A., and Watts, K. S. (1980). “The influence of confining pressure on the shear strength of compacted rockfill.” *Geotechnique*, 30(4), 353–367.
- Chern, J.-C. (1985). “Undrained Response of Saturated Sands with Emphasis on liquefaction and cyclic mobility.” PhD Dissertation, University of British Columbia.
- Cheung, G., and O’Sullivan, C. (2008). “Effective simulation of flexible lateral boundaries in two- and three-dimensional DEM simulations.” *Particuology*, 6(6), 483–500.
- Cho, G.-C., Dodds, J., and Santamarina, J. C. (2006). “Particle Shape Effects on Packing Density, Stiffness, and Strength: Natural and Crushed Sands.” *Journal of Geotechnical and Geoenvironmental Engineering*, 132(5), 591–602.
- Christoffersen, J., Mehrabadi, M. M., and Nemat-Nasser, S. (1981). “A Micromechanical Description of Granular Material Behavior.” *Journal of Applied Mechanics*, 48(June), 339–344.
- Cubrinovski, M., Bray, J. D., and de la Torre, C. (2018). “Liquefaction of Reclaimed Land at Wellington Port in the 2016 Kaikoura Earthquake.” *Geotechnical Earthquake Engineering and Soil Dynamics V*, 357–373.
- Cui, L., and O’Sullivan, C. (2006). “Exploring the macro- and micro-scale response of an idealised granular material in the direct shear apparatus.” *Géotechnique*, 56(7), 455–468.
- Cui, L., O’Sullivan, C., O’Neill, S., and Cui, L. (2007). “An analysis of the triaxial apparatus using a mixed boundary three-dimensional discrete element model.” *Géotechnique*, 57(10), 831–844.
- Cundall, P. A. (1971). “A computer model for simulating progressive, large-scale movements in blocky rock systems.” *Proceedings of the International Symposium on Rock Mechanics*, 132–150.
- Cundall, P. A. (1974). “A computer model for rock-mass behaviour using interactive graphics for the input and output of geometrical data.” *A Report Prepared under Contract Number DACW 45-74-C-006, for the Missouri River Division*.
- Cundall, P. A. (1988). *Computer Simulations of Dense Sphere Assemblies. Micromechanics of Granular Materials*, edited by M. Satake and J. T. Jenkins, eds. Amsterdam: Elsevier

Science Publishers B.V., Elsevier B.V.

- Cundall, P. A. (2001). "A discontinuous future for numerical modelling in geomechanics?" *Proceedings of the Institution of Civil Engineers - Geotechnical Engineering*, 149(1), 41–47.
- Cundall, P. A., and Hart, R. D. (1992). "Numerical modelling of discontinua." *Engineering Computations*, 9(2), 101–113.
- Cundall, P. A., and Strack, O. D. L. (1979a). "A discrete numerical model for granular assemblies." *Géotechnique*, 29(1), 47–65.
- Cundall, P. A., and Strack, O. D. L. (1979b). "The development of constitutive laws for soil using the distinct element method." *Numerical methods in geomechanics*, 1, 289–317.
- Dabeet, a., Wijewickreme, D., and Byrne, P. (2011). "Discrete element modeling of direct simple shear response of granular soils and model validation using laboratory element tests." *14th Pan-Am. Conference and 64th Canadian Geotechnical conference*.
- Dabeet, A. (2014). "Discrete Element Modeling of Direct Simple Shear Response of Granular Soils and Model Validation Using Laboratory Tests." PhD Dissertation, University of British Columbia.
- Dabeet, A., Wijewickreme, D., and Byrne, P. (2010). "Evaluation of the stress-strain uniformities in the direct simple shear device using 3D discrete element modeling." *63rd Canadian Geotechnical Conference & 6th Canadian Permafrost Conference*, 193–199.
- Dabeet, A., Wijewickreme, D., and Byrne, P. (2014). "Application of Discrete Element Modeling for Simulation of Cyclic Direct Simple Shear." *Tenth U.S. National Conference on Earthquake Engineering*.
- Dabeet, A., Wijewickreme, D., and Byrne, P. (2015). "Evaluation of stress strain non-uniformities in the laboratory direct simple shear test specimens using 3D discrete element analysis." *Geomechanics and Geoengineering*, Taylor & Francis, 10(4), 249–260.
- Degroot, D. J., Germaine, J. T., and Ladd, C. C. (1994). "Effect of Nonuniform Stresses on Measured DSS Stress-Strain Behavior." *Journal of Geotechnical Engineering*, 120(5), 892–912.
- DeGroot, D. J., Ladd, C. C., and Germaine, J. T. (1992). "Direct simple shear testing of cohesive soils." [Ralph M. Parsons Laboratory], Department of Civil Engineering, Massachusetts Institute of Technology.
- Dobry, R., and Ng, T. tat. (1992). "Discrete modelling of stress-strain behaviour of granular media at small and large strains." *Engineering Computations*, 9(2), 129–143.
- Doherty, J., and Fahey, M. (2011). "Three-Dimensional Finite Element Analysis of Direct Shear Test." *Computers and Geotechnics*, 38, 917–924.

- Dounias, G. T., and Potts, D. M. (1993). “Numerical Analysis of Drained Direct and Simple Shear tests.” *Journal of Geotechnical Engineering*, 119(12), 1870–1891.
- Drescher, A., and De Josselin De Jong, G. (1972). “Photoelastic Verification of a Mechanical Model for the Flow of a Granular Material.” *Journal of Mech. Phys. Solids*, 20, 337–351.
- Dyvik, R., Berre, T., Lacasse, S., and Raadim, B. (1987). “Comparison of truly undrained and constant volume direct simple shear tests.” *Géotechnique*, 37(1), 3–10.
- Finn, W. D. L., Vaid, Y. P., and Bhatia, S. K. (1978). “Constant volume simple shear testing.” *second International Conference on Microzonation for Safer Construction-Research and Application*, 839–851.
- Franke, E., Kiekbusch, M., and Schuppener, B. (1979). “New Direct Simple Shear Device.” *Geotechnical Testing Journal*, 2(4), 190–199.
- Garcia, F. E., and Bray, J. D. (2018). “Distinct Element Simulations of Shear Rupture in Dilatant Granular Media.” *International Journal of Geomechanics*, 18(9), 04018111 Int.
- Garcia, F. E., and Bray, J. D. (2019). “Modeling the shear response of granular materials with discrete element assemblages of sphere-clusters.” *Computers and Geotechnics*, Elsevier, 106(October 2018), 99–107.
- Geng, Y. (2010). “Discrete Element Modelling of Cavity Expansion in Granular Materials.” PhD Dissertation, University of Nottingham.
- Gong, G. (2008). “DEM Simulations of Drained and Undrained Behaviour.” PhD Dissertation; The University of Birmingham.
- Gu, X., Huang, M., and Qian, J. (2014). “DEM investigation on the evolution of microstructure in granular soils under shearing.” *Granular Matter*, 16(1), 91–106.
- Guo, Y., and Yu, X. B. (2015). “Understanding the microscopic moisture migration in pore space using DEM simulation.” *Journal of Rock Mechanics and Geotechnical Engineering*, Elsevier Ltd, 7(2), 171–177.
- Gutierrez, M., Ishihara, K., and Towhata, I. (1991). “Flow Theory For Sand During Rotation of Principal Stress Direction.” *Soils and Foundations*, 31(4), 121–132.
- Gutierrez, M., and Muftah, A. (2015). “Micro and macro behavior of granular materials in simple shear.” *Geomechanics from Micro to Macro – Soga et al. (Eds)*, (JANUARY), 91–96.
- Hamada, M. (2014). “Engineering for Earthquake Disaster Mitigation.” *Springer Series in Geomechanics and Geoengineering*.
- Hill, R. (1950). *The mathematical theory of plasticity*. Oxford University Press, Oxford.

- Huang, X., Hanley, K. J., O’Sullivan, C., and Kwok, F. C. Y. (2014). “Effect of sample size on the response of DEM samples with a realistic grading.” *Particuology*, 15.
- Hubler, J., Athanasopoulos-Zekkos, A., Ohm, H.-S., and Hryciw, R. (2014). “Effect of Particle Morphology on the Monotonic Response of Gravel-Sized Soils through Large-Scale Simple Shear Testing.” *Geo-Congress 2014*, (2006), 683–692.
- Hubler, J. F. (2017). “Laboratory and In-Situ Assessment of Liquefaction of Gravelly Soils.” PhD Dissertation, University of Michigan.
- Hubler, J. F., Athanasopoulos-Zekkos, A., and Zekkos, D. (2017). “Monotonic, Cyclic, and Postcyclic Simple Shear Response of Three Uniform Gravels in Constant Volume Conditions.” *Journal of Geotechnical and Geoenvironmental Engineering*, 143(9), 04017043.
- Ishibashi, I., and Capar, O. F. (2003). “Anisotropy and its relation to liquefaction resistance of granular material.” *Soils and Foundations*, 43(5), 149–159.
- Ishihara, K. (1993). “Liquefaction and flow failure during earthquakes.” *Géotechnique*, 43(3), 351–451.
- Itasca Consulting Group Inc. (2014). “PFC3D 5.00 Particle Flow Code in Three Dimensions.” Itasca Consulting Group, Inc., Minneapolis, Minnesota, USA.
- Iwashita, K., and Oda, M. (1998). “Rolling Resistance at Contacts in Simulation of Shear Band Development by DEM.” *Journal of Engineering Mechanics*, 124(3), 285–292.
- Jensen, R. P., Bosscher, P. J., Plesha, M. E., and Edil, T. B. (1999). “Dem Simulation of Granular Media - Structure Interface : Effects of Surface Roughness and Particle Shape.” *International Journal for Numerical and Analytical Methods in Geomechanics*, 23, 531–547.
- Jiang, M. J., Konrad, J. M., and Leroueil, S. (2003). “An efficient technique for generating homogeneous specimens for DEM studies.” *Computers and Geotechnics*, 30(7), 579–597.
- Jing, X. Y., Zhou, W. H., and Li, Y. (2017). “Interface Direct Shearing Behavior between Soil and Saw-tooth Surfaces by DEM Simulation.” *Procedia Engineering*, The Author(s), 175, 36–42.
- de Josselin de Jong, G. (1971). “Discussion Session 2. Stress-strain behavior of soils. In Proceedings, Roscoe Memorial Symposium. Edited by R. H. G. Parry, G. T. Foulis, and Co., Henley-on-Thames, United Kingdom.” *In Proceedings, Roscoe Memorial Symposium. Edited by R. H. G. Parry, G. T. Foulis, and Co., Henley-on-Thames, United Kingdom*, 258–261.
- de Josselin de Jong, G. (1988). “Elasto-plastic version of the double sliding model in undrained simple shear tests.” *Géotechnique*, 38(4), 533–555.

- Kallstenius, T., and Bergau, W. (1961). "Research on the texture of granular mass." *Proc. 5th Int. Conf. Soil Mech. Found. Eng., Vol. 1.*
- Kavazanjian Jr., E., Matasovic, N., and Bachus, R. C. (1999). "Large-diameter static and cyclic laboratory testing of municipal solid waste." in *Proceedings Sardinia - 7th International Waste Management and Landfill Symposium*, 437–444.
- Kittu, A., and Bernhardt, M. L. (2017). "Effects of Common Boundary Types in Direct Shear Tests." *Geotechnical Frontiers*, 606–614.
- Kjellman, W. (1951). "Testing the Shear Strength of Clay in Sweden." *Géotechnique*, 2(3), 225–232.
- Langston, P., Ai, J., and Yu, H. S. (2013). "Simple shear in 3D DEM polyhedral particles and in a simplified 2D continuum model." *Granular Matter*, 15(5), 595–606.
- Lim, W. L., and McDowell, G. R. (2005). "Discrete element modelling of railway ballast." *Granular Matter*, 7(1), 19–29.
- Liu, Y., Zhang, D., Wang, X., Yu, P., and Hu, W. (2019). "Anisotropic strength of granular material considering fabric evolution." *Latin American Journal of Solids and Structures*, 16(3), 1–14.
- Maeda, K., Hirabayashi, H., and Ohmura, A. (2006). "Micromechanical influence of grain properties on deformation-failure of granular media by DEM." *Proceedings of the International Symposium on Geomechanics and Geotechnics of Particulate Media, Ube, Japan.*
- Mao, X., and Fahey, M. (2003). "Behaviour of calcareous soils in undrained cyclic simple shear." *Géotechnique*, 53(8), 715–727.
- Marcuson, W. F. (1978). "Definition of Terms Related to Liquefaction." *Journal of the Geotechnical Engineering Division*, 104(9), 1197–1200.
- Matasovic, N., and Kavazanjian Jr., E. (1998). "CYCLIC CHARACTERIZATION OF OII LANDFILL SOLID WASTE." *Journal of Geotechnical and Geoenvironmental Engineering*, 124(2), 197–210.
- Matsuoka, H., and Liu, S. (1998). "Simplified Direct Box Shear Test on Granular materials and Its Application to Rockfill Materials." *Soils and Foundations*, 38(4), 275–284.
- Mindlin, R. D. (1949). "Compliance of elastic bodies in contact." *Journal of Applied Mechanics, ASME*, 16, 259–268.
- Mindlin, R. D., and Deresiewicz, H. (1953). "Elastic Spheres in Contact Under Varying Oblique Forces." *Journal of Applied Mechanics*, 20, 327–344.
- Mirghasemi, A. A., Rothenburg, L., and Matyas, E. L. (2002). "Influence of particle shape on

- engineering properties of assemblies of two-dimensional polygon-shaped particles.” *Geotechnique*, 52(3), 209–217.
- Mitchell, J. K., and Soga, K. (2005). *Fundamental of soil behavior, 3rd edn.* Chichester: John Wiley.
- Miura, K., Miura, S., and Toki, S. (1986). “Deformation behavior of anisotropic dense sand under principal stress axes rotation.” *Soils and Foundations*, 26(1), 36–52.
- Ng, T.-T. (2001). “FABRIC EVOLUTION OF ELLIPSOIDAL ARRAYS WITH DIFFERENT PARTICLE SHAPES.” 127(10), 994–999.
- Ng, T.-T., and Dobry, R. (1991). *CONBAL - simulated granular material using quartz spheres with the discrete element method. Report to NSF.*
- Ng, T., and Dobry, R. (1994). “Numerical Simulations of Monotonic and Cyclic Loading of Granular Soil.” *Journal of Geotechnical Engineering*, 120(2), 388–403.
- Nikolaou, S., Zekkos, D., Assimaki, D., and Gilsanz, R. (2014). “Earthquake Reconnaissance January 26th/February 2nd 2014 Cephalonia, Greece events Version 1.” *GEER/EERI/ATC.*
- Norris, G., Siddharthan, R., Zafir, Z., and Madhu, R. (1997). “Liquefaction and Residual Strength of Sands from Drained Triaxial Tests.” *Journal of Geotechnical and Geoenvironmental Engineering*, 123(3), 220–228.
- O’Sullivan, C. (2011). “Particulate discrete element modelling: a geomechanics perspective.” *International Journal of Geomechanics*, 11(6), 449–464.
- O’Sullivan, C., Bray, J., and Cui, L. (2006). “Experimental validation of particle-based discrete element methods.” *GeoCongress 2006*, (August), 1–18.
- O’Sullivan, C., Bray, J. D., and Riemer, M. (2004). “Examination of the Response of Regularly Packed Specimens of Spherical Particles Using Physical Tests and Discrete Element Simulations.” *Journal of Engineering Mechanics*, 130(10), 1140–1150.
- O’Sullivan, C., Cui, L., and Stuart, C. (2008). “Discrete Element Analysis of the Response of Granular Materials During Cyclic Loading.” *Soils and Foundations*, 48(4), 511–530.
- Oda, M., and Konishi, J. (1974a). “Microscopic Deformation Mechanism of Granular Material in Simple Shear.” *Soils and Foundations*, 14(4), 25–38.
- Oda, M., and Konishi, J. (1974b). “Rotation of Principal Stresses in Granular material During Simple Shear.” *Soils and Foundations*, 14(4), 39–53.
- Ohm, H. S., and Hryciw, R. D. (2013). “Translucent segregation table test for sand and gravel particle size distribution.” *Geotechnical Testing Journal*, 36(4), 592–605.
- Ouadfel, H. (1998). “Numerical Simulation of Granular Assemblies with Three-Dimensional

- Ellipsoid-Shaped Particles.” PhD Dissertation, University of Waterloo.
- Peacock, W. H., and Seed, H. B. (1968). “Sand liquefaction under cyclic loading simple shear conditions.” *Journal of Soil Mechanics & Foundations Div*, 94(3), 689–708.
- Pickering, D. J. (1973). “Drained liquefaction testing in simple shear.” *Journal of the Soil Mechanics and Foundations Division*, 99(12), 1179–1184.
- Plassiard, J. P., Belheine, N., and Donzé, F. V. (2009). “A spherical discrete element model: Calibration procedure and incremental response.” *Granular Matter*, 11(5), 293–306.
- Porcino, D., Caridi, G., and Ghionna, V. N. (2008). “Undrained monotonic and cyclic simple shear behaviour of carbonate sand.” *Géotechnique*, 58(8), 635–644.
- Poulos, S. J. (1981). “The Steady State of Deformation.” *Journal of Geotechnical Engineering Div. ASCE*, 107, 553–562.
- Powrie, W., Ni, Q., Harkness, R. M. M., and Zhang, X. (2005). “Numerical modelling of plane strain tests on sands using a particulate approach.” *Géotechnique*, 55(4), 297–306.
- Prevost, J.-H., and Høeg, K. (1976). “Reanalysis of simple shear soil testing.” *Canadian Geotechnical Journal*, 13, 418–429.
- Qian, J., Huang, M., and Sun, H. (2011). “Macro-micromechanical approaches for non-coaxiality of coarse grained soils.” *Science China Technological Sciences*, 54(1), 147–153.
- Qian, J., Li, W., Gu, X., and Xu, K. (2017). “Influence of inherent anisotropy on the soil behavior in simple shear test using DEM.” *Proc. of the 7th International Conference on Discrete Element Method*, 777–784.
- La Rochelle, P. (1981). “Limitations of Direct Simple Shear Test Devices.” *Laboratory Shear Strength of Soil, ASTM International*, 653–658.
- Roessler, T., Richter, C., Katterfeld, A., and Will, F. (2019). “Development of a standard calibration procedure for the DEM parameters of cohesionless bulk materials – part I: Solving the problem of ambiguous parameter combinations.” *Powder Technology, The Authors*, 343, 803–812.
- Roscoe, K. H. (1953). “An Apparatus for the Application of Simple Shear to Soil Samples.” *Proceeding of the 3rd International Conference in Soil Mechanics and Foundation Engineering*.
- Roscoe, K. H. (1970). “The influence of strains in soil mechanics.” *Geotechnique*, 20(2), 129–170.
- Roscoe, K. H., Bassett, R. H., and Cole, E. R. . (1967). “principal Axes observed during simple shear of sand.” *Proc. 4th Eur. Conf. Soil Mech. Found. Eng*, 231–237.

- Rothenburg, L., and Bathurst, R. J. (1989). "Analytical study of induced anisotropy in idealized granular material." *Géotechnique*, 39(4), 601–614.
- Rothenburg, L., and Bathurst, R. J. (1992). "Micromechanical features of granular assemblies with planar elliptical particles." *Géotechnique*, 42(1), 79–95.
- Salazar, A., Sáez, E., and Pardo, G. (2015). "Modeling the direct shear test of a coarse sand using the 3D Discrete Element Method with a rolling friction model." *Computers and Geotechnics*, Elsevier Ltd, 67, 83–93.
- Salot, C., Gotteland, P., and Villard, P. (2009). "Influence of relative density on granular materials behavior: DEM simulations of triaxial tests." *Granular Matter*, 11(4), 221–236.
- Sanin, M. V., and Wijewickreme, D. (2006). "Cyclic shear response of channel-fill Fraser River Delta silt." *Soil Dynamics and Earthquake Engineering*, 26(9), 854–869.
- Santamarina, J. C. (2001). "Soil Behavior at Microscale: Particle Forces." *ASCE Proc. Symp. Soil Behavior and Soft Ground Construction, in honor of C.C. Ladd, MIT, GSP 119, ed: Germaine, Sheahan, Whittman.*
- Santamarina, J. C., and Cho, G. C. (2004). "Soil behaviour: The role of particle shape." *Proceedings of Skempton Conference on Advances in Geotechnical Engineering*, (March).
- Satake, M. (1978). "Constitution of mechanics of granular Materials through the graph theory." *Continuum Mechanics and Statistical Approaches in the Mechanics of Granular Materials*, 47–62.
- Sazzad, M., and Suzuki, K. (2010). "Micromechanical behavior of granular materials with inherent anisotropy under cyclic loading using 2D DEM." *Granular Matter*, 12(6), 597–605.
- Shafipour, R., and Soroush, A. (2008). "Fluid coupled-DEM modelling of undrained behavior of granular media." *Computers and Geotechnics*, 35(5), 673–685.
- Shaw, P., and Brown, S. F. (1986). "Cyclic Simple Shear Testing of Granular Materials." *Geotechnical Testing Journal*, 9(4), 213–220.
- Shen, C. K., O'Sullivan, C., and Jardine, R. (2010). "A micromechanical investigation of drained simple shear tests." *Proceedings of the International Symposium on Deformation Characteristics of Geomaterials. Seoul, Korea.*
- Shen, C. K., Sadigh, K., and Herrmann, L. R. (1978). "Analysis of NGI Simple Shear Apparatus for Cyclic Soil Testing." *Dynamic Geotechnical Testing, ASTM Special Technical Publication 654*, 148–162.
- Silver, M. L., and Seed, H. B. (1971). "Deformation characteristics of sands under cyclic loading." *Journal of Soil Mechanics & Foundations Div*, 97(8), 1081–1098.

- Sitharam, T. (2003). "Discrete element modelling of cyclic behaviour of granular materials." *Geotechnical and Geological Engineering*, 21(4), 297–329.
- Sitharam, T. G., Dinesh, S. V., and Shimizu, N. (2002). "Micromechanical modelling of monotonic drained and undrained shear behaviour of granular media using three-dimensional DEM." *International Journal for Numerical and Analytical Methods in Geomechanics*, 26(12), 1167–1189.
- Sitharam, T. G., Jayan, S. V., and Ravishankar, B. V. (2008). "Evaluation of undrained response from drained triaxial shear tests : DEM simulations and experiments." *Geotechnique*, 58(7), 605–608.
- Sitharam, T. G., Vinod, J. S., and Rothenburg, L. (2005). "Shear behavior of glass beads using DEM." *Powders and grains*, 5, 257–260.
- Sivathayalan, S. (1994). "Static, Cyclic and Post Liquefaction Simple Shear Response of Sands." (December), 1–126.
- Sivathayalan, S. (2000). "Fabric, initial state and stress path effects on liquefaction susceptibility of sands." PhD Dissertation, University of British Columbia, Vancouver, BC, Canada.
- Smith, W. O., Foote, P. D., and Busang, P. F. (1929). "Packing of homogeneous spheres." *Physical Review*, 34(9), 1271–1274.
- Strahler, A., Stuedlein, A. W., and Arduino, P. W. (2016). "Stress-Strain Response and Dilatancy of Sandy Gravel in Triaxial Compression and Plane Strain." *Journal of Geotechnical and Geoenvironmental Engineering*, 142(4), 04015098(1–11).
- Sukumaran, B. (1996). "Study of the Effect of Particle Characteristics on the flow Behavior and Strength Properties of Particulate Materials." PhD Dissertation, Purdue University.
- Tatsuoka, F., Pradhan, T. B. S., and Horii, N. (1988). "Discussion on direct shear tests on reinforced sand." *Geotechnique*, 38(1), 148–153.
- Taylor, D. (1948). *Fundamental of Soil Mechanics*. Chapman and Hall, Limited, New York.
- Thornton, C. (2000). "Numerical simulations of deviatoric shear deformation of granular media." *Géotechnique*, 50(1), 43–53.
- Thornton, C., and Zhang, L. (2001). "A DEM comparison of different shear testing devices." *Powders and grains*, 183–190.
- Thornton, C., and Zhang, L. (2003). "Numerical Simulations of the Direct Shear Test using SPH." *International Conference on Geomechanics, Geo-energy and Geo-resources*, 26(2), 153–156.
- Thornton, C., and Zhang, L. (2006). "A numerical examination of shear banding and simple shear non-coaxial flow rules." *Philosophical Magazine*, 86(21–22), 3425–3452.

- Tickell, F. G. (1931). "The examination of fragmental rocks." *Stanford, California, USA: Stanford University Press.*
- Ting, J. M., Corkum, B. T., Kauffman, C. R., and Greco, C. (1989). "Discrete Numerical Model for Soil Mechanics." *Journal of Geotechnical Engineering*, 115(3), 379–398.
- Ting, J. M., Meachum, L., and Rowell, J. D. (1995). "Effect of particle shape on the strength and deformation mechanisms of ellipse shaped granular assemblages." *Engineering Computations*, 12(2), 99–108.
- Vaid, Y., and Chern, J. (1985). "Cyclic and monotonic undrained response of saturated sands." *in Advances in the Art of Testing Soils Under Cyclic Conditions*, ASCE, 120–147.
- Vaid, Y. P., and Sivathayalan, S. (1996). "Static and cyclic liquefaction potential of Fraser Delta sand in simple Shear and triaxial tests." *Canadian Geotechnical Journal*, 33(2), 281–289.
- Vavourakis, V., Loukidis, D., Charmpis, D. C., and Papanastasiou, P. (2013). "Assessment of remeshing and remapping strategies for large deformation elastoplastic Finite Element analysis." *Computers and Structures*, Elsevier Ltd, 114–115, 133–146.
- Verlet, L. (1967). "Computer 'Experiments' on Classical Fluids. I. Thermodynamical Properties of Lennard-Jones Molecules." *Physical Review*, 159(2), 98–103.
- Vincent, L. ., and Soille, P. (1991). "Watersheds in Digital Spaces: An Efficient Algorithm Based on Immersion Simulations." *IEEE Trans. Pattern Anal. Mach. Intell.*, 13(6), 583–598.
- Vucetic, M. (1981). *The influence of height versus diameter ratio on the behaviour of Haga clay in the NGI simple shear device. Internal Rep. No. 56204, 9.*
- Vucetic, M., and Dobry, R. (1988). "Degradation of marine clays under cyclic loading." *Journal of Geotechnical and Geoenvironmental Engineering*, 114(2), 133–149.
- Wang, B., Popescu, R., and Prevost, J. H. (2004). "Effects of boundary conditions and partial drainage on cyclic simple shear test results-a numerical study." *International Journal for Numerical and Analytical Methods in Geomechanics*, 28(10), 1057–1082.
- Wang, G., and Wei, J. (2016). "Microstructure evolution of granular soils in cyclic mobility and post-liquefaction process." *Granular Matter*, Springer Berlin Heidelberg, 18(3), 1–13.
- Wang, R., Fu, P., Tong, Z., Zhang, J.-M., and Dafalias, Y. F. (2017). "Strength anisotropy of granular material consisting of perfectly round particles." *International Journal for Numerical and Analytical Methods in Geomechanics*, 41, 1758–1778.
- Wang, X. L., and Li, J. C. (2014). "Simulation of triaxial response of granular materials by modified DEM." *Science China: Physics, Mechanics and Astronomy*, 57(12), 2297–2308.
- Wang, Y. H., and Mok, C. M. B. (2008). "Mechanisms of Small-Strain Shear-Modulus

- Anisotropy in Soils.” *Journal of Geotechnical and Geoenvironmental Engineering*, 134(10), 1516–1530.
- Wei, J., and Wang, G. (2016). “Evolution of fabric anisotropy in cyclic liquefaction of sands.” *Journal of Micromechanics and Molecular Physics*, 1, 1640005 (1–15).
- Wensrich, C. M., and Katterfeld, A. (2012). “Rolling friction as a technique for modelling particle shape in DEM.” *Powder Technology*, Elsevier B.V., 217, 409–417.
- Wijewickreme, D. (2010). “Cyclic Shear Response of Low Plastic Fraser River Silt.” *Proceedings of the 9th U.S. National and 10th Canadian Conference on Earthquake Engineering*.
- Wijewickreme, D., Dabeet, A., and Byrne, P. (2013). “Some observations on the state of stress in the direct simple shear test using 3d discrete element analysis.” *Geotechnical Testing Journal*, 36(2), 1–8.
- Wijewickreme, D., Sriskandakumar, S., and Byrne, P. (2005). “Cyclic loading response of loose air-pluviated Fraser River sand for validation of numerical models simulating centrifuge tests.” *Canadian Geotechnical Journal*, 42(2), 550–561.
- Wijewickreme, D., and Vaid, Y. P. (1991). “Stress Nonuniformities in Hollow Cylinder Torsional Specimens.” *Geotechnical Testing Journal*, 14(4), 349–362.
- Yamsiri, S., and Soga, K. (2010). “DEM analysis of soil fabric effects on behaviour of sand.” *Géotechnique*, 60(6), 483–495.
- Yang, L. T., Li, X., Yu, H. S., and Wanatowski, D. (2016). “A laboratory study of anisotropic geomaterials incorporating recent micromechanical understanding.” *Acta Geotechnica*, 11(5), 1111–1129.
- Yang, Z. X., Li, X. S., and Yang, J. (2007). “Undrained anisotropy and rotational shear in granular soil.” *Geotechnique*, 57(4), 371–384.
- Yimsiri, S., and Soga, K. (2011). “Effects of soil fabric on behaviors of granular soils: Microscopic modeling.” *Computers and Geotechnics*, Elsevier Ltd, 38(7), 861–874.
- Yoshimine, M., Ishihara, K., and Vargas, W. (1998). “Effects of principal stress direction and intermediate principal stress on undrained shear behavior of sand.” *Soils and Foundations*, 3(3), 179–188.
- Youd, T. E., Harp, E. L., Keefer, D. K., and Wilson, R. C. (1985). “The Borah Peak, Idaho Earthquake of October 28, 1983 Liquefaction.” *Earthquake spectra*, 2(1), 71–89.
- Yu, H. S., Yang, L. T., Li, X., and Wanatowski, D. (2016). “Experimental investigation on the deformation characteristics of granular materials under drained rotational shear.” *Geomechanics and Geoengineering*, Taylor & Francis, 11(1), 47–63.

- Zekkos, D., Athanasopoulos-Zekkos, A., Hubler, J., Fei, X., Zehtab, K. H., and Allen Marr, W. (2018). "Development of a large-size cyclic direct simple shear device for characterization of ground materials with oversized particles." *Geotechnical Testing Journal*, 41(2), 263–279.
- Zekkos, D., and Fei, X. (2017). "Constant load and constant volume response of municipal solid waste in simple shear." *Waste Management*, Elsevier Ltd, 63, 380–392.
- Zhang, L., and Evans, T. M. (2018). "Boundary effects in discrete element method modeling of undrained cyclic triaxial and simple shear element tests." *Granular Matter*, Springer Berlin Heidelberg, 20(4).
- Zhao, X., and Evans, T. M. (2009). "Discrete Simulations of Laboratory Loading Conditions." *International Journal of Geomechanics*, 9(4), 169–178.
- Zhao, X., and Evans, T. M. (2011). "Numerical analysis of critical state behaviors of granular soils under different loading conditions." *Granular Matter*, 13(6), 751–764.
- Zheng, J., He, H., and Li, Z. (2020). "Explanations of anisotropic strength and fabric evolution in granular soils by DEM simulations and buckling failure theory." *Geomechanics and Geoengineering*, Taylor & Francis, 00(00), 1–15.
- Zheng, J., and Hryciw, R. D. (2015). "Traditional soil particle sphericity, roundness and surface roughness by computational geometry." *Géotechnique*, 65(6), 494–506.
- Zhou, B., Huang, R., Wang, H., and Wang, J. (2013). "DEM investigation of particle anti-rotation effects on the micromechanical response of granular materials." *Granular Matter*, 15(3), 315–326.
- Zhuang, X., and Goddard, J. D. (1993). "Computer Simulation and Experiments on Quasi-Static Mechanics and Transport Properties of Granular Materials." University of California, San Diego.